



ADVANCED MASTERS IN STRUCTURAL ANALYSIS
OF MONUMENTS AND HISTORICAL CONSTRUCTIONS

Master's Thesis

Massimo Toesca

Thermo-Mechanical Analysis of Charles Bridge in Prague



Czech Technical University
in Prague



University of Minho



Education and Culture

Erasmus Mundus

ADVANCED MASTERS IN STRUCTURAL ANALYSIS
OF MONUMENTS AND HISTORICAL CONSTRUCTIONS

Master's Thesis

Massimo Toesca

Thermo-Mechanical Analysis of Charles Bridge in Prague

This Masters Course has been funded with support from the European Commission. This publication reflects the views only of the author, and the Commission cannot be held responsible for any use which may be made of the information contained therein.

DECLARATION

Name: Massimo Toesca

Email: Toesca.ma@gmail.com

Title of the Thermo-Mechanical Analysis of Charles Bridge in Prague
Msc Dissertation:

Supervisor(s): Eng. Tomáš Krejčí, Ph.D.

Year: 2014

I hereby declare that all information in this document has been obtained and presented in accordance with academic rules and ethical conduct. I also declare that, as required by these rules and conduct, I have fully cited and referenced all material and results that are not original to this work.

I hereby declare that the MSc Consortium responsible for the Advanced Masters in Structural Analysis of Monuments and Historical Constructions is allowed to store and make available electronically the present MSc Dissertation.

University: CVUT – Prague

Date: 25/07/2014

Signature:

A te.

So ne saresti fiero,

di nuovo.

ACKNOWLEDGEMENTS

This year was unimaginable and inspiring but also arduous. Surely I would not be here, right now, without the support received from many people and institutions.

First of all I am grateful to my supervisor, Eng. Tomáš Krejčí, who followed me from my arrival in Prague with competence, ability, support and enthusiasm about the developed work. Many thanks also to Professor Petr Kabele, who advised me many times and was exhausting in answering to every doubt. I would like also to thank our Secretary, Mrs. Alexandra Kurfurstova, for its prompt help during my staying in Prague, as well as Mrs. Ana Fonseca, who had same role in Guimarães.

Sincere gratitude to the MSc Consortium for the scholarship they provided me, indispensable support without which I would not have been able to begin this memorable experience.

My thanks to Professor Pere Roca and Luca Pelà who organized the integration week in Barcelona, together with Professor Paulo Lourenço. A great acknowledgement to the latter, whose enthusiasm made the course possible from many years ago. I sincerely admire what he and his colleagues made to allow students to go further in our favourite engineering field. I would also like to record my thanks to Professor Luis Ramos, who followed us in the applicative project. His teaching, as that of all the other Professors met in University of Minho, was deep and skilful, giving us the priceless chance to become better Engineers and Architects. The SAHC MSc was not only this: to live one year in an international and vibrant environment gave us the opportunity to become also better people, demolishing differences and prejudices, stimulating reflections and comparisons, bringing to an harmony that cannot be described, has to be lived.

I will never forget all the people met during this year, we enjoyed and faced unexpected difficulties together, I am sure the bond with some of them will last for a long time. A special thanks to Susana, who followed me in part of the path, enriching my professional and private life. My gratitude to all my friends, especially to Federica, Pablo, Ruggero and Michele who welcome me with open arms every time it was possible, allowing me not to loose the feeling of belonging home, but also to Alice, for its constant and essential presence in my life and to Kseniya for sharing always the right thought to go on in front of difficulties. All in all thanks to Karolina, Andrea, Marco, Ilaria, Asuka, Liv, Giulia, Licia, Alberto and Annamaria who did their best as me to stay in touch despite the distance, supporting me a lot.

Finally, I thank my family, who always believes in me, and supports me in all possible ways. Only thanks to them I undertook this career and I was able to arrive till here. I deeply love and respect them, wishing they could be always proud of me.

ABSTRACT

Thermo-Mechanical Analysis of Charles Bridge in Prague

Charles Bridge, icon of Prague, is an outstanding stone masonry arch structure. Peter Parléř built it in 1357–1406, for the will of Charles IV, Holy Roman Emperor. The task was to connect two Prague districts, the Lesser Town and the Old Town, detached by the Vltava River.

During its life, the bridge withstood erosion, floods and wars, suffering several damages and repairs. It was accessible by vehicles till 1967, when it was pedestrianized.

The actual structure is strongly influenced by the interventions of last Century, namely the reconstruction of 1960s–1970s (grouting, introduction of water-proofing layer, installation of stabilising reinforced concrete slab, replacement of facing masonry) and more recent actions.

The last intervention is dated 2007–2010 and it included repair of parapets, hydro-isolation of the pavement, introduction of dilatation joints, and rehabilitation of foundations. Computational and experimental studies suggested climatic loading as main cause of the actual damage on the structure, therefore in that occasion a measuring system (able to record temperature and moisture content at selected gauge points) was installed. This provided yearly records that were used as temperature cycle input for the numerical analysis.

The mechanical behavior of Charles Bridge influenced by climatic loading is reproduced by a finite element analysis based on a provided simulation of heat transfer using in situ measurements. The investigation is focused only on one representative bridge segment (arch No. 3).

After a thermo-elastic analysis to validate the model and the procedure, the non-linear analysis is run with two different software (Adina and SIFEL) in way to compare the results. The most damages areas are identified in parapets and breast walls; among the seasons, winter provokes worst conditions. The analysis is repeated with different damage models and strain norms to reach a reliable damage distribution. The study is performed on two different 3D models, in way to compare the behavior before/after the last rehabilitation, able to change the damage distribution but not always to reduce it.

The possible crack nucleation is then studied on a more years cycle in way to predict its potential development.

The main achievements are finally generalized for similar structures, and hypothesis for the rehabilitation are provided. Furthermore, a simple numerical calculation (finite difference method) is applied on a breast wall to consider the problem from a different point of view.

Keywords: masonry arch bridge, heat transfer, damage model, temperature cycling effect, Finite Element Analysis, thermo-elastic analysis, non-linear analysis, strain norm, rehabilitation, prognosis of crack evolution, Finite Difference Method

ABSTRAKT

Tepelně mechanická analýza Karlova mostu v Praze

Karlův most spojující Staré Město a Malou Stranu patří k nevýznamnějším historickým stavbám ve střední Evropě. Byl vybudován v letech 1357 až 1406. Císař Karel IV. svěřil jeho výstavbu Petru Parléřovi. Most sloužil Praze do roku 1967 jako obchodní a dopravní tepna. Dnes je určen pouze chodcům a turistům. Po staletí odolával most mnoha pohromám - erozí, povodní i válkám. Prošel několika poškozeními a následnými opravami. Současná stavba byla nejvíce ovlivněna poslední opravou v minulém století, v letech 1960 až 1970. Zhotovila se ztužující železobetonová deska, vložily hydroizolační vrstvy, vyměnily nejvíce poškozené kamenné bloky. Byla provedena injektáž podloží a mnohé další opravy.

Poslední rekonstrukce mostu proběhla v období 2007 až 2010. V této době se opravily zejména parapety, zábradlí mostu a nichvyměnily kamenné bloky. Byla zcela zrekonstruována hydroizolace mostu a vytvořeny nové dilatační spáry v zábradlích a mezi vnějším pláštěm a vrstvami mostovky a v železobetonové desce. Navíc byla provedena rekonstrukce základů. Výsledky numerických a experimentálních studií, které doprovázely poslední rekonstrukci mostu, ukazují na klimatické vlivy jako na největší původce poškození mostu. Z tohoto důvodu byl během zmíněné rekonstrukce instalován měřící systém, který zaznamenává aktuální teploty a obsah vlhkosti ve vybraných místech. Tato měření slouží jako základ pro následné numerické analýzy předpovědi chování mostu.

Cílem této práce je simulace mechanické odezvy Karlova mostu pomocí metody konečných prvků s využitím výsledků měření teplot přímo v konstrukci mostu ovlivněné klimatickými podmínkami. Numerická analýza je zaměřena pouze na reprezentativní trojrozměrný model Karlova mostu - polovinu třetího oblouku, pro který jsou pro srovnání uvažovány dva modely. První model odpovídá stavu před poslední rekonstrukcí a druhý stavu po poslední rekonstrukci, ve kterém jsou uvažovány nově vybudované dilatační spáry. Po počáteční tepelně elastické analýze, jejímž úkolem bylo ověřit funkčnost modelu, následovalo srovnání výsledků vypočtených dvěma různými programy (komerčním ADINA a volně šířitelným SIFEL) pomocí nelineární analýzy. Výsledky této nelineární analýzy ukazují zóny možného poškození v parapetech a zábradlích a v poprsních stěnách. Zóny s větším poškozením se jeví pro teploty v zimním období. Pro získání spolehlivých výsledků je navíc analýza provedena pro různé modely poškození s různými přístupy výpočtu ekvivalentních deformací. Následně je analýza rozšířena pomocí víceletých teplotních cyklů, které mají za úkol předpovědět možný rozvoj a vznik trhlin. V závěru této práce jsou výsledky studie zobecněny pro podobné mostní konstrukce a jsou navrženy možné postupy oprav. Mimoto je jako jednoduchý nástroj pro získání představy o rozložení napětí v konstrukcích nastíněn jednoduchý výpočet napjatosti v poprsní stěně od zatížení změnou teploty pomocí metody sítí.

Klíčová slova: kamenný most, přenos tepla, model poškození, efekt teplotních cyklů, tepelně elastická analýza, nelineární úloha, norma deformace, sanace, prognóza rozvoje trhlin, metoda sítí

ABSTRACT

Analisi termo-mecanica del Ponte Carlo a Praga

Il Ponte Carlo, icona di Praga, è un notevole struttura ad archi in muratura di pietra. Fu costruito da Peter Parléř tra il 1357 ed il 1406, per volere di Carlo IV, Imperatore del Sacro Romano Impero. L'obiettivo fu quello di connettere 2 zone di Praga sulle sponde opposte del Moldava, la Città Minore e la Città Antica.

Durante la sua vita, il ponte sopportò erosione, piene e guerre, venendo danneggiato e ricostruito svariate volte. Fu accessibile al traffico carrabile fino al 1967, quando fu reso unicamente pedonale.

La struttura è fortemente influenzata dagli inteventi subiti durante l'ultimo secolo, in particolare dalla ricostruzione degli anni '60 e '70 (iniezioni di malta, impermeabilizzazione, soletta in calcestruzzo armato, sostituzione elementi danneggiati della muratura) e azioni successive.

L'ultimo intervento è datato 2007–2010 e riguardò: riparazione dei parapetti, impermeabilizzazione del pavimento, introduzione di giunti di dilatazione e riabilitazione delle fondazioni. Studi computazionali e sperimentali identificarono il carico termico come causa principale dei danni presenti nella struttura, per questo in quell'occasione fu installato anche un sistema di misurazione (in grado di registrare temperatura e percentuale di umidità in diversi nodi). Questo fornì registrazioni annue, utilizzate poi come input ciclico di temperatura per l'analisi numerica.

Il comportamento meccanico del Ponte Carlo sotto l'influenza del carico termico è riprodotto grazie ad una analisi agli elementi finiti, basata su una (ornita simulazione di trasferimento di calore (usando le misurazioni in situ). Lo studio è concentrato su un solo segmento rappresentativo del ponte (arco No. 3). Dopo un analisi termo-elastica per validare il modello e la procedura, l'analisi non lineare è performata con 2 differenti software (Adina e SIFEL) per compararne i risultati. Le aree più degradate sono localizzate in parapetti e murature di spalla; tra le stagioni, l'invernale è quella che cause le condizioni peggiori. L'analisi è ripetuta con diversi modelli di danno ed approssimazioni della deformazione al fine di raggiungere una ragionevole distribuzione della degradazione. Lo studio è sviluppato con 2 differenti modelli 3D, in modo da comparare il comportamento prima/dopo l'ultima riabilitazione, capace di cambiare la distribuzione del danno ma non sempre di attenuarlo. Il possibile sviluppo di fessurazioni è poi studiato su un ciclo di più anni, per predirne il potenziale andamento.

I principali risultati sono infine generalizzati per strutture simili e sono fornite alcune ipotesi di intervento. Inoltre, un semplice metodo numerico (metodo delle differenze finite) è applicato ad una muratura di spalla per considerarne il problema da un differente punto di vista.

Parole chiave: ponte in muratura, trasferimento di calore, modello di danno, effetti ciclici della temperatura, analisi agli elementi finiti, analisi termo-elastica, analisi non lineare, riabilitazione strutturale, prognosi dell'evoluzione del danno, metodo alle differenze finite

TABLE OF CONTENTS

Index of Chapters

1	INTRODUCTION	1
1.1	Work plan	2
2	THE MONUMENT	3
2.1	History	3
2.2	Materials.....	5
2.3	Structural elements	6
2.4	Damages and repairs	8
2.4.1	The last intervention	12
2.5	Current damage state and causes	15
2.6	Monitoring of temperature field.....	18
2.6.1	Monitoring of deformations	20
3	MODELING	21
3.1	Introduction.....	21
3.2	FEM model	22
3.3	Material properties	24
3.4	Actions	25
3.4.1	Self-weight	25
3.4.2	Thermal load	25
4	THERMO-MECHANICAL ANALYSIS	27
4.1	Thermo-Elastic analysis.....	27
4.1.1	Temperature loading	28
4.1.2	Displacements	29
4.1.3	Stresses	31
4.1.4	Comparison: mechanical boundary conditions	33
4.1.5	Inner material	35
4.1.6	Comparison: structure pre/post repair	35
4.1.7	Comparison: linear analysis with two different software.....	37
4.2	Non-linear analysis (Adina)	39
4.2.1	Mechanical properties for non-linear analysis.....	39
4.2.2	Results: temperature combination A	39
4.2.3	Results: temperature combination B	42
4.3	Non-linear analysis (SIFEL) – Isotropic scalar damage model	45
4.3.1	Temperature combination A.....	46
4.3.2	Temperature combination B.....	46
4.3.3	Temperature combination C	49
4.3.4	Temperature combination D	49

4.3.5	Software comparison.....	52
4.4	Non-linear analysis (SIFEL) – Orthotropic damage model	53
4.4.1	Temperature combination A (Rankine norm)	54
4.4.2	Temperature combination A (simple equivalent strain norm).....	57
4.4.3	Temperature combination B (Rankine norm)	58
4.4.4	Temperature combination B (simple equivalent strain norm).....	60
4.5	Non-linear analysis (SIFEL) – One year cycle	62
4.5.1	Second year of computation	67
4.5.2	Further years of computation	69
4.6	Model refinement.....	74
4.6.1	Boundary conditions for heat transfer analysis.....	74
4.6.2	Non-local approach	74
4.6.3	Approximation of cracks interaction (Kachanov model)	75
4.7	Simple numerical approach (finite difference method)	76
4.7.1	Results	78
4.7.2	Comparison with finite element analysis	82
5	CONCLUSIONS	83
5.1	Generalization and alternative solutions.....	83
6	REFERENCES	87
7	ANNEXES	89
7.1	Thermo-Elastic analysis.....	89
7.1.1	Comparison between Adina and SIFEL	89
7.1.2	Definitive properties and models comparison	92
7.1.3	Connection parapet – pier	94
7.2	Continuum damage mechanics	95
7.2.1	Isotropic scalar damage model	95
7.2.2	Isotropic scalar damage model: implementation in SIFEL	97
7.2.3	Isotropic damage model for concrete	98
7.2.4	Concrete damage model (Adina)	99
7.2.5	Anisotropic damage model	100
7.2.6	Implementation in the software (SIFEL)	101
7.3	Non-linear analysis	102
7.3.1	Low-speed dynamics (feature of Adina)	102
7.3.2	Comparison: one year cycle and computation from average values (SIFEL)	103
7.3.3	Temperature steps	105
7.4	Finite difference method (stretching of a plate)	107
7.4.1	Further development	110
7.5	Rehabilitation	112

Index of Tables

Table 2.1 – History of Charles Bridge and interventions, based on (Zeman, 2008) and (Prikryl, 2011)	9
Table 2.2 – Maximum values of one-day (Δ_{day}) and one-month (Δ_{month}) deformations of the structure....	20
Table 3.1 – Homogenized parameters (Sejnoha, 2006) of the materials related to post 1975 state	24
Table 3.2 – Mechanical properties of implemented materials (state before 1960's)	24
Table 3.3 – Mechanical properties of implemented material (state after 2010)	25
Table 4.1 – Temperatures and variations.....	28
Table 4.2 – Thermo-elastic analysis, maximum vertical displacements (values in mm), Config. A	29
Table 4.3 – Thermo-elastic analysis, transversal displacements (values in mm), Config. A	31
Table 4.4 – Principal stresses and strains for the different elastic analysis, Config. A.....	31
Table 4.5 – Max. displacements related to different temp. combinations (compare to Par.4.1)	33
Table 4.6 – Principal stresses for the different combinations.....	34
Table 4.7 – Structure before 1960: maximum displacements related to the different combinations.....	35
Table 4.8 – Structure before 1960: principal stresses for the different combinations.....	35
Table 4.9 – Structure after 2010: maximum displacements related to the different combinations.....	36
Table 4.10 – Structure after 2010: principal stresses for the different combinations.....	36
Table 4.11 – Mechanical parameters of materials (related to the post 1975 state).....	37
Table 4.12 – Mechanical properties of implemented materials (after 2010 state).....	37
Table 4.13 – Comparison of principal stress (smoothed) for combinations (2010 mod.)	38
Table 4.14 – Material properties for stress-strain relation in concrete model	39
Table 4.15 – Stresses and displacements for different time steps of 1975 model and of 2010 model ..	40
Table 4.16 – Stresses and displacements for different time steps of 1975 model and 2010 model	42
Table 4.17 – Material properties for stress-strain relation in isotropic scalar damage model	45
Table 4.18 – Maximum displacements, stresses and damage for both models (Comb. A).....	46
Table 4.19 – Maximum displacements, stresses and damage for both models (Comb. B).....	46
Table 4.20 – Maximum displacements, stresses and damage for both models (Comb. C).....	49
Table 4.21 – Maximum displacements, stresses and damage for both models (Comb. D).....	49
Table 4.22 – Material properties for stress-strain relation in orthotropic damage model.....	53
Table 4.23 – Maximum displacements, stresses and damage for both models (Comb. A).....	54
Table 4.24 – Maximum displacements, stresses and damage for both models (Comb. A).....	57
Table 4.25 – Maximum displacements, stresses and damage for both models (Comb. B).....	58
Table 4.26 – Maximum displacements, stresses and damage for both models (Comb. B).....	60
Table 4.27 – Maximum displacements, stresses and damage for 1975 model	62
Table 4.28 – Maximum displacements, stresses and damage for 2010 model	64
Table 4.29 – Maximum displacements, stresses and damage for 2010 model (second year)	67
Table 4.30 – Maximum displacements, stresses and damage for 2010 model (summer results)	70
Table 4.31 – Maximum displacements, stresses and damage for 2010 model (winter results).....	70
Table 4.32 – Vertical maximum displacement of node 64213 and horizontal max. displ. of 71701.....	70
Table 4.33 – Maximum damage parameter and crack width for element 311678 (summer results)	71
Table 4.34 – Maximum damage parameter and crack width for element 311678 (winter results).....	71
Table 7.1 – Comparison of maximum displacements considering only selfweight (1975 model)	89
Table 7.2 – Comparison of maximum dispacements for all the thermal combinations (1975 model) ...	89
Table 7.3 – Comparison of max. principal stresses (unsmoothed) for combinations	90
Table 7.4 – Comparison of max. principal stresses (smoothed) for combinations	90

Index of Figures

Figure 1.1 – View of the Bridge from South; St. Vitus Chatedral and the Castle on the background	1
Figure 2.1 – Comparison between Charles Bridge and the previous Judith's Bridge	3
Figure 2.2 – Position of Karluv Most, between Most Legii and Manesuv Most.....	4
Figure 2.3 – Bridges in the city centre (Charles Bridge is the second one)	4
Figure 2.4 – Periodic sandstone	5
Figure 2.5 – Non-periodic sandstone	5
Figure 2.6 – Filling	5
Figure 2.7 – 3D view of the Bridge with A–A section (Sýkora, 2012)	6
Figure 2.8 – Elements in A–A section.....	6
Figure 2.9 – Cross-section at the top of the arch before the last repair (Zak, 1995).....	6
Figure 2.10 – Position of the sampling sites on Charles Bridge (Přikryl, 2010)	7
Figure 2.11 – Cross–section through the fill masonry of arch XIV (Přikryl, 2010), in mm	7
Figure 2.12 – Results of the main floods.....	8
Figure 2.13 – Flood in 1872	8
Figure 2.14 – The 1890 flood, collapse of 3 bridge vaults (Zeman, 2008).....	8
Figure 2.15 – Schematization of the bridge elements (Zeman, 2008).....	9
Figure 2.16 – Bridge section after the 1960s–1970s intervention	10
Figure 2.17 – Replacement of the layers upon vault	11
Figure 2.18 – Suggested prestressing (V. Křížek, 2012)	11
Figure 2.19 – Works on the foundation of pillars 8th and 9th with mechanization from water lever	12
Figure 2.20 – Detail of the connection between parapet and pavement (Mott MacDonald, 2011)	13
Figure 2.21 – Work into chess-like sections.....	14
Figure 2.22 – Dilatation joint and contrast between old/new blocks	14
Figure 2.23 – Historical section of the bridge	16
Figure 2.24 – 1966–1975 intervention (Witzany, 2008).....	16
Figure 2.25 – Composition of the bridge body filling layers as recorded in test holes in 2000	17
Figure 2.26 – Tension joints and shear cracks in the face surface of vault arch IX (Witzany, 2007) ...	17
Figure 2.27 – Selected cross-sections for monitoring side (Krejci, 2014).....	18
Figure 2.28 – CR.-SEC. No. 3 (11 gauge points = 33 temperature sensors and 11 moisture)	18
Figure 2.29 – CR.-SEC. No. 4 (15 gauge points = 45 temperature sensors and 15 moisture)	19
Figure 3.1 – After 70's model divided by groups (southern side)	22
Figure 3.2 – Model with wire-frame	22
Figure 3.3 – Plant view of the model (measures in metres).....	22
Figure 3.4 – Lateral elevation of the model (m).....	22
Figure 3.5 – Cross-section at the crown of the arch (measures in metres)	23
Figure 3.6 – After 70's model, meshed (northern side)	23
Figure 3.7 – After 2010 model, meshed (northern side)	23
Figure 3.8 – Spatial distribution of temperatures during summer at the crown of the arch	26
Figure 3.9 – Spatial distribution of temperatures during summer in the pier (Krejci, 2014).....	26

Figure 4.1 – Initial temperature condition (northern side)	28
Figure 4.2 – Initial temperature condition (southern side).....	28
Figure 4.3 – Summer temperatures	28
Figure 4.4 – Winter temperatures	28
Figure 4.5 – Z-displacement, Comb. C	29
Figure 4.6 – Z-displacement, Comb. D	29
Figure 4.7 – Temperature measurements in CR.-SEC. No 4 (compare to Figure 2.29)	30
Figure 4.8 – X-displacement, Comb. C	30
Figure 4.9 – X-displacement, Comb. D	30
Figure 4.10 – Maximum and minimum principal stresses (smoothed), related to only self-weight	32
Figure 4.11 – Maximum and minimum principal stresses (smoothed), Comb. C	32
Figure 4.12 – Maximum and minimum principal stresses (smoothed), Comb. D	32
Figure 4.13 – X and Y displacement with deformed shape (Comb. C: from average to summer).....	33
Figure 4.14 – X and Y displacement with deformed shape (Comb. D: from average to winter)	33
Figure 4.15 – Maximum (σ_1) and minimum (σ_3) principal stress (smoothed), Comb.C	34
Figure 4.16 – σ_1 , Comb.A	34
Figure 4.17 – Maximum (σ_1) and minimum (σ_3) principal stress (smoothed), Comb. D	34
Figure 4.18 – σ_3 , Comb.B	34
Figure 4.19 – Maximum principal stress, Comb. C	35
Figure 4.20 – Minimum principal stress, Comb. D	35
Figure 4.21 – Maximum and minimum principal stress (smoothed), Comb. C (structure after 2010) ...	36
Figure 4.22 – Maximum and minimum principal stress (smoothed), Comb. D (structure after 2010) ...	37
Figure 4.23 – σ_1 , Comb. C, 1975 model	38
Figure 4.24 – σ_1 , Comb. C, 2010 model	38
Figure 4.25 – σ_3 , Comb. C, 1975 model	38
Figure 4.26 – σ_3 , Comb. C, 2010 model	38
Figure 4.27 – Tensile and compressive stress plots (Comb. A)	40
Figure 4.28 – Evolution of the release of stresses on the pavement (time steps: 1.875 2.00 3.00)....	40
Figure 4.29 – Crack flag and number of cracks in 1975 model (Comb. A)	41
Figure 4.30 – Crack evolution at step 4 of 25, 7 of 25, 8 of 25 and 25 of 25	41
Figure 4.31 – Crack flag and number of cracks in 2010 model (Comb. A)	41
Figure 4.32 – Strain plot, 1975 Model (Comb. A)	42
Figure 4.33 – Strain plot, 2010 model (Comb. A)	42
Figure 4.34 – Tensile and compressive stress plots (Comb. A), 1975 model.....	42
Figure 4.35 – Evolution of the release of tension on the pavement (time steps: 0.5 1.5 2.5)	43
Figure 4.36 – Crack evolution (Comb. B)for different steps	43
Figure 4.37 – Crack flag and number of cracks in 1975 model (Comb. B)	43
Figure 4.38 – Crack flag and number of cracks in 2010 model (Comb. B)	44
Figure 4.39 – Strain plot, 1975 Model (Comb. B)	44
Figure 4.40 – Strain plot, 2010 model (Comb. B)	44
Figure 4.41 – Strain plot, 1975 Model (Comb. B)	44

Figure 4.42 – Strain plot, 2010 model (Comb. B)	44
Figure 4.43 – Max. princ. stress (1975 model), Comb. A	47
Figure 4.44 – Max. princ. stress (2010 model), Comb. A	47
Figure 4.45 – Damage parameter (1975 model), Comb. A.....	47
Figure 4.46 – Damage parameter (2010 model), Comb. A.....	47
Figure 4.47 – Crack width (m) (1975 model), Comb. A	47
Figure 4.48 – Crack width (m) (2010 model), Comb. A	47
Figure 4.49 – Max. princ. stress (1975 model), Comb. B	48
Figure 4.50 – Max. princ. stress (2010 model), Comb. B	48
Figure 4.51 – Damage parameter (1975 model), Comb. B.....	48
Figure 4.52 – Damage parameter (2010 model), Comb. B.....	48
Figure 4.53 – Crack width (m) (1975 model), Comb. B	48
Figure 4.54 – Crack width (m) (2010 model), Comb. B	48
Figure 4.55 – Max. princ. stress (1975 model), Comb.C	50
Figure 4.56 – Max. princ. stress (2010 model), Comb.C	50
Figure 4.57 – Damage par. (1975 model), Comb. C	50
Figure 4.58 – Damage par. (2010 model), Comb. C	50
Figure 4.59 – Crack width (m) (1975 model), Comb. C	50
Figure 4.60 – Crack width (m) (2010 model), Comb. C	50
Figure 4.61 – Max. princ. stress (1975 mod.), Comb. D.....	51
Figure 4.62 – Max. princ. stress (2010 mod.), Comb. D	51
Figure 4.63 – Damage parameter (1975 mod.), Comb. D	51
Figure 4.64 – Damage parameter (2010 mod.), Comb.D	51
Figure 4.65 – Crack width (m) (1975 model), Comb. D	51
Figure 4.66 – Crack width (m) (2010 model), Comb. D	51
Figure 4.67 – Max. princ. stress (1975 model), Comb. A	55
Figure 4.68 – Max. princ. stress (2010 model), Comb. A	55
Figure 4.69 – Damage par. P1 (1975 mod.), Comb. A.....	55
Figure 4.70 – Damage par. P1 (2010 mod.), Comb. A	55
Figure 4.71 – Damage par. P2 (1975 mod.), Comb. A	55
Figure 4.72 – Damage par. P2 (2010 mod.), Comb. A	55
Figure 4.73 – Crack width P1 (1975 model), Comb. A	56
Figure 4.74 – Crack width P1 (2010 model), Comb. A	56
Figure 4.75 – Crack width P2 (1975 model), Comb. A	56
Figure 4.76 – Crack width P2 (2010 model), Comb. A	56
Figure 4.77 – Crack width P1 (1975 model), Comb. A	57
Figure 4.78 – Crack width P1 (2010 model), Comb. A	57
Figure 4.79 – Crack width P2 (1975 model), Comb. A	58
Figure 4.80 – Crack width P2 (2010 model), Comb. A	58
Figure 4.81 – Max. princ. stress (1975 model), Comb. B	59
Figure 4.82 – Max. princ. stress (2010 model), Comb. B	59

Figure 4.83 – Damage par. P1 (1975 mod.), Comb. B	59
Figure 4.84 – Damage par. P1 (2010 mod.), Comb. B	59
Figure 4.85 – Damage par. P2 (1975 mod.), Comb. B	59
Figure 4.86 – Damage par.P2 (2010 mod.), Comb. B	59
Figure 4.87 – Crack width P1 (1975 model), Comb. B	60
Figure 4.88 – Crack width P1 (2010 model), Comb. B	60
Figure 4.89 – Crack width P2 (1975 model), Comb. B	60
Figure 4.90 – Crack width P2 (2010 model), Comb. B	60
Figure 4.91 – Crack width P1 (1975 model), Comb. B	61
Figure 4.92 – Crack width P1 (2010 model), Comb. B	61
Figure 4.93 – Crack width P2 (1975 model), Comb. B	61
Figure 4.94 – Crack width P2 (2010 model), Comb. B	61
Figure 4.95 – Crack width P1, 1975 model (26/08/11)	63
Figure 4.96 – Crack width P1, 1975 model (10/11/11)	63
Figure 4.97 – Crack width P1,1975 model (07/01/12)	63
Figure 4.98 – Crack width P1, 1975 model (12/02/12)	63
Figure 4.99 – Crack width P2, 1975 model (26/08/11)	63
Figure 4.100 – Crack width P2, 1975 model (10/11/11)	63
Figure 4.101 – Crack width P2,1975 model (07/01/12)	64
Figure 4.102 – Crack width P2, 1975 model (10/11/11)	64
Figure 4.103 – Crack width P1, 2010 model (26/08/11)	65
Figure 4.104 – Crack width P1, 2010 model (10/11/11)	65
Figure 4.105 – Crack width P1,2010 model (07/01/12)	65
Figure 4.106 – Crack width P1, 2010 model (12/02/12)	65
Figure 4.107 – Crack width P2, 2010 model (26/08/11)	65
Figure 4.108 – Crack width P2, 2010 model (10/11/11)	65
Figure 4.109 – Crack width P2,2010 model (07/01/12)	66
Figure 4.110 – Crack width P2, 2010 model (10/11/11)	66
Figure 4.111 – Displacements on 10/06/2011 and 30/07/2011.....	66
Figure 4.112 – Displacements on 26/08/2011 and 10/11/2011.....	66
Figure 4.113 – Displacements on 07/01/2012 and 12/02/2012.....	66
Figure 4.114 – Crack width P1 (2010 mod.), 26/08/2011	68
Figure 4.115 – Crack width P1 (2010 mod.), 26/08/2012	68
Figure 4.116 – Crack width P2 (2010 mod.), 26/08/2011	68
Figure 4.117 – Crack width P2 (2010 mod.), 26/08/2012	68
Figure 4.118 – Crack width P1 (2010 model), 12/02/2012.....	69
Figure 4.119 – Crack width P1 (2010 model), 12/02/2013.....	69
Figure 4.120 – Crack width P2 (2010 model), 12/02/2012.....	69
Figure 4.121 – Crack width P2 (2010 model), 12/02/2013.....	69
Figure 4.122 – Displacements on control nodes 64213 (Z direction) and 71701 (X direction)	70
Figure 4.123 – Damage parameter evolution on control element 311678 in direction P1 and P2.....	71

Figure 4.124 – Crack width evolution on control element 311678 in direction P1 and P2.....	71
Figure 4.125 – Damage par.P1 (2010 mod.), 26/08/2012	72
Figure 4.126 – Damage par.P1 (2010 mod.), 26/08/2015	72
Figure 4.127 – Dam. par.P2 (2010 mod.), 26/08/2012	72
Figure 4.128 – Dam. par.P2 (2010 mod.), 26/08/2015	72
Figure 4.129 – Damage par.P1 (2010 mod.), 12/02/2013	73
Figure 4.130 – Damage par.P1 (2010 mod.), 12/02/2016	73
Figure 4.131 – Damage par.P2 (2010 mod.), 12/02/2013	73
Figure 4.132 – Damage par.P2 (2010 mod.), 12/02/2016	73
Figure 4.133 – Set up of boundary conditions and finite difference mesh.....	76
Figure 4.134 – Thermal loading acting on the fictitious frame (summer temperatures)	77
Figure 4.135 – Bending moment and axial force diagrams (summer temperatures)	77
Figure 4.136 – Thermal loading acting on the fictitious frame (winter temperatures).....	77
Figure 4.137 – Bending moment and axial force diagrams (winter temperatures).....	77
Figure 4.138 – Principal stresses direction (summer condition).....	78
Figure 4.139 – Principal stresses direction (winter condition).....	79
Figure 4.140 – Stresses in section line "b"-“p" (summer condition).....	80
Figure 4.141 – Stresses in section line "f"-“l" (summer condition).....	80
Figure 4.142 – Stresses in section line "u"-“i" (summer condition)	80
Figure 4.143 – Stresses in section line "b"-“p" (winter condition)	81
Figure 4.144 – Stresses in section line "f"-“l" (winter condition)	81
Figure 4.145 – Stresses in section line "u"-“i" (winter condition)	81
Figure 5.1 – Concept of reconstruction of stone bridge body (Witzany, 2008)	85
Figure 7.1 – σ_1 (Comb. B, only temperatuer effects).....	90
Figure 7.2 – σ_1 (Comb. B).....	90
Figure 7.3 – Element No. 344566 (axonometric view).....	91
Figure 7.4 – Element No. 344566 (plane view)	91
Figure 7.5 – Maximum principal stress in the fine grained concrete layer (Adina).....	91
Figure 7.6 – Maximum principal stress in the fine grained concrete layer (SIFEL)	91
Figure 7.7 – 1975 model, Comb. C (from winter to summer), max. and minimum principal stresses ..	93
Figure 7.8 – 2010 model, Comb. C (from winter to summer), max. and minimum principal stresses ..	93
Figure 7.9 – 1975 model, Comb. D (from summer to winter), max. and minimum principal stresses ..	93
Figure 7.10 – 2010 model, Comb. D (from summer to winter), max. and minimum principal stresses ..	93
Figure 7.11 – σ_1 , Comb. C, 1975 model.....	94
Figure 7.12 – σ_1 , Comb. C, 2010 model.....	94
Figure 7.13 – σ_3 , Comb. C, 1975 model.....	94
Figure 7.14 – σ_3 , Comb. C, 2010 model.....	94
Figure 7.15 – σ_1 , Comb. D, 1975 model.....	94
Figure 7.16 – σ_1 , Comb. D, 2010 model.....	94
Figure 7.17 – σ_3 , Comb. D, 1975 model.....	94
Figure 7.18 – σ_3 , Comb. D, 2010 model.....	94

Figure 7.19 – Loading surface for Rankine definition of equivalent strain (Jirásek, 1998)	96
Figure 7.20 - Uniaxial stress-strain relation used in the concrete model (ADINA R & D, 2011)	99
Figure 7.21 – Different configurations of max. princ. stress due to the use of low-speed dynamics ..	102
Figure 7.22 – Crack width P1 (1975 model), 26/08/2011.....	103
Figure 7.23 – Crack width P1 (2010 model), 26/08/2011.....	103
Figure 7.24 – Crack width P2 (1975 model), 26/08/2011.....	103
Figure 7.25 – Crack width P2 (2010 model), 26/08/2011.....	103
Figure 7.26 – Crack width P1 (2010 model), 26/08/2011.....	104
Figure 7.27 – Crack width P2 (2010 model), 26/08/2011.....	104
Figure 7.28 – Crack width P1 (1975 model), 12/02/2012.....	104
Figure 7.29 – Crack width P1 (2010 model), 12/02/2012.....	104
Figure 7.30 – Crack width P2 (1975 model), 12/02/2012.....	104
Figure 7.31 – Crack width P2 (2010 model), 12/02/2012.....	104
Figure 7.32 – Temperature evolution for representative nodes	105
Figure 7.33 – Temperature values on 10/06/2011.....	106
Figure 7.34 – Temperature values on 30/07/2011.....	106
Figure 7.35 – Temperature values on 26/08/2011.....	106
Figure 7.36 – Temperature values on 10/11/2011.....	106
Figure 7.37 – Temperature values on 07/01/2012.....	106
Figure 7.38 – Temperature values on 12/02/2012.....	106
Figure 7.39 – Grid numeration (Prochazka, 1999)	108
Figure 7.40 – Template of multipliers (Prochazka, 1999)	108
Figure 7.41 – Multipliers for stresses (Prochazka, 1999).....	108
Figure 7.42 – Average temperatures	110
Figure 7.43 – Summer temperatures	110
Figure 7.44 – Winter temperatures	110
Figure 7.45 – Average temperatures	110
Figure 7.46 – Summer temperatures	110
Figure 7.47 – Winter temperatures	110
Figure 7.48 – Temperature distribution in April, August and February for 2 vertical sections	111
Figure 7.49 – Longitudinal cracks in the vault (Gattesco, 2012)	112
Figure 7.50 – Possible out-of-plane mechanism in the breast wall (Gattesco, 2012)	112
Figure 7.51 – Intervention without backfill removal.....	113
Figure 7.52 – Intervention with backfill removal	113
Figure 7.53 – Use of GFRP reinforced coating	114
Figure 7.54 – Use of hybrid GFRP-stainless steel tendon net	114
Figure 7.55 – Iteration forces between cable (in tension) and arch (in compression)	114

1 INTRODUCTION

The present thesis deals with one of the symbols of the city of Prague (Czech Republic), the famous Charles Bridge (Karlův most). It is among the listed National Historic Monuments within Prague's historic city centre, also protected by UNESCO, and it connects the two sides of the Vltava River (Lesser Town and Old Town), since 1406 (Figure 1.1).



Figure 1.1 – View of the Bridge from South; St. Vitus Chatedral and the Castle on the background

The Monument, a classical arch stone bridge, has a long history and it suffered different disasters and repairs. Recent computational and experimental studies identified climatic loading as one of the main causes of crack nucleation and development. Especially in continental climates, winter temperatures strongly below 0 °C and high summer values can cause problems to structures; the gradient of temperature between surface and internal layer is also accounted as possible trigger of faults. Masonry adapts to these “non-mechanical effects” through stresses in the structure and the interaction of the external layers with the bridge body filler develops in cracks and deformations.

To understand the effects of climatic loading, a thermo-mechanical analysis will be performed on a finite element model of a representative part of the bridge. During the last repair, a measuring system was installed to record the values of temperature and moisture content at selected gauge points; part of those data (two years records) will be used for the analysis. The bridge behavior will be simulated in way to estimate the real influence of temperature on damage, using suitable damage models.

The aim of the study is to be useful for designing further stage of the bridge repair; e.g., the retrofit of the bridge's sandstone cladding is the next planned intervention (Krejci, 2014).

The thesis is organized as follows: it will be immediately exhibited the work plan followed for developing the study, listing also the main faced topics (Par. 1.1); then the monument will be presented (Ch. 2) explaining damages and repairs that brought to the actual state. The FEM model will be introduced in Ch. 3 and the analysis explained in Ch. 4. Finally a different approach to the problem will be obtained using a simpler numerical method, in way to make a rough comparison with previous analysis (Par. 4.7). Conclusions will be provided in Ch. 5, followed by References, and Annexes to examine some of the faced topics in more detail.

1.1 Work plan

1. Introduction to problem: approach [April, 4th – April, 19th]

(historical survey, inspection of the structure; study of previous reports and interventions, analysis and in-situ measurements; current state; heat transfer theory and damage models)

2. Set up of numerical model [April, 14th – April, 20th]

(choice of a suitable computational software; material properties, boundary and initial condition, set up of self-weight, live load and temperature loading, material properties)

3a. Numerical computation: thermo-elastic analysis [April, 17th – April, 30th]

(correct material properties; validation and verification of numerical model, comparison between model pre/post intervention, evaluation of results, comparison between different software)

3b. Numerical computation: non-linear analysis [April, 25th – May, 15th]

(validation of model and mechanical properties for non-linearity, comparison of the results with linear analysis and between different software, etc.)

3c. Numerical computation: analysis for prevision of crack nucleation [April, 25th – June, 25th]

(choice of suitable mechanical models: simple scalar isotropic damage model, orthotropic damage model, computation over one and more years to consider cyclic effects, evaluation of results)

4. Simple numerical calculation (Finite Difference Method) [June, 20th – June, 25th]

(simple numerical model of a 2D representative part of the structure for mechanical response to temperature loading; comparison with FEM numerical model)

5. Final assessment [May, 1st – July, 11th]

(evaluation of results; evaluation of models used; prediction of bridge behavior and possible damage evolution; recommendations for rehabilitation; generalization to other similar masonry bridges).

2 THE MONUMENT

2.1 History

The bridge was built from 9th July 1357, when Charles IV of the Luxembourg Dynasty, King of Bohemia, Germany and Italy and Holy Roman Emperor (Zeman, 2008) laid the foundation stone.

The date and time in which the cornerstone was laid had a ritual meaning: it is only odd numbers that combined form an ascending and descending line (a numerical bridge): year 1357, 9.7, 5:31 AM and it is also referred to a Sun-Saturn conjunction which, according to astrologers, was a particularly suitable time for starting the work (Praha.eu, 2010).

The King decided the Swabian builder Peter Parlér (who created also St. Vitus Cathedral) and his stone mason's workshop to manage the construction of the monument, which ended in 1406. The Quarter towers (Staroměstská věž and Malostranská věž) today standing at the extremes of the bridge, were both built later (Praha.eu, 2010).

It was the second bridge in Prague, built to substitute the collapsed Judith's Bridge (Prikryl, 2011) and it was simply known as "Stone Bridge" ("Kamenný most") (Zak, 1995) or "Prague Bridge" until 1870. Judith Bridge (Figure 2.1), so called referring to King Vladislav's (1140 – 1172) wife, had Romanesque style and it was built from 1158 to 1171. The structure was damaged by a flood in 1272 and finally collapsed in 1273 due to water again. The event was considered a national disaster and a wooden bridge was used instead of it, till the construction of Charles Bridge (Praha.eu, 2010).



Figure 2.1 – Comparison between Charles Bridge and the previous Judith's Bridge (highlighted in red)

The Bridge links both banks of the Vltava River, connecting the Old Town (Staroměstská) and the Lesser Quarter (Malá Strana) of Prague (Figure 2.2). Considering the age and the non circular shape of the vaults (so the presence of horizontal thrusts), it is likely to be built as simultaneous construction of the arches (Smith, 2008).



Figure 2.2 – Position of Karlův Most, between Most Legii and Mánesův Most

The bridge is decorated with 31 statues in baroque style (depicting saints, historical and biblical characters) dating from the beginning of the 18th Century (many of them are copies, the originals can be seen in the Lapidarium of the National Museum). It had been lighted up by gas lighting since 1866, then it was adapted to electricity and (during the last restoration) to gas again.

The bridge is only pedestrian from 1966 but it was for five Centuries an important trade route (the only means to cross the Vltava in the adjacent 100 km) and it was used also as transport line for the city's tram and bus network (Smith, 2008).

The bridge is 516.7 m long and 9.1–9.7 m wide, with 16 arches whose span varies from 16.6 to 23.4 m. It stands on 17 piers (each shielded by an ice guard) with cross section varying from 6.3 to 10.8 m by 24–25 m. Originally founded on millstones (either supported by oaken grillages or boxes anchored to the bed of the river), the piers have heads sharpened at an angle of 65°, in way to protect it against water stream and drifting ice. The subsoil is formed by a 5–10 m layer of coarse-grained gravel (with the particle size of up to 0.5 m) that lies on a rock massif consisting of Ordovic shales and quartzite (Zeman, 2008).

After Charles Bridge, many other structures were built to link the two sides of the river; today 16 bridges pass through it in the urban area of Prague (Figure 2.3).



Figure 2.3 – Bridges in the city centre (Charles Bridge is the second one)

2.2 Materials

The bridge is mainly made up of Bohemian sandstone masonry, which is homogeneous only at mesoscopic level.

Three different mesoscopic heterogeneity patterns can be distinguished in the body (Zeman, 2008):

- regular periodic sandstone (upper cretaceous quartz sandstone and carboniferous arkoses) ashlar (opus quadratum) facing of vaults (Figure 2.4; element “A” in Figure 2.8), bound on lime mortar from sandstone stucco and hydraulic lime (Witzany, 2008);
- sandstone masonry (opus quadratum) with a non-periodic arrangement of blocks used in the facing of breast walls (Figure 2.5; element “B” in Figure 2.8);
- filling irregular quarry masonry (opus caementicum) consisting of arenaceous marl blocks and mortar made of sand and black hydraulic lime (Figure 2.6; element “C” in Figure 2.8). Classified as structural mortared rubble masonry (MRM technique) (Přikryl, 2010) according to the heterogeneous granulometry (from 5 to 50 cm) and the coarse particles. The aggregates are macroscopically very fine-grained (aleuropelitic) sedimentary rock of light beige to ochre colour.



Figure 2.4 – Periodic sandstone



Figure 2.5 – Non-periodic sandstone



Figure 2.6 – Filling

The masonry has units of different types of local sandstone (quartz arenites, litharenites and arkosic arenites from Carboniferous and Upper Cretaceous sediments in Prague's neighbourhoods) used either in construction and repairs. 7 quarry areas can be traced, providing the 2 major rock types, Carboniferous arkoses and Cretaceous sandstones (Přikryl, 2010) used till the 19th Century. Siliceous sandstone of the Cretaceous age and kaolinitic sandstone were used in the repair after the flood of 1890 (Witzany, 2007), while the last interventions did not respect the original types of stones, so new varieties were introduced (fine-grained glauconitic quartz sandstone with clay matrix, and medium-grained arkosic sandstone) (Přikryl, 2010), till to be the 35% of the components in some areas (Přikryl, 2011).

A legend says that the builder mixed egg yolks into the mortar to increase the strength of the binder (Shanberg, 2010) (but no evidence about this is provided).

2.3 Structural elements

The arch bridge is a simple structure (Figure 2.7) where massive piers support the arches that form the vaults. An internal infill (laterally covered by breast walls) makes the proper level for the flooring, that includes today hydro-isolation, concrete slab and granite paving (Figure 2.9, el. "D" in Figure 2.8).

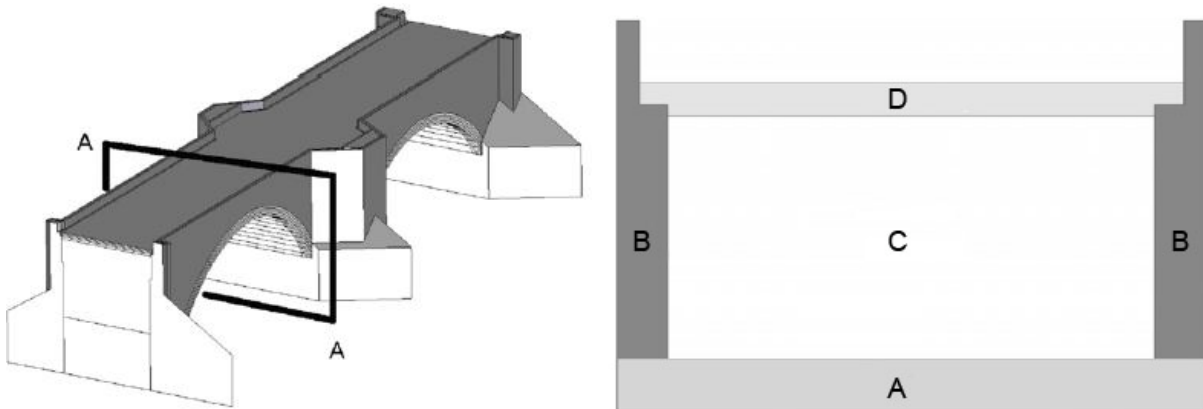


Figure 2.7 – 3D view of the Bridge with A–A section
(Sýkora, 2012)

Figure 2.8 – Elements in A–A section

The breast walls (Figure 2.5; element "B" in Figure 2.8) are laid on the bridge arches; in the lower part they are 0.6 m thick, while in the upper one the thickness is 0.4 m. They were built without expansion joints and they are reinforced at the connection with piers by masonry pillars that are also pedestals for statues (Witzany, 2008). As the breast walls, also piers and vault arches are built using bush-hammered blocks.

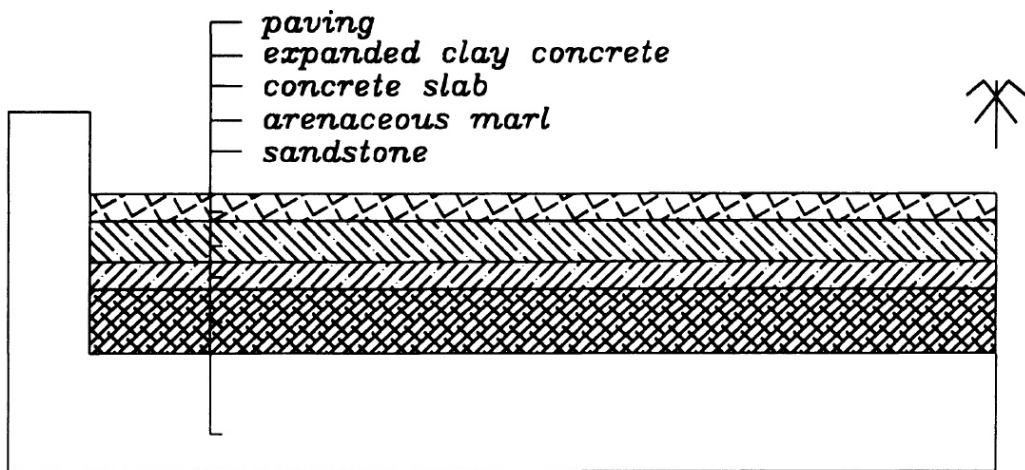


Figure 2.9 – Cross-section at the top of the arch before the last repair (Zak, 1995)

The pier masonry is made up of granite blocks up to the level of the Vlatva water, while upper than it, the sandstone is used; the quartz sandstone (66% of the units) has not always good quality (Witzany, 2008). The material to level the layers above the vault arches (element "C" in Figure 2.8), as the piers filler, is arenaceous marl rockfill; it was overlaid with loamy backfill and cob, and an insulation layer of cast clay (Witzany, 2007).

Before the invasive intervention of the 1960s–1970s, the original irregular masonry of the infill transferred the load from the deck to the vaults without loading the breast walls with horizontal spacing stresses, thus transverse stresses preceded longitudinal cracking on the underside of the vaults. The pavement with loamy joint filler allowed free expansion of individual pavement blocks.

The back side of the bridge vaults was probably treated with an insulation layer of loamy clay, to drain of the water absorbed from the deck surface, toward the pier footings (Witzany, 2008).

The mortar used in the filling is a mixture of hydraulic lime binder and fine-grained filler (river sand) that keeps together pieces of porous fine-grained clayey-calcareous silicate (Přikryl, 2010) coming from the beds of the Upper Cretaceous sedimentary rocks that outcrop on Bílá Hora Hill in Prague.

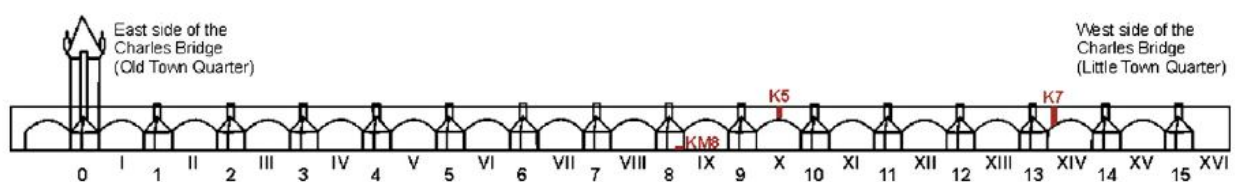


Figure 2.10 – Position of the sampling sites on Charles Bridge (Přikryl, 2010)

A recent study (Přikryl, 2010) based on the samples obtained from the red areas of Figure 2.10, let to analyse the cross-section of the structure, identifying the presence of a second arch on the transition zone between the base of the fill masonry and the internal side of the facing masonry (element [6a] in Figure 2.11).

According to Figure 2.11, the layers [1] – [5] come from the intervention of 1960s–1970s (paving, concrete and waterproofing, removed in 2007), then there are the original Gothic filling masonry [6] and the internal arch [6a] built of natural stone slabs (8–12 cm thick and 45–50 cm long) of same nature of the aggregates in the MRM. On the external side, the rectangular sandstone ashlar (both Upper Cretaceous quartz sandstone and Carboniferous arkoses) of the vault are laid [7] (Přikryl, 2010) with a thickness between 0.7 and 0.9 m.

The layers are the same in every vault, except the 5th, 6th and 7th calculated from the Old Town, that present lightening spaces above the arches (Velflik system), built after the 1890 flood.

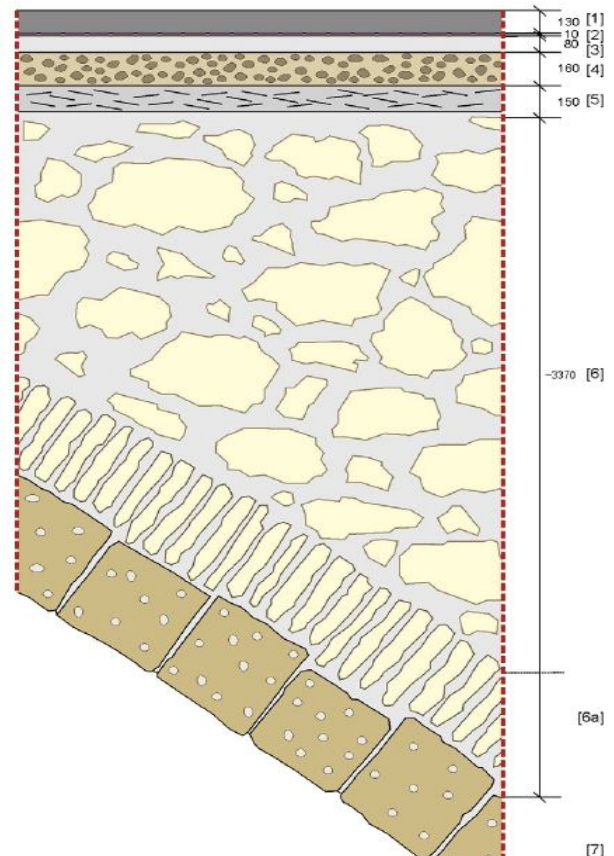


Figure 2.11 – Cross-section through the fill masonry of arch XIV (Přikryl, 2010), dimensions in mm

2.4 Damages and repairs

The bridge was damaged many times, mainly from floods and water erosion that caused periodic reconstruction, rehabilitation or strengthening (Table 2.1), giving to the monument great variability of materials and construction technologies in its different parts. The floods happened during the construction (in 1359, 1367, 1370, 1373 ad 1374) as well as after the completion (the worst in 1432, 1496, 1655, 1784 and 1890; compare to Figure 2.12).

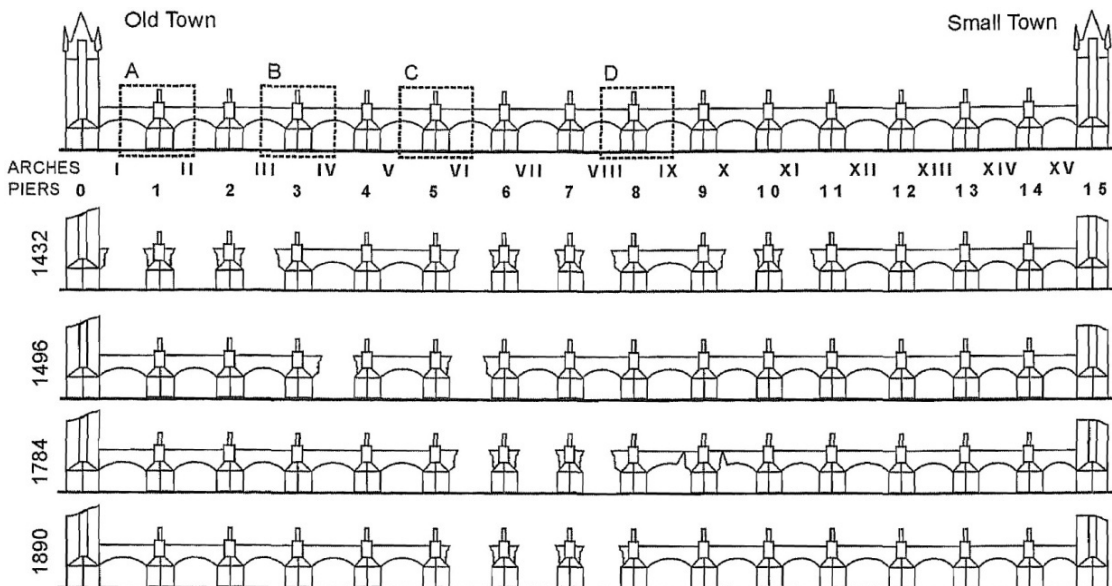


Figure 2.12 – Results of the main floods

The floods can cause three main problems to bridge piers: angular rotation, subsidence, and shift (Smith, 2008). These are forced deformations that provoke tensile cracks, even if piers are tapered toward the flow in way to reduce their vulnerability.

The 1890 flood was the last catastrophic event that brought to the collapse of 3 bridge spans (5th, 6th, and 7th vault) as can be seen in Figure 2.12 and Figure 2.14).



Figure 2.13 – Flood in 1872



Figure 2.14 – The 1890 flood, collapse of 3 bridge vaults (Zeman, 2008)

Table 2.1 – History of Charles Bridge and interventions, based on (Zeman, 2008) and (Prikryl, 2011)

Year	Event	Cause
1357	First stone is laid	
1406	Completion of the works	
1432	Damage to piers No. 3, 4, 7, 8, 10	Flood
1496	Collapse of two arches (No. 3 and No. 4) and one pillar (No. 3) already eroded	Heavy load on eroded pillar
till 1503	Repair of damage from years 1432 and 1496	
1648	Old Town Bridge Tower damaged by Swedes	Thirty Years' War
1655	Damage to pier foundations	Flood
1784	Partial damage to the foundation of three piers and five vaults	Flood
till 1788	Repair of damage from year 1784	
1844	Replacement of the stairway to Kampa Island	
1866	Placement of pseudo-Gothic gas lights	
1870s	Bridge became way for public transports	
1874–1883	Reconstruction of the Bridge Towers	
1890	Vaults No. 5, 6 and 7 destroyed, piers No. 4, 8 damaged	Flood
1893	Repair of damage from year 1890	
1903	Rehabilitation of piers No. 3, 4 and 7 (Velflik arches)	
1905–1912	Replacement works (with Horice sandstone) on facing masonry of piers No. 1, 2, 8, 11 and 12 and neighbouring arches	Use of low durability stone
1926–1928	Replacement works (with Horice sandstone) on facing masonry of piers No. 4, 5, 9 and 10 and neighbouring arches	Use of low durability stone
1966–1975	Major reconstruction, grouting, water-proofing layer, stabilising reinforced concrete slab installed, replacement of facing masonry; it is pedestrianized	Use of Portland cement based mortar as binder
1980s	Additional localized replacements	Cement mortar
1994–1997	Study leading to the undone large-scale repair	
2002	More than 100-year flood, the bridge survived	
2004–2005	Strengthening of foundations (piers No. 8 and No. 9)	
2007–2010	Repair of parapets, dilatation joints, hydro-isolation of the pavement, rehabilitation of foundations, gas lighting	

Due to floods, the original foundations (millstones) were gradually replaced: piers 5 and 6 were founded on a vault supported by two six-meter caissons (1892 reconstruction), while (in 1902–1903) piers 3, 4 and 7 were rebuilt on a concrete slab resting on seven caissons of 2.5 m diameter (Zeman, 2008) (compare to Figure 2.15).

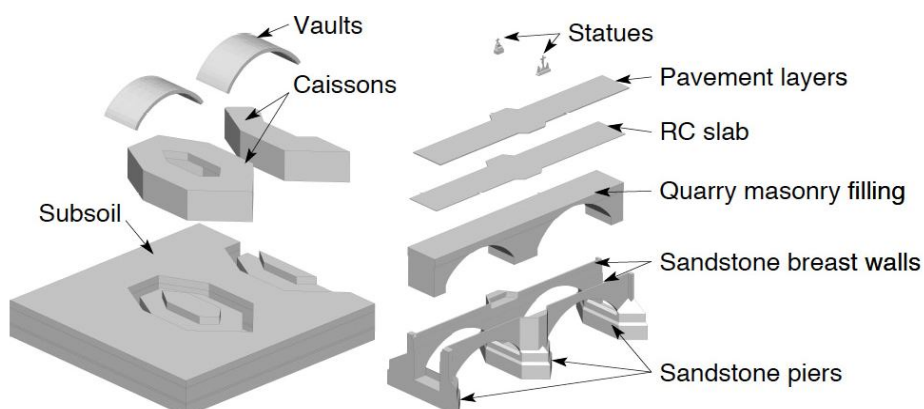


Figure 2.15 – Schematization of the bridge elements (Zeman, 2008)

Despite the numerous interventions, the fill masonry is considered a Gothic original, since it is preserved in 13 out of 15 pillars (two were rebuilt after the flood of 1890) and in 13 arches out of 16 (three were re-erected after the same flood) (Přikryl, 2010).

In 1966–1975 the bridge was strengthened by high-pressure grouting and by a reinforced concrete slab (without expansion joints), covered by a bituminous water-proofing layer, forming the today's section (Figure 2.16); the passage to vehicles was excluded (Zeman, 2008). The intervention was strongly criticized because cement was used in the grout mixture (instead of lime mortar). Moreover the bitumen layer had low durability, hence it was not able to prevent water and salt penetration (Bergman, 2009).

The stone replacement regarded only the outer part of the blocks: new elements 200 mm thick were bonded to the original stones by 100 mm of hardened Portland cement paste, creating a dishomogeneous sandwich-like structure. The stone used to repair shows odd colours (beige to rusty yellow) and rock fabric easily recognizable from the original sandstones (of dark grey colour due to pollution) (Přikryl, 2010). The use of sandstone types with different properties (since the original quarries were closed) can accelerate the deterioration of the facing masonry due to their low resistance (granular disintegration by salt weathering followed by the surface retreat of 1 cm after 30 years). Certainly the use of cement-based concrete to fix newly inserted ashlar is a menace for the material conservation, because the hardened paste makes a barrier to water, having permeability three to four orders lower than the original mortar. The low permeability created the accumulation of water-soluble salts (specially nitrates) in the facing ashlar, causing both sub- and efflorescence as well as other decay forms: granular disintegration, scaling and flaking, exocrust formation, blistering, fracturing, honeycomb/alveoli formation, and biocolonisation (Přikryl, 2011).

The source of the water-soluble salts was found in previous restoration attempts: chemical cleaning (black crust removal) by nitric acid, ammonium hydroxide (ammonium water), and ammonium hydrogen carbonate, all similar in the high nitrate content (Přikryl, 2011).

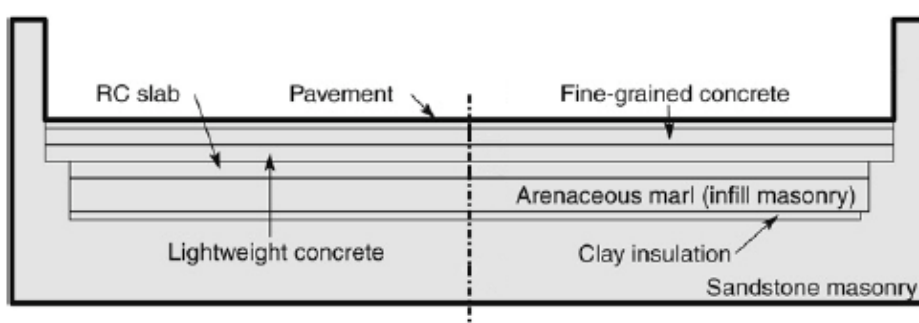


Figure 2.16 – Bridge section after the 1960s–1970s intervention

Since the 1890 intervention, no ordinary maintenance was performed, so the degradation was continuous. The greatest renovation project was studied from 1994, with the aim to restore the load-bearing capacity and stability of the bridge, supported by experimental in situ investigations, covering mineralogical and petrographical analyses, chemical and biochemical degradation processes as well as monitoring of temperature and moisture fields (Zeman, 2008).

The study, completed in 1997, brought to the concept of large-scale repair to solve the state (considered critical) subsequent to the reconstruction of 1966–1975. The plan dealt with removing and replacing the layers upon the vaults (Figure 2.17), and strengthening the structure at the level of the slab (Figure 2.18), almost without considering the value of the monument (V. Křížek, 2012).

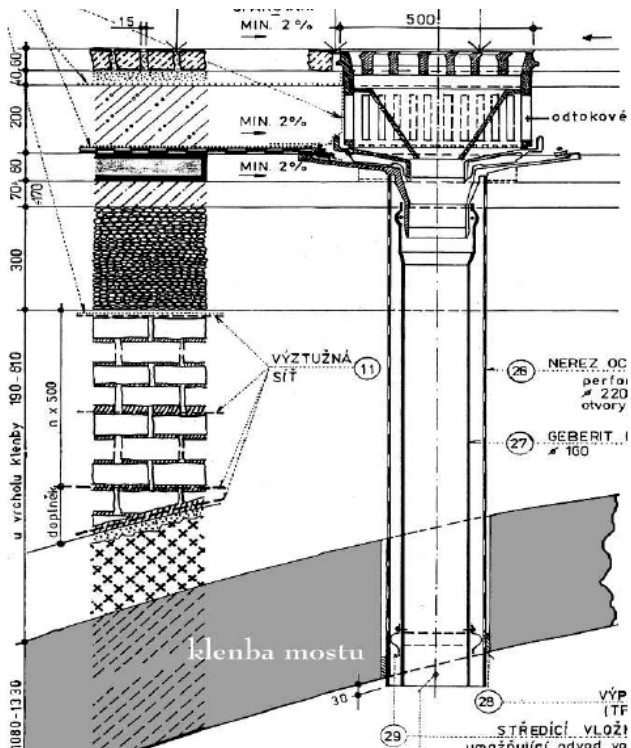


Figure 2.17 – Replacement of the layers upon vault

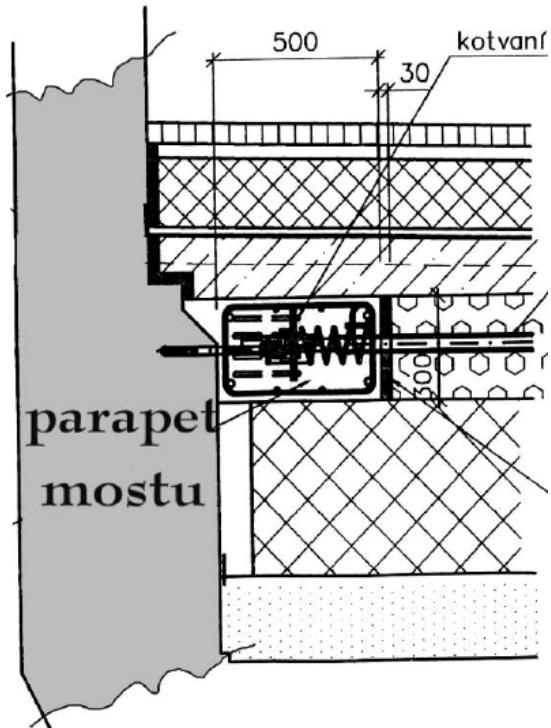


Figure 2.18 – Suggested prestressing (V. Křížek, 2012)

The scientific community was divided and part of it did not consider necessary a so invasive intervention that also did not give solutions for foundation undermining and inadequate drainage system. The flood of 2002 (500-year event), during which the metro system and several districts were flooded, was sustained by the bridge, proving the great residual capacity of the structure.

Even without considering the empirical behaviour, further studies noticed that the computational assessment of the bridge was based on the assumptions of linear elasticity and dimensionally reduced models (Zeman, 2008) therefore more realistic simulations were required.

The study started in 1994 and was carried on till 2004. 12 dug holes (diameter of 137 mm) were used to obtain samples of sandstone blocks, arenaceous marl backfill, hydraulic black lime mortar, reinforced concrete slab and pavement layers, covering the entire bridge. The specimens let to determine static and dynamic Young's modulus, Poisson ratio, compressive and tensile strength, and fracture energy. Since some parts of the bridge show higher moisture content, the reduction of mechanical properties due to this (maximum above 20%) was quantified with testing under fully saturated conditions. The study assessed that the structure is vulnerable to temperature loads, the load bearing capacity is influenced by the slab and that foundations are the most critical zone (Zeman, 2008).

2.4.1 The last intervention

To solve in a compatible way the problems created by the 1960's–1970's repair, an intervention (signed Mott MacDonald, for the client Prague Municipality) was performed in 2007–2010. It consisted in the rehabilitation of foundations (Figure 2.19) as first step, followed by the hydro-isolation of the pavement. Then repair of parapets, new navigation signs, and gas lighting (instead of electric sodium lights) to end of the work.



Figure 2.19 – Works on the foundation of pillars 8th and 9th with mechanization from water lever (Křížek, 2012)

The hydro-isolation was necessary against rain water poured into the bridge and melting snow from on top of the pavement with salts (Bergman, 2009). It is 3 mm thick (two layers of 1.5 mm), formed by the acrylic (methyl methacrylate) waterproofing membrane (Stirling Lloyd's "Eliminator"). To apply it, two concrete layers with the old waterproofing were removed (by the contractor HELIFIX CZ), reaching the level of the concrete slab. This was cut at the middle and at the borders in way to create expansion joints in it, to reduce the stresses related to its dilatation. The expansion joint in contact with the breast wall is 150 mm thick and it is filled with gravel, while the one in the middle of the slab has thickness 20 cm and it is formed by extruded polystyrene (Mott MacDonald, 2011). It was seen that the borders of the slab were already detached from the breast walls due to shrinkage of concrete (only the reinforcement connected the two elements); the intervention let to release the constrain between them, that had caused cracks in breast walls. A geotextile layer (5 mm thick) divides the slab from slanted and levelling concrete layers, on the first one the hydro-isolation is applied, sprayed on a primer to seal the concrete (Figure 2.20). The new waterproofing has a bond strength of 2 MPa, higher then the minimum requirement from the concrete layers (1.6 MPa) (Stirling Lloyd, 2013).

A drainage geotextile mat is placed on the waterproofing (thanks to a structural adhesive) and connected to the parapet masonry, followed by 100 mm of concrete and the original granite bedded in a stabilizing layer of sand and lime. The layers upon the slab are detached from the breast walls by an extruded polystyrene mat 30 mm thick.

According to the touristic vocation, for limiting the impact and the disruption, the work was carried out to just one 150m² area at any one time (Figure 2.21), therefore the refurbishment of the whole surface (4,500m²) was programmed in two years (Stirling Lloyd, 2013).

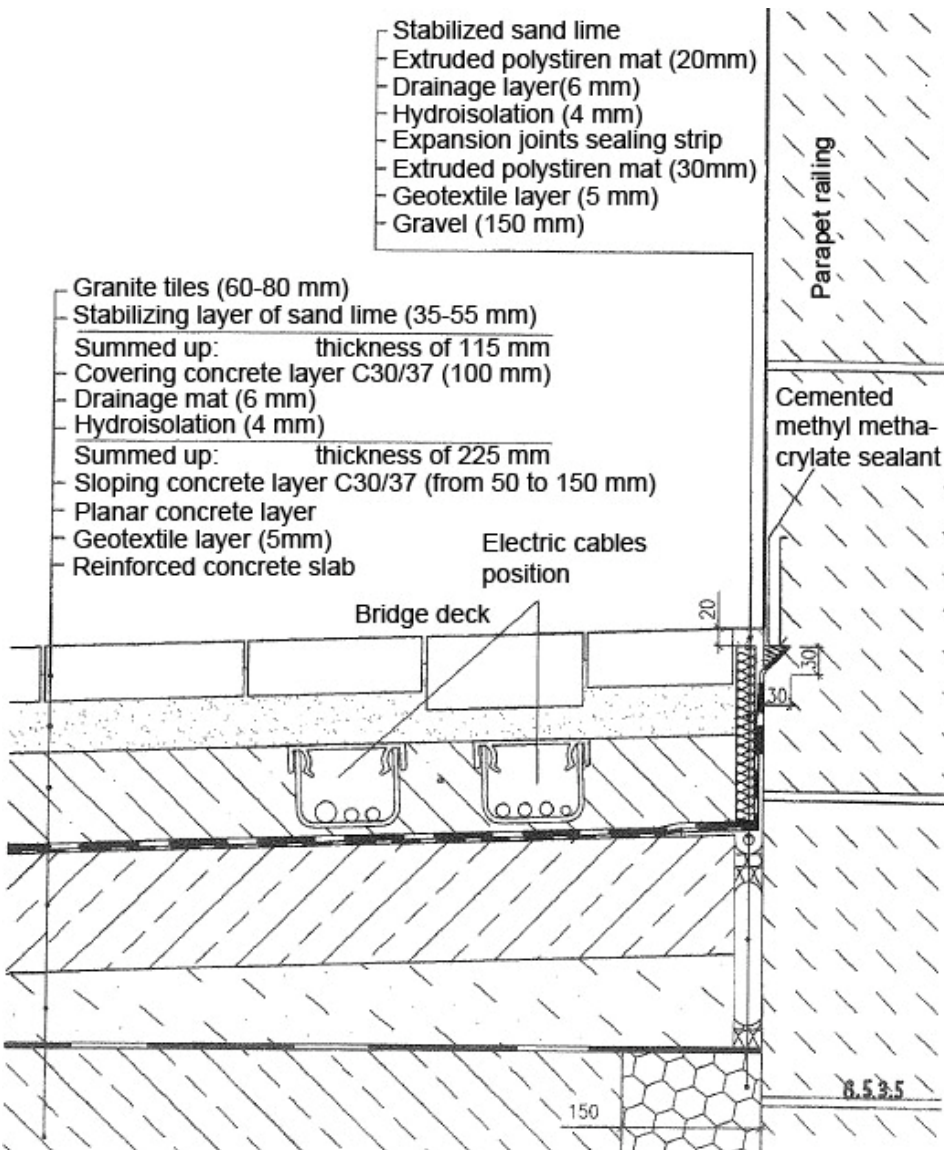


Figure 2.20 – Detail of the connection between parapet and pavement (Mott MacDonald, 2011)

The repair of the bridge stonework railing was criticized by the Historical Inspectorate of the Ministry of Culture, due to this the public opinion was against the intervention (persuaded that not enough surveys were done), even if the different organisms successfully cooperated and archaeological probes were carried out and documented (Bergman, 2009).

The replaced sandstone blocks come from the East Bohemian Kocbeře quarry; their quality was discussed as the fact that they could replace stones with stonemason's marks (actually no mark was identified in the removed stones). The replacement was done defining the precise dimensions of sandstone blocks and singularly discussing them by a board whose members were also the representatives of the National Historical Institute. They chose to replace the blocks with shorter life

(up to 30 years), using the best material available according to physical and mechanical properties, weathering resistance and similarity to previous stones. The original stonework layout on the parapet walls was documented and maintained, as well as all the stone blocks in good condition (Bergman, 2009). The work provided experience for next step of the intervention, that will be the replacement of sandstone blocks in vaults and breast walls.

The parapets are the part that reacts faster to temperature changes, because they do not have the same accumulation capacity of the thick body; due to this, cracks appeared in their masonry and in the connection with breast walls. Moreover, the parapets are also affected by the up/down movement of the vault (breathing) related to summer/winter changes.

Dilatation joints have been made in the stone railing masonry in correspondence with vault/pier intersection (and usually every 4 m); they are done of a “plastic” mortar mixed with stone fragments (Figure 2.22). Despite all the efforts, the replacement was strongly criticized because the new stones do not match aesthetically the historical ones they are next to.



Figure 2.21 – Work into chess-like sections

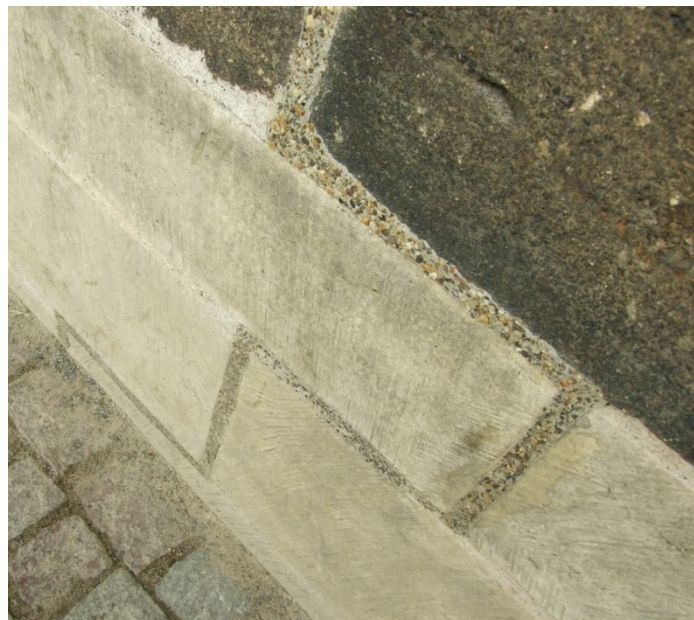


Figure 2.22 – Dilatation joint and contrast between old/new blocks

During the last intervention a measuring system was installed in way to monitor and record temperature and moisture content, and it is still working. The sensors were fitted into the bridge before completing moisture insulation (Krejci, 2014). In-situ monitoring after the conclusion of the intervention is becoming almost standard to evaluate the work but also to improve the predictive capability of theoretical models (Sýkora, 2012). In the case of Charles Bridge, the intervention allowed to develop a complete information system (<http://iskarluvmost.fsv.cvut.cz/>).

2.5 Current damage state and causes

According to the visual inspection, the structure presents cracks with thickness of some millimetres in vaults, breast walls and parapets. In the vaults the cracks are aligned and located at about 1 m from the external face of the breast wall, being due to the interaction between the two elements. They are present also in buttresses, near the pedestals for statues and in the corners between buttress and breast wall. Many minor cracks exist in the monument but they do not represent a menace for the structural stability.

According to the latest studies, the cause of the crack development are the non-stress effects causing the interaction of stone bridge structure, bridge body filler and breast walls, which prominently affects the vertical deformations of the bridge vaults (Witzany, 2007).

The gradient of the non-uniform temperature changes of individual bridge parts (spatial distribution of temperature field) causes cyclic deformation and permanent strain. Those provoke a gradual disintegration of the stone masonry, growing tilt of breast walls (Witzany, 2007) and shear stresses close to the external surface, therefore in the layers along the interface between sandstone masonry and irregular quarry masonry (Zeman, 2008). The shear stresses are balanced by tensile stresses which cause the crack nucleation and development in breast wall faces and vaults (Krejci, 2014).

The initial deformation (due to the single temperature change) is not manifested but it causes a mechanical state of tension; each deformation cycle is accompanied by a gradual growth in permanent deformations.

Thanks to previous repair, the damage is not related to movements of foundation (Zeman, 2008).

The parapets have been recently repaired (2007–2010) but they are expected to show again cracks due to the periodic action of (Krejci, 2014):

- shear stresses related to gradient of temperature between upper and lower part of the parapet ($\Delta T \approx 3^\circ\text{C}$);
- vertical movements of the vaults (upwards in summer and downwards in winter).

It is considered that, on the long period, the mechanism will bring to the ultimate damage in horizontal joints and the need to repair again the parapet. To limit this, vertical joints of “plastic” deformable mortar (from the top of the parapet till 2 meters down) have been added during the last repair (Figure 2.22). Generally, both for the tensile or shear failure, a gradual decrease of mechanical resistance under a continuous increase of deformation is predicted (softening).

The erroneous interventions of the 1960s–1970s brought to high moisture due to rainwater leakage through the faulty damp proofing. Its contamination by salts activated chemical, biochemical and physical degradation processes, existing also on new materials added during the interventions.

The increased rigidity of the bridge body filler (due to grouting) and its interaction with the stone structure had a negative effect on the overall behaviour, contributing to the gradual mechanical disintegration (Witzany, 2007).

The breast walls exhibited initially a good flexibility thanks to lime mortar in the joints and probably also partially unfilled vertical head joints. During the 1960s-1970s the arenaceous marl rockfill was partially grouted with a cement mix (named colcrete), while the loamy backfill and the cob were replaced by screed concrete, overlaid with a diagonal mesh of reinforcing steel ($\Phi 14$, steel 10425) concreted on both sides with a layer of a total thickness of 0.12–0.20 m, anchoring the diagonal mesh into the breast walls (using clip angles and steel grouting pipes) (Figure 2.24). This means that the deck started to load the breast walls with horizontal spacing stresses (and to uniform the behavior of the two walls), while the loads before were transmitted only to the vaults (Witzany, 2008).

The coupling of the breast walls reduces total deformations but increases transversal tensile stresses and the stiffness. The crack formation and development in the structure due to cyclic effects is set off by reaching the limit deformations, not the limit stress values; they depend on intensity and frequency of load cycles (Witzany, 2007).

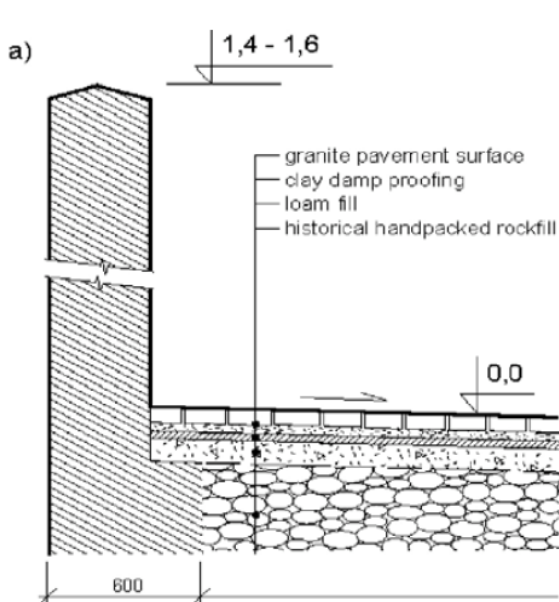


Figure 2.23 – Historical section of the bridge

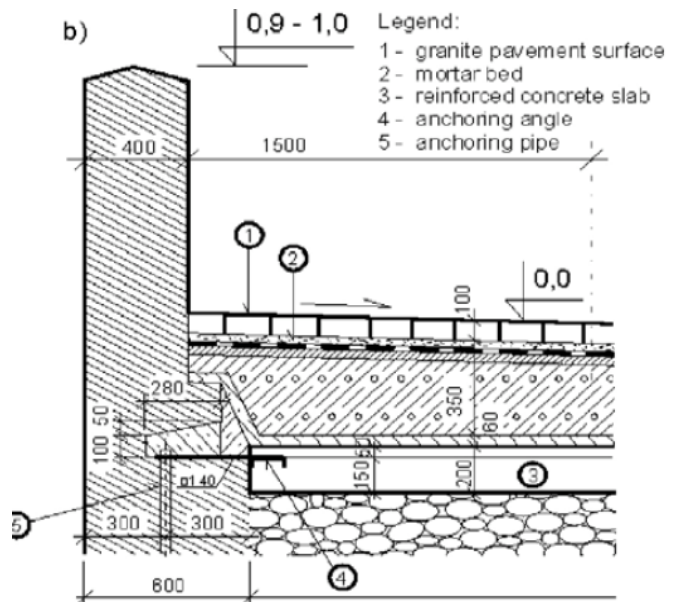


Figure 2.24 – 1966–1975 intervention (Witzany, 2008)

Upon the slab there is a layer of expanded-clay concrete (thickness varying from 0.15 m to 0.50 m) and the damp proofing (Witzany, 2007). The dug holes and boreholes performed revealed great differences in the bridge original layers but also about the recent interventions, rising questions about their function (some holes did not detect the concrete slab or the diagonal meshing) (Figure 2.25). The insufficient anchorage of the slab into the breast walls reduces the possible positive effect of the slab as a tie against out of plane mechanisms, without avoiding the back-effect of the element as a strut of the breast walls (Witzany, 2008).

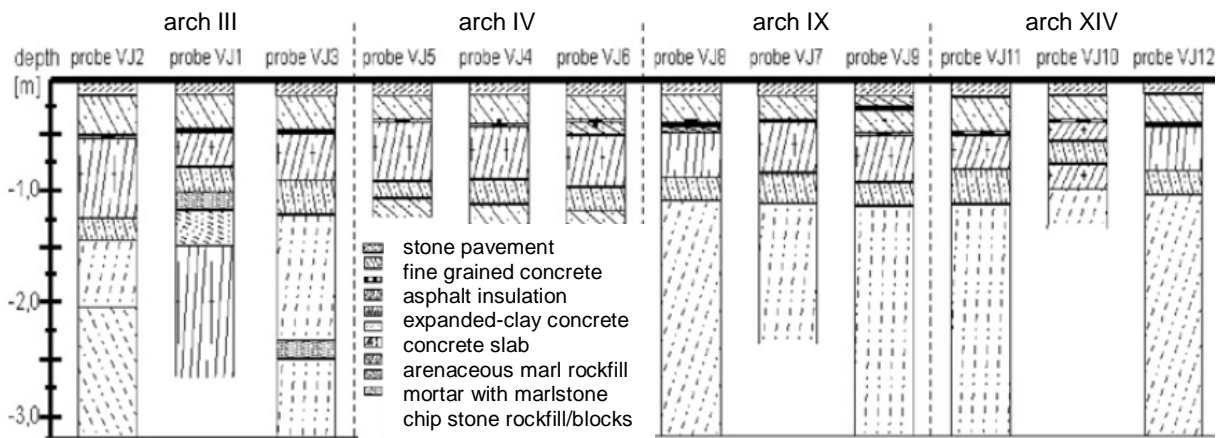


Figure 2.25 – Composition of the bridge body filling layers as recorded in test holes in 2000 (Witzany, 2007)

The damage in the structure is encouraged by the non-constant temperature pattern in the cross-section, which causes cyclic shape changes. The phenomenon, already existing in the original structure, is intensified by the presence of the expanded-clay concrete layer that acts as thermal insulation increasing the temperature gradient along the cross-section (during transitory seasons).

The cyclic deformations of arches are inhibited by the presence of the breast walls coupled by the concrete slab; due to this, shear cracks develop at the edges of the vault arches (Figure 2.26).

The breast walls are affected by horizontal deformations (causing also tilting) and they present cracks along the heel bed joint between arch and wall. Other damage can be seen in the bed joint at the level of the protective concrete layer below the granite paving and in the interface vault-pier.

The cyclical temperature effects are also hair cracks on the face of vault arches, developing to tension joints and shear cracks passing through both the joints of the stone masonry and the stone blocks (Figure 2.26) (Witzany, 2007).

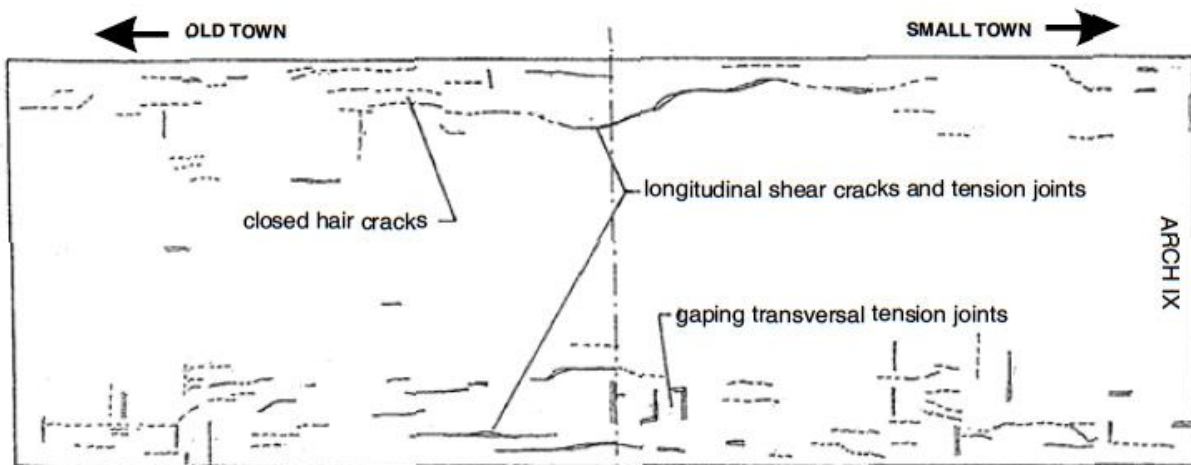


Figure 2.26 – Tension joints and shear cracks in the face surface of vault arch IX (Witzany, 2007)

2.6 Monitoring of temperature field

Since accurate studies, e.g., (Witzany, 2007), explained the sensitivity of the structure to the effects of induced deformations due to non-stress loading, temperature and moisture are monitored. The actual analysis deals with temperature data and their changes, while the moisture content evolves only insignificantly during the period (Krejci, 2014), in fact it varies in space but almost not in time (causing questions on the utility of the hydro-isolation of the bridge's deck made during the last intervention).

The net of sensors includes 4 cross-sections of the bridge: in the middle of the span of 8th and 11th vault (CR.-SEC. No 3, CR.-SEC. No 1), and in their vertical connection with piers (CR.-SEC. No 4, CR.-SEC. No 2). The control system is located under the 12th vault on the Lesser Town's side (Krejci, 2014). Cross-sections 1 and 2 (situated in the 11th vault) are respectively 34 m and 36 m far from the logger while cross-sections 3 and 4 (in the 8th vault) are 128 m and 134 m far from it (Figure 2.27).

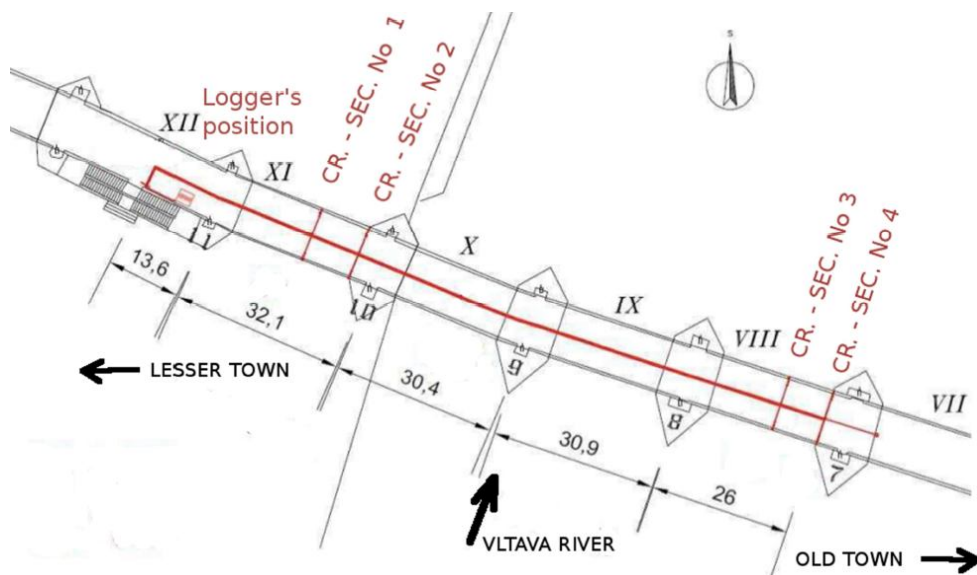


Figure 2.27 – Selected cross-sections for monitoring side (Krejci, 2014)

Each measuring point has three temperature sensors and one moisture sensor; CR.-SEC. No 1 has 11 points, CR.-SEC. No. 2 has 13 points while CR.-SEC. No. 3 has 11 points (Figure 2.28) and CR.-SEC. No 4 has 15 points (Figure 2.29).

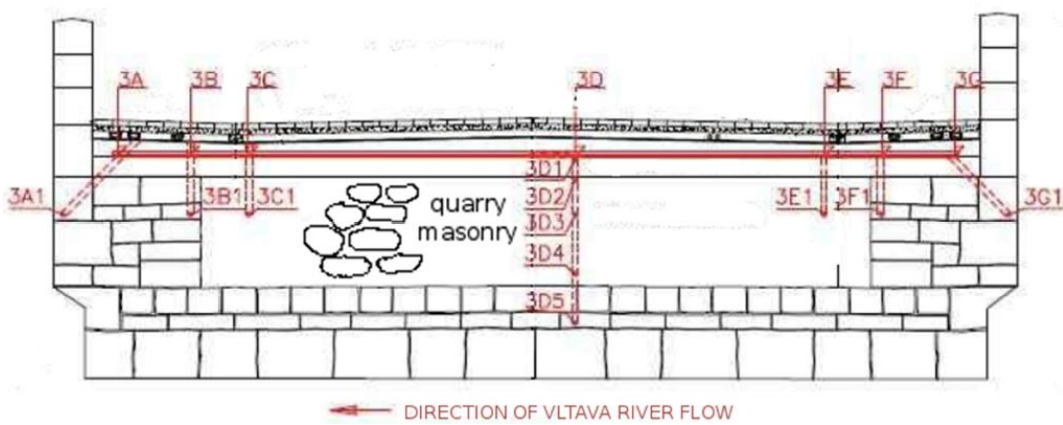


Figure 2.28 – CR.-SEC. No. 3 (11 gauge points = 33 temperature sensors and 11 moisture sensors)

Since the temperature sensors are not accessible, they are placed in triplets to enhance the reliability of the data detecting defects (2 correct solutions on 3). It was not possible to do the same with moisture sensors due to their higher price.

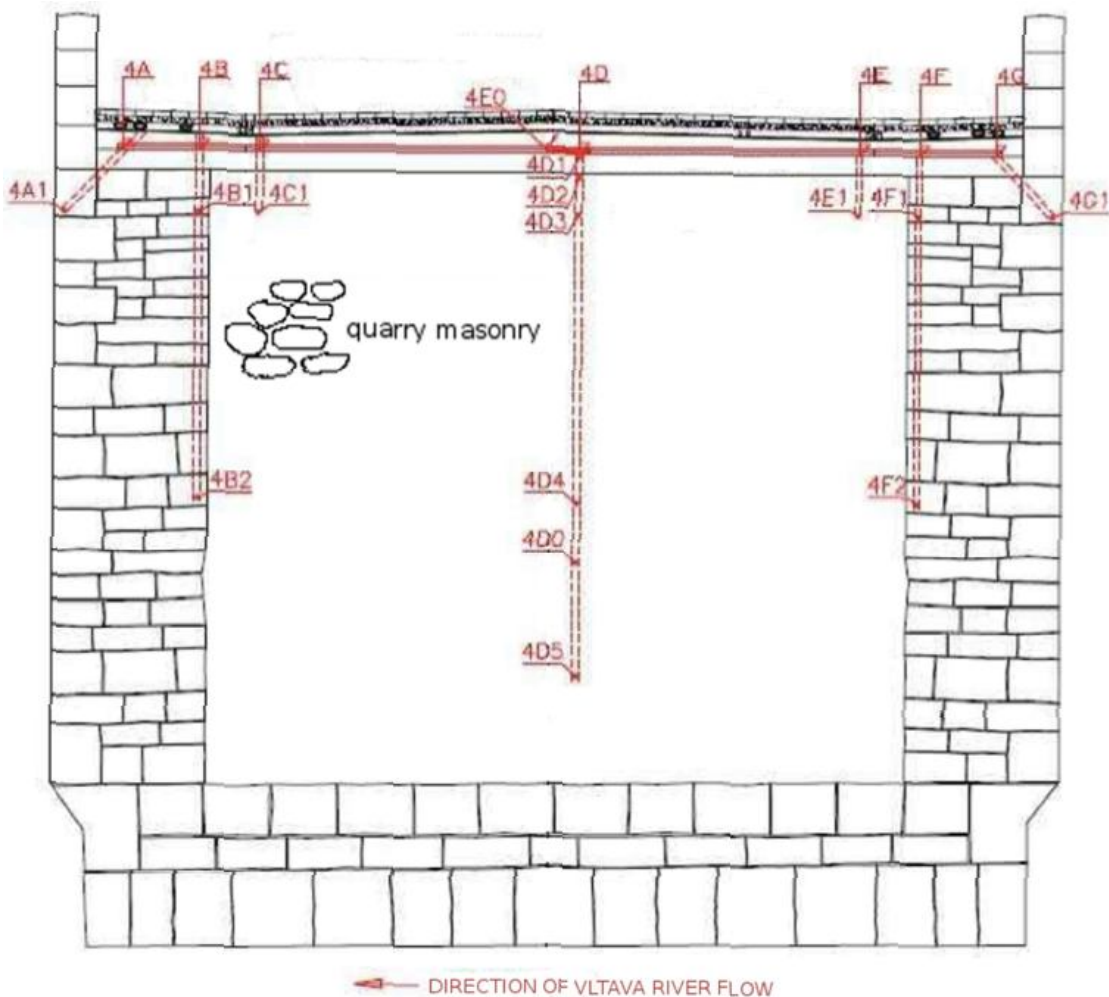


Figure 2.29 – CR.-SEC. No. 4 (15 gauge points = 45 temperature sensors and 15 moisture sensors)

About the nomenclature of the gauge points, they indicate the cross-section, the borehole and the number of the point, e.g., 4D1 is relative to cross-section 4, borehole D and gauge point 1. In the case of temperature sensors, their number is added at the end of the acronym: e.g. BT 4D1:2 stands for temperature sensor 2, while number 4 is assigned to moisture sensors (e.g. BH 4D1:4). The data are stored in the Information System (ISKarluvMost, 2010) according to this notation (Krejci, 2014).

Pt1000 thermometers were used for temperature measuring, imbedding them in resin in a stainless casing (6 mm of diameter). All sensors were subjected to a quickened ageing in climatic chamber but moisture sensors were also imbedded in porous ceramics and connected with an electric resistivity-voltage transducer (Krejci, 2014).

2.6.1 Monitoring of deformations

Deformations and strains (in direct connection with temperature and moisture variations) were monitored too, showing a cyclical strain in the stone bridge structure (compare to Table 2.2) decomposable in vertical deformations of bridge arches, horizontal and vertical deformations of breast walls, tilting of breast walls, and changes in the crack width on the bridge vault facing.

Table 2.2 – Maximum values of one-day (Δ_{day}) and one-month (Δ_{month}) deformations of the stone structure

	Summer season		Winter season	
	Δ_{day}	Δ_{month}	Δ_{day}	Δ_{month}
Horizontal deformations of breast wall tops (Δ_x) (mm)	$\pm 1,5$	+2,5 -3	$\pm 1,4$	± 2
Transverse tilts of breast walls (φ) (seconds)	+42 -79	+210 -100	+100 -75	± 250
Vertical deformations of breast wall tops (vertical deformations of bridge arches) (Δ_y) (mm)	+2,97 -3,58	+3 -4	± 4	$\pm 1,5$
Change in width of longitudinal cracks on bridge vault facing (Δ_x) (μm)	10 + 20	200 ÷ 420	15 ÷ 40	400 ÷ 700
Legend:	Δ_{day} maximum deformation measured within a one-day cycle Δ_{month} maximum deformation measured within a several months' cycle			

During the all-year cycle, vertical deformations in bridge arches (deflection/flattening) reach values ranging from 1/7500 to 1/2500 of the span (at the arch crown), with a range of maximum 10 mm and a distribution corresponding to the course of the outdoor temperatures. Comparing to previous measuring, it's clear that values tend to become higher in time (from 0.4 to 0.7 mm/year) causing progressive cracking and disintegration in masonry (Witzany, 2007); subsequent monitoring (5th, 6th and 9th arch) revealed that the length of open cracks is increasing (Witzany, 2008).

3 MODELING

3.1 Introduction

A computational assessment of a real complex structure should consider multi-physics, multi-scale, time-dependent and three-dimensional aspects of the problem.

According to recent studies (Zeman, 2008), the computational analysis of Charles Bridge should deal with a conservative estimate of the load-carrying capacity and several external actions:

- self-weight of the structure;
- water pressure including possible uplift;
- floating vessel impact;
- effects of heavy machinery used to remove debris during floods;
- loading due to spatially and temporarily varying temperature changes.

A multi-scale, multi-physics analysis would be required to consider all the actions, but the lack of reliable data to describe the interaction mechanisms lead to “decouple” the analysis into several independent simplified components, whose results would then be input for the coupled analysis (macroscopic non-linear mechanical analysis with material constants derived from meso-scale simulations) to study the overall behavior of the structure (Zeman, 2008).

The present work is related to the last point of the above list, performing a thermo-mechanical analysis on one representative three-dimensional arch of the bridge (whose dimensions come from a previous photogrammetric survey) in way to take into account the climatic loading as cause of crack formation and development (Krejci, 2014).

Following the uncoupled engineering approach, the heat transport problem was solved independently from the mechanical analysis. The only thermo-mechanical coupling considered is related to the effective thermal expansion coefficient (hence it is a one way coupled analysis).

Generally, according to (Lourenco, 2002) a complex analysis tool does not necessarily provide more reliable results than a simpler tool, in fact some key aspects are:

- compatibility of the analysis tool and the information sought;
- availability of analysis tools to the practitioner involved in the project;
- cost, available financial resources and time requirements.

3.2 FEM model

The model, provided by previous studies at Czech Technical University (CTU) in Prague, represents the third arch (starting from the Old Town) after the intervention of the 1960s–1970s; thanks to the symmetry, only half of the structure is analyzed.

The input is divided in 10 different element groups (pier masonry, infill of the pier, vault, infill of the vault, northern breast wall, southern breast wall, concrete slab, first layer upon the concrete slab, second layer upon the concrete slab, pavement) (Figure 3.1, Figure 3.2).

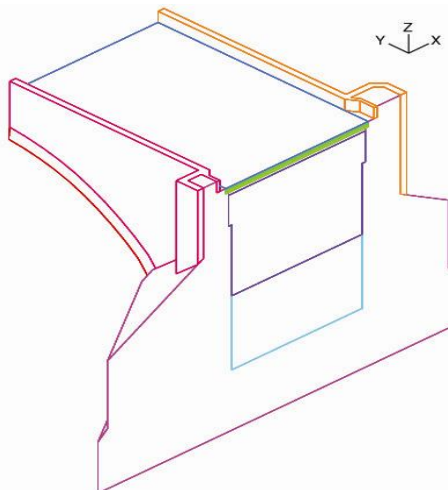


Figure 3.1 – After 70's model divided by groups (southern side)

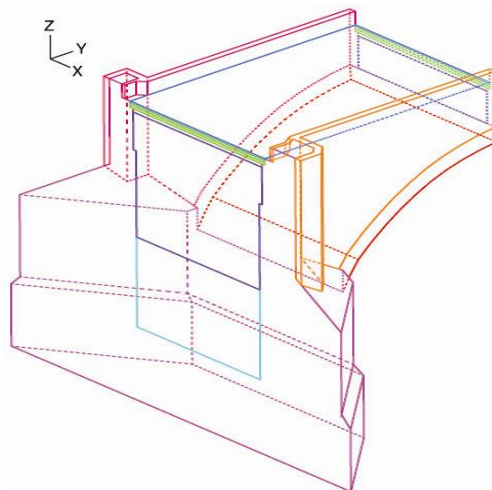


Figure 3.2 – Model with wire-frame

The dimensions of the model are shown in Figure 3.3 and Figure 3.4, while Figure 3.5 represents the cross-section at the crown of the arch. In it the materials are identified: zone A is regular sandstone masonry of the vault, zone B is non-periodic masonry of breast walls and parapets, zone C is quarry masonry of the infill while zone D includes the paving layers. These are, from top to down: granite pavement, first concrete layer, second concrete layer (later characterized), concrete slab.

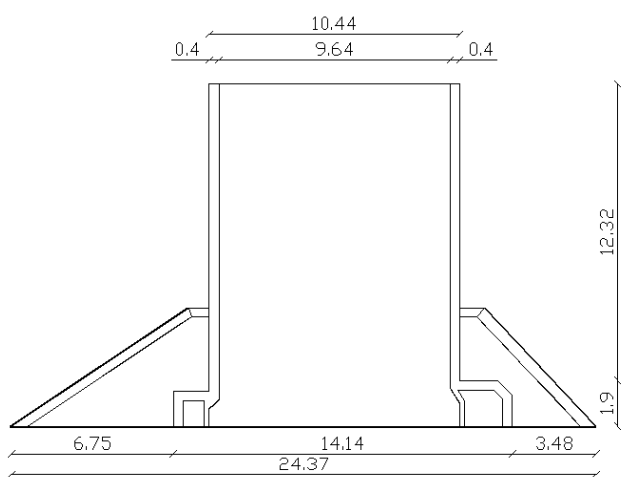


Figure 3.3 – Plant view of the model (measures in metres)

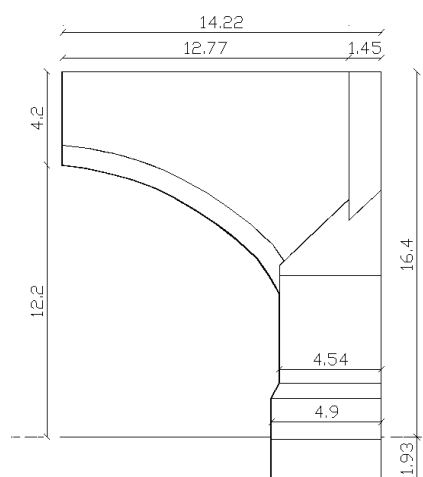


Figure 3.4 – Lateral elevation of the model (m)

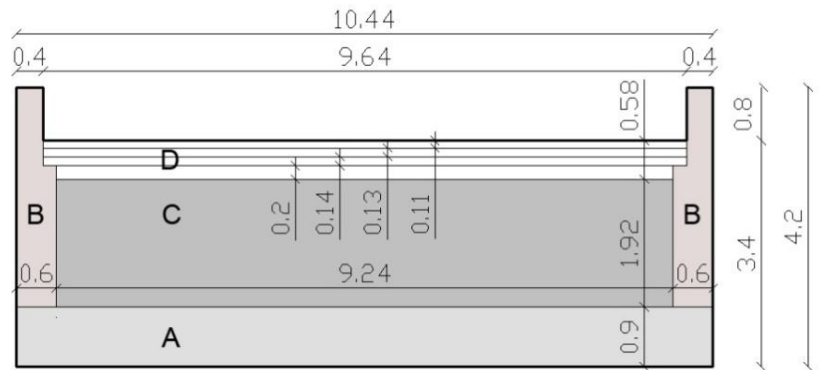


Figure 3.5 – Cross-section at the crown of the arch (measures in metres)

Two variations to the principal model are made: one without concrete layers (representing the state previous 1960s–1970s intervention), the other one with expansion joints (black rectangles in Figure 3.7) and the slab separated from the masonry (expressing the 2007–2010 intervention); new groups were required for the last model.

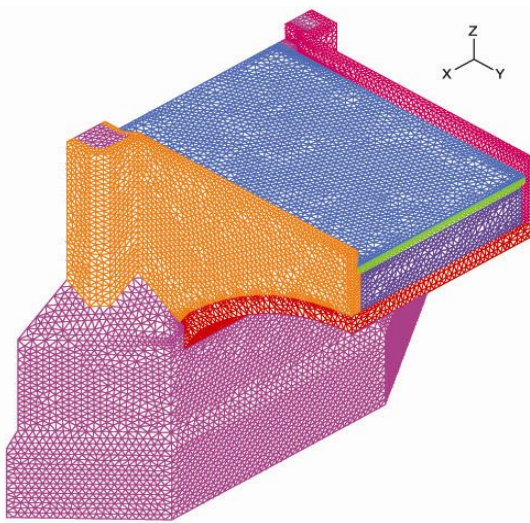


Figure 3.6 – After 70's model, meshed (northern side)

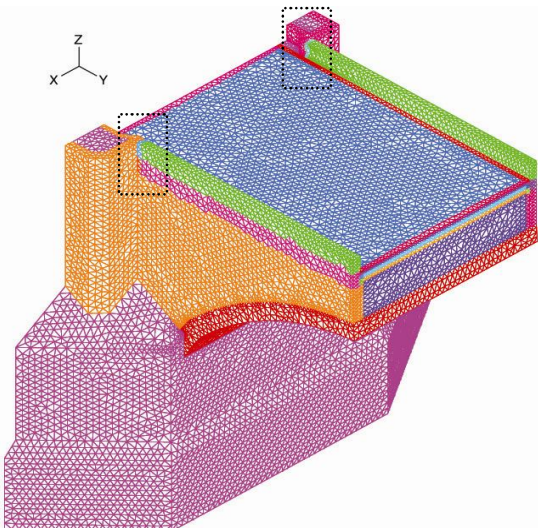


Figure 3.7 – After 2010 model, meshed (northern side)

All the models have the same mesh, made of 3D solid elements (4 nodes tetrahedral elements, isoparametric displacement-based, with linear approximation functions), forming 73749 nodes and 387773 elements (Figure 3.6, Figure 3.7). These are spatially isotropic in respect to integration points location and interpolation functions; 1-point Gauss integration is used for this typology of elements (ADINA R & D, 2011).

Two different kinds of boundary conditions are going to be tested:

- in configuration “A” the bottom of the pier is clamped, while on both vertical symmetry axes, displacements are fixed for X and Y direction (compare to Figure 3.6 for the axis position);
- in configuration “B” the base is fixed only in Z direction (with one node clamped for stability), while on both vertical symmetry planes only the Y direction is fixed, according to the principles of using symmetry.

3.3 Material properties

Masonry is a heterogeneous material consisting of units and joints, its features are strongly dependent from the properties of single components. The heterogeneity is considered thanks to homogenization techniques between the mechanical properties of the 2 masonry components. The chosen properties for the principal model (Sejnoha, 2006) on courtesy of Professor J. Zeman, are calculated according to first-order homogenization schemes. Each heterogeneity pattern is characterized by a statically equivalent periodic unit cell (SEPU), subjected to a defined loading history parameterized by the macroscopic strain tensor. The use of periodic boundary conditions on the boundary of the unit cell lets to consider the influence of the surrounding materials. The behavior of the homogenized material is calculated from strain-average stress relation in the unit cell (Zeman, 2008). The properties are summarized in Table 3.1.

Table 3.1 – Homogenized mechanical parameters (Sejnoha, 2006) of the materials related to the post 1975 state

#	Material	Element	E (Gpa)	ν	ρ (kg/m ³)	α (1/K)
1	Periodic sandstone masonry	Arch, pier	20.2	0.15	2700	7e-06
2	Non-periodic sandstone masonry	Breast wall	20.2	0.17	2700	8e-06
3	Quarry masonry	Infill	10.4	0.17	2500	8e-06
4	Granite pavement and bedding	Paving	1.0	0.2	2600	5e-06
5	Fine-grained concrete	1 st layer	29.0	0.2	2300	3e-06
6	Lightweight concrete (with hydro-isolation and geotextile)	2 nd layer	1.0	0.2	2300	1.2e-05
7	Reinforced concrete	Concrete slab	27.5	0.2	2600	1.2e-05

The material properties aforementioned well describe the condition after the intervention of the 1960s–1970s. Since the monument had a substantial evolution during the last century, two variations of the properties are executed in way to consider the “original” state before/after main repairs and suit the two variations of the main model. Therefore three different states of the monument are going to be considered and characterized by their materials:

- before 1960 state (asphalt paving, original deck);
- after 1975 state (granite paving, reinforced concrete slab, concrete layers);
- after 2010 state (presence of expansion joints in railing, paving and concrete slab).

This will let to make comparisons between the different conditions, studying the bridge response. The substituted materials (with their properties) can be found in Table 3.2 and Table 3.3 (the “#” numbers are related to the layer that they replace). Since the contact with the producer did not bring to the exact composition of the “plastic” mortar in expansion joints, hypothesized properties for it are assumed.

Table 3.2 – Mechanical properties of implemented materials (state before 1960's)

#	Material	Element	E (Gpa)	ν	ρ (kg/m ³)	α (1/K)
4	Asphalt and bedding layer	Paving	2.0	0.35	2300	5e-06
5	Mortar and loam	1 st layer	14.3	0.18	1800	1e-05
6	Sand and crushed gravel	2 nd layer	0.6	0.35	1500	5e-06
7	Quarry masonry	Infill	10.4	0.17	2500	8e-06

Table 3.3 – Mechanical properties of implemented material (state after 2010)

#	Material	Element	E (Gpa)	ν	ρ (kg/m ³)	α (1/K)
4	Granite pavement and lime mortar	Paving	1.0	0.2	2600	5e-06
5	Light concrete and hydro-isolation	1 st layer	19.0	0.2	2000	8e-06
6	Concrete (with steel net, geotextile)	2 nd layer	16.0	0.2	2000	8e-06
-	Extruded polystyrene	Joint in slab	3.0	0.3	35	6e-05
-	Crushed gravel	Joint slab-wall	0.6	0.35	1500	5e-06
-	Plastic mortar	Joint in railing	2.0	0.37	1300	1e-05

Real Young modulus of polystyrene and plastic mortar are lower, but values of Table 3.3 are assumed to limit the effect of those materials, since their thickness in the model is 10 times bigger than in reality. This was inevitable because the mesh is not editable (previously computed temperature values are assigned to nodes, therefore those cannot be changed). Moreover, the plastic mortar joint (with its interlocking of blocks) is simplified as vertical. Anyway the values will be later changed.

The strength of materials will be shown later (Table 4.14). In the non-linear analysis with Adina, joints will be implemented as elastic, so no tensile and compressive strength will be required. According to (Zeman, 2008), testing the masonry under macroscopically fully constrained conditions, it was understood that the homogenized coefficient of thermal expansion α reaches almost 0 due to extensive cracking, even for a moderate temperature change. Therefore a conservative value of $7 \cdot 10^{-6} \text{ K}^{-1}$ (corresponding to the temperature change $\Delta T \approx -3 \text{ }^{\circ}\text{C}$) can be employed in the macroscale analysis (Zeman, 2008).

3.4 Actions

Since the bridge is today accessible to pedestrians only, the actions on the structure are represented by self-weight, live load, temperature changes in the course of the year and water pressure; further studies took into account also flood and inertia effects due to a possible ship impact (Zeman, 2008). Among those actions, self-weight, pedestrian live load (5 KN/m^2 according to Eurocodes) and temperature changes are the loading considered in the present work.

3.4.1 Self-weight

It is the dominant permanent action due to the massive structure and it is considered by the program as a mass proportional load with magnitude equal to the gravity force.

3.4.2 Thermal load

A coupled non-stationary analysis (Zeman, 2008), considering temperature and moisture variations, explained the relevance of temperature effects compared to other loading.

The distribution of temperature field was determined for a 2 years period in way to involve every climatic change. The values follow the annual cycle and vary from about -14 to 45 °C.

The previous numerical simulation demonstrated that the temperature variation is confined to layers close to the boundary while the temperature in the bridge interior remained constant in space and varied between 6 and 17 °C. The extreme surface temperatures were extrapolated to -15 and 52 °C, respectively (Zeman, 2008).

Further studies (Krejci, 2014) highlighted that the maximum summer temperatures on the southern surface are 7–8 °C higher than on the opposite northern surface, due to radiation of sun (Figure 3.8, Figure 3.9). Moreover it was noticed a possible shift between simulated and monitored data, ascribed to imprecise material parameters (additional testing is required).

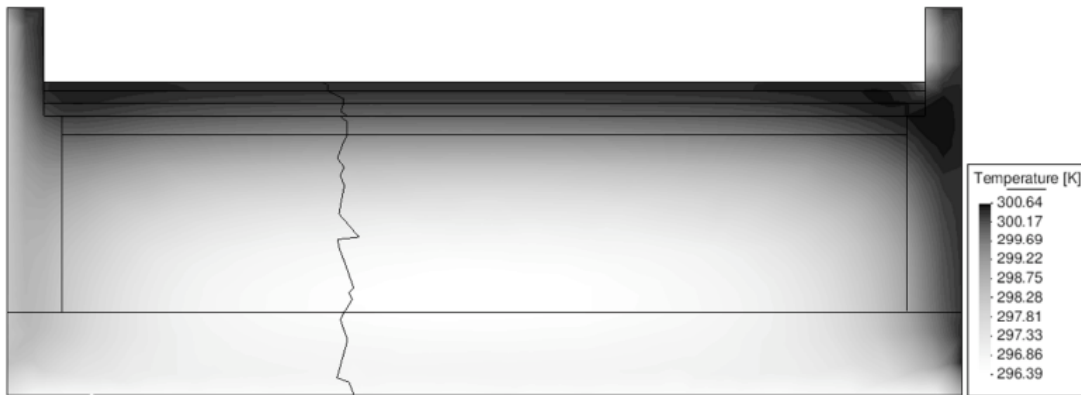


Figure 3.8 – Spatial distribution of temperatures during summer at the crown of the arch (Krejci, 2014)

The shift is bigger in points closer to the surface of the vault, because there the temperature is influenced by the shielding against sun and also by the water running under the bridge (Figure 3.8). The analysis of data displayed also that stronger daily fluctuations are found closer to the bridge surface in respect to the smoother fluctuations in the internal areas of the bridge (Krejci, 2014).

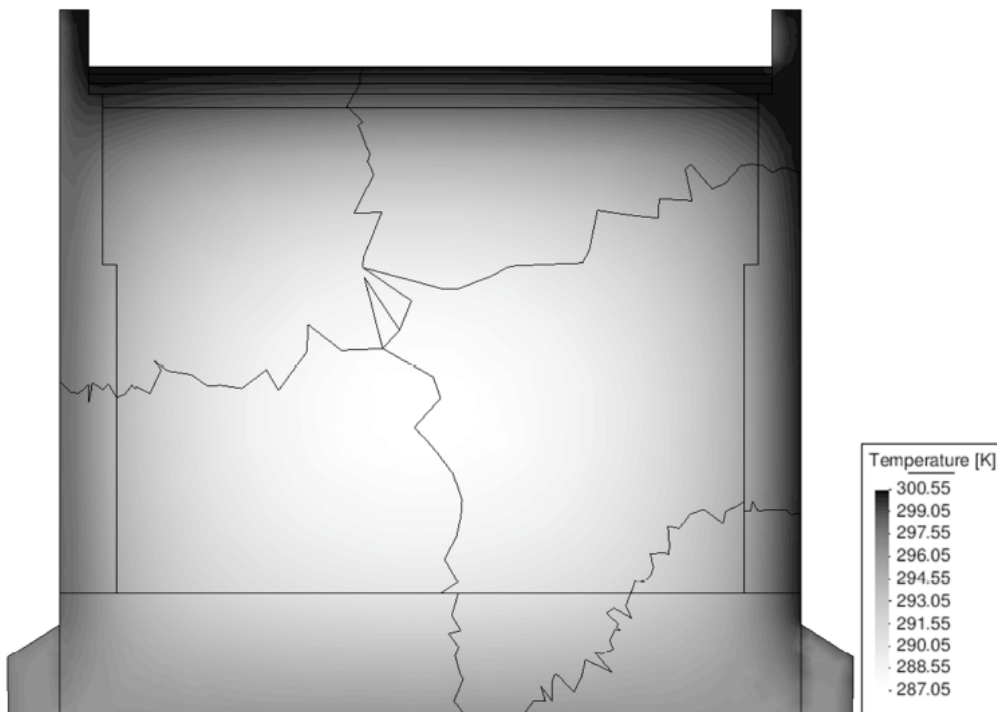


Figure 3.9 – Spatial distribution of temperatures during summer in the pier (Krejci, 2014)

4 THERMO-MECHANICAL ANALYSIS

A previous study (Witzany, 2008) used a temperature range of $\Delta T_{\text{summer}} = +37 \text{ }^{\circ}\text{C}$ and $\Delta T_{\text{winter}} = -24 \text{ }^{\circ}\text{C}$ considering the initial stress and deformation state of the structure due to the dead load. Their analysis showed that the interaction between vaults, breast walls and body filling contributes to increase tensile stresses and the tilting of breast walls (Witzany, 2008).

The model explained an unfavourable effect of coupling breast walls with the reinforced concrete slab, mainly in the area of the bridge arch crown: increasing of transversal normal stresses (causing cracks in arches and breast walls) and increasing of horizontal cyclic deformations.

The interaction arch-breast walls creates also a shift in the funicular (compression) line at the bridge vault's crown close to the arch edges (so where the breast walls are), making longitudinal tensile stresses on the vault's face, that provoke an increase of normal stresses in tension in the resisting cross section of the vault (Witzany, 2008).

4.1 Thermo-Elastic analysis

The heat transport problem is the first step for the non-linear and mechanics-oriented simulation of the bridge, carried out in a one way coupled format (the mechanical part is influenced by the thermal one) to manage the model complexity. The simulation of the heat transport is provided by a previous study at Czech Technical University (CTU) in Prague (Krejci, 2014), with the monitored temperatures as input and computed values at every node of the structure as output.

Temperature values in Kelvin degrees are set for every node at the initial condition (average values, corresponding at the annual temperature in April) (Figure 4.1, Figure 4.2) and at the final condition.

This can be the highest values (Figure 4.3) recorded on 26th August 2011, or the lowest (Figure 4.4) recorded on 12th February 2012. An elastic analysis considering self-weight, pedestrian live load (5 KN/m²) and temperature variations is performed, considering the following temperature combinations:

- Comb. A, from average values to highest (summer) values;
- Comb. B, average values to lowest (winter) values;
- Comb. C, from lowest to highest values;
- Comb. D, from highest to lowest values.

The analysis is run before with the configuration A of mechanical boundary conditions (base of the pier clamped, X and Y directions fixed on the symmetry planes), in way to compare later the results with Config. B (base fixed only in Z direction and symmetry planes only in Y direction).

Two FEA software will be used and their results compared:

- ADINA (Automatic Dynamic Incremental Nonlinear Analysis), a comprehensive finite element system developed from an American society. It will be exploited in the first part of the analysis;
- SIFEL (Simple Finite EElements), open source code written by the Department of Mechanics at the Faculty of Civil Engineering in Czech Technical University (Prague). It will be used in the second part of the work.

4.1.1 Temperature loading

The input temperatures are summarized in Table 4.1. After the maximum and minimum value for every condition, the ΔT_{\max} between initial values (Figure 4.1, Figure 4.2) and summer/winter condition (Figure 4.3/Figure 4.4) is shown. The maximum variation between the two extremes is $\Delta T_{\max} = 38.35$ (64852). The number in parenthesis close to the variation is the node of the FEM model to which the value is referred: they are marked in following figures and mentioned in Table 4.1. Values of node 890 could be influenced by the sharpness of the mesh element but the presence of similar numbers in all the side of the pier confirms their reliability. On the other hand, node 179 (minimum value of Figure 4.4) and the closest, seem to be an inaccuracy of the computation (they are in sharp elements and it is unreliable the presence of so low temperatures on southern side). The last line of the table ($\Delta T_{\text{average}}$) shows the averaged value of variation between initial and final condition. About the comparison between summer and winter temperatures, $\Delta T_{\text{average}} = 20.40$; values are going to be commented in the next paragraph. For temperature evolution during seasons, in mentioned nodes, compare to Par. 7.3.3.

Table 4.1 – Temperatures and variations

Temperatures (K)	Initial condition	Summer	Winter
Max	285.04 (890)	305.84 (890)	285.32 (29195)
Min	274.23 (49729)	282.14 (18978)	260.29 (64852)
ΔT_{\max}		21.58 (72535)	19.74 (64852)
$\Delta T_{\text{average}}$		13.92	6.47

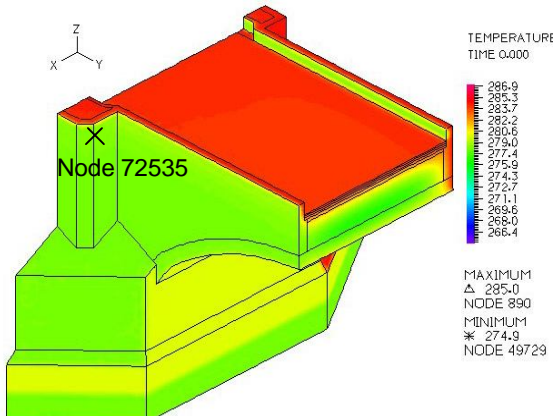


Figure 4.1 – Initial temperature condition (northern side)

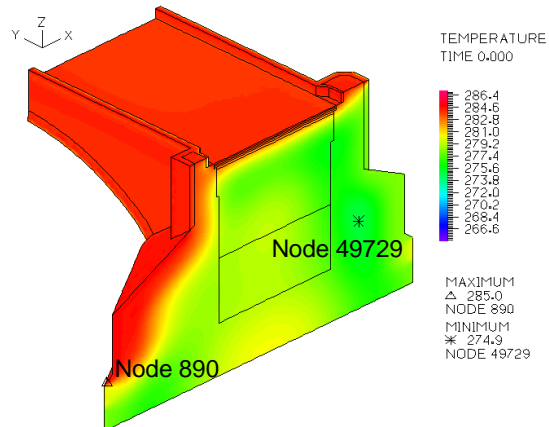


Figure 4.2 – Initial temperature condition (southern side)

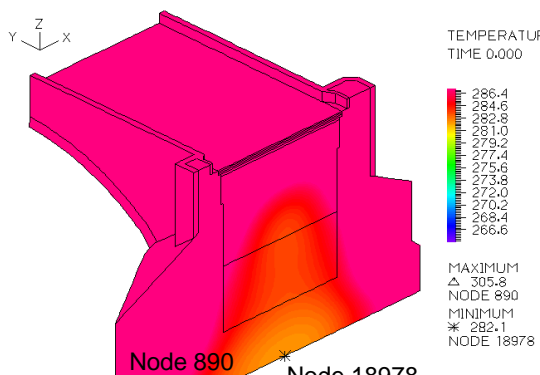


Figure 4.3 – Summer temperatures

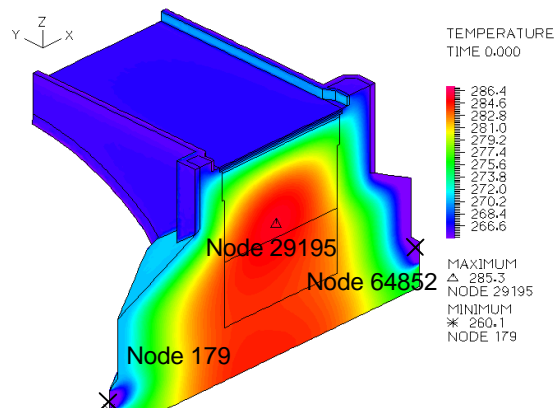


Figure 4.4 – Winter temperatures

4.1.2 Displacements

The first processing of the thermo-elastic analysis with Adina is about displacements. A computation considering only self-weight and another one with only temperatures are run in way to compare them to the analysis with actions combined. The aforementioned Config. A of boundary conditions is used. The self-weight brings to a maximum deflection of 0.72 mm as it could be expected from the structure. Considering only temperatures, the combination A (from average to summer values) creates a positive vertical displacement of 3.70 mm due to thermal expansion, while the combination B (from average to winter values) makes a vertical negative displacement of -1.17 mm, that can be physically accepted.

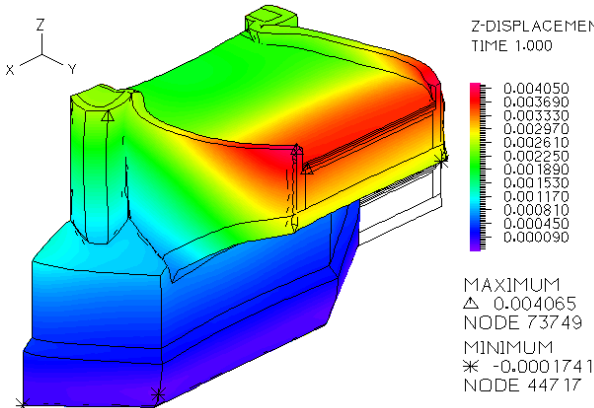


Figure 4.5 – Z-displacement, Comb. C

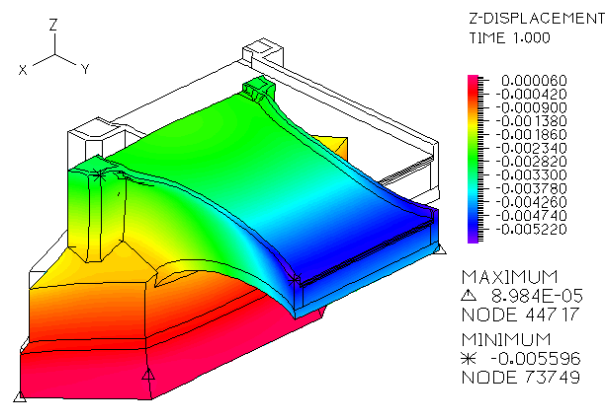


Figure 4.6 – Z-displacement, Comb. D

The analysis is run again considering self-weight, temperature loading and pedestrian live load (as it will be in all the next ones) obtaining the values in Table 4.2. The maximum deflections are related to the highest differences in temperature (combinations C and D) as it could be expected; those combinations are run to consider the extreme possible thermal load acting on the bridge (Figure 4.5, Figure 4.6).

Table 4.2 – Thermo-elastic analysis, maximum vertical displacements (values in mm), Config. A

Z _{max} -displacements (mm)	Comb. A	Comb. B	Comb. C	Comb. D
Only self-weight	-0.72	-0.72	-0.72	-0.72
Only temperatures	3.70	-1.17	4.79	-4.79
SelfW.+Temp.	2.99	-1.85	4.08	-5.57
SelfW.+Temp.+LiveLoad	2.96	-1.88	4.06	-5.60

Considering the variation between average and summer/winter temperatures, Comb. A shows higher displacements, even if self-weight and pedestrian live load act both in opposite direction, reducing the final value of positive translation. This happens because the applied thermal load (provided by previous studies at CTU in Prague) shows a higher variation from average to summer ($\Delta T_{\text{max}} = 21.58$; $\Delta T_{\text{average}} = 13.92$) than from average to winter ($\Delta T_{\text{max}} = 19.98$; $\Delta T_{\text{average}} = 6.47$). The averaged variation of temperatures between initial condition and winter ($\Delta T_{\text{average}} = 6.47$) is so low because temperatures in the infill at the core of the pier are higher in the final step than in the initial condition (compare Figure 4.4 with Figure 4.2).

The phenomenon happens due to the delay in heat conduction at the core of the pier, if compared to the external layers, according to the measured (Figure 4.7) and computed data. The following graph well explains it: superficial sensors (4A1, 4C1, 4D0, 4D1, 4D2, 4D3, 4E0, 4E1, 4F1, 4G1) show higher temperatures in April and lower in February than sensors placed at the interior (4B2, 4D4, 4D5, 4F2).

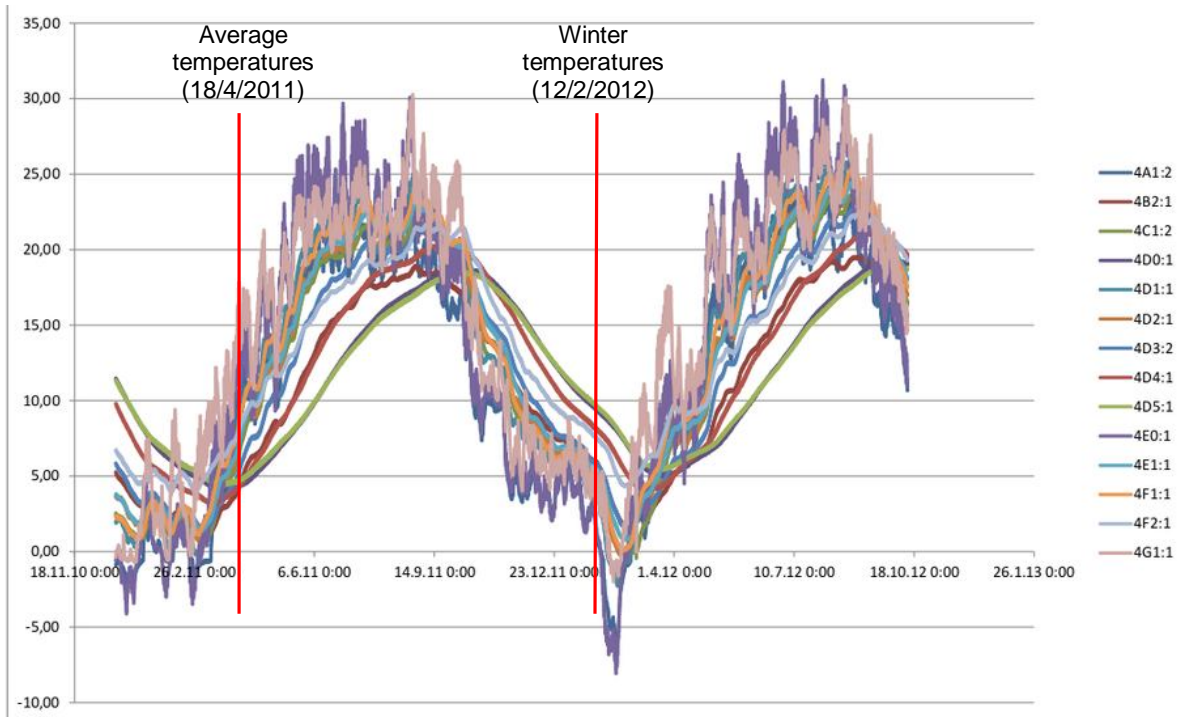


Figure 4.7 – Temperature measurements in CR.-SEC. No 4 (compare to Figure 2.29)

If the analysis is performed between extremes of temperature (Comb. C and Comb. D, both with same ΔT), the deflections are higher (in absolute value) for the transition summer to winter (Comb. D) because all the loads act in the same direction (-Z).

Since parapet and breast walls are one of the critical points of the structure, it is worthy to consider also the transversal displacements (Figure 4.8, Figure 4.9).

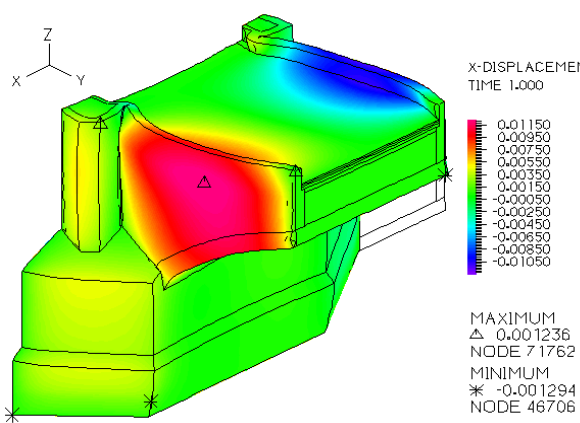


Figure 4.8 – X-displacement, Comb. C

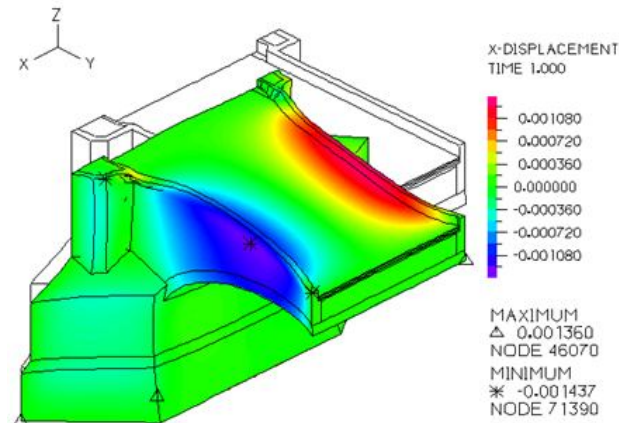


Figure 4.9 – X-displacement, Comb. D

According to Table 4.3, Comb. A reaches higher values than Comb. B, for the reason already explained (Figure 4.7). In all the cases the movement (toward the exterior if the temperature increases and toward the pavement if the temperature decreases) is almost not influenced by self-weight and live load, reaching the highest value (-1.44 mm) in Comb. D.

Table 4.3 – Thermo-elastic analysis, transversal displacements (values in mm), Config. A

X _{max} -displacements (mm)	Comb. A	Comb. B	Comb. C	Comb. D
Only self-weight	-0,02	-0,02	-0,02	-0,02
Only temperatures	0,97	-0,42	1,30	-1,43
SelfW.+Temp.	0,96	-0,43	1,29	-1,44
SelfW.+Temp.+LiveLoad	0,96	-0,43	1,29	-1,44

4.1.3 Stresses

The maximum ($\sigma_{1\max}$) and minimum ($\sigma_{3\max}$) principal stresses are considered for the 4 different analysis and compared to the stress state due to the only self-weight (Table 4.4). The smoothing technique, able to make continuous the results defined over adjacent Gauss points, is used (here and in following) to consider the average as mean value.

Table 4.4 – Principal stresses and strains for the different elastic analysis, Config. A

P. stress (MPa)	Self-weight	Comb. A	Comb. B	Comb. C	Comb. D
$\sigma_{1\max}$	0.70	1.90	11.01	2.46	29.41
$\sigma_{3\max}$	-2.26	-18.56	-1.72	-29.09	-2.86
P. strain (%)	Self-weight	Comb. A	Comb. B	Comb. C	Comb. D
$\varepsilon_{1\max}$	0.003%	0.028%	0.039%	0.051%	0.116%
$\varepsilon_{3\max}$	-0.008%	0.075%	-0.025%	-0.113%	-0.053%

According to the homogenized mechanical properties of the materials (compare to Table 3.1) and considering only the self-weight of the structure, cracks may appear due to tension in the parapet (Figure 4.10) and in the quarry masonry of the infill (due to its low tensile strength). The implementation of the temperature brings the stress state to overcome both tensile and compressive strength with high values but further analysis (first of all changing boundary conditions) will establish it. The task of this preliminary study is just to give a prediction of damage, toward the stress plotting. The nucleation of vertical cracks can be likely in the parapet (in correspondence to the concrete slab), due to thermal expansion in summer season (red rectangle in Figure 4.11), while the transition to the winter temperatures would cause cracks in the parapet at the connection with the pier and at the intrados of the vault (red circles in Figure 4.12). High compressive stresses would be located at the crown of the arch (Comb. C) and in the parapet in correspondence to the concrete layers (Comb. D), this will be taken into account in next analysis.

Please notice that, unluckily, following images have not the same plotting scale, due to difficulties in setting it with Adina and to the great range of values between different combinations (therefore the use of only one scale would bring to loss of particulars). This problem will be better managed with the next software used (SIFEL) thanks to its direct plot scale editing.

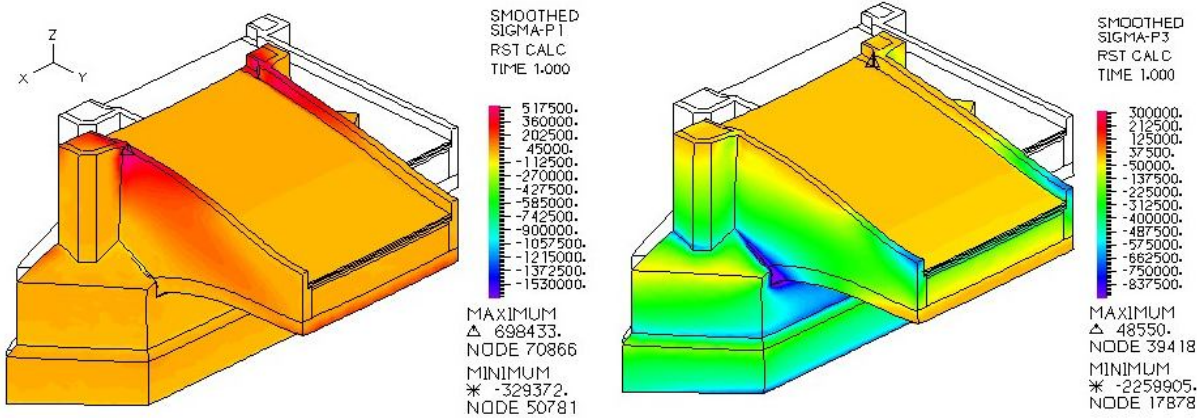


Figure 4.10 – Maximum and minimum principal stresses (smoothed), related to only self-weight

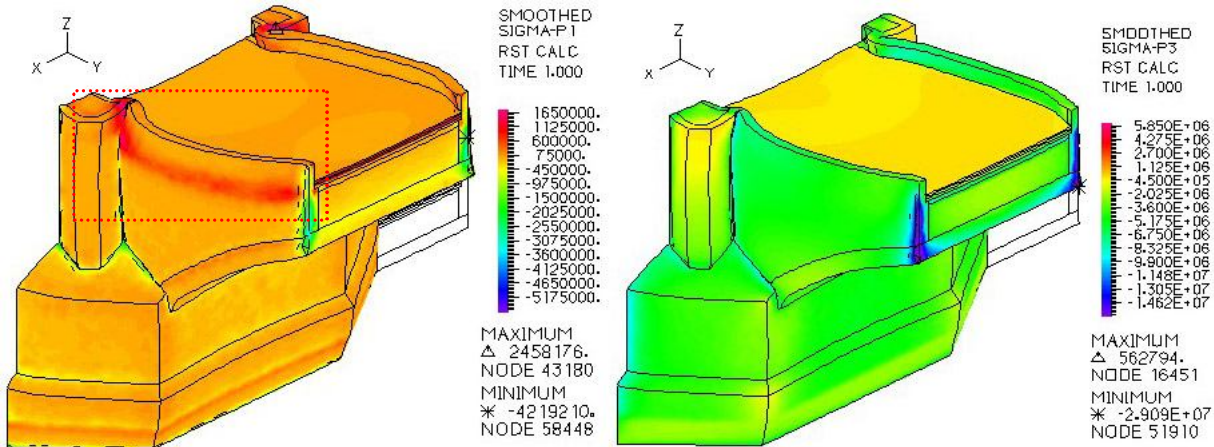


Figure 4.11 – Maximum and minimum principal stresses (smoothed), Comb. C

The images show the result for Comb. C and Comb. D but the stresses have same propagation than in Comb. A and Comb. B respectively. The analysis between the extreme values winter-summer and summer-winter is used to consider maximal temperature changes and it allows to be in favour of safety.

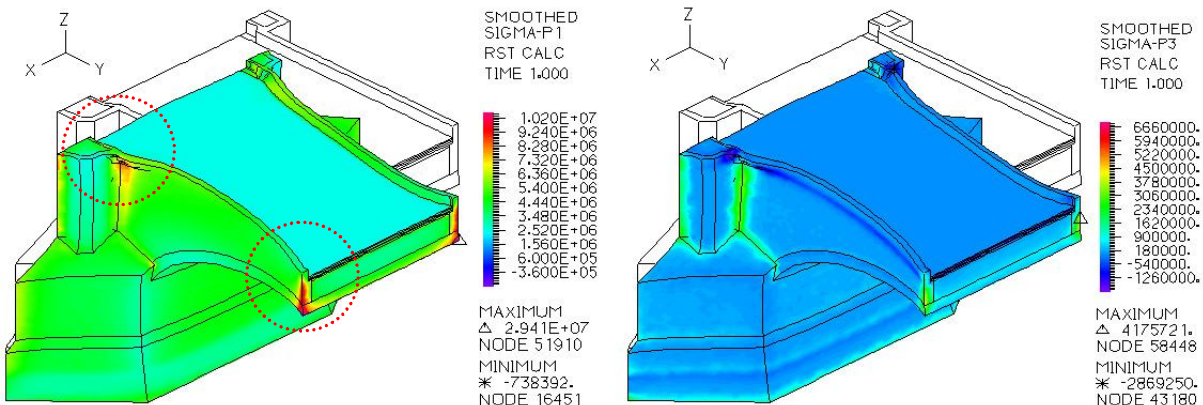


Figure 4.12 – Maximum and minimum principal stresses (smoothed), Comb. D

4.1.4 Comparison: mechanical boundary conditions

The aforementioned results concern the configuration A of boundary conditions. The analysis is repeated with the configuration B (basement fixed only in Z direction, except a clamped node, and symmetry planes fixed in Y direction), obtaining the values in Table 4.5 and Table 4.6.

Table 4.5 – Max. displacements related to different temp. combinations (compare to Par.4.1 for description)

Z _{max} -displacement (mm)	Self-weight	Comb. A	Comb. B	Comb. C	Comb. D
SelfW.+Temp.+LiveLoad	-0.75	2.64	-1.79	3.58	-5.10
X _{max} -displacement (mm)	Self-weight	Comb. A	Comb. B	Comb. C	Comb. D
SelfW.+Temp.+LiveLoad	-0.09	1.37	-0.62	2.11	-1.76

Since the structure has different boundary conditions (there is no more X-constrain on the vertical planes and X,Y-constraints at the basement, except than for one node) the vertical displacement is reduced (highest value of -5.10 mm instead of -5.60 mm) while the horizontal one is increased (2.11 mm to compare with 1.44 mm). The new configuration changes the deformed shape due to temperature loading, as can be see from Figure 4.13 and Figure 4.14, if compared with Figure 4.5 – Figure 4.9, where the X-constrain on the symmetry axis created an unrealistic deformed shape in the railing. Another difference is the deformation of the pier on the symmetry plane, now free to move in X (and Z) direction.

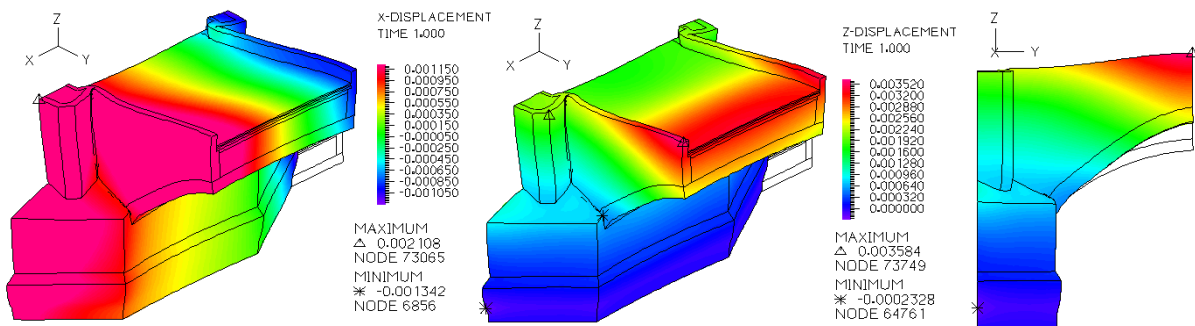


Figure 4.13 – X and Y displacement with deformed shape (Comb. C: from average temperature to summer)

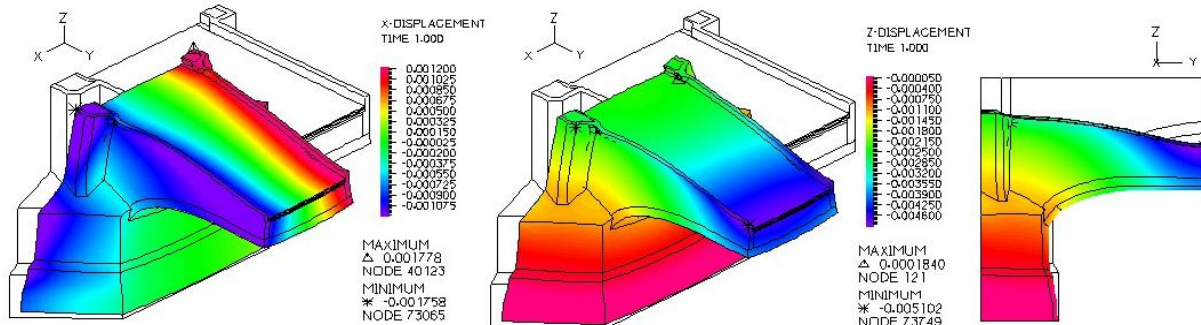


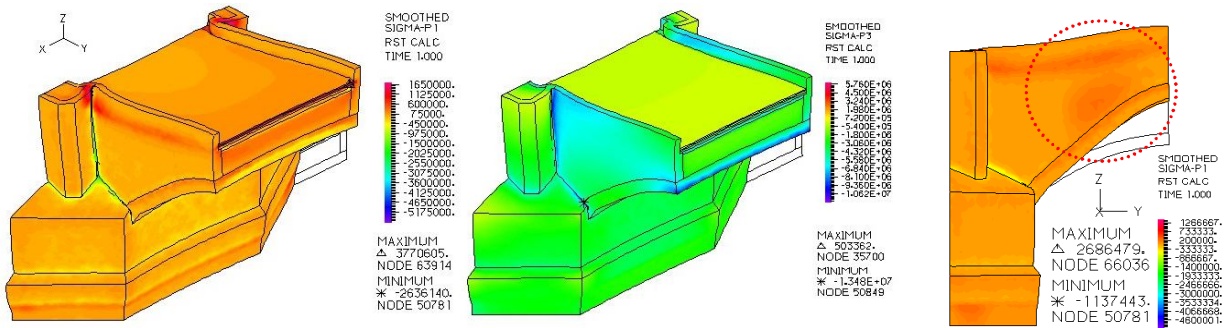
Figure 4.14 – X and Y displacement with deformed shape (Comb. D: from average temperature to winter)

Thanks to the absence of constrains in X-direction for the symmetry planes, principal stresses (Table 4.6) are lower than in the previous analysis (Table 4.4), showing maximum tension (σ_1) of 11.36 MPa (instead of 29.41 MPa) and maximum compression (σ_3) of -13.48 MPa (to compare with -29.09 MPa).

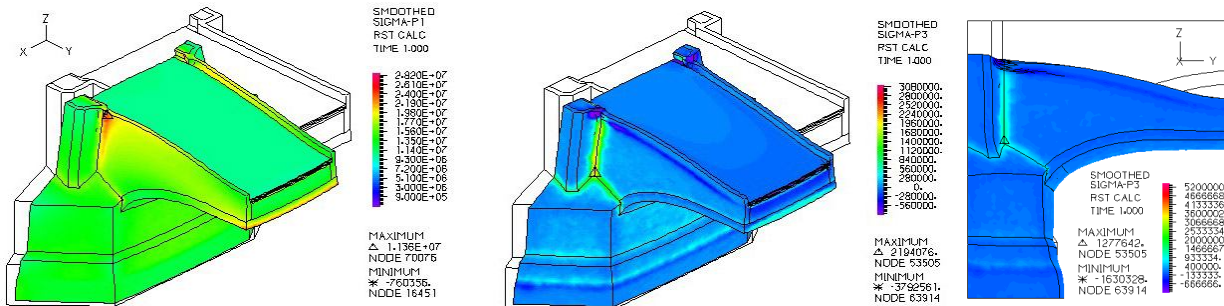
Table 4.6 – Principal stresses for the different combinations

P. stress (MPa)	Self-weight	Comb. A	Comb. B	Comb. C	Comb. D
$\sigma_{1\max}$	0.65	2.69	5.69	3.77	11.36
$\sigma_{3\max}$	-2.31	-7.05	-1.63	-13.48	-3.79

The stress configurations are similar to those already shown in Par. 4.1.4. but comparing them with Figure 4.15 and Figure 4.17 it is possible to notice how the stresses are proportionally lower at the crown of the arch (in respect to the connection between railing and pier) than before. This is due to the different boundary conditions used.

Figure 4.15 – Maximum (σ_1) and minimum (σ_3) principal stress (smoothed), Comb.CFigure 4.16 – σ_1 , Comb.A

The combinations between average temperature and summer (Comb. A) or winter (Comb. B) lead to lower stresses but there are some changes in their pattern. In Comb. A there are tension areas in the breast walls also close to the vault (red rectangle in Figure 4.16), while in Comb. B (Figure 4.18) the compression band in the railing is proportionally lower to the other stresses than in Comb. D.

Figure 4.17 – Maximum (σ_1) and minimum (σ_3) principal stress (smoothed), Comb. DFigure 4.18 – σ_3 , Comb.B

Configuration B of boundary conditions satisfies requirements of symmetry as Config. A, but it is more realistic and the deformed shapes confirm it, therefore this is the set of constrains that will be used for next analysis.

Extend explanation of the stress state (and its causes) at the connection between parapet and pier is provided in Par. 7.1.3 of the Annexes.

4.1.5 Inner material

Observing the model on the side of the symmetry plane of the pier, it is possible to notice high concentration of tensile stresses in Comb. A and Comb. C (Figure 4.19) while the same part has great compressive stresses in Comb. B and Comb. D (Figure 4.20). This is due to the temperature variations of the external areas of the pier, higher than in the internal zone (according to Par. 4.1.1): during summer this makes an expansion of the pier volume provoking tension in its interior, while during winter the external layers reduce volume compressing the inner material.

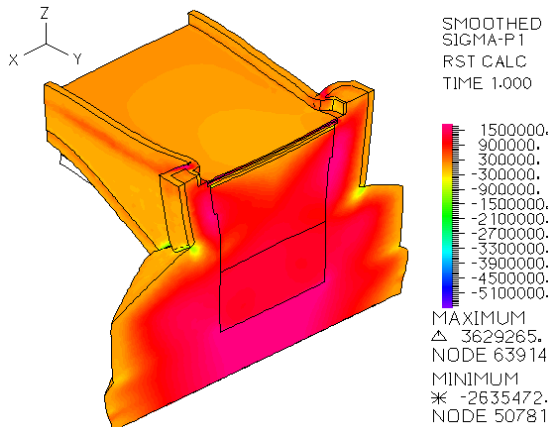


Figure 4.19 – Maximum principal stress, Comb. C

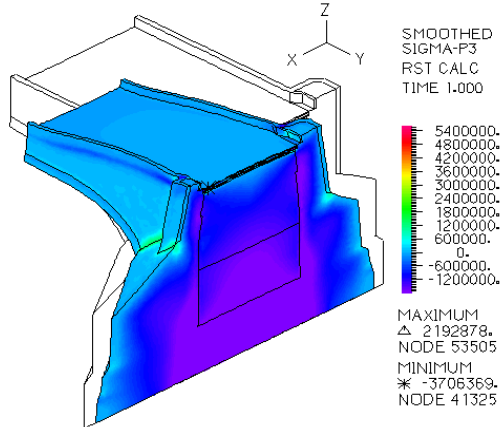


Figure 4.20 – Minimum principal stress, Comb. D

4.1.6 Comparison: structure pre/post repair

A further comparison is done to evaluate the structure before the invasive repair of the 1960s–1970s and after the last intervention (with configuration B of constrains, considered more reliable), comparing them with the model representing 1960s–1970s actions. The results can be appreciated in next tables.

Table 4.7 – Structure before 1960: maximum displacements related to the different temperature combinations

Z _{max} -displacements (mm)	Self-weight	Comb. A	Comb. B	Comb. C	Comb. D
SelfW.+Temp.+LiveLoad	-0.78	2.67	-1.94	3.75	-5.33
X _{max} -displacements (mm)	Self-weight	Comb. A	Comb. B	Comb. C	Comb. D
SelfW.+Temp.+LiveLoad	-0.11	1.31	-0.52	1.67	-1.56

Table 4.8 – Structure before 1960: principal stresses for the different combinations

P. stress (MPa)	Self-weight	Comb. A	Comb. B	Comb. C	Comb. D
$\sigma_{1\ max}$	0.73	1.46	5.94	2.29	11.82
$\sigma_{3\ max}$	-2.35	-7.14	-1.63	-13.30	-2.78

As it can be seen comparing the output of Table 4.7 and Table 4.8 with Table 4.5 and Table 4.6 (structure after the 1960s–1970s intervention), the vertical displacements of the bridge before 1960 are slightly higher (0.2 mm) since the structure has less stiffness (absence of concrete slab), while the horizontal displacements are reduced probably due to the lower thermal expansion coefficient of the pavement layers (concrete is considered replaced by quarry masonry).

On the other hand, stresses have similar configuration but their magnitude is greater in tension (11.82 vs. 11.36 MPa) and smaller in compression (-13.30 vs. -13.48 MPa). This is provoked by the lower rigidity of the structure.

The 1960s–1970s intervention increased the stiffness sensitising the structure to thermal variations and linking the opposite breast walls with reinforcement of the concrete slab, creating spaced stresses in them. To avoid these effects the 2007–2010 repair introduced expansion joints in the railing and in the slab, cutting it at the middle and at the borders, deleting its connection with breast walls.

The results for the model representing the last intervention are shown in Table 4.9 and Table 4.10.

Table 4.9 – Structure after 2010: maximum displacements related to the different temperature combinations

Z _{max} -displacements (mm)	Self-weight	Comb. A	Comb. B	Comb. C	Comb. D
SelfW.+Temp.+LiveLoad	-0.75	2.6	-1.79	3.55	-5.08
X _{max} -displacements (mm)	Self-weight	Comb. A	Comb. B	Comb. C	Comb. D
SelfW.+Temp.+LiveLoad	-0.10	1.28	-0.67	1.69	-1.76

Table 4.10 – Structure after 2010: principal stresses for the different combinations

P. stress (MPa)	Self-weight	Comb. A	Comb. B	Comb. C	Comb. D
$\sigma_{1\ max}$	0.55	1.38	6.91	2.06	12.10
$\sigma_{3\ max}$	-2.31	-7.58	-1.62	-13.35	-2.58

The representation of the last intervention shows slightly lower displacements (comparing Table 4.9 with Table 4.5) because the self-weight is reduced and the structure has less sensitivity to temperature changes. The principal stress values are similar to the previous model but they have a different configuration. The minimum principal stress is no more placed as the connection between pier and railing but below this, due to the presence of the expansion joint that has similar effect also on the maximum principal stress (red circle in Figure 4.22). The new joints in the slab allow not to have a concentration of stresses at its connection with the parapet as it was in the red rectangle of Figure 4.11 or in the minimum principal stresses of Figure 4.12.

Both structures will be studied in non-linearity, from now on, they will be named just “1975 model” and “2010 model”. For a punctual contrast between the two models, please compare Par. 7.1.2 (Annexes).

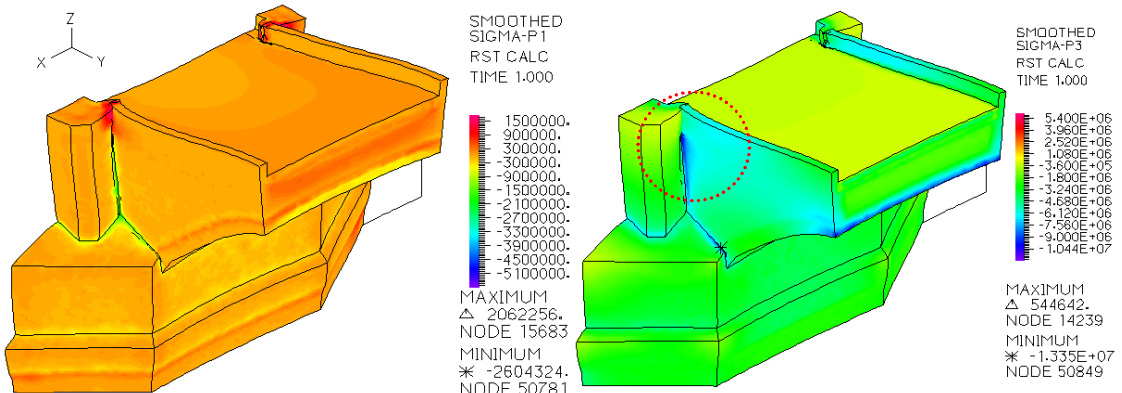


Figure 4.21 – Maximum and minimum principal stress (smoothed), Comb. C (structure after 2010)

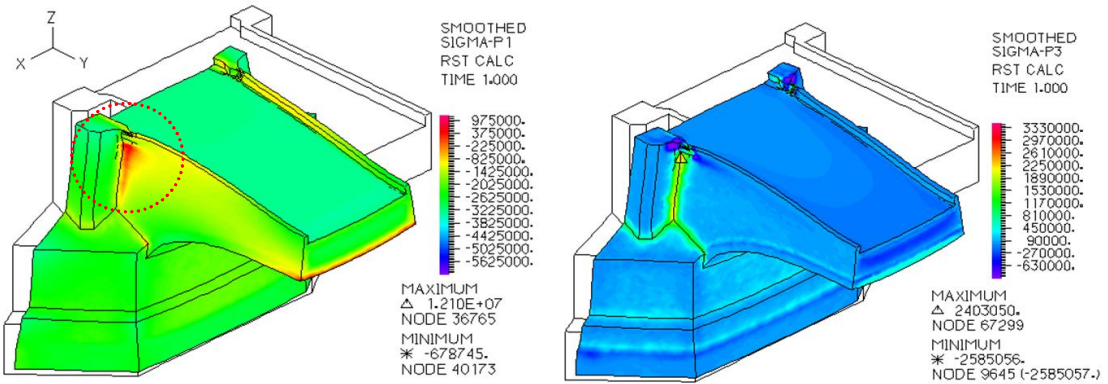


Figure 4.22 – Maximum and minimum principal stress (smoothed), Comb. D (structure after 2010)

4.1.7 Comparison: linear analysis with two different software

The analysis till here performed with Adina is compared to the output of the software SIFEL (post-processed by CIMNE GiD), that will be later used for the non-linear analysis, therefore an assessment of the 2 tools is required.

According with the structural response and further studies at the Muzeum Karlova Mostu about the deck layers, some material properties have been differently assumed (Table 4.11 and Table 4.12) in way to obtain a more realistic behavior. The same will be used in the non linear analysis, to reach comparable results.

Table 4.11 – Mechanical parameters of materials (related to the post 1975 state)

#	Material	Element	E (GPa)	ν	ρ (kg/m ³)	α (1/K)
1	Periodic sandstone masonry	Arch, pier	20.2	0.15	2700	7.0e-06
2	Non-periodic sandstone masonry	Breast wall	20.2	0.17	2700	8.0e-06
3	Quarry masonry	Infill	10.4	0.17	2500	8.0e-06
4	Granite pavement (cement mortar)	Paving	14.0	0.20	2600	5.0e-06
5	Fine-grained concrete	1 st layer	22.0	0.20	2300	5.0e-06
6	Lightweight concrete (with hydro-isolation and geotextile)	2 nd layer	1.0	0.20	2300	1.0e-05
7	Reinforced concrete	Concrete slab	27.5	0.20	2600	1.2e-05

Table 4.12 – Mechanical properties of implemented materials (after 2010 state)

#	Material	Element	E (GPa)	ν	ρ (kg/m ³)	α (1/K)
4	Granite pav. (lime mortar, sand bedding)	Paving	7.0	0.20	2600	5.0e-06
5	Light concrete and hydro-isolation	1 st layer	9.0	0.20	1900	7.0e-06
6	Concrete with steel net and separation cloth	2 nd layer	16.0	0.20	2300	1.0e-05
-	Extruded polystyrene	Joint in slab	3.0	0.30	35	8.0e-06
-	Crushed gravel	Joint slab-wall	2.0	0.35	1500	5.0e-06
-	Plastic mortar	Joint in railing	5.0	0.37	1300	1.0e-05

The effects of the change in properties, as well as the difference between the 2 software, are extendedly explained in Par. 7.1 of the Annexes. For the 1975 model, the calculated displacements of the two software are the same (0.5% of variance), while the inaccuracy in stresses is of 5% (SIFEL provides higher values) that increases of 1% if the results are smoothed. The smoothing, able to make

continuous the results defined over adjacent Gauss points, is used in both software to consider the average as mean value.

The implementation of the 2007–2010 intervention (with the new chosen properties) in the model highlights that this is able to decrease stresses (of 5%) and modify their configuration in comparison to the 1975 model, leaving almost unaltered the displacement. Extended description about it can be find in Par. 7.1.2. Table 4.13 shows the comparison of stress values between the two software; even in this case SIFEL provides results slightly higher than Adina. Computed values must be the same but likely the post-processing algoritm differently shows local stresses in the narrowest elements (Adina cuts peaks with an averaging procedure, while GiD has no manipulation of results) as explained in Par. 7.1.1. Since those elements are more diffused in thin layers, it will be convenient to reduce the relative difference in their thermal expansion coefficients to avoid convergence problems (due to local stress peaks) in the non-linear analysis with SIFEL. Linear analysis was really useful to arrange models and their properties in way to approach the non-linear analysis.

Table 4.13 – Comparison of principal stress (smoothed) for combinations and temp. effects only (2010 mod.)

σ_{Princ} (MPa) smoothed	Self-weight	Comb. A only T	Comb. A	Comb. B only T	Comb. B	Comb. C only T	Comb. C	Comb. D only T	Comb. D
$\sigma_{1\max}$ Adina	0.57	1.28	1.18	7.50	6.19	2.42	2.21	11.62	11.93
$\sigma_{3\max}$ Adina	-2.31	-7.90	-7.59	-1.32	-1.62	-11.62	-13.37	-2.42	-2.63
$\sigma_{1\max}$ SIFEL	0.59	1.55	1.40	7.56	6.62	2.51	2.29	13.19	13.62
$\sigma_{3\max}$ SIFEL	-2.47	-7.90	-7.60	-1.32	-1.62	-13.19	-13.58	-2.51	-2.73
Inaccuracy	3.85%	21.18%	19.14%	0.76%	6.84%	6.84%	3.98%	13.50%	14.19%
Average: 6.50%	6.70%	0.05%	0.10%	0.38%	0.03%	0.03%	1.60%	3.79%	3.68%

The dilatation joints at the connection pavement-parapet and pier-parapet are considered in the same way by the two software and are able to decrease the stress in critical points. E.g., in Comb. C analysis, the arch crown lifts up and the connection pier-parapet suffers composite stresses (Figure 4.23, Figure 4.25) that the vertical joint is able to decrease with its deformation (Figure 4.24, Figure 4.26). For an exhaustive analysis of dilatation joints action please compare to Par. 7.1.3 of Annexes.

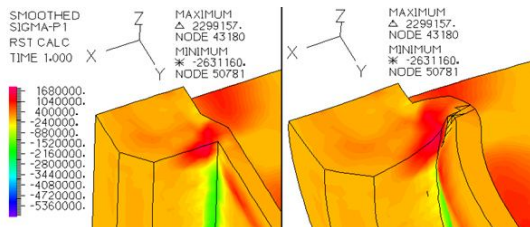


Figure 4.23 – σ_1 , Comb. C, 1975 model

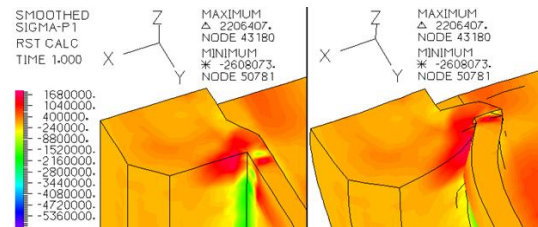


Figure 4.24 – σ_1 , Comb. C, 2010 model

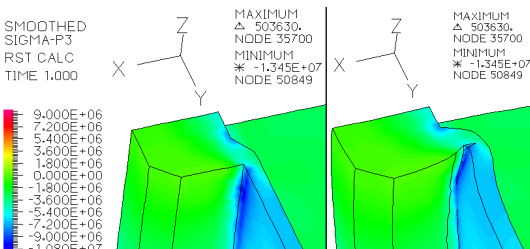


Figure 4.25 – σ_3 , Comb. C, 1975 model

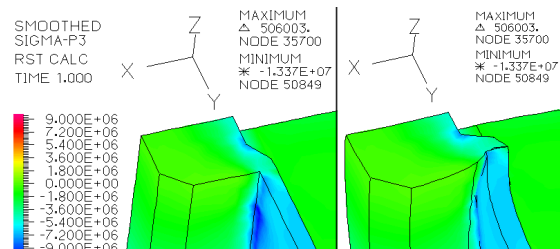


Figure 4.26 – σ_3 , Comb. C, 2010 model

4.2 Non-linear analysis (Adina)

The material non-linearity may be considered in Adina through the “concrete material model”, valuable for 2D and 3D solid elements. The main features of the material model are (ADINA R & D, 2011):

- tensile failure at a maximum, relatively small principal tensile stress;
- compression crushing failure at high compression;
- strain softening from compression crushing failure to ultimate strain at which the material totally fails;
- the tensile and compression crushing failures are governed by relative failures envelopes.

Despite the name, its basic characteristics make the concrete model suitable for other materials. Due to non-linearity, the stress-strain relation is linear only until tensile failure, at which the critical stress happens. During unloading, the material is assumed to be isotropic, while in loading it is considered orthotropic with directions of orthotropy defined by the principal stress directions. Once cracking occurs in any direction i , that direction is fixed from that point onward in calculating principal stresses. Further information about the model is available in Par. 7.2.4 of Annexes.

4.2.1 Mechanical properties for non-linear analysis

The concrete model requires the same material information used for linear analysis (Table 4.11, Table 4.12) plus maximum tensile stress $\sigma_{t\ max}$, post cracking tensile stress σ_{tp} , crushing stress $\sigma_{c\ max}$ and its corresponding strain $\varepsilon_{c\ max}$, ultimate compressive stress $\sigma_{c\ ult}$ and strain $\varepsilon_{c\ ult}$, fracture energy G_f .

The components of the dilatation joints (plastic mortar, XPS, gravel) are maintained as elastic materials (Table 4.12). Compressive strength is overestimated in way to focus the analysis on tensile cracking (that actually present on the monument), supporting also the convergence (because stability problems occurred with Adina's computation).

Table 4.14 – Material properties for stress-strain relation in concrete model

Material	$\sigma_{t\ max}$ (Mpa)	$\varepsilon_{t\ max}$ (%)	$\sigma_{c\ max}$ (Mpa)	$\varepsilon_{c\ max}$ (%)	$\sigma_{c\ ult}$ (Mpa)	$\varepsilon_{c\ ult}$ (%)	G_f (N/m)
Periodic sandstone	0.50	0.0025	-9.60	-0.0480	-7.50	-0.09	80
Non-periodic sandstone	0.50	0.0025	-9.60	-0.0480	-7.50	-0.09	80
Quarry masonry	0.30	0.0029	-6.20	-0.0600	-5.00	-0.10	40
Granite pavement	0.75	0.0054	-9.00	-0.0650	-8.00	-0.10	10
Fine-grained concrete (1975)	1.40	0.0068	-24.00	-0.1100	-21.00	-0.15	36
Lightweight concrete (1975)	1.40	0.1400	-24.00	-2.4000	-21.00	-4.00	36
Reinforced concrete	1.60	0.0058	-24.00	-0.0900	-21.00	-0.16	36
Light concrete+Hydr. (2010)	1.40	0.0156	-24.00	-2.6700	-21.00	-4.00	36
Concrete with steel net (2010)	1.50	0.0094	-24.00	-0.1500	-21.00	-2.00	36

4.2.2 Results: temperature combination A

Since temperatures were computed by another software, the implementation in Adina did not allow to consider increments but only final values, obstructing the convergence of the non-linear analysis. The obstacle was overtaken creating by hand 26 temperature steps between initial and final value and transforming them in input rearranging the mapping file. Even modifying the convergence criterion, the analysis was still unstable because, if the convergence was not reached, the program could not reduce the temperature step but only the other loads. The “low-speed dynamics feature” of Adina was

used to carry on the work. The technique allows to overcome convergence difficulties including dynamic effects in a static problem, adding inertia and stiffness proportional damping (the explanation of the process is provided in Par. 7.3.1 of the Annexes). The analysis was run for Comb. A and Comb. B, using Newton-Raphson and modified Newton-Raphson method, in way to compare the results with those from SIFEL. The final step (for Comb. A) provided maximum values of 1 MPa in tension, 7 MPa in compression and 2.60 mm of vertical displacement (Table 4.15).

Table 4.15 – Stresses and displacements for different time steps of 1975 model and final results of 2010 model

Time step:	0.5 ₁₉₇₅	1.0 ₁₉₇₅	1.5 ₁₉₇₅	2.0 ₁₉₇₅	2.5 ₁₉₇₅	3.0 ₁₉₇₅	3.0 ₂₀₁₀
(MPa)	0.52	1.05	1.12	1.06	1.03	1.01	0.78
(MPa)	-2.75	-5.52	-5.66	-5.94	-6.36	-6.92	-7.25
Displ. Z _{max} (mm)	0.81	1.63	2.01	2.39	2.49	2.60	2.60

Results are in agreement with the linear analysis as the stress configuration along the railing (Figure 4.27), while tensile stresses on the pavement are influenced by the appearance of damage at time step 1.625, when maximum tension decreases of 1 MPa. Then the damage evolves as can be seen from Figure 4.28, that shows the release of stresses on the pavement for different time steps. Actually the stress configuration on the external pavement layer is fictitious since it is formed by embedded blocks therefore it would not be able to accept any stress, but it is adequate for lower layers.

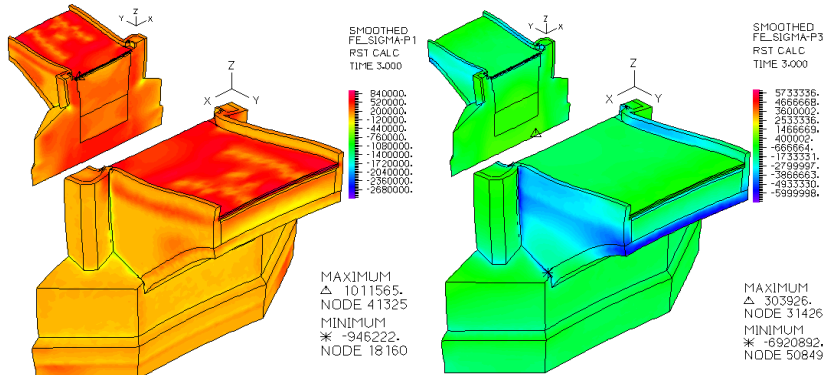


Figure 4.27 – Tensile and compressive stress plots (Comb. A)

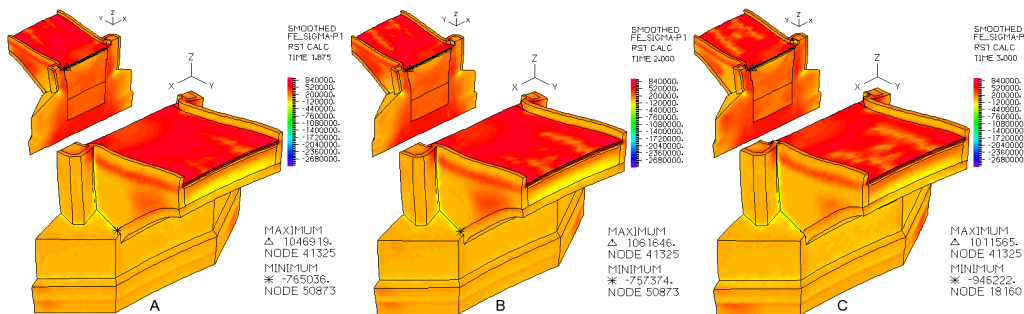


Figure 4.28 – Evolution of the release of stresses on the pavement (time steps: 1.875 2.00 3.00)

The damage can be studied in the software by the “crack flag”. It is a three digit number (P1)(P2)(P3), where each digit represents a principal stress coordinate direction. (0) means no crack, (1) is an open crack, (2) is a closed crack. (3)(3)(3) refers to a material crush. “Number of cracks” is a crack quantification at each integration point. Figure 4.29 shows open cracks in pavement, railing, connection railing-pier and connection railing-vault due to the uplift of the vault body provoked by the

increase of temperature (Comb. A). “Number of cracks” explains where damage is most active: peaks of 2-3-4 cracks per integration point in the connection railing-pier (Figure 4.29, red rectangle “B”).

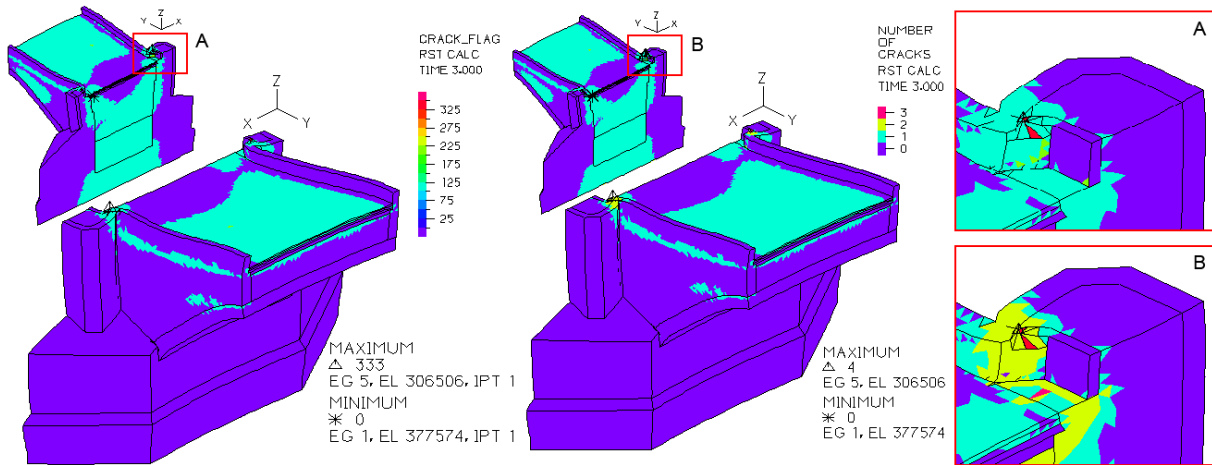


Figure 4.29 – Crack flag and number of cracks in 1975 model (Comb. A)

According to Figure 4.30, the damage starts at the connection between railing ad pier, then inside the pier (at the boundary with the filling), successively cracks develop on pavement and railings too.

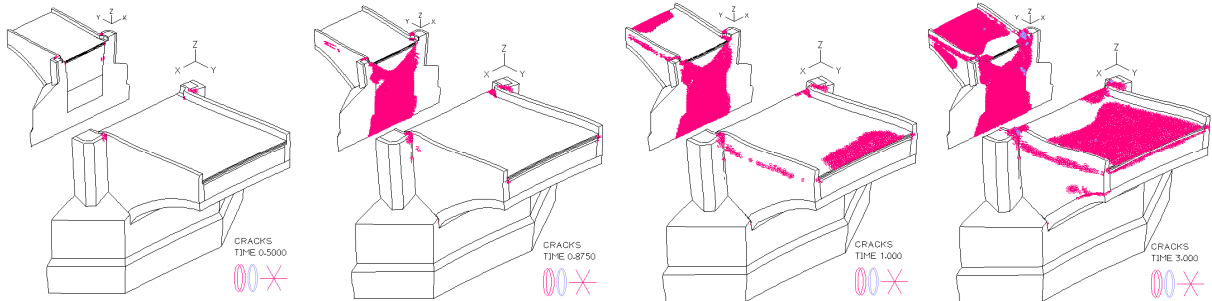


Figure 4.30 – Crack evolution at step 4 of 25, 7 of 25, 8 of 25 and 25 of 25

The effect of the 2010 intervention was studied. It lets to avoid tensile cracks along the railing thanks to the releave of the connection railing-slab (Figure 4.31). It allows also to reduce the global stress state (compare to Table 4.15) and that between railing and pier, decreasing the peak number of cracks from 4 to 2 (red rectangle “B”), moving the high damaged area from the pier to the railing itself.

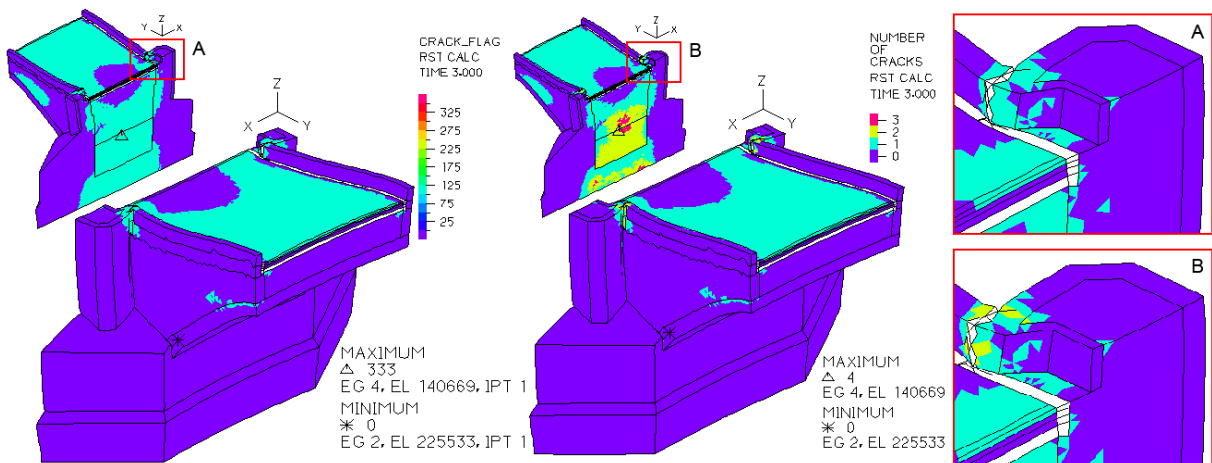


Figure 4.31 – Crack flag and number of cracks in 2010 model (Comb. A)

On the other hand the lower lateral stiffness, due to the release of the connection slab-breast walls, provokes an higher increase of pier volume in the external layers (caused by temperature loading). This is responsible of tensile stresses in the core where cracks appear (purple colour on the symmetry plane at the pier). The high damage at its basis could be not realistic since the model is influenced by constraints: springs (based on subsoil Young modulus and area of a representative mesh element) were implemented to study the phenomenon but the difference in results was lower than 2%.

The dilatation joints on pavement layers (as the use of more compatible materials) allow to avoid the excessive cracking on the surface, as can be seen comparing Figure 4.32 with Figure 4.33. Areas of high strain (red vectors) of the first one, are not visible in the second one (unluckily, due to a problem with the software, it was not possible to set the two plots exactly at the same scale as preferable).

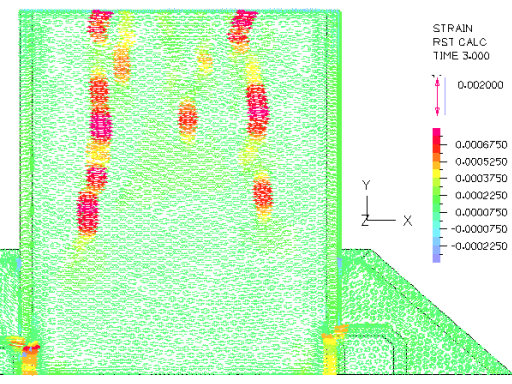


Figure 4.32 – Strain plot, 1975 Model (Comb. A)

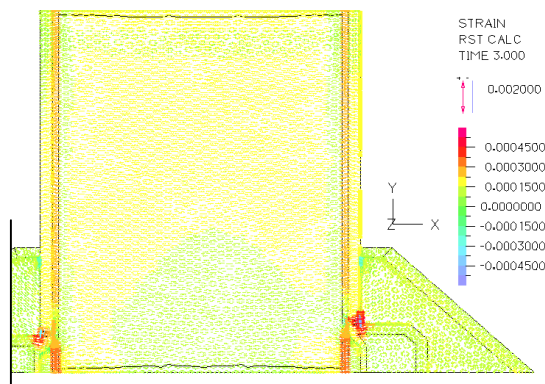


Figure 4.33 – Strain plot, 2010 model (Comb. A)

4.2.3 Results: temperature combination B

The non-linear analysis with temperature loading from average to winter values shows high concentration of stresses (up to 1.09 MPa, compare to Table 4.16) in the pavement layers due to the down-lift of the vault. On the other side, the minimum principal stress (-1.45 MPa) is higher in the core of the pier due to the "shrinking" provoked by the decreasing temperature (Figure 4.34). The maximum deflection is -2.22 mm, according to the expectations from linear analysis.

Table 4.16 – Stresses and displacements for different time steps of 1975 model and final results of 2010 model

Time step:	0.5_{1975}	1.0_{1975}	1.5_{1975}	2.0_{1975}	2.5_{1975}	3.0_{1975}	3.0_{2010}
$\sigma_1 \text{ max}$ (MPa)	1.16	1.17	1.16	1.08	1.08	1.09	1.17
$\sigma_3 \text{ max}$ (MPa)	-0.28	-0.40	-0.78	-1.11	-1.28	-1.45	-1.45
Displ. Z _{max} (mm)	-0.24	-0.47	-1.05	-1.65	-1.99	-2.22	-2.20

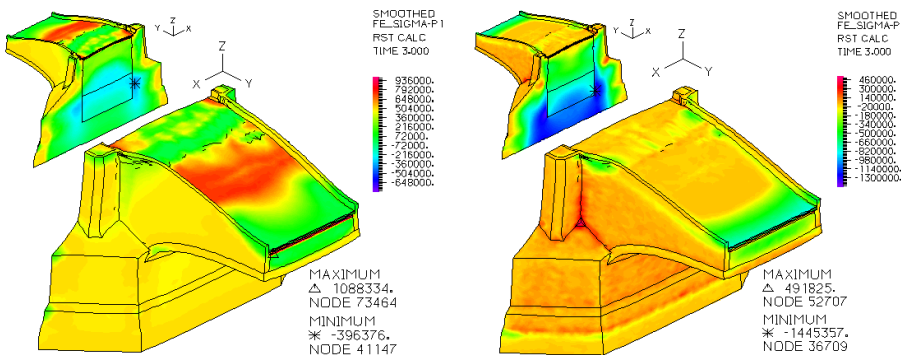


Figure 4.34 – Tensile and compressive stress plots (Comb. A), 1975 model

The tensile stress configuration is different from the thermo-elastic analysis. The implementation of the decreasing temperature makes the down-lift of the arch crown provoking tension in pavement layers. The increasing of deflection brings to cracking and release of tension in the part of the pavement in correspondence with the pier, causing the “translation” of the maximum values of tensile stress downward, toward the arch crown (Figure 4.35).

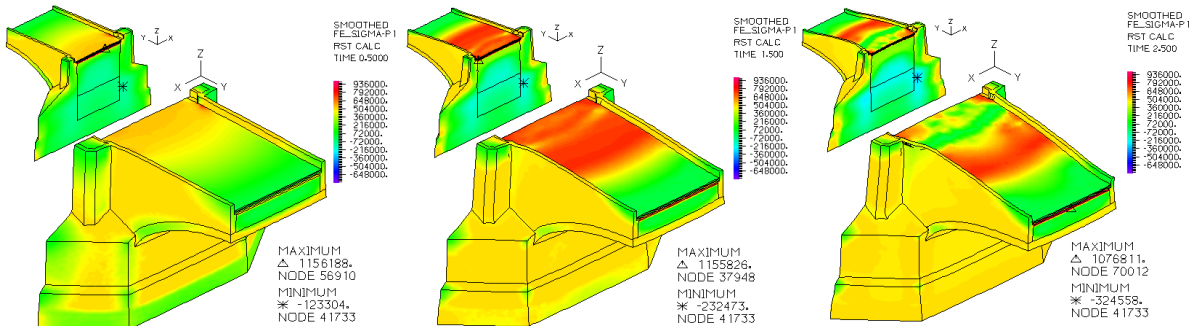


Figure 4.35 – Evolution of the release of tension on the pavement (time steps: 0.5 1.5 2.5)

The result of this process is a damage evolution as in Figure 4.36, with cracks beginning at connection railing-pier and then spreading on sandstone masonry and pavement, starting from pier side.

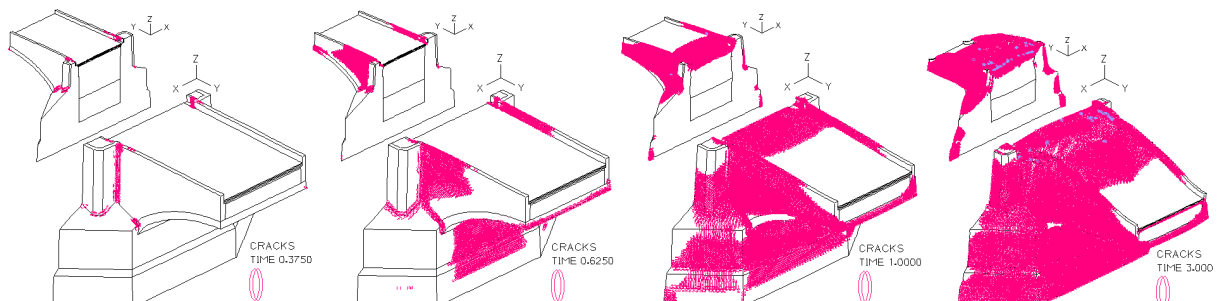


Figure 4.36 – Crack evolution (Comb. B) for different steps

The damage is high at the connection railing-pier (red rectangles in Figure 4.37) but the rehabilitation of 2010 successfully reduces its occurrence (Figure 4.38), proving the utility of the intervention (for the sandstone masonry) even in winter conditions.

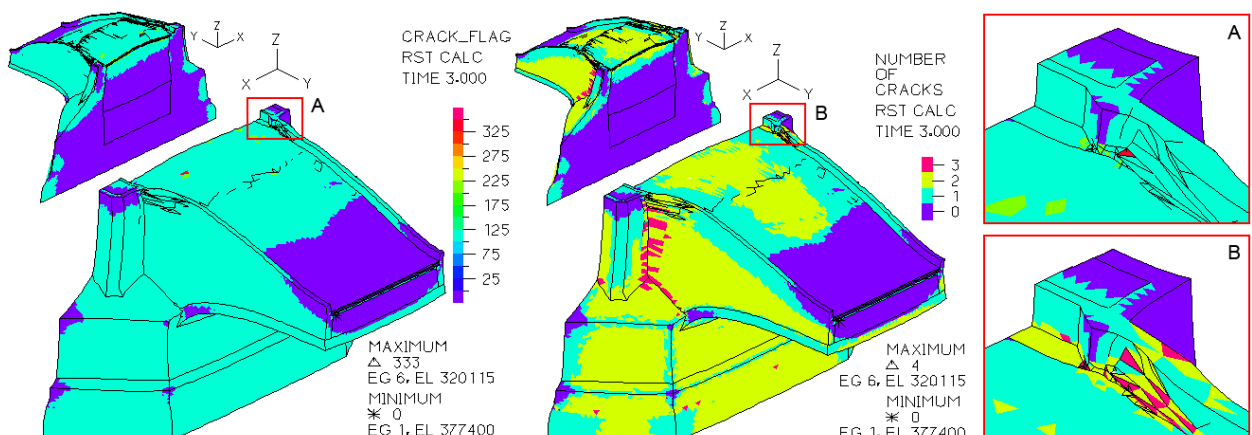


Figure 4.37 – Crack flag and number of cracks in 1975 model (Comb. B)

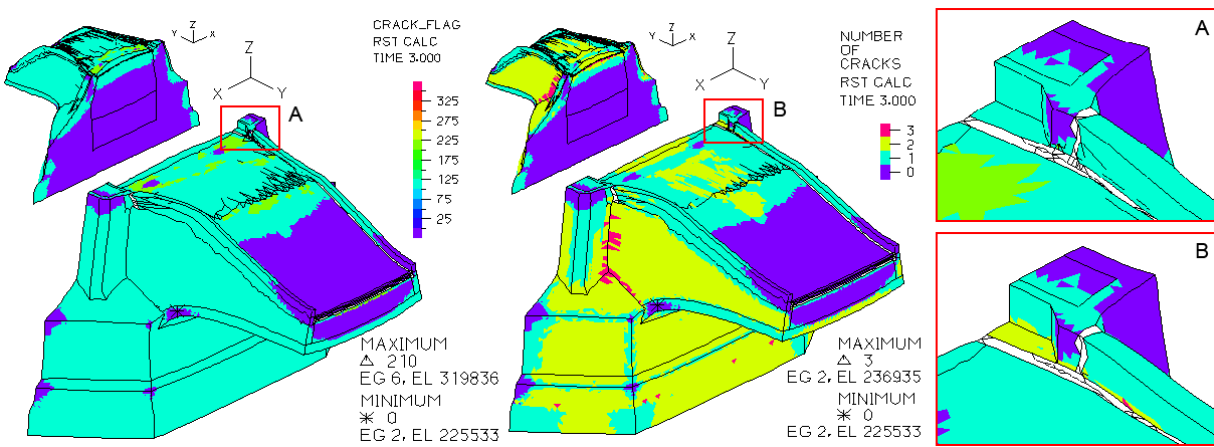


Figure 4.38 – Crack flag and number of cracks in 2010 model (Comb. B)

Despite this, the implementations of 2007–2010 are not able to limit damage on pavement (that even increases, compare to Figure 4.39 and Figure 4.40) but the new joints let to significantly decrease the cracking on the masonry parapet (compare Figure 4.42 with Figure 4.41). Unluckily, due to a problem with the software, it was not possible to set the two plots exactly at the same scale as preferable.

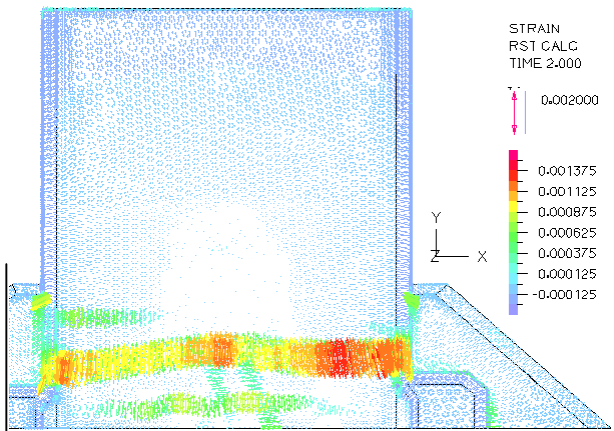


Figure 4.39 – Strain plot, 1975 Model (Comb. B)

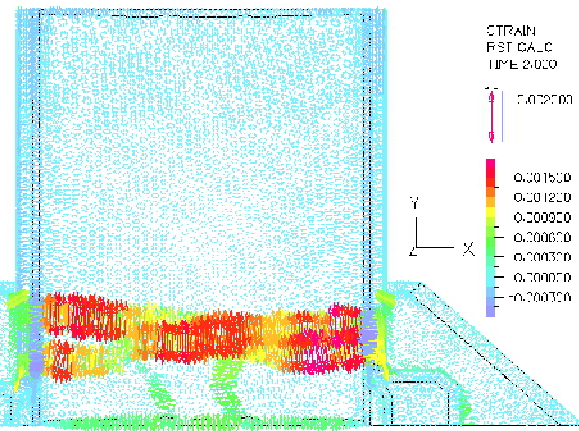


Figure 4.40 – Strain plot, 2010 model (Comb. B)

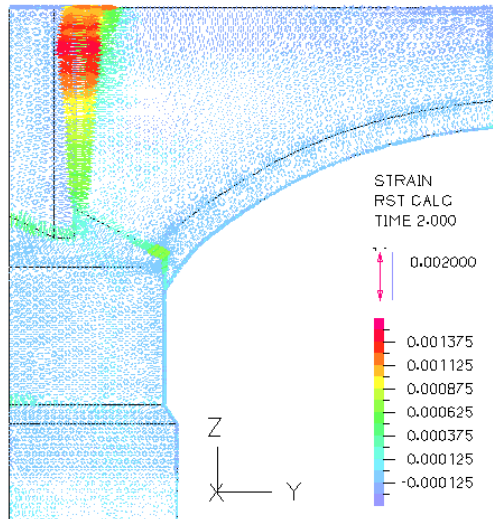


Figure 4.41 – Strain plot, 1975 Model (Comb. B)

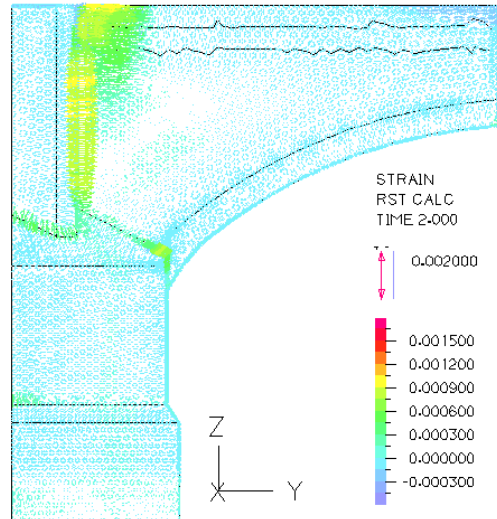


Figure 4.42 – Strain plot, 2010 model (Comb. B)

4.3 Non-linear analysis (SIFEL) – Isotropic scalar damage model

The damage is the reduction of strength and stiffness caused by propagation and interaction of defects (voids, cracks, delamination). In quasi-brittle materials (as concrete and masonry) the evolution of strain brings to microcracks and microvoids. If the strain evolution continues, some microcracks localize in discrete cracks, while the others stop to increase (localization of inelastic strains) (Koudelka, 2011). The phenomenon can be described by damage models (explained in Par. 7.2 of Annexes) that characterize density and orientation of microdefects toward (Jirásek, 1998):

- an equation relating damage variables and apparent stiffness;
- a loading function specifying the elastic domain (hence it says when the damage does not evolve);
- a law governing the evolution of damage variables.

SIFEL allows to study the problem with several damage models, the first used is the simple isotropic scalar damage model (compare to Par.7.2.1 and Par. 7.2.2 of the Annexes). It considers the degradation as isotropic (the stiffness matrix changes proportionally in every direction, according to the damage parameter). Moreover it uses only one (scalar) parameter and takes Poisson's ratio as independent from damage.

For the computation of equivalent strain the Mazars norm is used (compare to Par. 7.2.2 in the Annexes). It selects only positive strains in principal direction ($\tilde{\varepsilon} = \sqrt{\langle \varepsilon_I \rangle : \langle \varepsilon_I \rangle}$ where ε_I are principal strains and Macaulay brackets $\langle \dots \rangle$ indicate the selection of positive components). Therefore the input material parameters are tensile strength and maximum crack width ($u_{t,max} = G_f / \sigma_{t,max}$), in addition to Young modulus, Poisson's ratio, density, and thermal dilatation coefficient.

The analysis is run using Newton-Raphson and modified Newton-Raphson method with convergence criterion based on the norm of vector of unbalanced forces. The post-processing is performed by GiD (<http://www.gidhome.com/>), focusing on damage parameter (ω) and crack width as output. Selected material properties are shown in Table 4.17.

Table 4.17 – Material properties for stress-strain relation in isotropic scalar damage model

Material	E (GPa)	ν	ρ (kg/m ³)	α (1/K)	$\sigma_{t,max}$ (MPa)	G_f (N/m)	$u_{t,max}$ (mm)
Periodic sandstone	20.20	0.15	2700	7.0e-06	0.50	80	0.16000
Non-periodic sandstone	20.20	0.17	2700	8.0e-06	0.50	80	0.16000
Quarry masonry	10.40	0.17	2500	8.0e-06	0.30	40	0.13333
Granite pavement (cement mort.)	14.00	0.20	2600	5.0e-06	0.75	10	0.01333
Fine-grained concrete	22.00	0.20	2300	5.0e-06	1.40	36	0.02571
Lightweight concrete	1.00	0.20	2300	10.0e-06	1.40	36	0.02571
Reinforced concrete	27.50	0.20	2600	12.0e-06	1.60	36	0.02250
Granite pav. (lime mortar) (2010)	7.00	0.20	2600	5.0e-06	0.75	10	0.01333
Light concrete+Hydr. (2010)	9.00	0.20	1900	7.0e-06	1.40	36	0.02571
Concrete with steel net (2010)	16.00	0.20	2300	10.0e-06	1.50	36	0.02400
Extruded polystyrene (2010)	0.03	0.30	35	8.0e-06	1.00e10	10	1.00e-15
Crushed gravel (2010)	0.02	0.35	1500	5.0e-06	1.00e10	10	1.00e-15
Plastic mortar (2010)	0.05	0.37	1300	10.0e-06	1.00e10	10	1.00e-15

Differently from Adina, in SIFEL the non-linear analysis with linear properties to dilatation joints can not provide plotting results related to damage. Therefore joints are simulated as linear materials conferring them high tensile strength ($*10^{10}$) and reduced Young Modulus ($*10^{-2}$) in respect to previous analysis. This dissimilar input may cause differences between results of the 2 software.

4.3.1 Temperature combination A

All temperature combinations are considered, the results are shown before for Comb. A, from average to summer values (Table 4.18), and they are in agreement with Adina's non-linear analysis except that the minimum principal stress, here decreased after intervention (-5.99 MPa vs. -7.25 MPa of Adina).

Table 4.18 – Maximum displacements, stresses and damage for both models (Comb. A)

	Displ. Z _{max} (mm)	Displ. X _{max} (mm)	σ_1 max (MPa)	σ_3 max (MPa)	Damage par. _{max}	Crack width _{max} (mm)
1975 Model	2.61	1.37	1.21	-6.51	0.850	0.018
2010 model	2.61	1.37	0.69	-5.99	0.856	0.022

Figure 4.43 (1975 model) shows lower tensile stresses on the pavement than Figure 4.44 (2010 model) because cracks already appeared, as can be confirmed looking to damage parameter (Figure 4.45) or crack width (Figure 4.47).

Comparing Figure 4.45, Figure 4.47 with Figure 4.46 and Figure 4.48 it is possible to see how the intervention avoids the diffuse cracking on the pavement and along breast walls. The damage at the connection railing-pier is prevented while it is still present between railing and vault. On the other hand, the damage punctually concentrates at the bottom of the dilatation joint in the railing (impossible to see in the deformed shape). Moreover the degradation inside the filling and on its boundary with the pier increases due to the higher expansion of the volume (provoked by lower lateral stiffness). The plotting is in agreement with Adina output, both software place damage at the basis of the pier (studied with springs to avoid influence on the supports). Adina shows cracks also in the middle of the filling while in SIFEL those are at the boundary with the regular sandstone masonry. The second configuration seems to be more realistic thinking to the real difference between the two materials.

4.3.2 Temperature combination B

The analysis considers the temperature variation from average to winter values and provides the results shown in Table 4.19. Tensile stress is high in concrete layers of the pavement since they have higher thermal expansion coefficient, therefore they are more sensitive to temperature variations but their contraction is opposed by the other materials.

Table 4.19 – Maximum displacements, stresses and damage for both models (Comb. B)

	Displ. Z _{max} (mm)	Displ. X _{max} (mm)	σ_1 max (MPa)	σ_3 max (MPa)	Damage par. _{max}	Crack width _{max} (mm)
1975 Model	-2,30	-0,45	1,47	-1,44	0,976	0,090
2010 model	-2,31	-0,51	1,59	-1,45	0,987	0,103

The stress configuration (Figure 4.49, Figure 4.50) is in agreement with Adina output, as σ_3 and deflections, while the tensile stress has here higher values, as already happened in linear analysis.

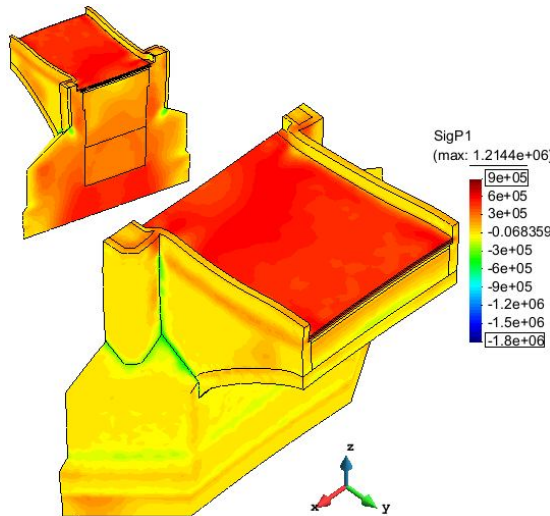


Figure 4.43 – Max. princ. stress (1975 model), Comb. A

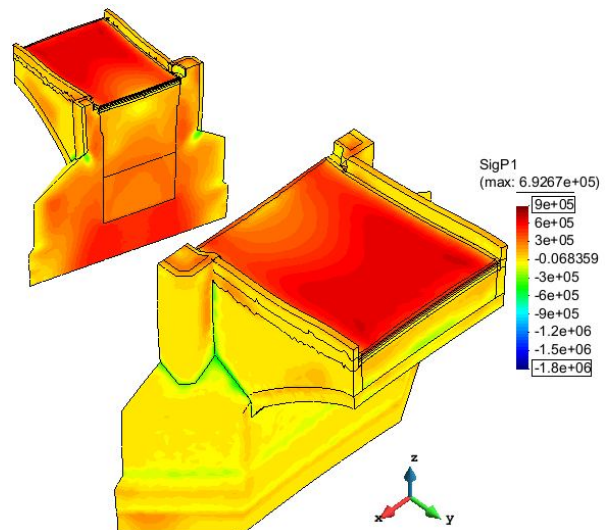


Figure 4.44 – Max. princ. stress (2010 model), Comb. A

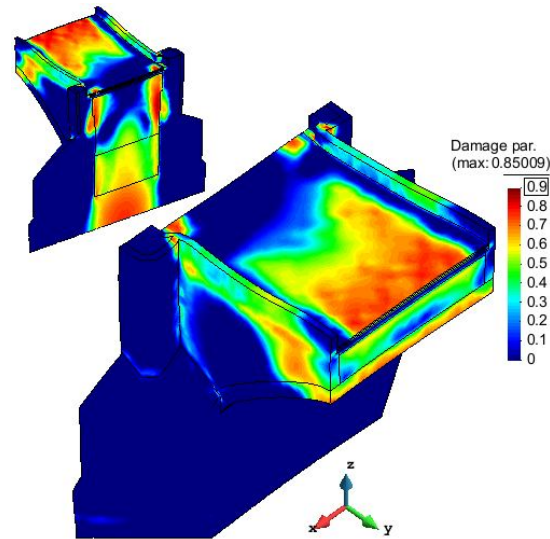


Figure 4.45 – Damage parameter (1975 model), Comb. A

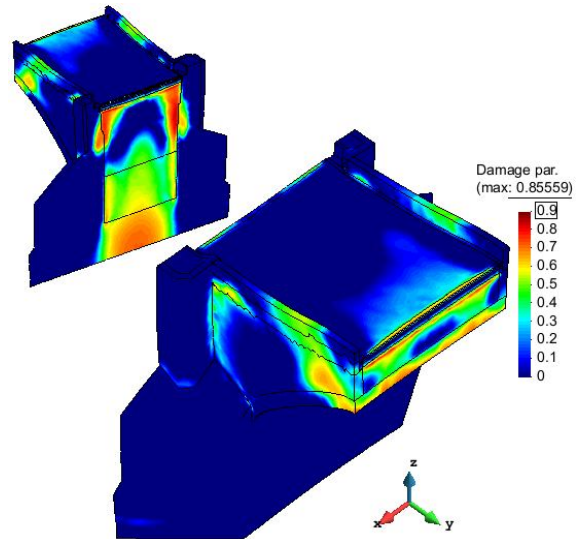


Figure 4.46 – Damage parameter (2010 model), Comb. A

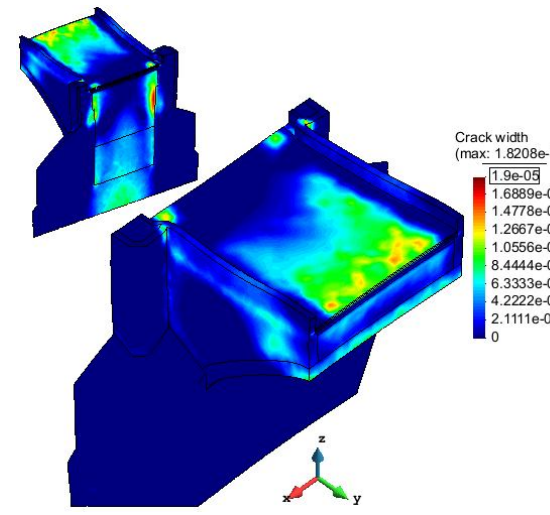


Figure 4.47 – Crack width (m) (1975 model), Comb. A

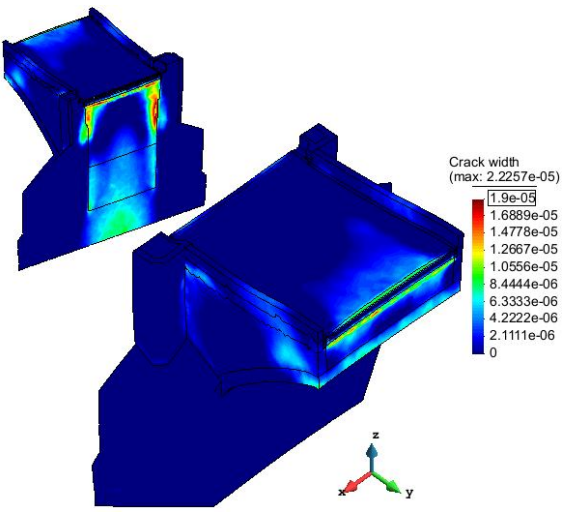
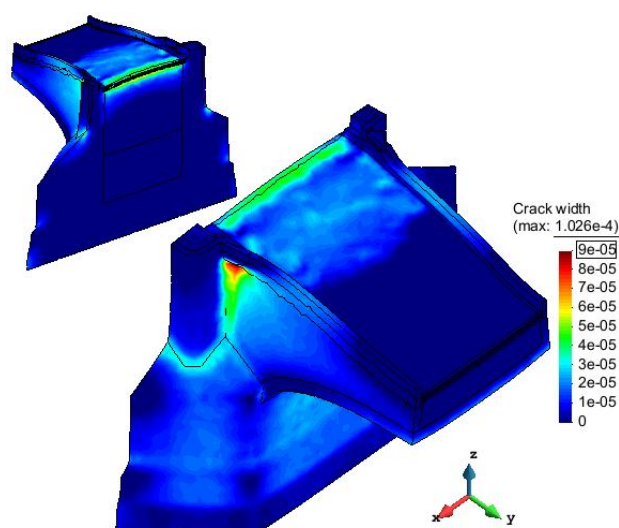
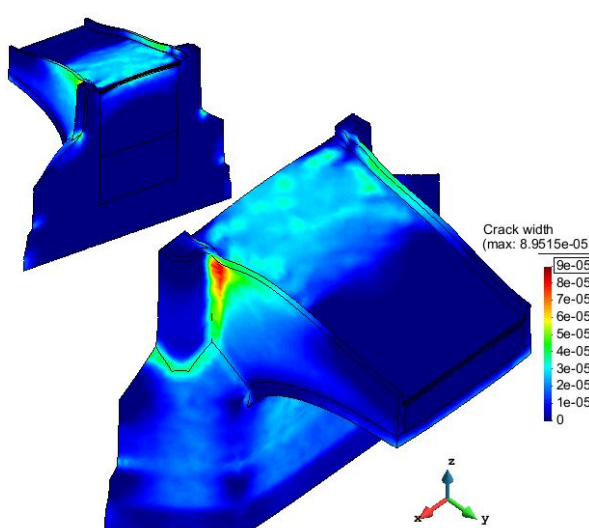
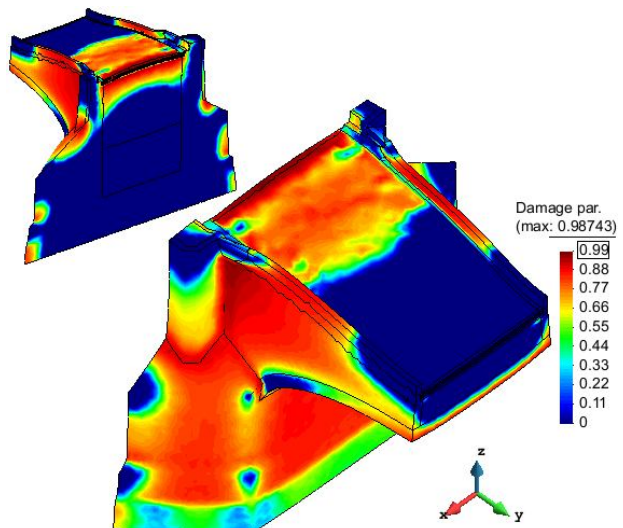
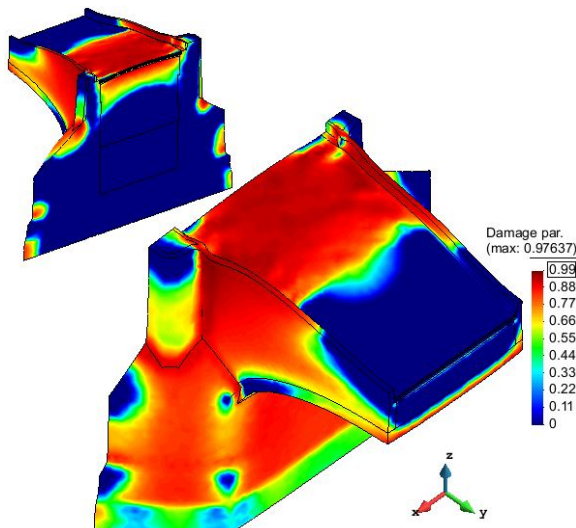
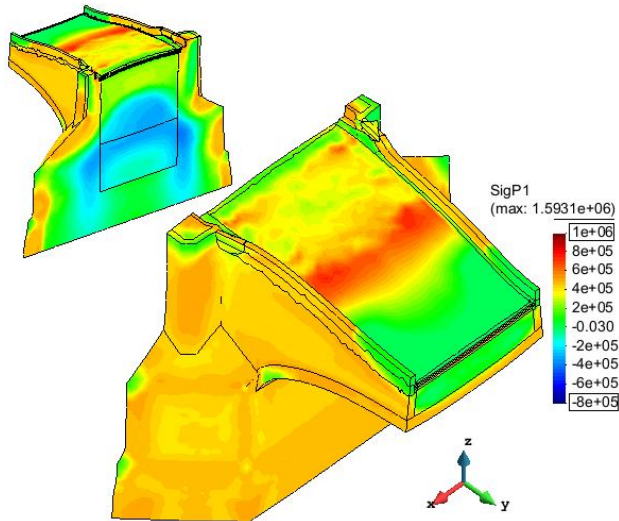
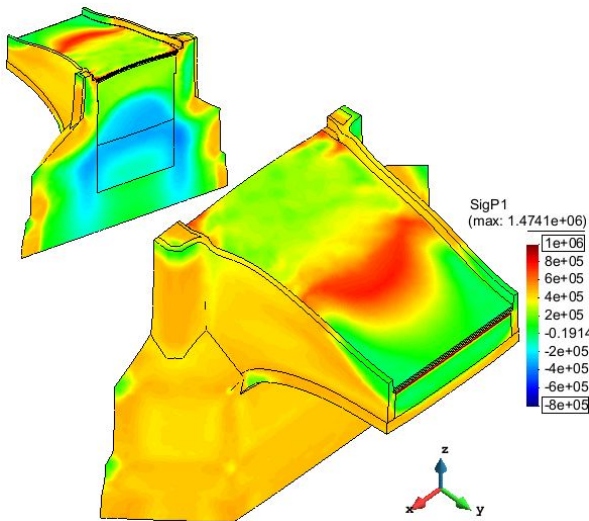


Figure 4.48 – Crack width (m) (2010 model), Comb. A



The 2007–2010 intervention is able to better distribute the stress on pavement layers (Figure 4.50) but the peak of maximum principal stress is higher than the 1975 model (Figure 4.49). Displacements slightly increase, due to the lower stiffness of the structure.

The variance (up to 30%) between SIFEL and Adina is provoked by different features to arrange results (compare to Par. 7.1.1) but also by modelling of joints. In Adina they are linear materials with no deformation, while in SIFEL their simulation (with low Young modulus and high strength) deforms as other materials. The last rehabilitation decreases the extension of damaged areas, as can be seen from Figure 4.51 – Figure 4.54. Thanks to dilatation joints, a lower number of cracks appears on the pavement and in the railing (Figure 4.54). Unluckily the damage is just shifted below this element, at its connection with the breast wall, where cracks are even wider than before, passing the dimension of 0.1 mm. As can be seen comparing Figure 4.50, Figure 4.52 and Figure 4.54 with Figure 4.38, the deformation of the plastic mortar joint in the railing (absent in Adina) changes the damage pattern of the area intensifying it in breast walls. According to SIFEL, the rehabilitation is not able to avoid the damage but it modifies its distribution. Results are more accurate than previous analysis, since joints undeformability was inadequate.

4.3.3 Temperature combination C

Comb. C (between winter and summer) and Comb. D (between summer and winter) are studied too, even if they do not provide comparison to a real climatic change, because they can help to understand structural behavior and rehabilitation response to extreme thermal variations. Comb. C displacements are in agreement with linear analysis as the decreasing in stresses after the intervention (Table 4.20).

Table 4.20 – Maximum displacements, stresses and damage for both models (Comb. C)

	Displ. Z _{max} (mm)	Displ. X _{max} (mm)	σ _{1 max} (MPa)	σ _{3 max} (MPa)	Damage par. _{max}	Crack width _{max} (mm)
1975 Model	3.73	2.16	1.11	-8.38	0.946	0.068
2010 Model	3.72	2.14	0.71	-7.35	0.944	0.066

The negative interaction between slab and railing is avoided thanks to dilatation joints (Figure 4.56), as already noticed for Comb. A. Differently from that, here the effect is also a slight reduction in damage parameter (Figure 4.58) and crack width (Figure 4.60) for railing and pavement in respect to 1975 model. The rehabilitated structure shows an adequate overall behavior in response to increase of temperature.

4.3.4 Temperature combination D

The vertical displacement resulting from the analysis with temperature Comb. D is bigger than in the linear analysis (-7.02 mm vs. -5.17 mm) while principal stresses and their reduction thanks to the rehabilitation (Table 4.21) are in agreement with that. As already explained for Comb. B, the 2010 intervention changes the damage distribution but it is not able to reduce cracks appearance and width.

Table 4.21 – Maximum displacements, stresses and damage for both models (Comb. D)

	Displ. Z _{max} (mm)	Displ. X _{max} (mm)	σ _{1 max} (MPa)	σ _{3 max} (MPa)	Damage par. _{max}	Crack width _{max} (mm)
1975 Model	-7.02	-1.44	1.64	-2.75	0.993	0.128
2010 Model	-6.97	-1.40	1.12	-2.39	0.998	0.159

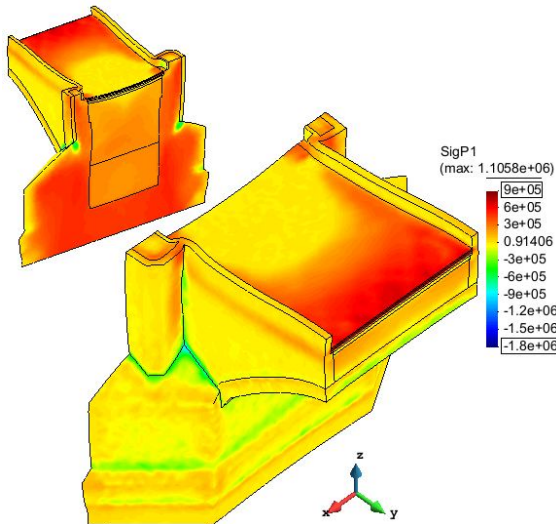


Figure 4.55 – Max. princ. stress (1975 model), Comb.C

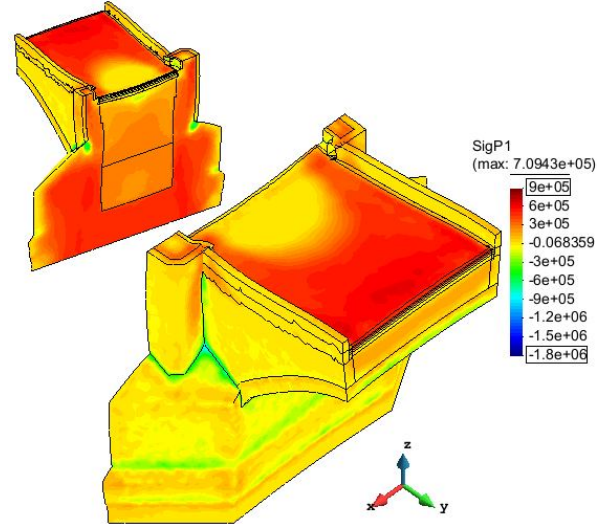


Figure 4.56 – Max. princ. stress (2010 model), Comb.C

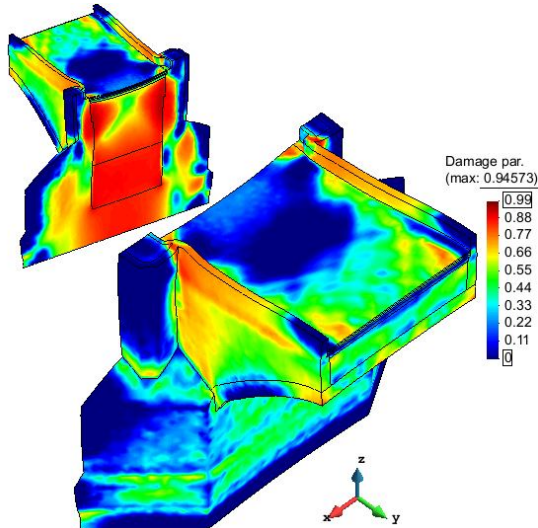


Figure 4.57 – Damage par. (1975 model), Comb. C

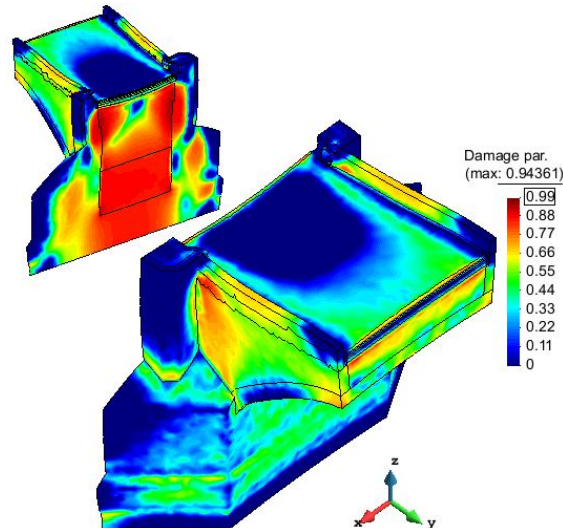


Figure 4.58 – Damage par. (2010 model), Comb. C

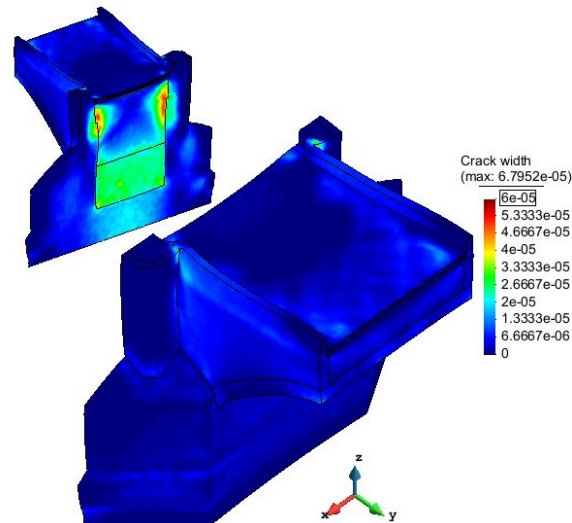


Figure 4.59 – Crack width (m) (1975 model), Comb. C

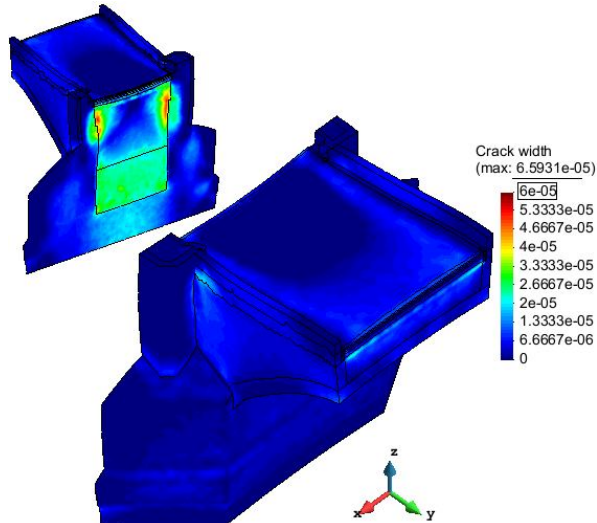


Figure 4.60 – Crack width (m) (2010 model), Comb. C

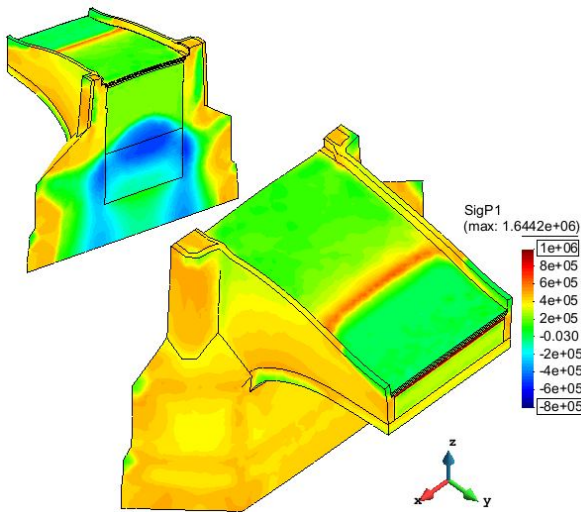


Figure 4.61 – Max. princ. stress (1975 mod.), Comb. D

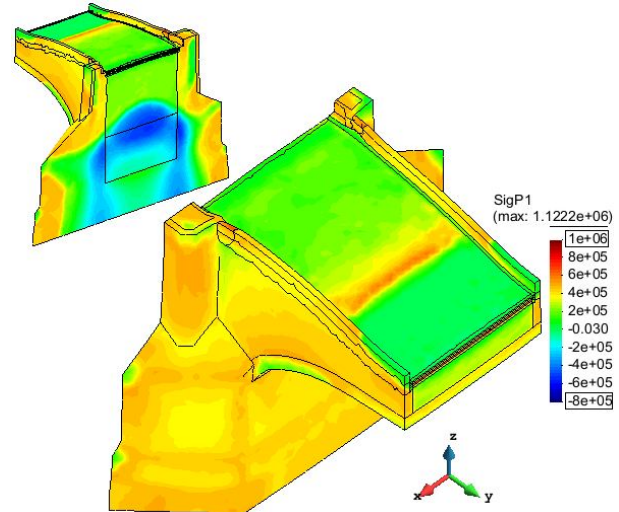


Figure 4.62 – Max. princ. stress (2010 mod.), Comb. D

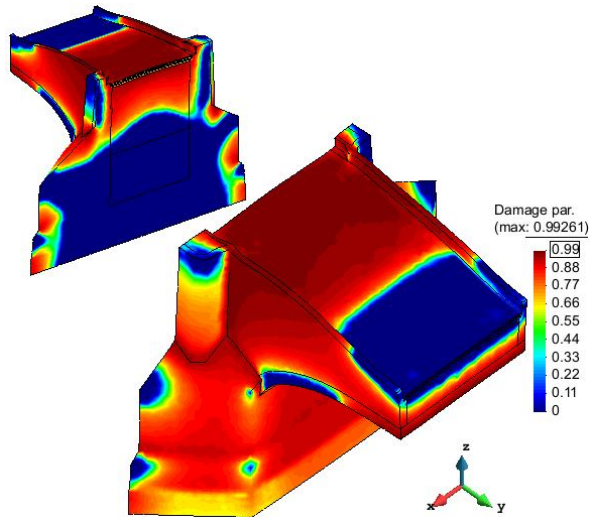


Figure 4.63 – Damage parameter (1975 mod.), Comb. D

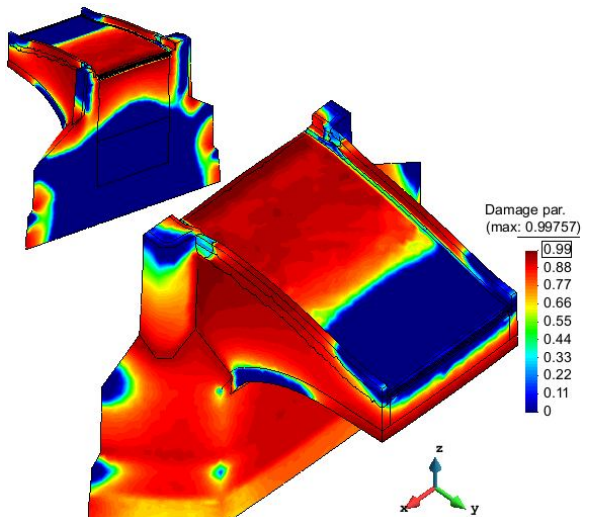


Figure 4.64 – Damage parameter (2010 mod.), Comb.D

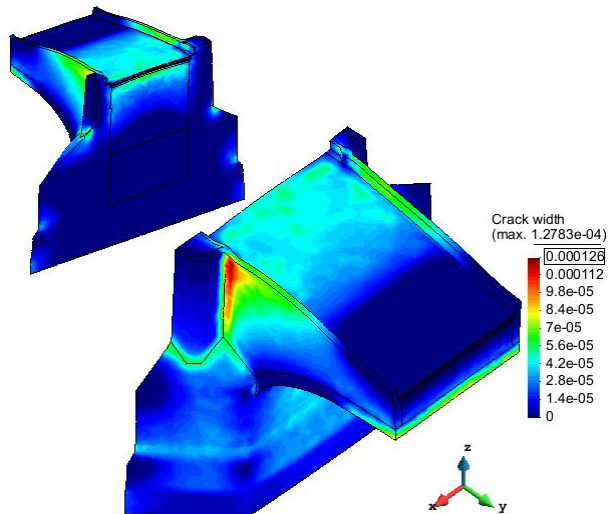


Figure 4.65 – Crack width (m) (1975 model), Comb. D

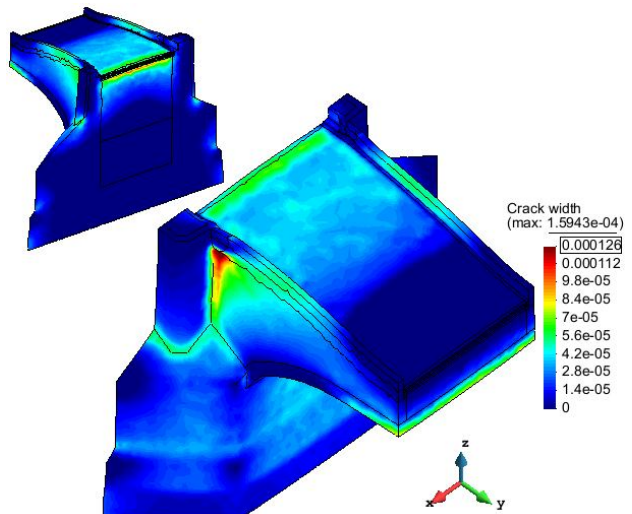


Figure 4.66 – Crack width (m) (2010 model), Comb. D

The smaller displacement of the rehabilitated structure can be related with lower sensitivity to extreme temperature variations (hence lower extension of damaged areas and of stiffness reduction).

Figure 4.64 and Figure 4.66 show that the damage is lower (than 1975 model) on pavement and railing but cracks concentrate in breast walls, at the bottom of dilatation joints, where they can be wide up to 0.16 mm. Results underline that the reduction of temperature is the worst menace for the bridge, provoking the highest displacement, stress and damage. The rehabilitated structure is not able to avoid this: it reduces the extension of the damaged areas but the degradation in them is even higher.

4.3.5 Software comparison

Both software have pros and cons according to functions necessary in different analysis; some considerations are going to be provided according to the experience developed by the author during the present thesis.

Being an in-house software, SIFEL lets to correct bugs and customize the analysis: this was fundamental for the developed research since it allowed to fix occurring problems and quickly input temperatures as increments. Both software are able to perform thermo-mechanical analysis, therefore if the study had been carried out with Adina from the beginning, the temperature loading would not have been an obstacle even with that program. Since it was not, the software required the implementation of hand made temperature steps, a time demanding procedure with high risk of error (since the mapping file is re-arranged for the scope). Using this method, Adina could not decrease the load if the convergence was not reached in the time step; for this the low speed dynamics feature was used but it brought an additional 5% of possible error in the computation (compare to Par. 7.3.1).

Adina allows to control the non-linear procedure, modifying both time steps and time functions. SIFEL uses the same solution tools (Newton-Raphson and modified Newton-Raphson method) and it gives even more tailoring (time dependence) just editing the input file. The former software shows all calculated steps and the development of parameters in them, giving precious clues to understand the evolution of phenomena and possible errors, but slowing the analysis. Editing SIFEL code, it is possible to avoid this option, to speed a long computation as done in the following “one year cycle” analysis (compare to Par. 4.5). Adina is able to maintain linear materials in a non linear analysis while in SIFEL this choice would not provide any outcome about damage, but the use of low Young modulus and high strength can avoid the problem, simulating the same behavior. Despite this, the deformation of the “simulated” linear material in SIFEL is different from Adina, where such material maintains its original shape, having no strain. Unluckily this reduced the comparability of the 2 analysis.

About damage mechanics, SIFEL allows the introduction of several damage models (and equivalent strain norms) facilitating a deep study, while Adina is limited to the predefined material models in the software but it would be a powerful tool for studying the single crack nucleation and its propagation. In the performed analysis it was less satisfying in showing damage conditions of the whole structure than SIFEL, which fully accomplished the issue with damage parameter and crack width plotting.

Exploiting the two software together, it was possible to reach good knowledge of the problem and to provide adequate explanation and graphical output for it.

4.4 Non-linear analysis (SIFEL) – Orthotropic damage model

In the scalar isotropic damage model, the only parameter used reduces the stiffness in every direction independently from that where the limit strain is exceeded (damage parameter is directionally independent). This is inaccurate because stiffness degradation is usually faster in the direction of largest stretching, making the macroscopic properties of the material turn in anisotropic, therefore a three-dimensional problem can be better described by an anisotropic damage model (in which the damage is directionally dependent).

To take it into account, the damage has to be tensorially represented. The general case uses an eight-order tensor Ω to transform the elastic stiffness D_e into the secant stiffness D_s of the damaged material. Theory and formulae are provided in Par. 7.2.5 of the Annexes.

The anisotropic damage model requires many internal variables, and the laboratory measurements for them can be difficult. To avoid this, the model used by SIFEL is orthotropic (Par. 7.2.6 of the Annexes). It deals with damage that is different in 3 principal directions, and with effective strain defined through the principle of strain equivalence.

In the input material properties, strength and maximum crack width ($u_{max} = G_f/\sigma_{max}$) are required both in tension and compression (Table 4.22). The first option for the equivalent strain computation was the Rankine norm (suggested by literature mainly for concrete): $\tilde{\varepsilon} = \frac{1}{E} \max_{i=1,2,3} \langle D_e : \varepsilon \rangle_i$. In it equivalent strains are computed from principal stresses (obtained by constitutive equations) divided by Young Modulus. McAuley brackets consider only positive part of their argument, hence compression stresses are neglected for tension but stresses are influenced also by negative strains. For more information and the graphical representation please compare to Par. 7.2.1 of Annexes. Other material properties are those already used in the isotropic scalar damage model (compare to Table 4.17).

Table 4.22 – Material properties for stress-strain relation in orthotropic damage model

Material	G_f (N/m)	σ_t max (MPa)	u_t max (mm)	σ_c max (MPa)	u_c max (mm)
Periodic sandstone	80	0.50	0.16000	-7.40	0.01081
Non-periodic sandstone	80	0.50	0.16000	-7.40	0.01081
Quarry masonry	40	0.30	0.13333	-3.10	0.01290
Granite pavement (cement mort.)	10	0.75	0.01333	-4.86	0.00206
Fine-grained concrete	36	1.40	0.02571	-12.75	0.00282
Lightweight concrete	36	1.40	0.02571	-12.75	0.00282
Reinforced concrete	36	1.60	0.02250	-12.75	0.00282
Granite pav. (lime mortar) (2010)	10	0.75	0.01333	-4.00	0.00250
Light concrete+Hydr. (2010)	36	1.40	0.02571	-12.75	0.00282
Concrete with steel net (2010)	36	1.50	0.02400	-12.75	0.00282
Extruded polystyrene (2010)	10	1.00e10	1.00e-15	-1.00e10	1.00e-15
Crushed gravel (2010)	10	1.00e10	1.00e-15	-1.00e10	1.00e-15
Plastic mortar (2010)	10	1.00e10	1.00e-15	-1.00e10	1.00e-15

The low value of strength of concrete (according to (Sejnoha, 2006)) is on safety side and it can consider the presence of decay. The choice to maintain the same value also for the new concrete layers wants to give a long term forecast of the material behavior.

The compressive strength of sandstone masonry is higher than in literature (Sejnoha, 2006) since a lower value brought to convergence problems. Damage model holding in tension and linear elasticity in compression (where the former is not convenient having poor stability) are chosen for the performed analysis with SIFEL. Therefore material parameters have to be set in way to obtain quasi-brittle material behavior in tension and linear elastic behavior in compression.

The analysis with damage model is not able to describe in a totally reliable way the behavior in compression branch for materials as masonry and concrete. Experiments demonstrated that a plasticity model holding in compression would provide better results. The combination of damage model and plasticity model in SIFEL is implemented but still not properly validated.

In any case the chosen compressive strength is a reliable value for a good quality stone masonry, as it is in the bridge. Moreover the temperature loading mainly influence the tensile branch, this justifies the analysis with damage models.

4.4.1 Temperature combination A (Rankine norm)

Thanks to the different damage model, damage parameter and crack width are available as tensors. It is chosen to provide the plotting on first and second principal directions (named P1 and P2) because the third one (P3) corresponds to compression, branch considered as linear elastic by the analysis with damage model. The damage parameter plot according to P1 is in relation (similitude) with that along X direction, while the plot according to P2 is in relation with that along Z direction.

The computed values (Table 4.23) are in agreement with the isotropic damage model analysis but stresses are here higher while damage parameter is lower (about 10%) and maximum crack width is halved. This was expected because the selected damage model reduces the stiffness only in one direction (that of damage) instead than in all 3 directions equally. In fact the damage parameter for isotropic damage model is influenced by all positive principal strains while the orthotropic model separates parameters for direction.

Table 4.23 – Maximum displacements, stresses and damage for both models (Comb. A)

Model	Displ. Z _{max} (mm)	Displ. X _{max} (mm)	σ_1 _{max} (MPa)	σ_3 _{max} (MPa)	Damage par. P1 _{max}	Damage par. P2 _{max}	Crack width P1 _{max} (mm)	Crack width P2 _{max} (mm)
1975	2.61	1.36	1.35	-7.21	0.784	0.497	0.009	0.002
2010	2.62	1.38	0.74	-7.18	0.785	0.549	0.014	0.012

The tensile stress plot of the 1975 model (Figure 4.67) shows similar features to the previous analysis except the pattern on the pavement: the central area is here already damaged and it has a dark red (higher tension) ring around it. Damage parameter (Figure 4.69) and crack width (Figure 4.71) referred to the maximum principal direction confirms it. They also show that the degradation inside the pier develops more on the northern side, while on the pavement the southern one is the more damaged; this is due to the higher variation of temperature in those areas.

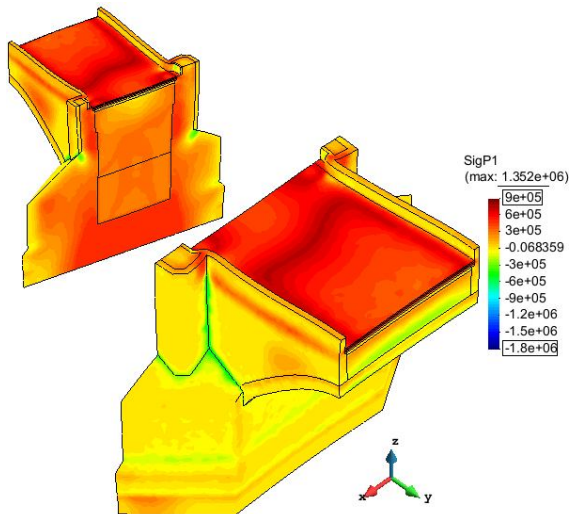


Figure 4.67 – Max. princ. stress (1975 model), Comb. A

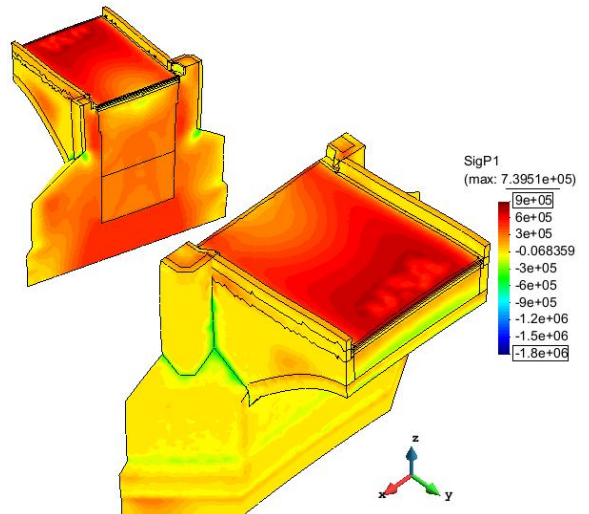


Figure 4.68 – Max. princ. stress (2010 model), Comb. A

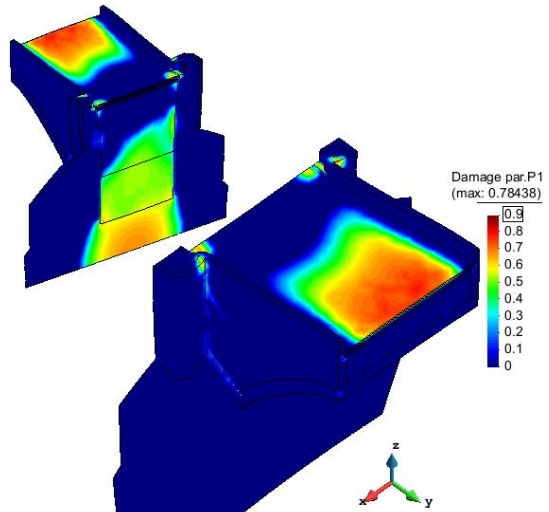


Figure 4.69 – Damage par. P1 (1975 mod.), Comb. A

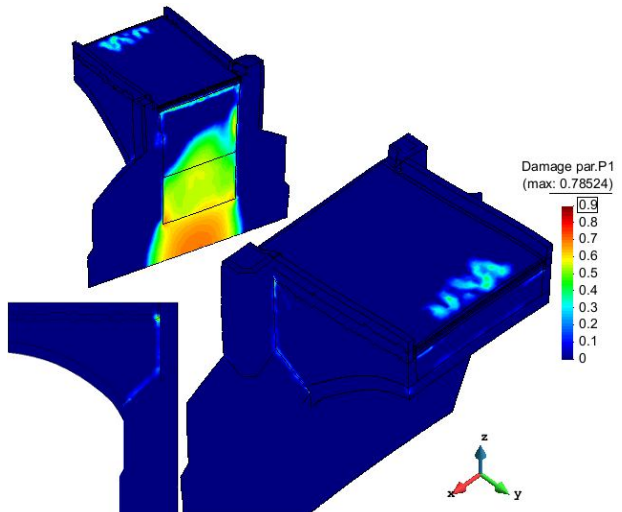


Figure 4.70 – Damage par. P1 (2010 mod.), Comb. A

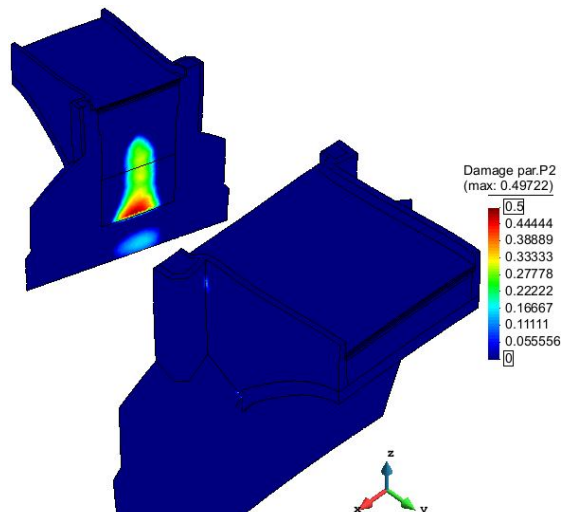


Figure 4.71 – Damage par. P2 (1975 mod.), Comb. A

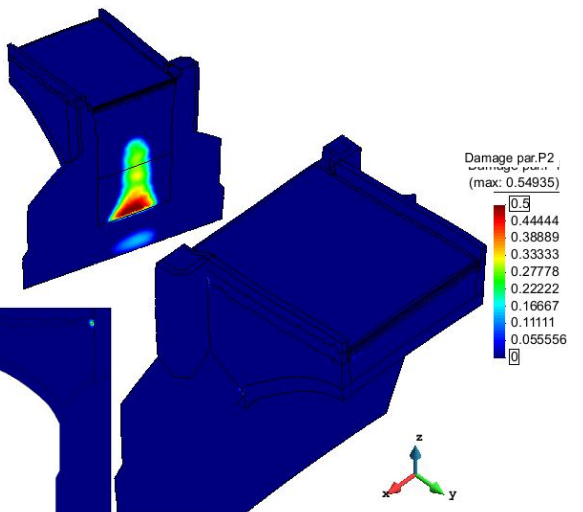


Figure 4.72 – Damage par. P2 (2010 mod.), Comb. A

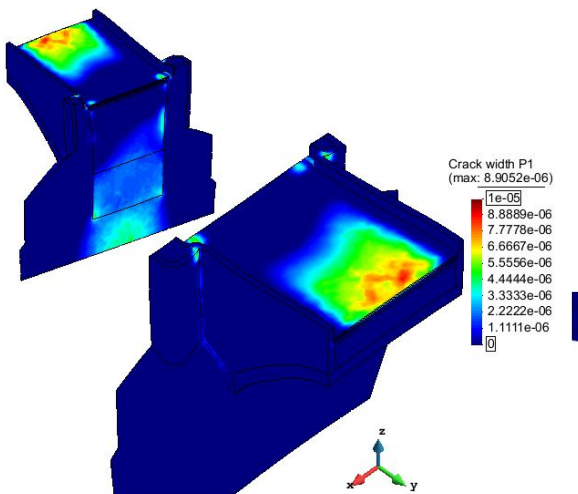


Figure 4.73 – Crack width P1 (1975 model), Comb. A

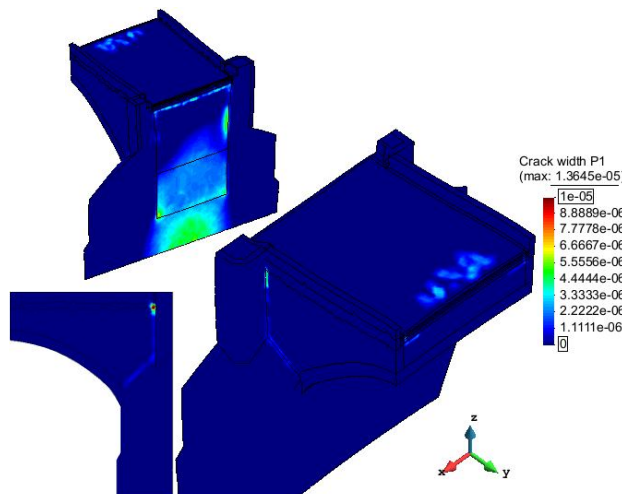


Figure 4.74 – Crack width P1 (2010 model), Comb. A

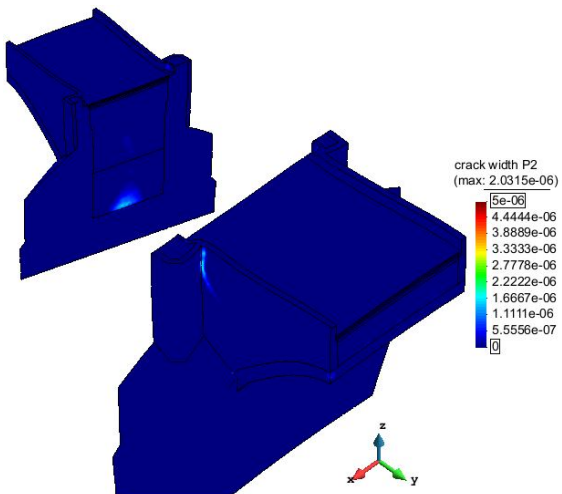


Figure 4.75 – Crack width P2 (1975 model), Comb. A

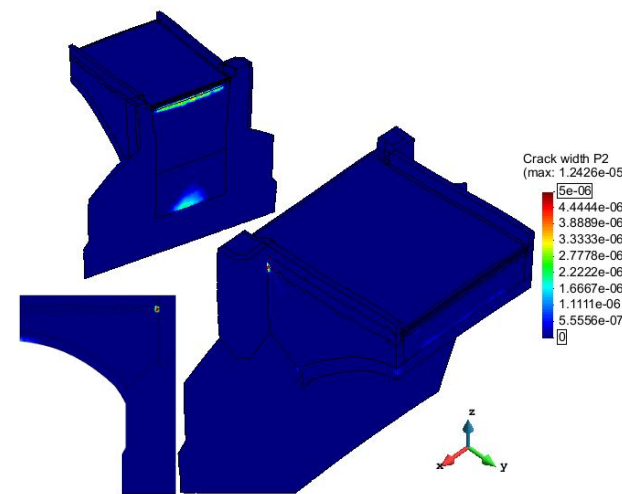


Figure 4.76 – Crack width P2 (2010 model), Comb. A

A comparison with previous analysis (Par. 4.3.1) highlights the absence of damage on breast walls, that were before one of the most interested areas. Also the other zones (with exception of the pavement) show lower deterioration than in the previous study. This is provoked by the different norm used for the equivalent strain computation, and it will be discussed in the next paragraph.

The rehabilitation of 2007–2010 decreases the size of the damage on pavement (Figure 4.70) even if this enlarges in the inner pier (at the boundary masonry-filling) and in correspondence to dilatation joints, due to the lower stiffness (so higher dilatation) of the structure. The low characteristics of the filling and the presence of shear stresses at the interface joint-slab-filling (caused by the higher thermal expansion coefficient of concrete) provoke the damage below pavement layers. In the case of railing, the implicated area is lowered than 1970 model but the degradation at the bottom of the plastic mortar joint is higher (because concentrated).

The presence of the undeformed lateral elevation in Figure 4.70 – Figure 4.76 wants to underline the occurrence of damage in the breast wall (due to the effect of the dilatation joint) not possible to see in the deformed shape.

4.4.2 Temperature combination A (simple equivalent strain norm)

The results of the study with Rankine norm do not show damage on breast walls, while these were one of the most degraded areas in isotropic damage model analysis. There is low comparability between Rankine norm in orthotropic damage model and previously used Mazars norm (in scalar isotropic damage model), because Rankine norm comprises also negative strains for tensile branch into the computation, which can give lower equivalent strains for the actual stress state.

Since the location of damage depends from the equivalent strain computation, the analysis is run again with a more suitable norm, focusing on the different degradation distribution. The simple equivalent strain norm is chosen, for it the equivalent strain (in tension) is equal to the positive strain in the actual principal direction ($\tilde{\varepsilon} = \langle \varepsilon_i \rangle$). The analysis is more comparable with that of isotropic damage model (and Mazars norm), the results (Table 4.24) shows similar stresses and lower damage. In respect to the previous computation with Rankine norm, the damage parameter in direction P2 is decreased (7.5%) while that in direction P1 is increased (8.5%), for the crack width the gap is even more noticeable (35%).

Table 4.24 – Maximum displacements, stresses and damage for both models (Comb. A)

Model	Displ. Z _{max} (mm)	Displ. X _{max} (mm)	σ_1 max (MPa)	σ_3 max (MPa)	Damage par. P1 _{max}	Damage par. P2 _{max}	Crack width P1 _{max} (mm)	Crack width P2 _{max} (mm)
1975	2.59	1.37	1.12	-7.32	0.842	0.663	0.011	0.007
2010	2.61	1.37	0.71	-7.08	0.852	0.506	0.019	0.007

Noticeable is the decreasing of damage in direction P2 from 1975 to 2010 model, differently from previous study. It is due to the fact that in this analysis the damage at the interface joint-slab-filling has less relevance on P2 direction while the degradation in breast walls is considered. This is reduced in 2010 model by the presence of the longitudinal dilatation joints between slab and masonry (compare Figure 4.80 with Figure 4.79) as already noticed in previous analysis.

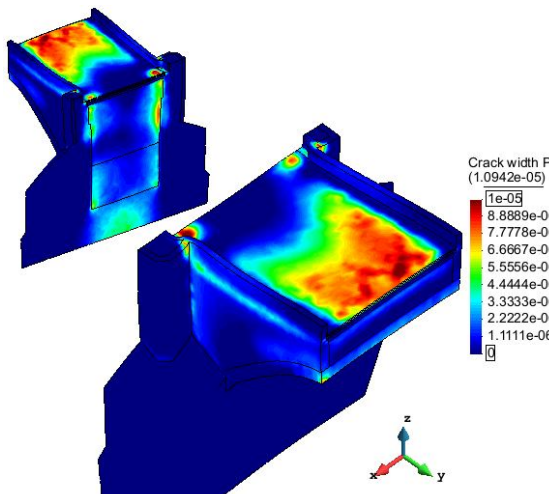


Figure 4.77 – Crack width P1 (1975 model), Comb. A

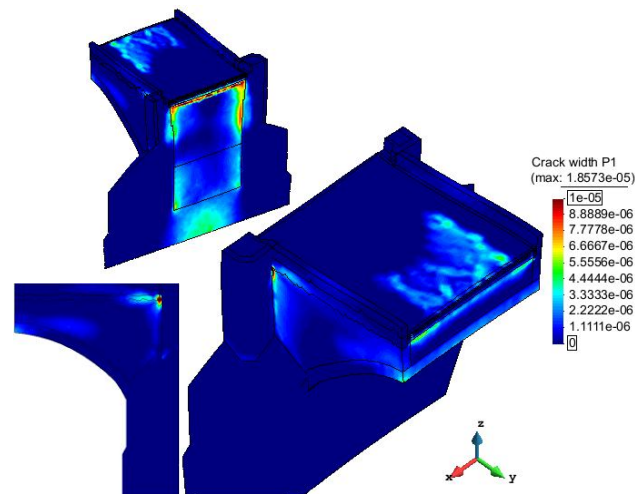


Figure 4.78 – Crack width P1 (2010 model), Comb. A

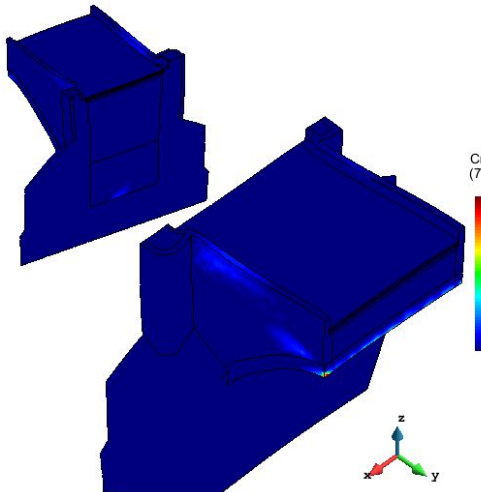


Figure 4.79 – Crack width P2 (1975 model), Comb. A

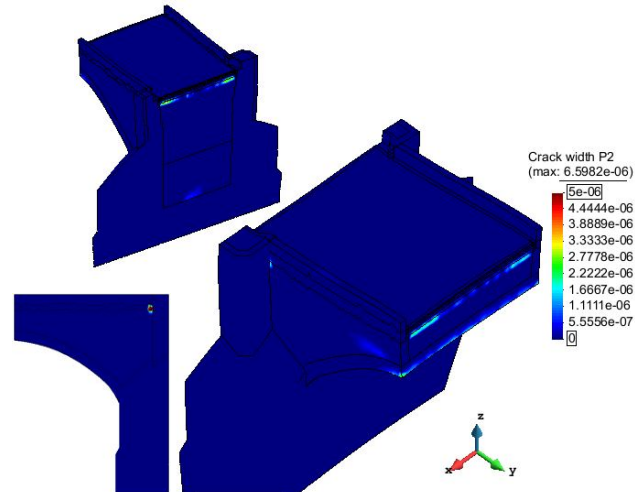


Figure 4.80 – Crack width P2 (2010 model), Comb. A

4.4.3 Temperature combination B (Rankine norm)

The results of the analysis for temperature loading from average to winter values (Table 4.25) are in agreement with the scalar isotropic damage model computation but they present a slightly (about 10%) higher damage parameter and lower crack width. As already said this is due to the different damage model used (reducing the stiffness only in one direction instead than in all three equally) and different equivalent strain computation.

Table 4.25 – Maximum displacements, stresses and damage for both models (Comb. B)

Model	Displ. Z _{max} (mm)	Displ. X _{max} (mm)	σ_1 max (MPa)	σ_3 max (MPa)	Damage par. P1 _{max}	Damage par. P2 _{max}	Crack width P1 _{max} (mm)	Crack width P2 _{max} (mm)
1975	-2.35	-0.44	1.56	-1.47	0.988	0.973	0.071	0.024
2010	-2.23	-0.50	1.56	-1.47	0.997	0.953	0.095	0.020

A relation (of similitude) is visible between damage parameter according to principal directions and along Cartesian axis, namely the plot in principal direction P1 (Figure 4.83) is in relation with Cartesian direction Y while the plotting in P2 is in relation with Cartesian direction X.

The tensile stress plot (Figure 4.81) is different from the isotropic damage model analysis (Par. 4.3.2) because here the higher stress pattern makes a “ring” around damaged zones no more able to bear tension. Damage parameter and crack width (Figure 4.83 and Figure 4.85) confirms it, highlighting the central area as more deteriorated.

About the railing, the area of wider cracks is the same than previous analysis but the maximum value is lower. The crack width according to direction P2 allows to focus on the damage in the pavement.

2010 model shows lower damage on the pavement (Figure 4.84, Figure 4.86) but it has elevate concentration below the dilatation joint in the railing, provoking high crack width (Figure 4.88).

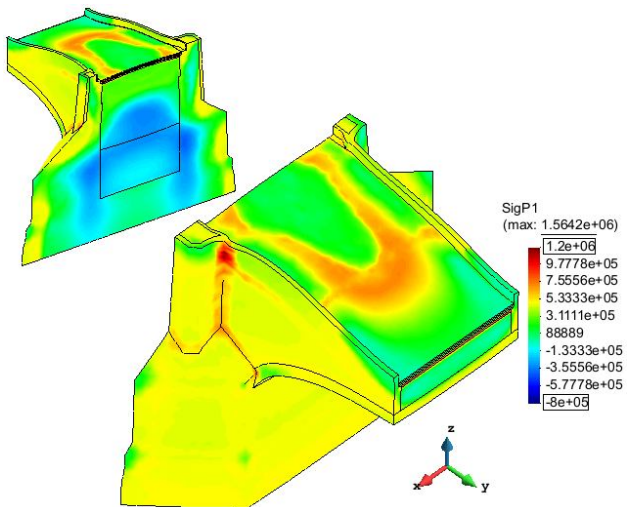


Figure 4.81 – Max. princ. stress (1975 model), Comb. B

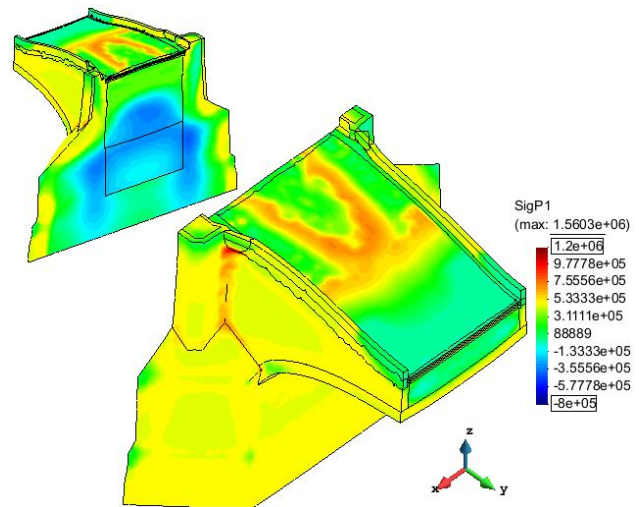


Figure 4.82 – Max. princ. stress (2010 model), Comb. B

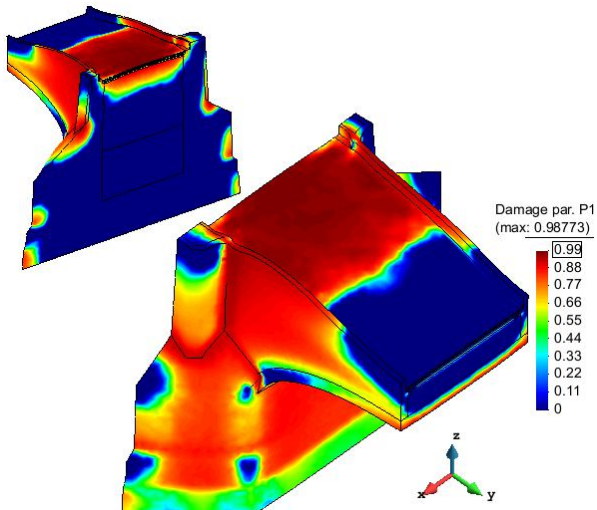


Figure 4.83 – Damage par. P1 (1975 mod.), Comb. B

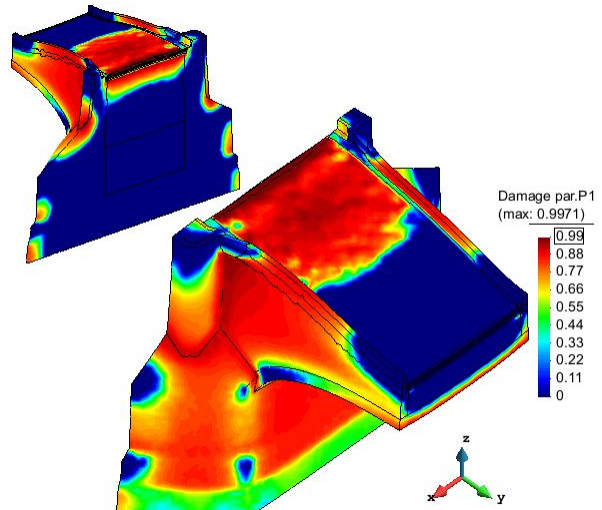


Figure 4.84 – Damage par. P1 (2010 mod.), Comb. B

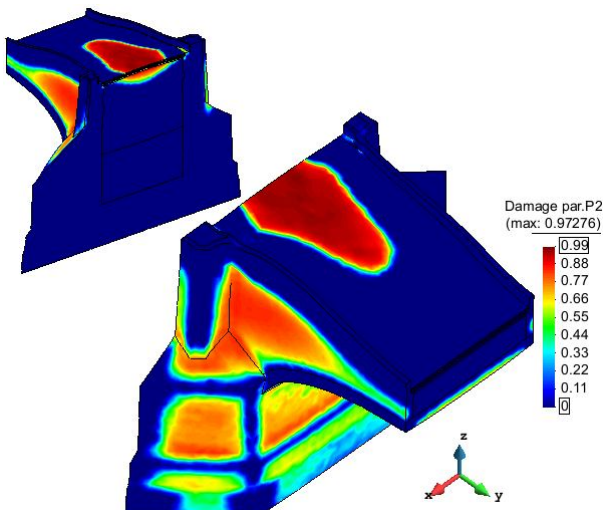


Figure 4.85 – Damage par. P2 (1975 mod.), Comb. B

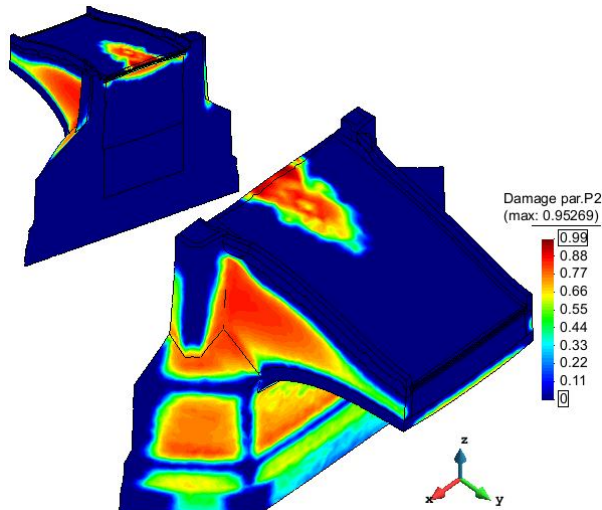


Figure 4.86 – Damage par. P2 (2010 mod.), Comb. B

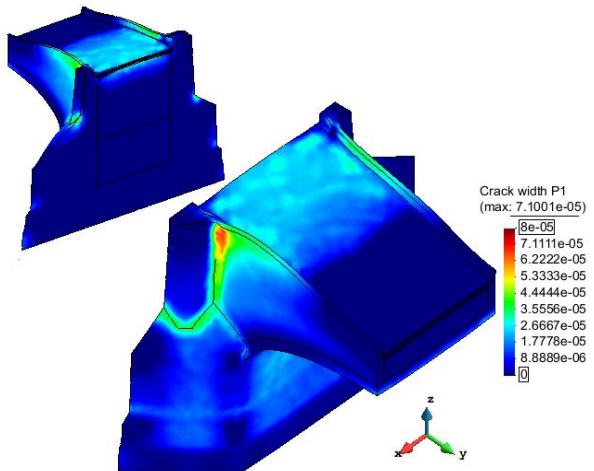


Figure 4.87 – Crack width P1 (1975 model), Comb. B

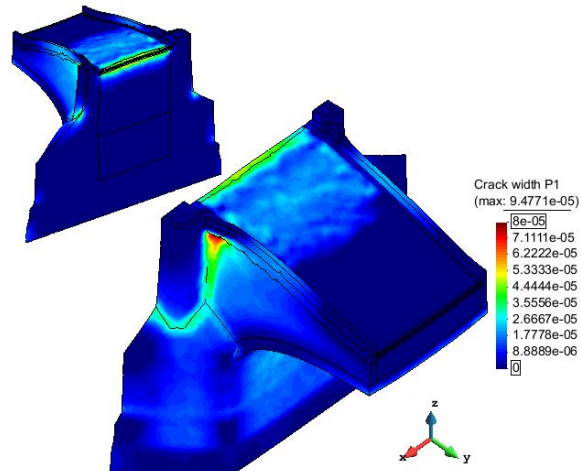


Figure 4.88 – Crack width P1 (2010 model), Comb. B

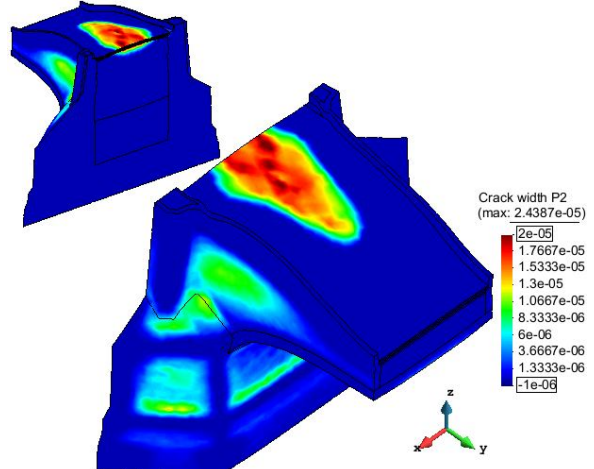


Figure 4.89 – Crack width P2 (1975 model), Comb. B

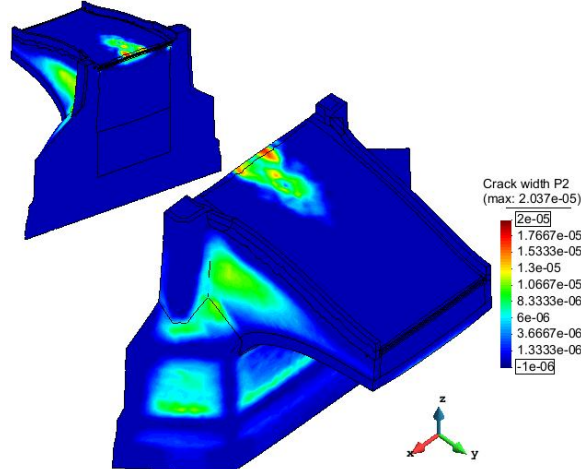


Figure 4.90 – Crack width P2 (2010 model), Comb. B

4.4.4 Temperature combination B (simple equivalent strain norm)

The orthotropic damage model analysis with simple norm of the equivalent strain is carried out also for the temperature combination from average to winter, obtaining results in Table 4.26. Differently from Comb. A, here the comparison between the two norms marks a big gap (60%) in the maximum principal stress, higher with simple norm. On the other side, the damage is generally lower. This is more evident in direction P2, where the parameter is reduced of 20%, and the corresponding crack width is halved.

Table 4.26 – Maximum displacements, stresses and damage for both models (Comb. B)

Model	Displ. Z _{max} (mm)	Displ. X _{max} (mm)	σ_1 max (MPa)	σ_3 max (MPa)	Damage par. P1 _{max}	Damage par. P2 _{max}	Crack width P1 _{max} (mm)	Crack width P2 _{max} (mm)
1975	-2.37	-0.65	2.38	-1.50	0.968	0.831	0.055	0.012
2010	-2.17	-0.56	2.70	-1.49	0.997	0.877	0.089	0.013

According to previous analysis, the rehabilitation modifies the damage distribution without decreasing it. Part of the railing is excluded from cracking but this concentrates in the breast wall (Figure 4.92) while the damage is avoided on the pavement but generally increased also in P2 direction (Figure 4.94).

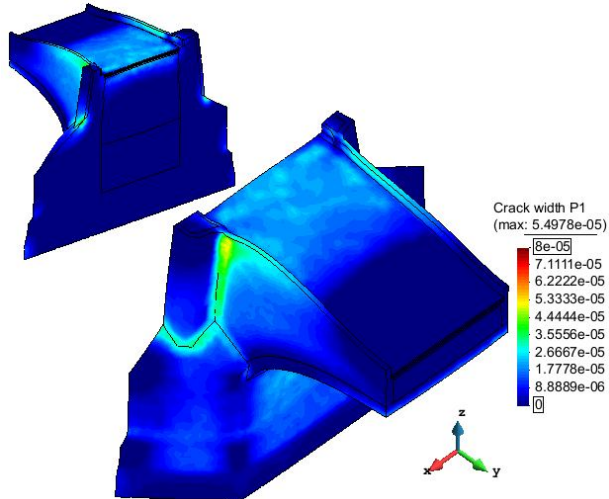


Figure 4.91 – Crack width P1 (1975 model), Comb. B

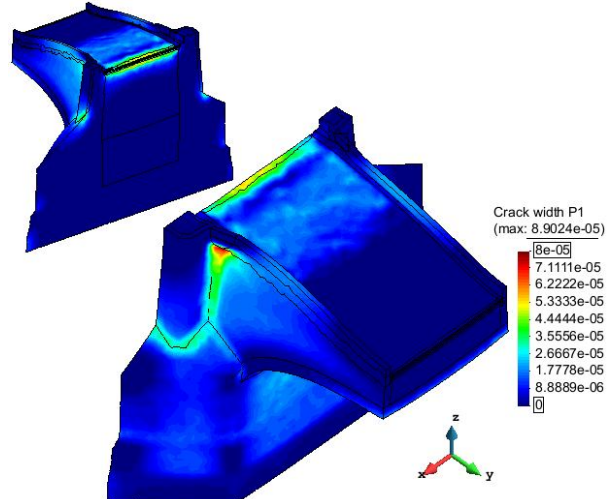


Figure 4.92 – Crack width P1 (2010 model), Comb. B

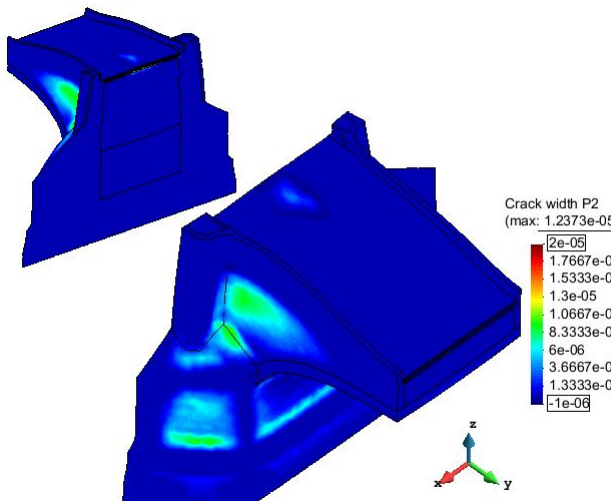


Figure 4.93 – Crack width P2 (1975 model), Comb. B

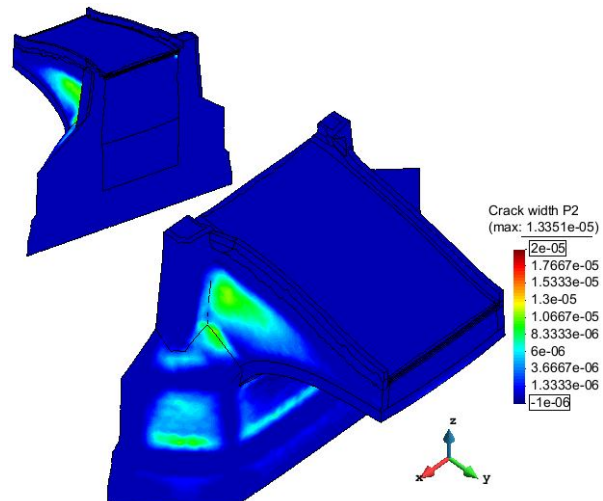


Figure 4.94 – Crack width P2 (2010 model), Comb. B

4.5 Non-linear analysis (SIFEL) – One year cycle

The analysis with orthotropic damage model and simple equivalent strain norm ($\tilde{\varepsilon} = \langle \varepsilon_I \rangle$) is repeated for a cycle of one year. The initial condition is the average temperature (18/04/2011) followed by the state in June, July and the maximum summer temperature (26/08/2011). Then values of November (10/11/2011) and January (07/01/2012) lead to the minimum winter temperature (12/02/2012) followed by the average values (18/04/2012) to close the cycle. For the graphical representation of temperature evolution, please compare to Par. 7.3.3 of Annexes.

The norm of vector of unbalanced forces, used for reaching stability (convergence criterion), is modified during the analysis, in way to suit before the steps towards summer and then those going to winter. Results are shown in Table 4.27 for the 1975 model and in Table 4.28 for the rehabilitated structure. Comparing them to the output between average-summer (Table 4.24) it is possible to notice as the gradual increase of temperature brings to slightly higher maximum displacement and lower stresses while the damage is considerably lower (max. damage parameter decreases of 30% while max. value of crack width is halved). Considering the results of 12/02/2012 and the previous average-winter analysis (Table 4.26), it is noticeable the similarity in displacement and stresses, as the difference in damage. This increases (of about 10%) because the structure is already weakened by summer temperatures effect. The use of smaller steps assures higher accuracy and stability because the subdivision of the load magnitude avoids big differences in stiffness matrix between steps.

Table 4.27 – Maximum displacements, stresses and damage for 1975 model

Date (dd/mm/yy)	Displ. Z _{max} (mm)	Displ. X _{max} (mm)	σ_1 _{max} (MPa)	σ_3 _{max} (MPa)	Damage par. P1 _{max}	Damage par. P2 _{max}	Crack width P1 _{max} (mm)	Crack width P2 _{max} (mm)
10/06/11	1,11	0,90	1,17	-6,28	0,674	0,139	0,007	0,001
30/07/11	2,17	1,14	1,25	-6,40	0,726	0,413	0,007	0,002
26/08/11	2,64	1,33	1,19	-7,20	0,726	0,489	0,007	0,003
10/11/11	1,32	0,83	1,51	-3,02	0,781	0,489	0,009	0,002
07/01/12	-0,82	-0,35	2,19	-1,33	0,913	0,705	0,028	0,005
12/02/12	-2,37	-0,65	3,01	-1,50	0,979	0,891	0,061	0,015
18/04/12	-0,90	-0,16	0,45	-2,58	0,979	0,891	0,019	0,004

The possible crack width is displayed for principal directions P1 and P2 in next figures, focusing on the steps between maximum and minimum temperatures. Only one scale is used in each principal direction, in way to make the steps comparable. About direction P1, in summer the damage is most probable on pavement and along the railing (Figure 4.95) while, decreasing the temperature (Figure 4.96, Figure 4.97), the damage focuses at the connection railing-pier (Figure 4.98). Comparing the images it is possible to notice the closure of already opened cracks, due to the inversion of temperature, as already documented in literature (Zeman, 2008). Anyway their presence will affect the structure during similar actions in following years.

On the other side, the most affected area of damage in P2 direction are the breast walls. Evolution in degradation can be seen in Figure 4.99 – Figure 4.102, culminating in possible cracks on railing and breast walls. On both principal directions, winter conditions provoke higher damage.

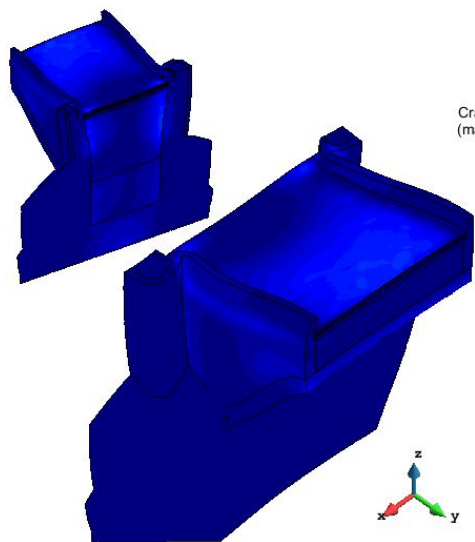


Figure 4.95 – Crack width P1, 1975 model (26/08/11)

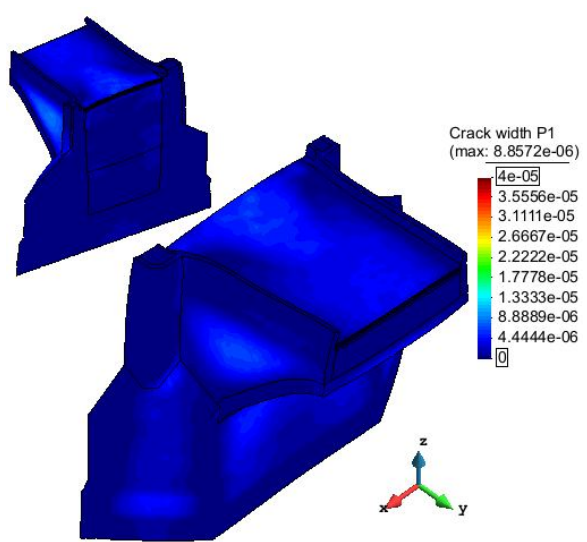


Figure 4.96 – Crack width P1, 1975 model (10/11/11)

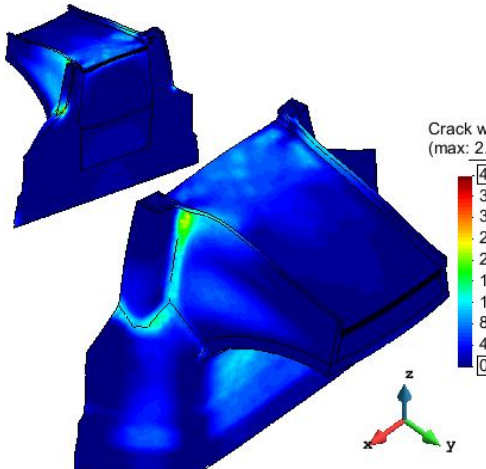


Figure 4.97 – Crack width P1, 1975 model (07/01/12)

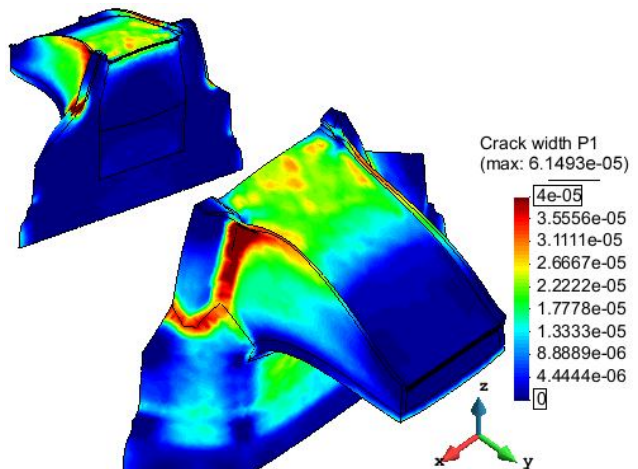


Figure 4.98 – Crack width P1, 1975 model (12/02/12)

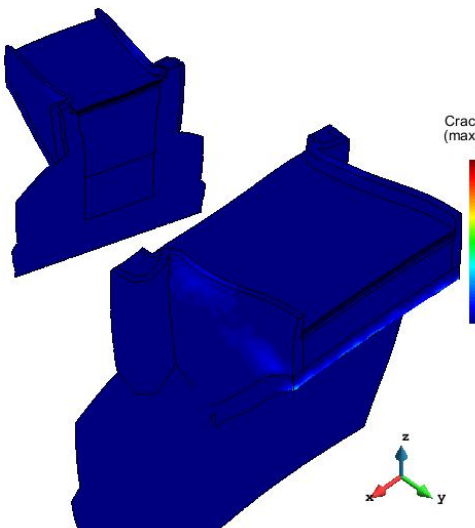


Figure 4.99 – Crack width P2, 1975 model (26/08/11)

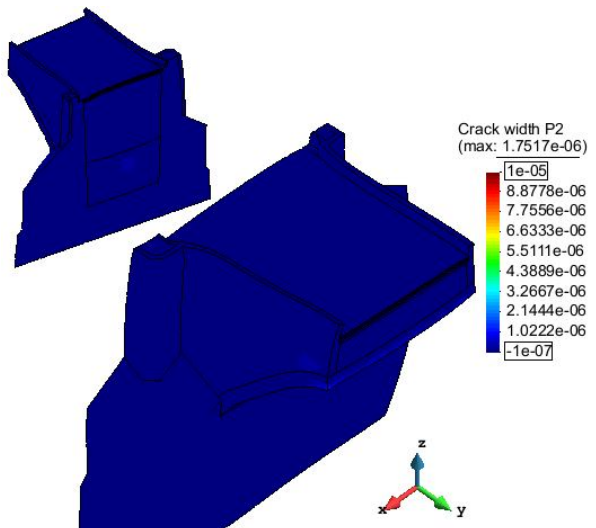


Figure 4.100 – Crack width P2, 1975 model (10/11/11)

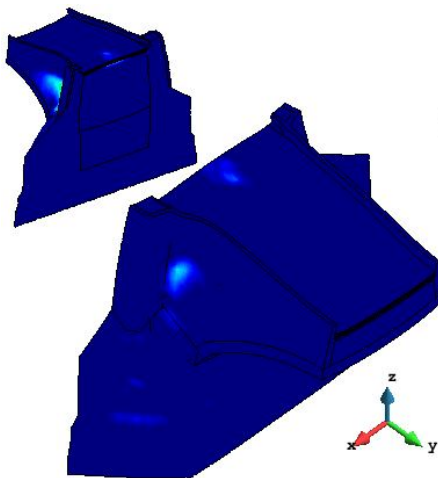


Figure 4.101 – Crack width P2, 1975 model (07/01/12)

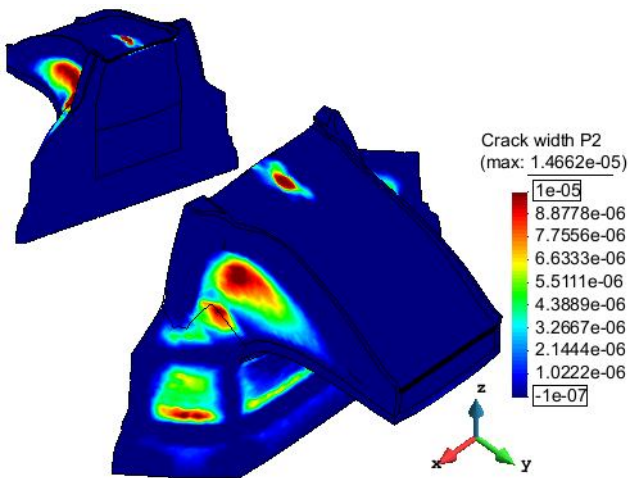


Figure 4.102 – Crack width P2, 1975 model (10/11/11)

As already noticed in previous analysis, the last rehabilitation changes the damage distribution but the maximum crack width (as the damage parameter) reaches higher level. The values obtained on 26/08/2011 are in agreement with previous average to summer analysis (with a gap of about 2%) while the date 12/02/2012 shows lower maximum displacement and stresses but higher damage (of about 5%).

In both models, the use of monthly steps bring to lower degradation during summer condition (thanks to the consideration of intermediate steps) and higher damage during winter state (since the structure is already weakened by summer effects).

Table 4.28 – Maximum displacements, stresses and damage for 2010 model

Date (dd/mm/yy)	Displ. Z _{max} (mm)	Displ. X _{max} (mm)	σ_1 _{max} (MPa)	σ_3 _{max} (MPa)	Damage par. P1 _{max}	Damage par. P2 _{max}	Crack width P1 _{max} (mm)	Crack width P2 _{max} (mm)
10/06/11	1,14	0,86	0,55	-6,17	0,587	0,140	0,004	0,001
30/07/11	2,12	1,16	0,73	-6,26	0,740	0,399	0,010	0,002
26/08/11	2,61	1,38	0,67	-7,09	0,837	0,505	0,019	0,007
10/11/11	1,33	0,85	1,47	-2,97	0,918	0,518	0,017	0,003
07/01/12	-0,77	-0,41	2,14	-1,33	0,947	0,776	0,038	0,006
12/02/12	-2,34	-0,57	2,76	-1,49	0,999	0,893	0,094	0,014
18/04/12	-0,88	-0,15	0,52	-2,60	0,999	0,893	0,045	0,005

The crack width plot for 2010 model in P1 direction has lower extension of damaged areas than in 1975 model and does not touch the zone of connection railing-pavement. The comparison of Figure 4.103 – Figure 4.106 with previous Figure 4.95 – Figure 4.98 underlines the lower occurrence of cracks on pavement and railing during summer. While, in winter, the pavement (on the pier side) is more damaged, as well as the breast walls (below the dilatation joints of the rehabilitated structure). Please remember that, as previously explained, the parameter distribution on the pavement is unrealistic for the external layer (unable to transmit stresses) but adequate for the lower ones.

Differently from the 1975 model (Figure 4.99 – Figure 4.102), the crack width plotting in P2 direction for the 2010 model (Figure 4.107 – Figure 4.110) focuses on breast walls avoiding the pavement; however maximum values for the two models are really close.

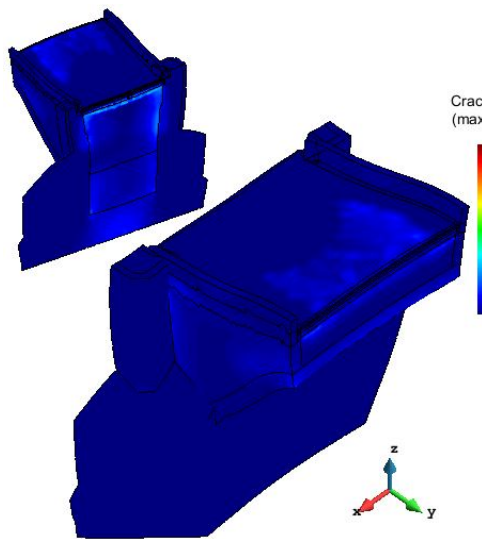


Figure 4.103 – Crack width P1, 2010 model (26/08/11)

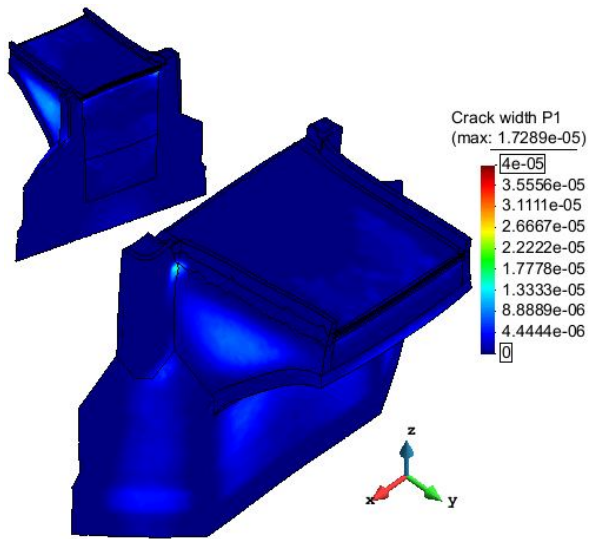


Figure 4.104 – Crack width P1, 2010 model (10/11/11)

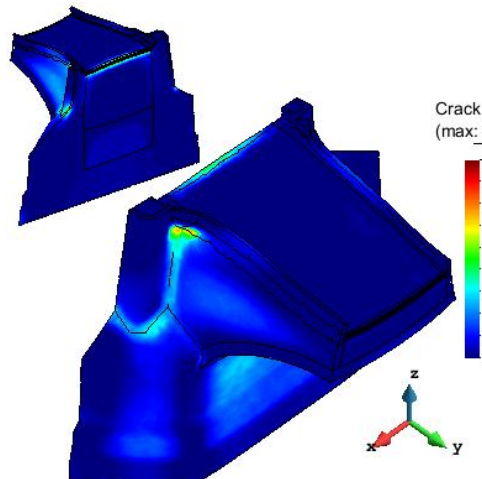


Figure 4.105 – Crack width P1, 2010 model (07/01/12)

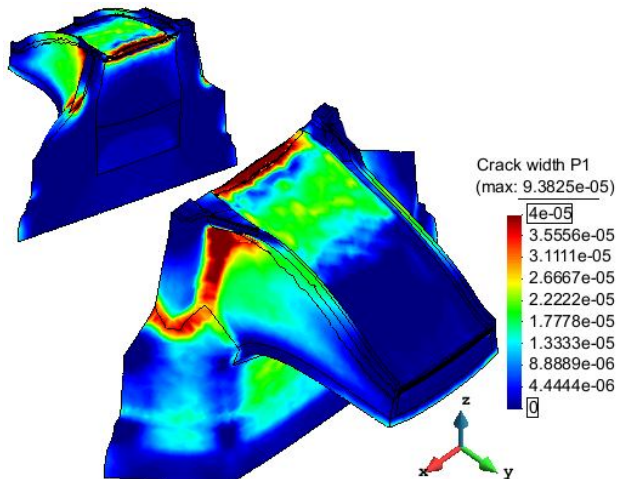


Figure 4.106 – Crack width P1, 2010 model (12/02/12)

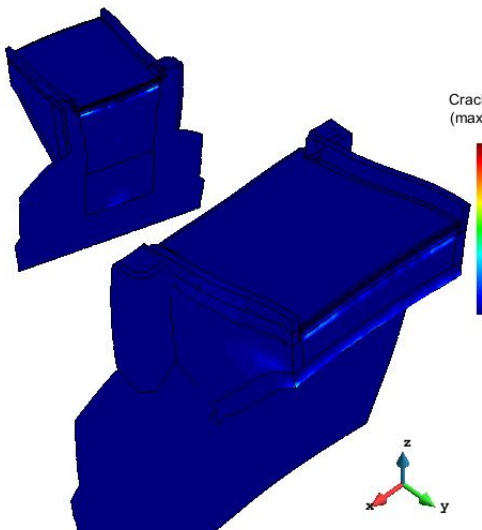


Figure 4.107 – Crack width P2, 2010 model (26/08/11)

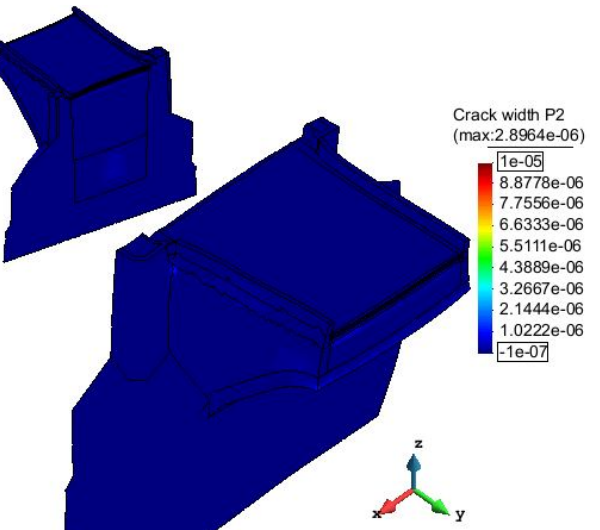


Figure 4.108 – Crack width P2, 2010 model (10/11/11)

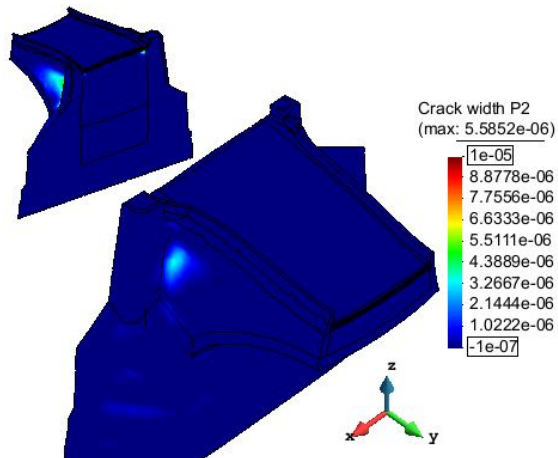


Figure 4.109 – Crack width P2, 2010 model (07/01/12)

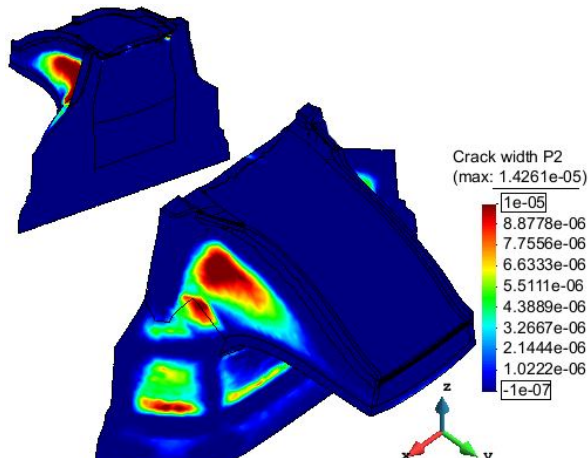


Figure 4.110 – Crack width P2, 2010 model (10/11/11)

The analysis of a year cycle allows to observe the displacement of the structure at every step (Figure 4.111, Figure 4.112, Figure 4.113). It is interesting to notice how the cross-section bends not only longitudinally but also transversally, when extreme values are reached. Moreover the railings do not move in the same way indeed, during summer, the northern side of the bridge expands more than the southern one, due to the higher increase of temperature from average values.

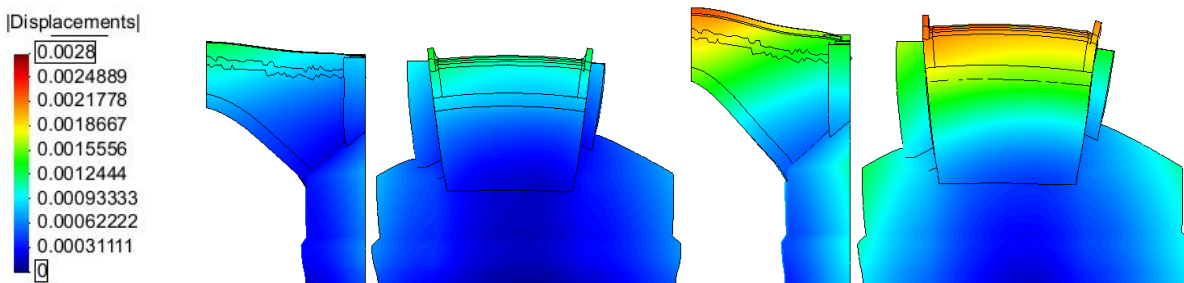


Figure 4.111 – Displacements on 10/06/2011 and 30/07/2011

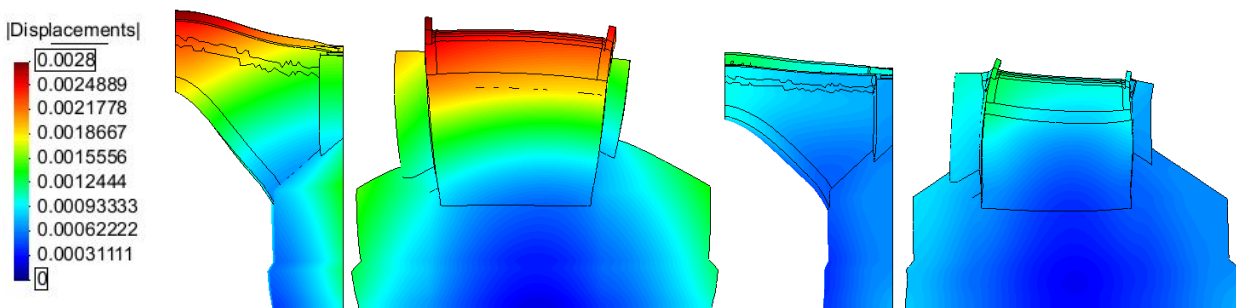


Figure 4.112 – Displacements on 26/08/2011 and 10/11/2011

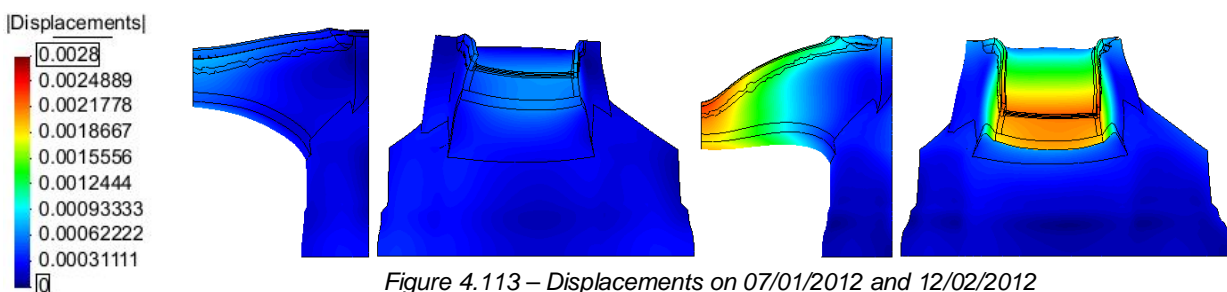


Figure 4.113 – Displacements on 07/01/2012 and 12/02/2012

To make a visual comparison with the analysis from average to summer and from average to winter temperatures, crack width in direction P1 and P2 have been plotted again, underlining the relative figure of Par. 4.4.2 and Par. 4.4.4. They are exhibited and discussed in Par. 7.3.2 of Annexes.

This step of the work marked another difference between SIFEL and the previously used Adina. Since the latter records and shows results for every computed sub-step in reaching the time step, a one year cycle analysis would be more difficult to handle, because of the slowness in recording and the size of output. Instead of this, editing its code, SIFEL will record and show only results for time steps, hence speeding up calculation and output analysis.

4.5.1 Second year of computation

A modification of the input file allows to continue the analysis from the backup at the end of the first year (18/04/2012). The process is developed only for the 2010 model, since this is the actual structure. Temperatures of the second year were not available so those of the previous one were used, assuming their similarity. A long computation, with several time steps, may bring to a bigger inaccuracy but the editing of the convergence criterion (norm of vector of unbalanced forces) avoids it. The previous analysis was based on the assumption of absence of damage at the starting point (26/04/2011) thanks to the rehabilitation, while this one begins from an already damaged condition, therefore a different behavior is expected; results are shown in Table 4.29.

Maximum displacements are about 10% higher, while the maximum principal stress decreases of about 20% in respect to previous year. The max. damage parameter at the first step (10/06/2012) assumes the last value of the previous analysis, reaching the unit value at the winter step (in P1 direction). For this reason the maximum crack width in P1 direction is more than doubled, reaching a maximum possible extension of 0.228 mm in winter step, while values in P2 direction are 300% higher than before.

Results confirm the intuition that temperature loading cannot be considered only during one year because its main effect is due to the reiteration in cycles.

Table 4.29 – Maximum displacements, stresses and damage for 2010 model (second year of computation)

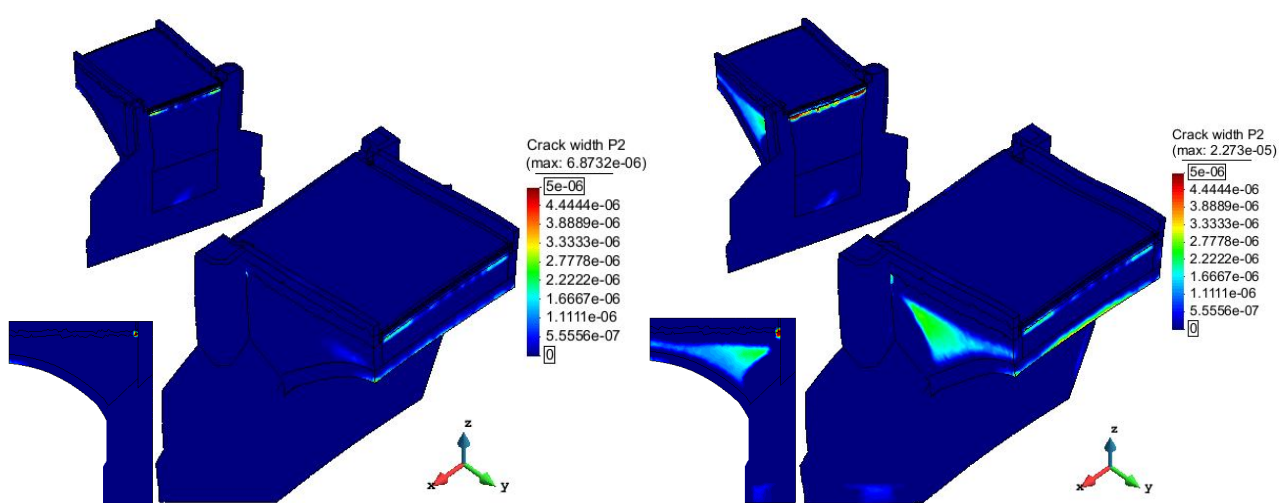
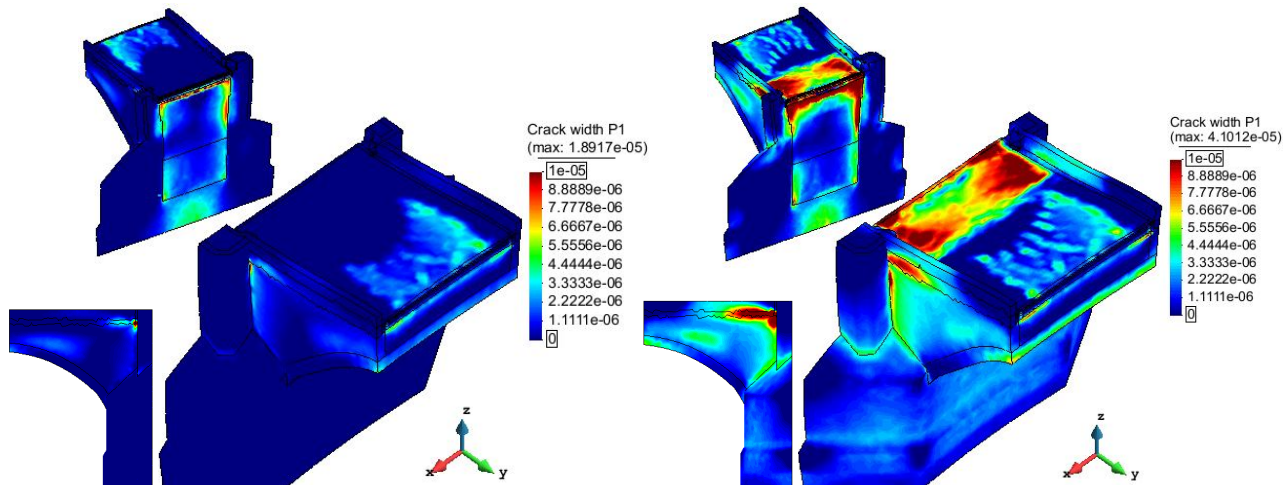
Date (dd/mm/yy)	Displ. Z _{max} (mm)	Displ. X _{max} (mm)	σ_1 _{max} (MPa)	σ_3 _{max} (MPa)	Damage par. P1 _{max}	Damage par. P2 _{max}	Crack width P1 _{max} (mm)	Crack width P2 _{max} (mm)
10/06/12	1,14	0,92	0,50	-6,22	0,9991	0,8932	0,021	0,009
30/07/12	2,14	1,20	0,75	-6,90	0,9991	0,8932	0,029	0,015
26/08/12	2,63	1,39	0,68	-8,41	0,9991	0,8932	0,041	0,023
10/11/12	1,36	0,89	1,09	-2,91	0,9991	0,8932	0,041	0,017
07/01/13	-0,89	-0,41	1,80	-1,29	0,9995	0,8932	0,087	0,036
12/02/13	-2,41	-0,49	2,06	-1,48	1,0000	0,9408	0,228	0,096
18/04/13	-0,87	-0,17	0,84	-2,61	1,0000	0,9408	0,076	0,030

Following images clearly show the increase of damage (in this case, crack width) between the same step of the first and second year. They are plotted in the same scale of the analysis with orthotropic

damage model between average and summer/winter temperatures (Par. 4.4) to make them comparable and highlight the degradation. The pattern on the pavement of Figure 4.115 evidently shows damage on the side of the pillar, due to the winter step of previous year analysis (Figure 4.118), hence the structure is subjected to the influence of previous cycle's damage.

The presence of the undeformed lateral elevation underlines the occurrence of degradation in breast walls, below vertical dilatation joints, otherwise masked by the deformed shape of summer computation.

From Figure 4.119 and Figure 4.121 it is possible to notice kind of corrugation on the pavement, close to the symmetry plane. Increasing the magnification scale of the deformed shape the defect expands on all the damaged areas of the pavement in Figure 4.119. It is due to the use of linear approximation functions in the mesh elements since when the damage parameter is equal to one, there is no stiffness and the elements deform.



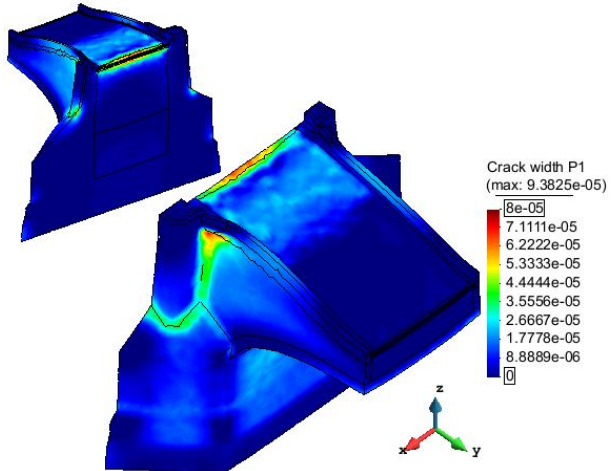


Figure 4.118 – Crack width P1 (2010 model), 12/02/2012

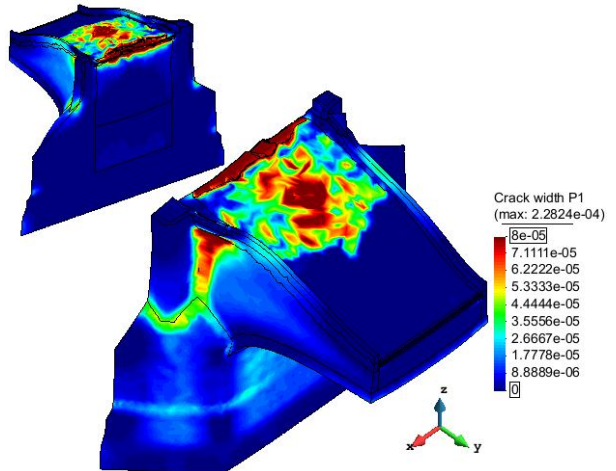


Figure 4.119 – Crack width P1 (2010 model), 12/02/2013

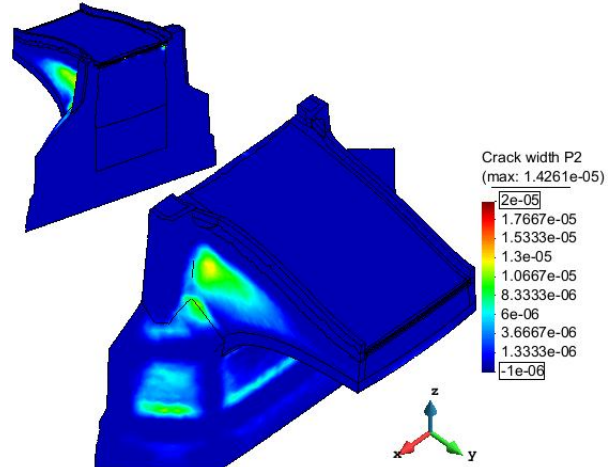


Figure 4.120 – Crack width P2 (2010 model), 12/02/2012

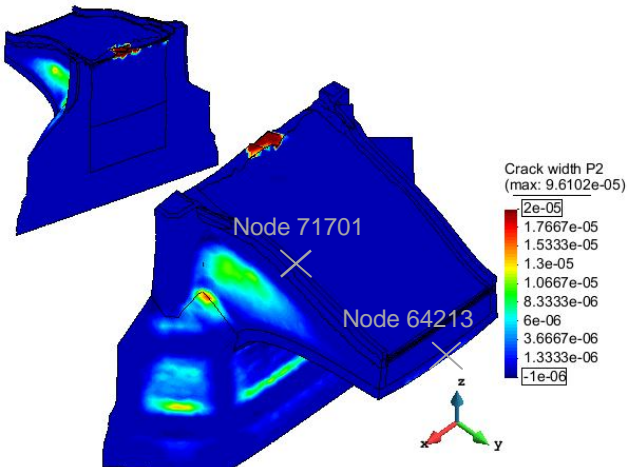


Figure 4.121 – Crack width P2 (2010 model), 12/02/2013

4.5.2 Further years of computation

The analysis was continued up to the fifth year, in way to give a forecast of the damage till 2016.

As can be seen from Table 4.30 and Table 4.31, after the second year of computation, maximum displacements find hard to increase. The phenomenon is studied in Table 4.32 and Figure 4.122 using two control nodes (number 64213 and 71701, located at arch crown and parapet as in Figure 4.121). During summer the maximum displacements increase of more than 5% from the first to the second year, but in subsequent years they change of only 0.8% in each step; comparable trend is shown during winter.

Maximum stresses follow a similar evolution, trend even more noticeable in the damage (Table 4.30, Table 4.31). The maximum damage parameter in principal direction P1 increases of 20% after the first summer, reaching soon the highest level; in direction P2 the modification after the first year is of about 70%, then reduced to 5% till reaching the maximum. Similarly it happens also in winter steps, seeing again higher changes in direction P2, since the parameter starts from a lower level.

About the maximum crack width the percentages of modification between first and second year of computation are higher but the subsequent trend can even be negative (in winter period). After reaching a peak of 0.24 mm during winter of the third year, following peaks are lower than it (later explained phenomenon).

The first year starts from a condition of absence of damage, while the second considers it, this explains the high variation between them. Subsequent years generally show lower gaps because in those cases the condition of absence of damage is no more considered.

Table 4.30 – Maximum displacements, stresses and damage for 2010 model (summer results for all the years)

Date (dd/mm/yy)	Displ. Z _{max} (mm)	Displ. X _{max} (mm)	σ_1 max (MPa)	σ_3 max (MPa)	Damage par. P1 _{max}	Damage par. P2 _{max}	Crack width P1 _{max} (mm)	Crack width P2 _{max} (mm)
26/08/11	2,61	1,38	0,67	-7,09	0,8366	0,5053	0,019	0,007
26/08/12	2,63	1,39	0,68	-8,41	0,9991	0,8932	0,041	0,023
26/08/13	2,64	1,40	0,68	-8,39	1,0000	0,9408	0,042	0,023
26/08/14	2,65	1,40	0,67	-8,35	1,0000	0,9511	0,045	0,023
26/08/15	2,66	1,40	0,68	-8,90	1,0000	0,9521	0,059	0,031

Table 4.31 – Maximum displacements, stresses and damage for 2010 model (winter results for all the years)

Date (dd/mm/yy)	Displ. Z _{max} (mm)	Displ. X _{max} (mm)	σ_1 max (MPa)	σ_3 max (MPa)	Damage par. P1 _{max}	Damage par. P2 _{max}	Crack width P1 _{max} (mm)	Crack width P2 _{max} (mm)
12/02/12	-2,34	-0,57	2,76	-1,49	0,9991	0,8932	0,094	0,014
12/02/13	-2,41	-0,49	2,06	-1,48	1,0000	0,9408	0,228	0,096
12/02/14	-2,41	-0,49	2,08	-1,48	1,0000	0,9511	0,236	0,098
12/02/15	-2,42	-0,49	1,93	-1,49	1,0000	0,9521	0,223	0,079
12/02/16	-2,42	-0,52	2,06	-1,49	1,0000	0,9544	0,209	0,076

Table 4.32 – Vertical maximum displacement of control node 64213 and horizontal maximum displ. of 71701

Date	Displ. Z _{max} (mm)	Displ. X _{max} (mm)	Date	Displ. Z _{max} (mm)	Displ. X _{max} (mm)
26/08/11	1,886	0,948	12/02/12	-2,010	-0,4713
26/08/12	1,968	1,015	12/02/13	-2,058	-0,290
26/08/13	1,970	1,026	12/02/14	-2,054	-0,259
26/08/14	1,969	1,022	12/02/15	-2,052	-0,271
26/08/15	1,991	1,053	12/02/16	-2,051	-0,263

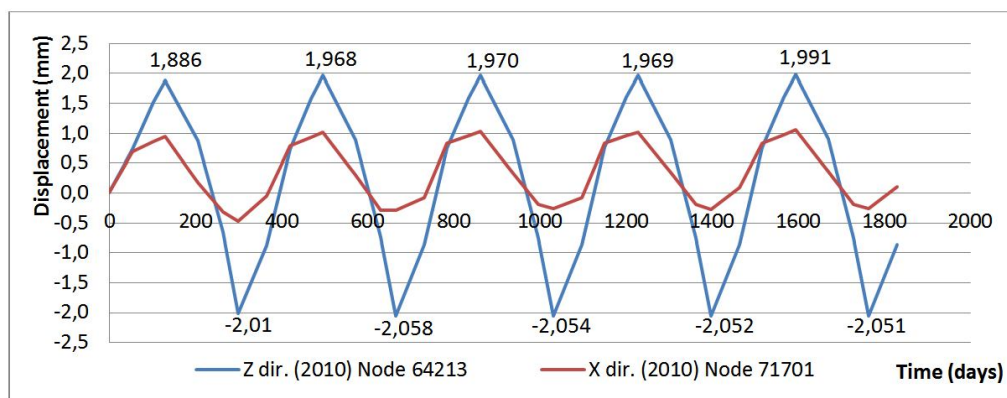


Figure 4.122 – Displacements on control nodes 64213 (Z direction) and 71701 (X direction)

To explain the negative trend, damage evolution was studied further, choosing a control element (number 311678) immediately below the vertical dilatation joint of the parapet (as in Figure 4.125). As can be seen from Table 4.33 and Table 4.34, the damage parameter on the control element increases in both directions as already explained, while the crack width always enlarges except than in the first principal direction during winter, where it reduces of about 8% in every step after second year; Figure 4.124 clearly shows it. It is noticeable that the highest crack width reached in the element (almost 0.2 mm) is the only one to decrease, while the other values still increase.

Table 4.33 – Maximum damage parameter and crack width for control element 311678 (summer results)

Date	Damage par. P1 _{max}	Damage par. P2 _{max}	Crack width P1 _{max} (mm)	Crack width P2 _{max} (mm)
26/08/11	0,6980	0,4790	0,023	0,015
26/08/12	0,9874	0,8768	0,046	0,040
26/08/13	0,9950	0,8865	0,046	0,040
26/08/14	0,9950	0,9030	0,048	0,042
26/08/15	0,9950	0,9195	0,058	0,050

Table 4.34 – Maximum damage parameter and crack width for control element 311678 (winter results)

Date	Damage par. P1 _{max}	Damage par. P2 _{max}	Crack width P1 _{max} (mm)	Crack width P2 _{max} (mm)
26/08/11	0,9874	0,4790	0,123	0,005
26/08/12	0,9950	0,8865	0,198	0,005
26/08/13	0,9950	0,9030	0,184	0,007
26/08/14	0,9950	0,9195	0,167	0,019
26/08/15	0,9950	0,9458	0,155	0,042

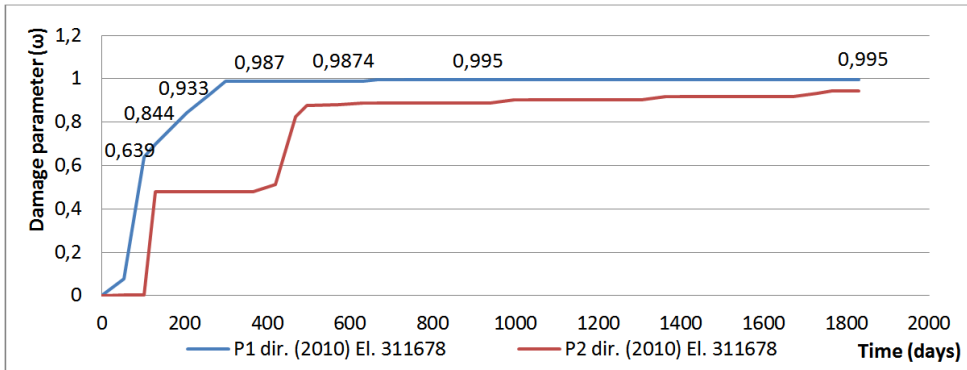


Figure 4.123 – Damage parameter evolution on control element 311678 in direction P1 and P2

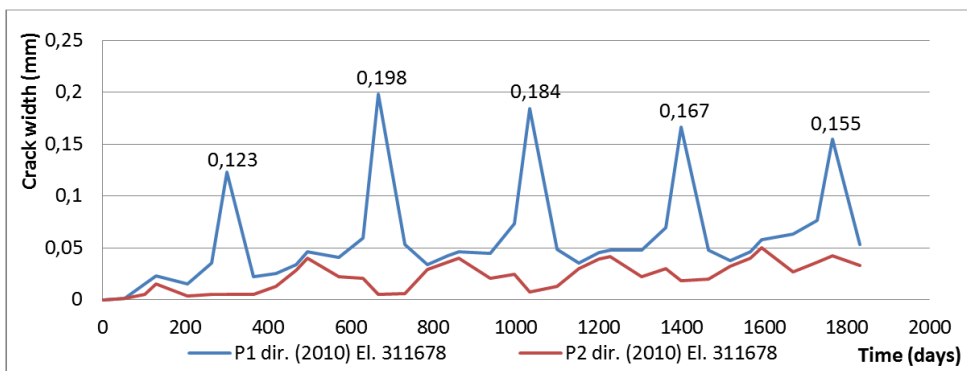


Figure 4.124 – Crack width evolution on control element 311678 in direction P1 and P2

The lowering max. crack width is related to the highest degradation (indeed the damage parameter reaches its absolute maximum only in winter and in first principal direction). Figure 4.125 – Figure 4.132 show the increase of damage parameter between second and fifth year: it is clear that, even if the maximum crack width reduces, the damage state get worse.

The decreasing of the width values can be associated with an expansion of the areas of possible heavy damage (hence a higher number of cracks will appear, or they will have higher extension) therefore their maximum width is reduced than before.

The damage model is able to describe smeared cracks but after the evolution of damage, it is not adequate to illustrate the discrete ones. However it is the best choice for studying a problem related to thermal loading at this scale.

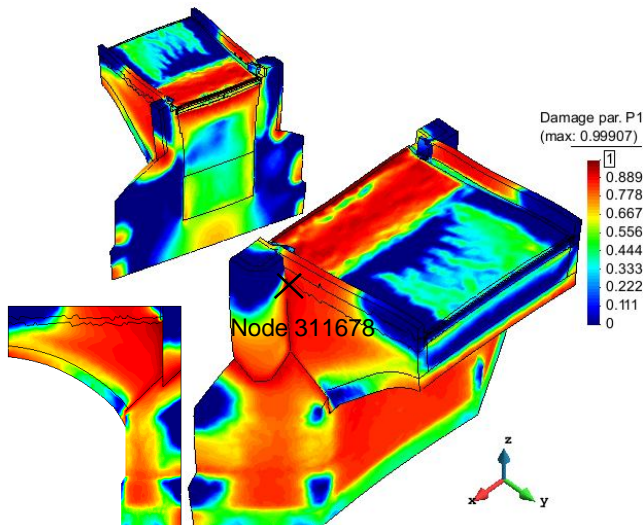


Figure 4.125 – Damage par.P1 (2010 mod.), 26/08/2012

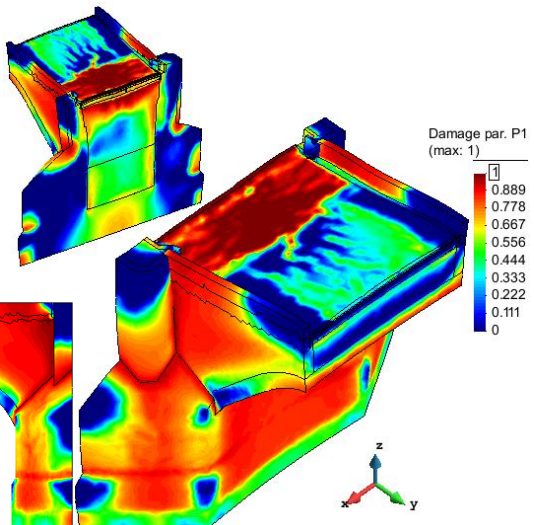


Figure 4.126 – Damage par.P1 (2010 mod.), 26/08/2015

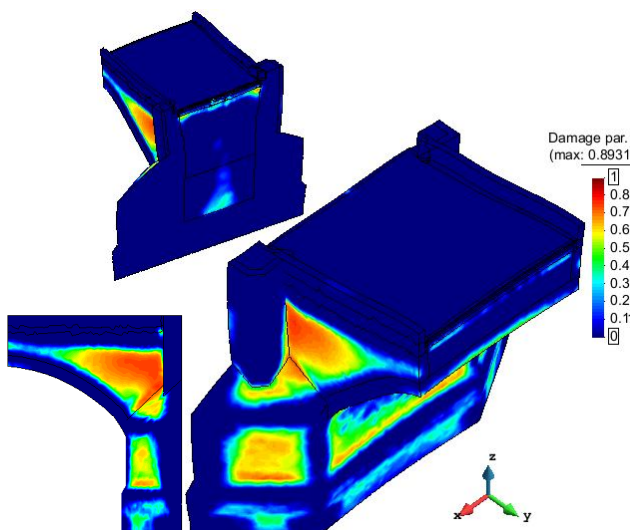


Figure 4.127 – Dam. par.P2 (2010 mod.), 26/08/2012

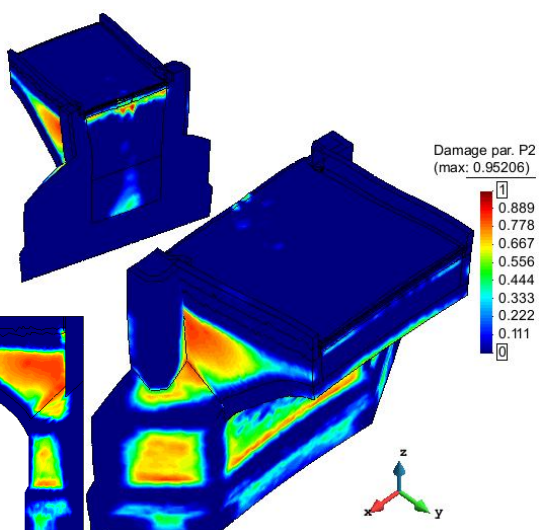


Figure 4.128 – Dam. par.P2 (2010 mod.), 26/08/2015

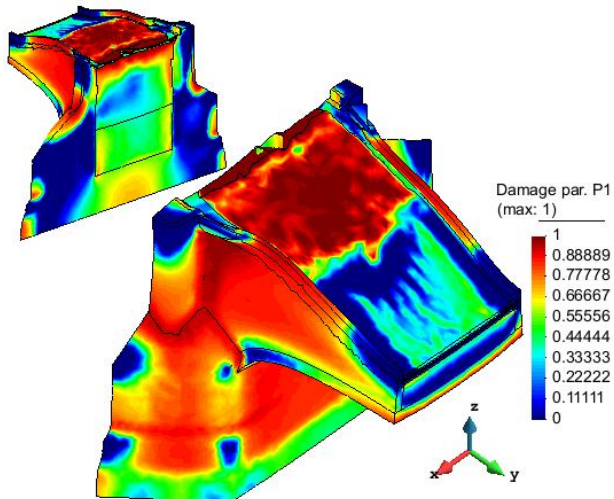


Figure 4.129 – Damage par.P1 (2010 mod.), 12/02/2013

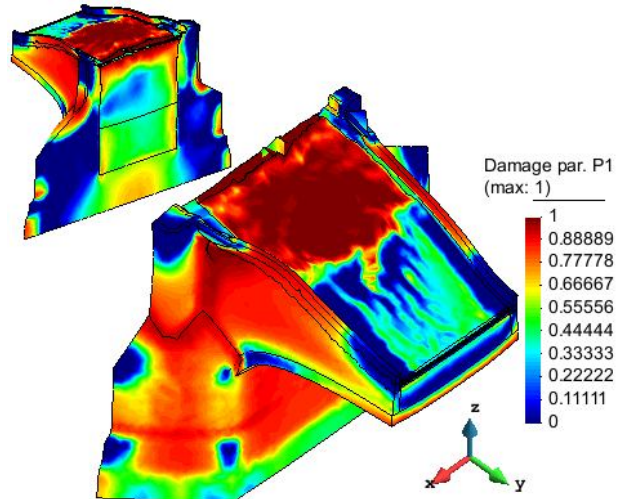


Figure 4.130 – Damage par.P1 (2010 mod.), 12/02/2016

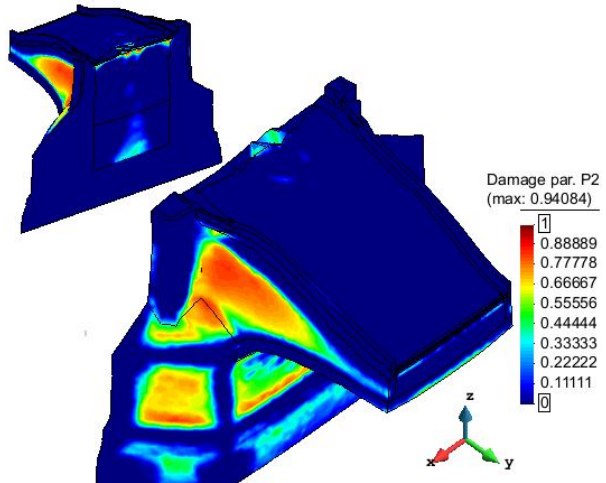


Figure 4.131 – Damage par.P2 (2010 mod.), 12/02/2013

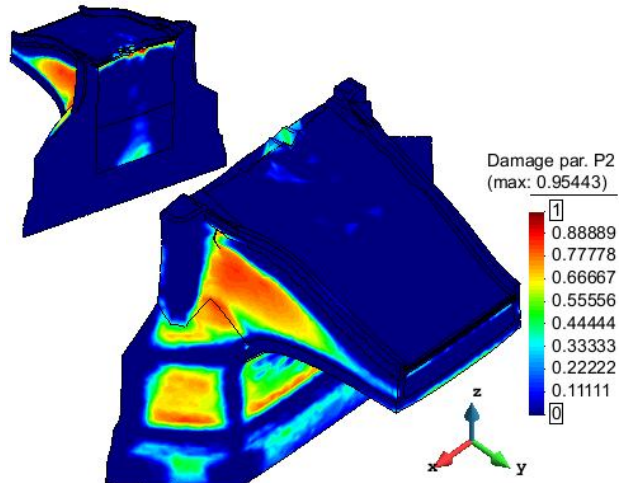


Figure 4.132 – Damage par.P2 (2010 mod.), 12/02/2016

4.6 Model refinement

Further analysis on Charles Bridge can be performed refining both thermal and mechanical aspects. On the one hand, changing the boundary conditions for heat transfer analysis, on the other hand, using the non-local theory (stresses/strains are averaged from the nearest area) or working on the approximation of cracks interaction.

4.6.1 Boundary conditions for heat transfer analysis

The presented thermo-mechanical analysis is based on the heat transfer analysis, where material parameters, and then boundary conditions, were validated and verified according to in-situ measurements (Krejci, 2014).

For further analysis and prognosis of structural behaviour, the boundary conditions for heat transfer can be specified with respect to representative climatic data (reference territorial climatic year) provided by the Czech Hydrometeorological Institute. They include effects of sun radiation, wind, rain, heat conditions, and the structure's orientation; for further information please compare to (Ďurana, 2013) and (ČHMÚ, 2014).

4.6.2 Non-local approach

The analysis was performed using scalar isotropic and orthotropic damage models in their local formulation, where the equivalent strain is computed from the strain tensor directly at a given point. This computation which could suffer by difficulties during the classical local approximation, where the damage may be inaccurately localized in a narrow band. The mentioned problem can be avoided using non-local computation based on non-local averaging, which is in principle applicable to any type of constitutive model (Jirásek, 1998). Non-local formulations were derived for a wide spectrum of models, including softening plasticity, smeared crack models, and microplane models. The basic idea of non-local approach is in replacing a certain variable by its non-local counterpart obtained by weighted averaging over a spatial neighbourhood of each point (ξ) under consideration (Jirásek, 1998). As for the isotropic and orthotropic damage models, a simple non-local formulation for the equivalent strain computed from the non-local strain tensor can be adopted. The local strain ε is replaced by its non-local average:

$$\varepsilon = \int_V \alpha(x, \xi) \varepsilon(\xi) d\xi \quad (4.1)$$

where $\alpha(x, \xi)$ is a non-local weight function.

For alternative formulations of the averaging operator (4.1), with descriptions of non-local averaging techniques, please compare to References (Jirásek, 1998) and (Bažant, 1994).

4.6.3 Approximation of cracks interaction (Kachanov model)

For further model extension, the approaches presented by Kachanov (Kachanov, 1995), (Kachanov, 2007), can be adopted.

The theory of effective elastic properties of cracked solids considers the degradation of stiffness, development of anisotropy and changes in wave speeds due to microcracking (Kachanov, 1995), therefore it is an interesting topic both for solid mechanics and ND techniques.

Cracks are a particular kind of inhomogeneity: they do not occupy a volume, they cause complex stress fields and they depend from orientation. For these features the study of cracked solids has some difficulties (Kachanov, 1995):

- the choice of crack density parameter is not trivial;
- the effective properties are usually anisotropic;
- the approximation of non-interacting cracks has a range of applicability wider than thought.

The simplest approach to the problem is the approximation of non-interacting cracks (developed from Bristow in the sixties); this approximation can remain accurate at high crack densities and strong interactions, since the interaction effect of different cracks may compensate each other (Kachanov, 1995). This is the method used in the presented work.

To go further in the subject, the problem consists of two different kinds of cracks interactions: they may "stiffen" the elastic response (if they are of predominant shielding nature) or "soften" it (if the amplifying interactions are dominant). The response is due to the mutual position of cracks, so on their predominant shielding or amplifying behaviour. It is also possible that the two different effects balance each other, in way that strong local effects have low relevance on the overall stiffness of the system (Kachanov, 2007). In the assumption of non-interacting cracks the effective moduli can be found, for an arbitrary crack orientation statistics, in both 2D and 3D. In this approach, each crack is considered isolated, embedded in the externally applied stress field σ without being influenced from any other crack. Averaging over a crack array is reduced to summation over orientations, since the cracks mutual positions are not considered (Kachanov, 1995).

The 3D case brings to a similar analysis but there is an effect of dimensionality for which, at the same crack density of 2D, the stiffness reduction due to cracks is weaker in 3D.

Computer experiments (Kachanov, 1995) were used to test the reliability of the approach:

- for random oriented cracks, the approximation of non-interacting cracks brought to good results;
- for parallel cracks, the results are acceptable but there is the tendency for the stiffening, according to the calculated Young modulus. This means that there is a dominance of the shielding mode of interactions. The experiments brought also to other results:
- the orthotropy (in 2D) is valid for non-interacting cracks and it can hold also at high ρ because the approximation of non-interacting cracks remains accurate at high crack densities (ρ up to 0.35, due to the fact that competing effects of stress shielding and stress amplification cancel each other);
- the characterization of crack arrays by the crack density tensor remains adequate even at high crack densities when interactions are strong.

4.7 Simple numerical approach (finite difference method)

To face the investigation from a different point of view, avoiding the finite element analysis, a simple numerical method is considered and solved by hand. The FEM is the most used and powerful tool, while the present approach has only the aim to analyse stresses on a 2D structural element of the bridge (after the estimation of boundary conditions), providing a rough comparison with previous comprehensive study. The analysed element includes breast wall and parapet (with a uniform averaged thickness of 0.576 m), without considering dilatation joints. The finite difference method (FDM) is used, according to theory and equations presented in Annexes (Par. 7.4).

It is a pure 2D analysis, considering the problem of stretching of a plate (with uniform thickness) in plane stress state ($\sigma_z = \tau_{xz} = \tau_{zy} = 0; \varepsilon_z \neq 0$) and solving it with force method (stresses considered as unknowns). The FDM allows to solve partial (or ordinary) differential equations by substitution of derivatives with their differences; the approximation leads to a system of linear algebraic equations. Using the force method, the operator is biharmonic and it leads to a non-homogeneous equation (for bending), or a homogeneous one (for stretching).

The biharmonic operator is solved using a difference scheme (grid). The grid (mesh) identifies nodal points with constant distance and its boundary involves boundary nodal points. It is applied to the breast wall (including parapet) with regular spacing of 1.82 m, as in Figure 4.133, where the dashed grey line represents the dimension of the real element. Constraints are set as sliding on three sides of the structure, two of them meet in point "q" of the grid, forming a hinge.

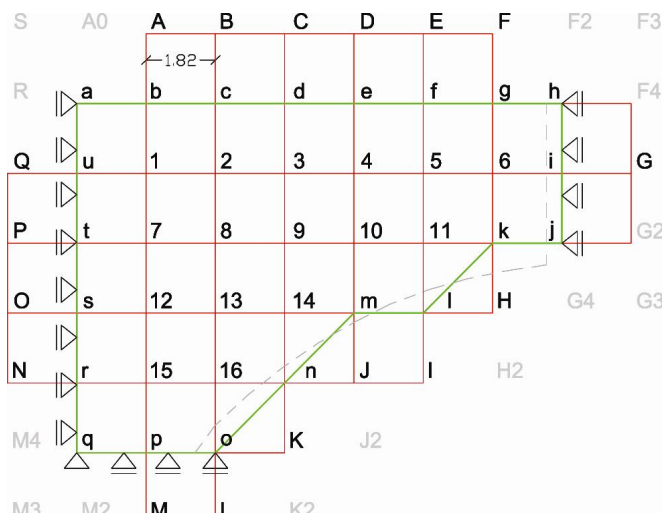


Figure 4.133 – Set up of boundary conditions and finite difference mesh

It is a many times statically undetermined problem, solvable with a principle of virtual displacements (compare to Eq. (7.35) in Annexes), but the calculation of all unknown reactions and virtual states would be demanding, therefore the simple estimation of boundary forces is preferred.

The analogy with fixed beam is applied in the upper part of the structure. In it the axial stress is computed from the constant uniform temperature loading $\sigma_x = -E\alpha t$ (Figure 4.134, Figure 4.136), where E is stone masonry Young modulus (= 20.2 GPa), α is coefficient of masonry thermal expansion ($= 8 \times 10^{-6} \text{ K}^{-1}$) and t is temp. variation ($= +17.14$ towards summer, -11.08 toward winter).

In the top part, the right boundary surface has constant stress distribution in horizontal direction, while the left surface shows linear stress distribution in same direction. Its maximal value computed to ensure the static equilibrium (Figure 4.134, Figure 4.136).

With respect to l'Hermite's analogy, the structure is cut on the oblique side, as displayed in Figure 4.134 (it is possible to cut the frame everywhere, finally obtaining equal stress distribution).

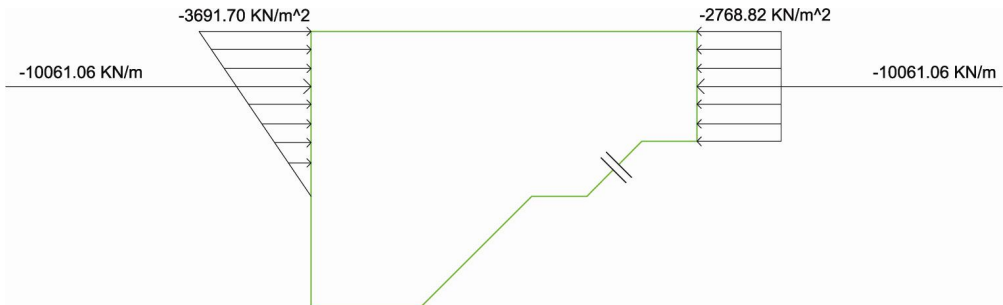


Figure 4.134 – Thermal loading acting on the fictitious frame (summer temperatures)

Bending moment and axial force are calculated on the fictitious frame (Figure 4.135, Figure 4.137). A moment provoking tension on external side of the frame is considered negative (Figure 4.135), while that provoking tension on the internal side is positive (Figure 4.137). Please notice that actions in Figure 4.134 and Figure 4.136 are not multiplied by the wall depth.

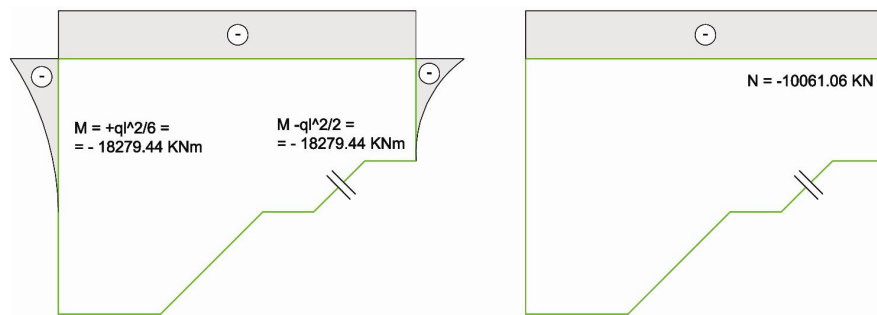


Figure 4.135 – Bending moment and axial force diagrams (summer temperatures)

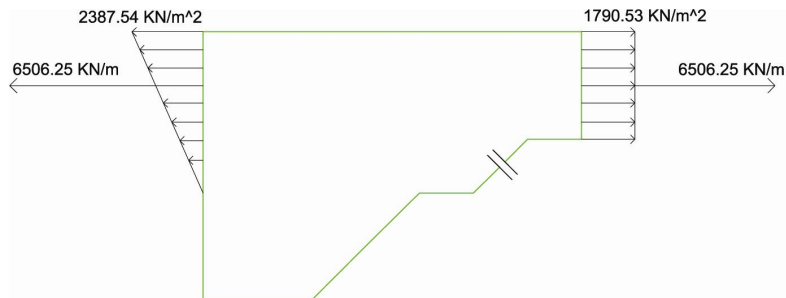


Figure 4.136 – Thermal loading acting on the fictitious frame (winter temperatures)

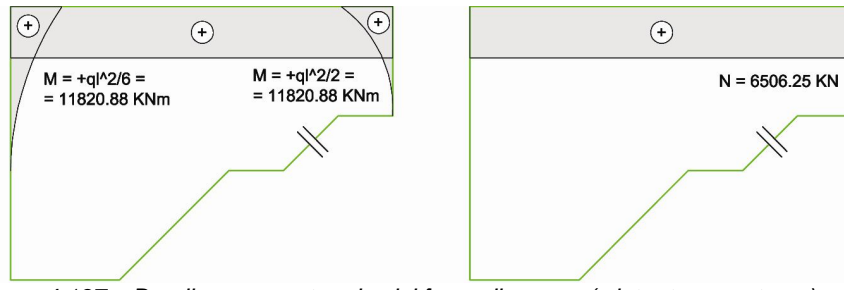


Figure 4.137 – Bending moment and axial force diagrams (winter temperatures)

Once mesh and actions are prepared, boundary points and points outside it are calculated according to the 2 theorems of L'Hermite's analogy (compare to Par. 7.4), used to obtain adequate boundary conditions.

The template of multipliers (Figure 7.40 in Annexes) can be applied to the grid, obtaining the final difference scheme of derivatives (Eq. (7.37) in Annexes). A system of algebraic linear equations with 16 unknowns is solved. The unknowns are values of Airy's stress function (applied to simplify the problem in only one unknown) and from them it is possible to calculate stresses in Cartesian coordinates, according to Figure 7.43 and Eq. (7.38), (7.39) of Annexes. The rotation from the original coordinate system allows then to compute principal stresses and their directions, as exhibited in Figure 4.138 and Figure 4.139.

4.7.1 Results

Principal stresses calculated at each node of the grid are plotted in following figures. Vectors are in relative scale, red colour indicates compression while blue means tension. Values lower than 50 Pa are neglected, while those bigger or equal to 1 MPa are represented with arrows.

The analysis using the difference of temperature between average (April) and summer (August) ($t = +17.14$ K) sees a maximum compression of -3.33 MPa at node "e", while node "n" shows the maximum tension of 0.20 MPa (Figure 4.138), due to geometric configuration and the secondary stress state caused by Poisson's ratio. For same reasons, tension appears also in nodes "10" and "11". As expected, the direction of minimum principal stresses is horizontal and their value is higher on the upper part of the breast wall, in which the constrains do not let a free expansion, that is instead allowed by the slides at the bottom of the structural element (where the free movement causes a condition of light tension in nodes "15", "16", "n", "o", "p", "r" as reaction to the main compression state).

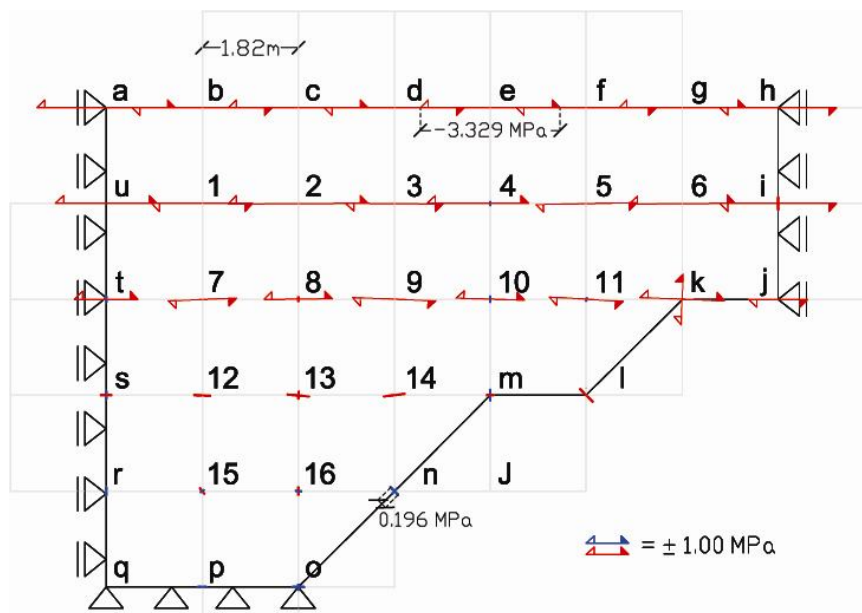


Figure 4.138 – Principal stresses direction (summer condition)

The analysis considering the temperature variation between average (April) and winter (February) (Figure 4.139) shows highest tension in node "e" (2.15 MPa) and maximum compression in node "s" (-0.20 MPa), due to geometry, constraints, and the secondary stress state caused by Poisson's modulus, as in nodes "10", "m", "n", "o", "p" and "r". Values are slightly lower than previous case (temperature variation is $t = -11.08$ K, lower than summer one) but the presence of persistent tensile state on the upper part of the wall, oriented in accordance with thermal load, is surely cause of damage. As already said, stresses are lower at the bottom due to the different configuration of constraints.

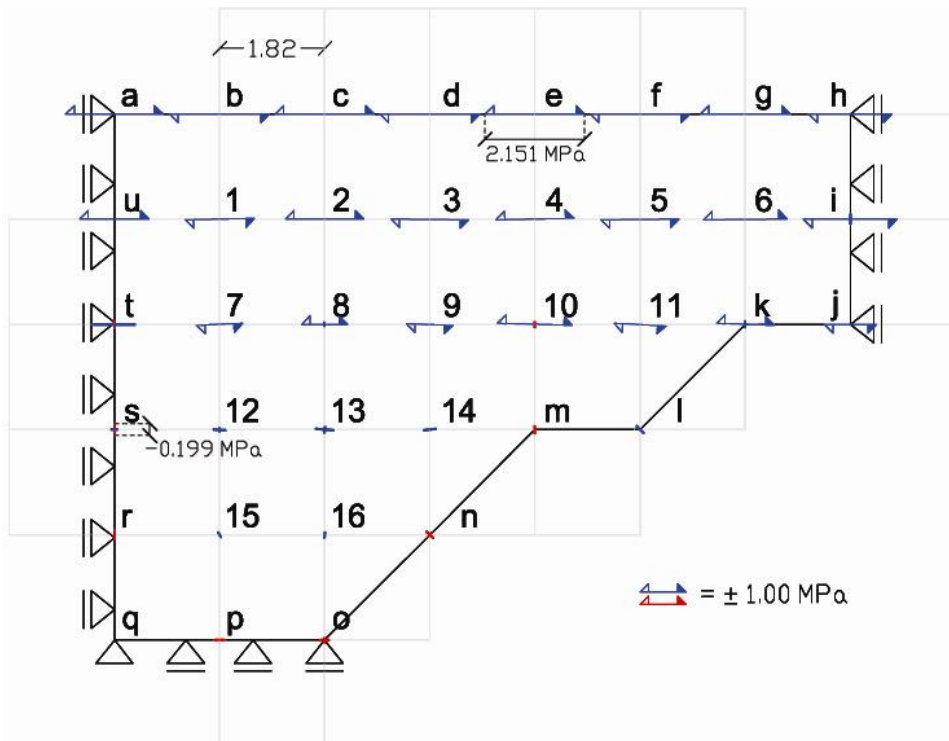


Figure 4.139 – Principal stresses direction (winter condition)

Cartesian and principal stresses are plotted on three representative wall sections: vertical lines "b"-“p" and "f"-“l", plus horizontal line "u"-“i", according to the nomenclature of Figure 4.139.

From both summer condition (Figure 4.140 – Figure 4.142) and winter condition (Figure 4.143 – Figure 4.145), it is possible to notice as the low presence of shear stresses (due to the choice of sliding as constraints) provokes a good correspondence between principal stress and respective in Cartesian coordinates.

According to expectations, summer condition graphs are dominated by compression (similarity between σ_x and σ_2) as well as in winter condition graphs, tension prevails (correspondence between σ_x and σ_1).

On the other hand, a similitude is the common trend to show higher results in the upper side, that go close to 0 at the bottom, effect of different boundary conditions in the two parts of the structure.

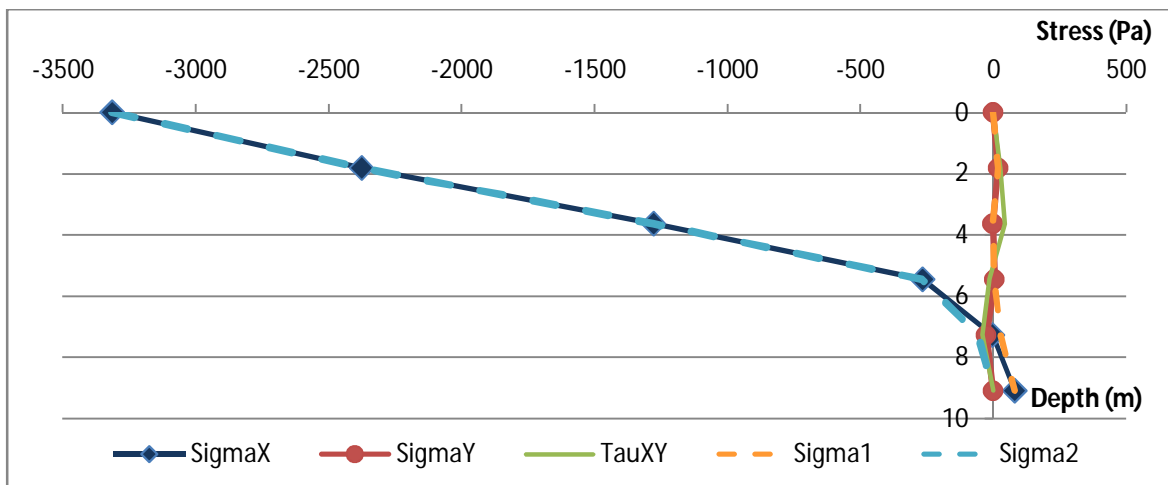


Figure 4.140 – Stresses in section line “b”-“p” (summer condition)

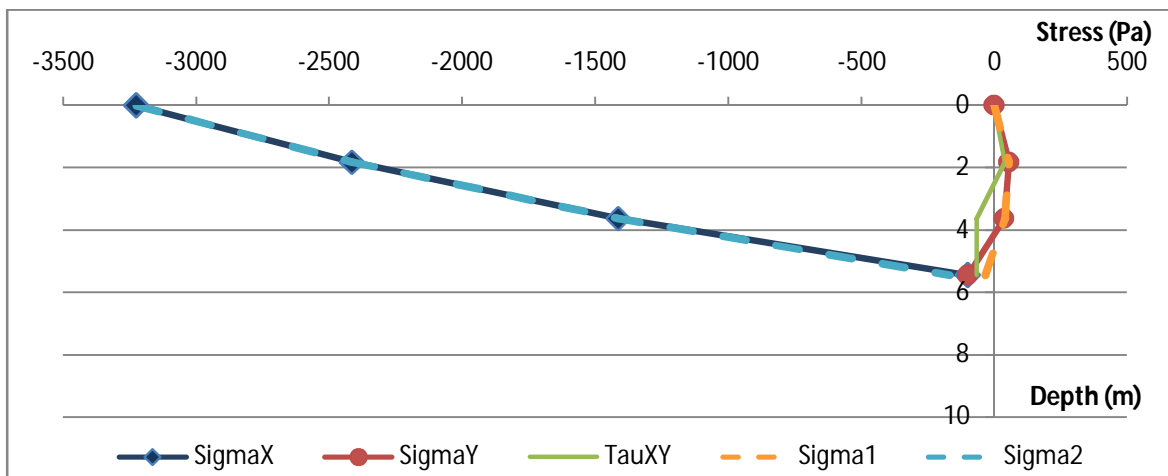


Figure 4.141 – Stresses in section line “f”-“l” (summer condition)

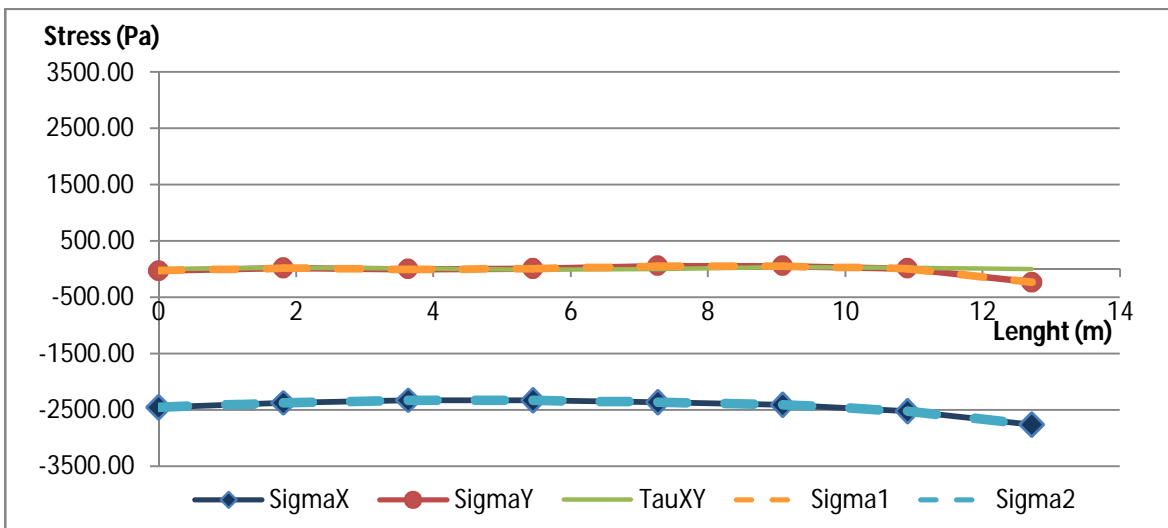


Figure 4.142 – Stresses in section line “u”-“i” (summer condition)

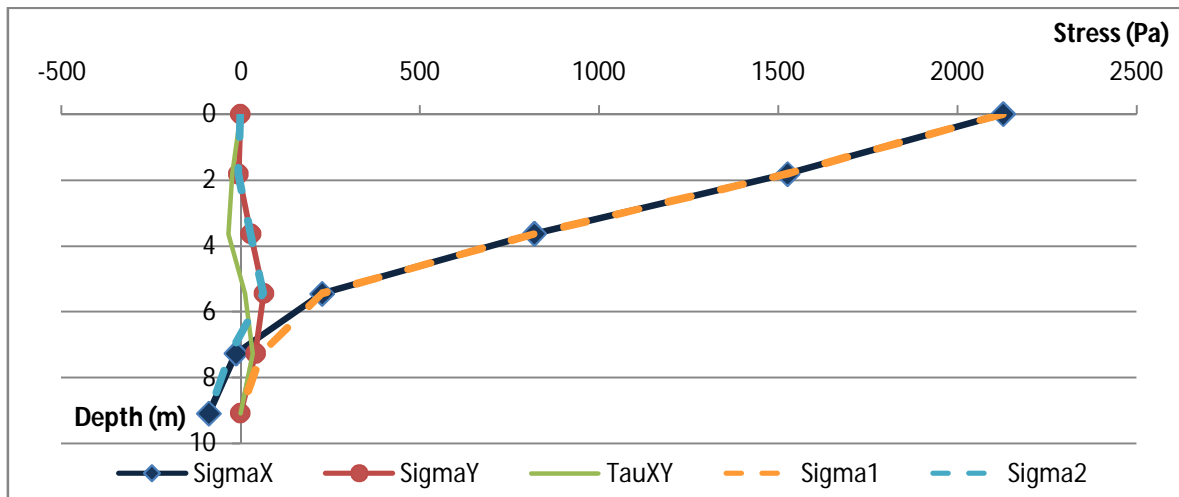


Figure 4.143 – Stresses in section line “b”-“p” (winter condition)

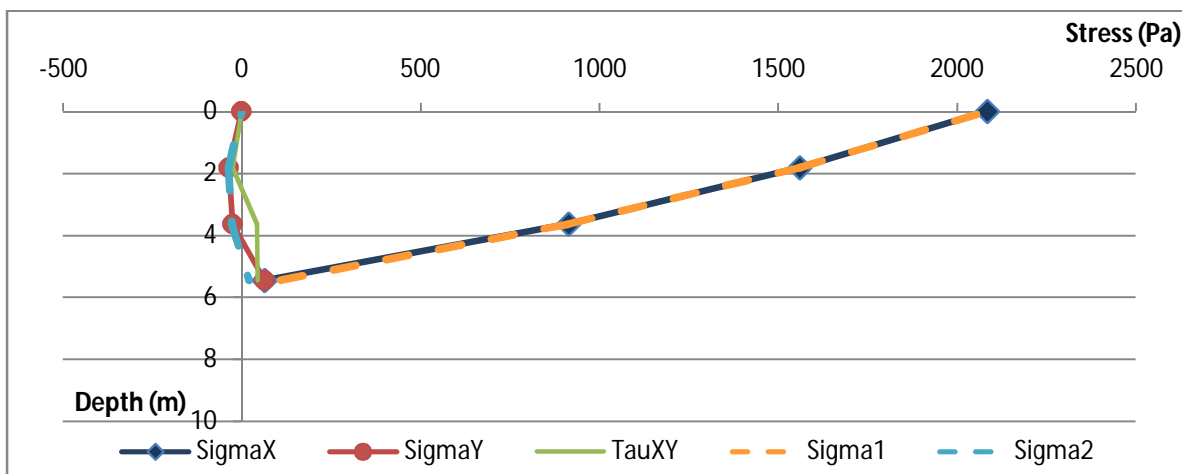


Figure 4.144 – Stresses in section line “f”-“l” (winter condition)

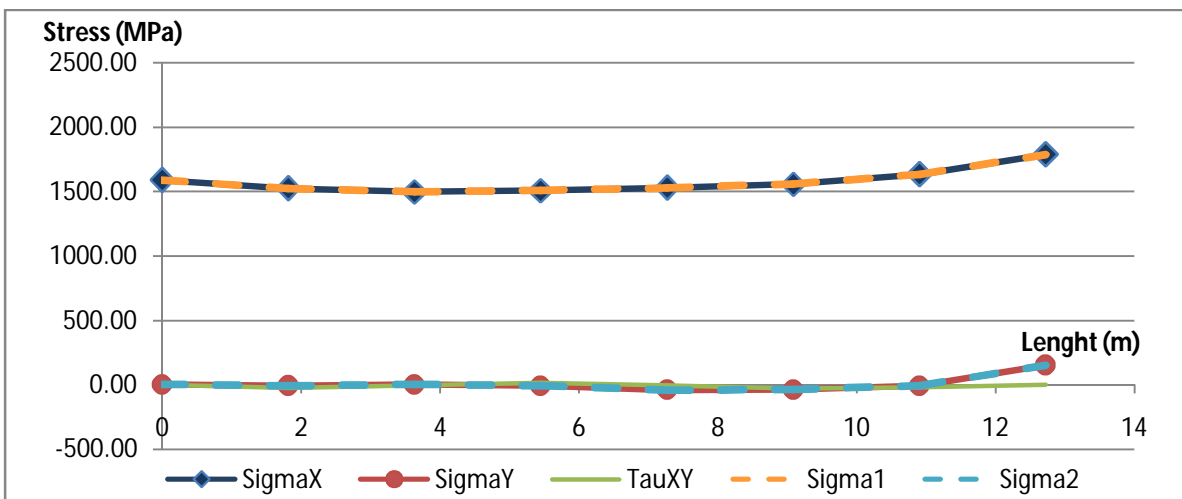


Figure 4.145 – Stresses in section line “u”-“i” (winter condition)

4.7.2 Comparison with finite element analysis

Being a linear elastic analysis, this computation cannot give exact address of cracks nucleation but the maximum tensile strength of stone masonry (assumed as 0.5 MPa in accordance with previous calculations) is overcome in all the upper part of the structure (till line "t"- "j") if winter temperature variation is considered. The redistribution of stresses due to appearance of damage can not be here simulated but the nucleation of cracks in the parapet is likely to be, precisely starting in correspondence of node "e", if the material is considered homogeneous.

Results are not easily comparable with the finite element linear elastic analysis (Par. 4.1.4) because, in the 3D model, the distribution of stresses on the breast wall is affected by the connection with the concrete slab (noticeable in the stripe of high stress concentration both in Figure 4.15 and Figure 4.17). Furthermore, in the FDM the stress state is strongly influenced by the set up of loading, and the rough mesh used surely brings to inaccuracy. However, the minimum principal stress calculated by FDM for summer configuration (-3.33 MPa) is close to the one obtained with Adina on breast wall/parapet (-4.0 MPa) in Comb. A, while the maximum principal stress here computed (0.20 MPa), is far from FEM analysis (0.75 MPa). Values obtained with FDM are lower because it can neither consider the interactions parapet-pier and breast wall-concrete slab, nor the effects of bridge breathing due to temperature loading. Anyhow, a comparison between Figure 4.138 and Figure 4.16, clearly shows the discordance in the high tension strip corresponding to the connection with the concrete slab, but it marks also another tension area, closer to the arch key, visible in both analysis.

On winter condition, Adina maximum tensile stress on the breast wall/parapet for Comb. B is about 3.0 MPa, comparable with present analysis (2.15 MPa) whereas the maximum compressive stress is -1.6 MPa, higher than FDM (-0.20 MPa). Again, the highest values of Adina can be related to the consideration of the relation between pier, parapet, breast wall and concrete slab.

Moreover, maximum stresses of the 3D model are localized mainly between parapet and pier (as effect of their relation and of bridge breathing), while in the simple numerical 2D model they are not affected by the critical section at the connection of the two elements, being placed on the upper boundary of the isolated wall.

The two methods are in agreement about the predominant stress for every temperature variation, while the FDM lacks of accuracy in the evaluation of the secondary stress state.

Another important consideration is that the temperature variation has been considered constant on all the body while it varies, mainly on the depth, as explained in Par. 7.4.1, where suggestions for the refinement of the finite difference method analysis are provided.

5 CONCLUSIONS

The practical outcomes of the presented analysis started from the acknowledgment that the structure is currently stable and safe and that the thermal loading has the highest impact on bridge behaviour. Precisely the slowing down of temperatures toward winter provokes the highest tensile stress state and therefore the biggest damage. As already underlined by (Zeman, 2008), considering the temperature cycle it can be noticed that this loading is not a threat for the stability of the structure (according to the used model, the maximum displacement does not reach 2.7 mm).

The results show the tendency of the structure to damage in agreement with real crack distribution observed directly in situ, mainly on arches 5th, 6th, 11th and 12th where the damage state is higher than arch 3th (the one represented in the model since the exact geometry was provided).

The last rehabilitation can be discussed because, according to the used FEM model, its effects are conflicting. The release of the connection between breast walls and concrete slab positively avoids the damage of the former, but the vertical dilatation joints (filled with plastic mortar) spare the damage on parapets concentrating it on breast walls (exactly underneath the joints). The bad aesthetic effect of degradation, visible by pedestrians on the bridge, is excluded but cracks concentrate in breast walls, where they are more dangerous and the blocks are difficult to replace.

The conclusion is that the damage related to thermal loading in the structure cannot be totally avoided. It is possible to change its distribution, trying to distance it from the weakest structural parts or just from the eye (as obtained with the last intervention). On the other side, the low maximum crack width (0.24 mm) computed for the actual bridge configuration states that the problem is mainly aesthetic and only the repetition of cycles with exceptional temperatures, combined with the presence of low quality blocks or mortar, can lead to clearly visible damage.

A final aspect to notice is that the initial condition of the FEM model (absence of damage) is slightly different from the real one, where some small cracks were still visible even after the rehabilitation and replacement of blocks, therefore the reliability of the model cannot be absolute.

5.1 Generalization and alternative solutions

The present research can provide useful results also for other similar analysis. The application of thermal loading through in situ recorded temperature values, then computed on all nodes of the model thanks to the thermal analysis, is an effective way to face the problem. Yearly recordings are required and results are subjected to chosen parameters for heat transfer: testing is necessary to obtain reliable values.

The one way coupled engineering approach allows to consider results of the thermal analysis in the mechanical one. This is influenced by the choice of mechanical parameters (and homogenization techniques) therefore, again, lab testing is a fundamental aspect for a trustable output.

As already highlighted, the intervention of 2007–2010 has both positive and negative aspects, but it is not possible to totally avoid thermal effects, even using further strategies. Generally, in the rehabilitation of an historic bridge, the original relatively flexible fillers in the body were strengthened or replaced with more rigid pavements, including also concrete slabs. The increase in rigidity as well as the tempt to link together different elements of the structure (vault-breast wall, breast wall-breast wall or slab-breast wall) can lead to changes in the structural behaviour and strain properties, as well as an higher sensitivity to non-stress effects, mainly temperature related (Witzany, 2008), hence to a reduction of the longevity.

In the case of transversal deformation of breast walls (in the direction inside the bridge), the concrete slab and the rigidity of the filling can create undesirable spacing effects, that cause shear cracks and shifting in wall joints. The insertion of a separation layer with low shear rigidity limits the mutual interaction and load transfer between different masonries both via shear forces and via deformations; the layer reduces the gradual growth of permanent strains in the structure (Witzany, 2008). The separation between body filler and breast walls (as well as between pavement layers and breast walls) through a continuous expansion joint (about 50 mm in width) would limit the transverse horizontal stresses on breast walls due to lateral pressures of filling layers, thus reducing transverse deformation and tilting. The expansion layer can be used also as ventilation system, in way to reduce the moisture content.

On this concept the intervention suggested by J. Witzany in 1997 is based, with the aim of bringing back the Monument to the original behavior of stone bridge vault construction. It would limit the mutual interaction of different elements of the bridge caused by volume changes (due mainly to temperature), reducing also the causes of chemical decay (decreasing moisture). This idea was successfully applied on the bridge deck in 2007-2010 intervention, when the arguable vertical dilatation joints in parapets were disposed too.

J. Witzany suggested also another separation, between the pavement structure and the downer body filling; even if difficult to realize in Charles Bridge, it is here quoted for its general relevance. It can be executed through a stratum yielding to shear, in way that the layers of the 1960s–1970s intervention can be laid onto the original structure in a flexible way (Figure 5.1).

These concept are not new, in fact more than 20 years ago the rigidity issue was already understood (Zak, 1995) and it was suggested to remove the concrete slab from Charles Bridge, creating joints of expanded clay concrete and embedding the granite paving in sand.

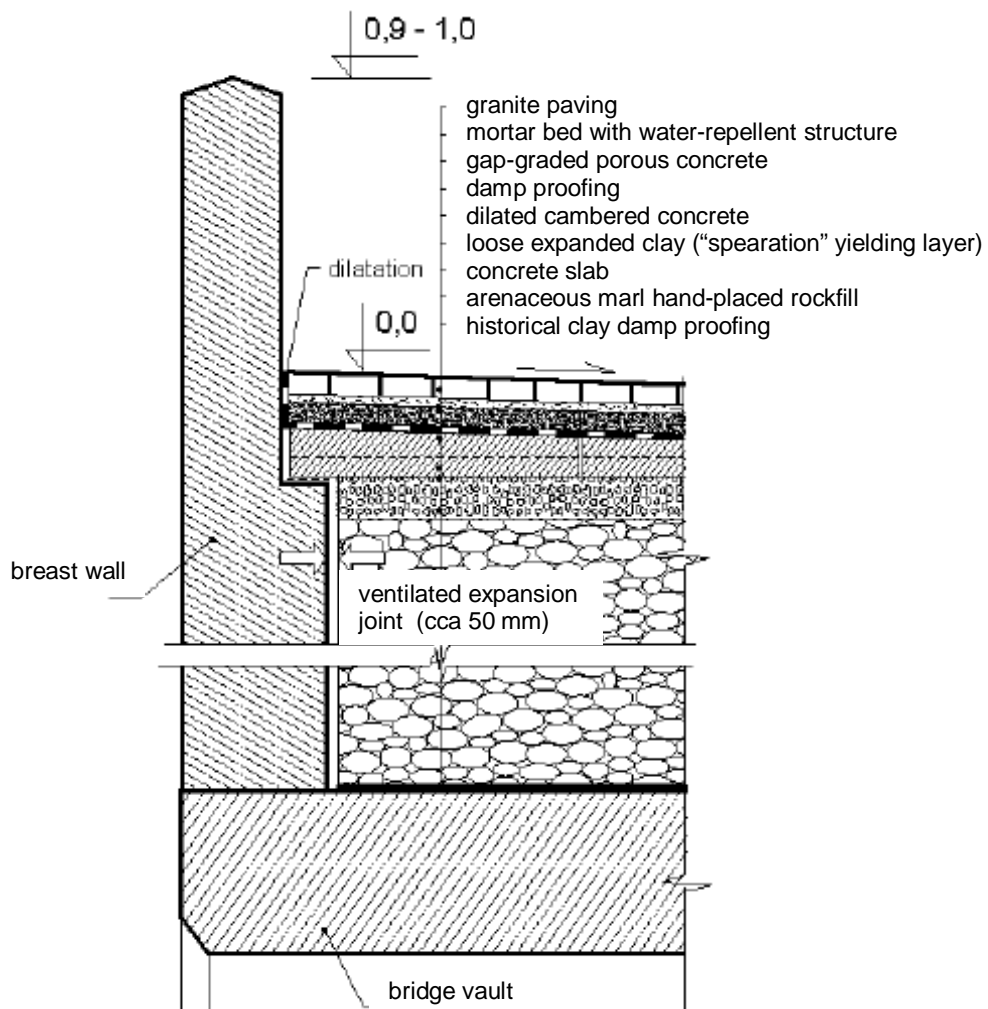


Figure 5.1 – Concept of reconstruction of stone bridge body (Witzany, 2008)

Furthermore, to increase the durability of the monument, a study about material conservation (Prikryl, 2011) suggests to:

- avoid chemical cleanings (that brought nitrates);
- entirely replace the decayed ashlar blocks that were maintained behind new stone and cement mortar, because they can severely decrease the mechanical properties of the sandwich-like block and they contain high concentration of water soluble salts;
- avoid the use of Portland cement mortar as binder (Czech Republic does not produce traditional hydraulic binders but they can be imported);
- use the stone varieties utilized in the Gothic construction (mainly Carboniferous arkoses); for doing this old quarries should be open again: (Prikryl, 2010) identified at least 2 potential sites where the quarrying could be possible.

The monument consists of approximately 60000 blocks and it has been estimated that around 15 % of them will need to be replaced, in a period of about 10 years.

Many observations done for Charles Bridge can be easily extended to similar masonry structures. Further generalization about bridges rehabilitation is provided in Par. 7.5 of the Annexes.

6 REFERENCES

- ADINA R & D, Inc. ADINA Structures - Theory and Modeling Guide, 2011.
- Z. P. Bažant, Nonlocal damage theory based on micromechanics of crack interactions. *Journal of Engineering Mechanics*, ASCE, 1994: 593-617.
- Z. Bergman, Charles Bridge Museum. (<http://www.charlesbridgemuseum.com/>), 2009.
- Český Hydrometeorologický Ústav, Portál ČHMÚ.
(http://www.chmu.cz/portal/dt?portal_lang=en&menu=JSPTabContainer/P1_0_Home), 2014.
- N. Gattesco, R. Franceschinis, V. Kristek, A. Kravtsov, J. Rimal. Strengthening Effectiveness of Ancient Masonry Bridges. *Bridge Maintenance, Safety, Management, Resilience and Sustainability – Biondini & Frangopol (Eds)*. Stresa: Taylor & Francis Group, London, ISBN 978-0-415-62124-3, 2012: 1055-1062.
- K. Ďurana, J. Maděra, R. Černý. Database of climatic data as a rewarding tool for inclusion of weather observations in computational service life assessments of historical buildings. *WITTransactions on the Built Environment*, 131: 245-256, 2013.
- ISKarluvMost. Karlův most IS. (<http://iskarluvmost.fsv.cvut.cz/>), 2010.
- M. Jirásek, Numerical Modeling of Deformation and Failure of Materials. Prague: Czech Technical University, 1998.
- L. Jurina, Strengthening of masonry arch bridges with “RAM” – Reinforced Arch. *Bridge Maintenance, Safety, Management, Resilience and Sustainability – Biondini & Frangopol (Eds)*. Stresa: © 2012 Taylor & Francis Group, London, ISBN 978-0-415-62124-3, 2012: 1063-1070.
- M. Kachanov, Effective elastic properties of cracked solids. *Conf-9305134*, Fischer-Tropsch Arch., 1995.
- M. Kachanov, On the effective elastic properties of cracked solids - Editor's comments. *Int J Fract* 146, 2007: 295-299.
- T. Koudelka, T. Krejci, J. Kruis. Modeling of building constructions in SIFEL environment. Prague: Czech Technical University, 2011.
- T. Krejci, J. Sejnoha. «Evolution of temperature and moisture fields in Charles Bridge in Prague, Computational prediction and measurement.» *International Journal of Architectural Heritage*, 2014.
- V. Křížek, V. Kristek, J. Římal. «Remedial Works and Repairs of Prague’s Historical Charles Bridge.» *Bridge Maintenance, Safety, Management, Resilience and Sustainability – Biondini & Frangopol (Eds)*. Stresa: © 2012 Taylor & Francis Group, London, ISBN 978-0-415-62124-3. 2012: 1071-1077.
- H. M. Kunzel, K. Kiessl. Calculation of heat and moisture trasfert in exposed building components. *Int. J. Heat Mass. Tran.* 40, 1997: 159-167.
- P. B. Lourenco, Computations on historic masonry structures. *Prog. Struct. Engng Mater.* 4, 2002: 301–319.
- Mott MacDonald, Partial report on Charles Bridge. Prague, 2011.

- Praha.eu. (<http://www.praha.eu/>), 2010.
- R. Prikryl, A. Šťastná. Contribution of clayey–calcareous silicite to the mechanical properties of structural mortared rubble masonry of the medieval Charles Bridge in Prague (Czech Republic). *Engineering Geology* 115, 2010: 257-267.
- R. Prikryl, Á. Török. Natural stones for monuments: their availability for restoration and evaluation. Geological Society, London, Special Publications v.333, 2010: 1-9.
- R. Prikryl, z. Weishauptova, M. Novotna, J. Prikrylova, A. St'astna. Physical and mechanical properties of the repaired sandstone ashlar in the facing masonry of Charles Bridge in Prague (Czech Republic) and an analytical study for the causes of its rapid decay. *Env. Earth Sci*, 63, 2011: 1623-1639.
- P. Prochazka, The Theory of Elasticity 20. Prague: CVUT, 1999.
- SAHC Advanced Masters Course. SAHC SA2 Notes on Damage Mechanics. Prague, 2008.
- J. Sejnoha, Z. Bittnar, M. Sejnoha, Z. Zeman, J. Novak, Z. Janda. Vypočet stavu napětí a porusení Karlova mostu v Praze. 2006.
- D. Shanberg, Charles Bridge (Karlův most). 2010. (<http://www.myczechrepublic.com/prague/>).
- SIFEL Group, SIFEL Theory. Prague: Czech Technical University, 2008. (<http://mech.fsv.cvut.cz/~sifel>)
- M. D. Smith, A Critical Analysis of Charles Bridge, Prague. Proceedings of Bridge Engineering 2 Conference 2008. Bath, 2008.
- Stirling Lloyd, Stirling Lloyd Products Inc. (www.stirlinglloyd.com), 2013.
- J. Sykora, J. Vorel, T. Krejci, M. Sejnoha, J. Sejnoha. Analysis of coupled heat and moisture transfer in masonry. *Materials and Structures* 42, 2009: 1153–1167.
- J. Sykora, T. Krejčí, J. Kruis, M. Šejnoha. Computational homogenization of non-stationary transport processes in masonry structures. *Journal of Computational and Applied Mathematics* 236, 2012: 4745–4755.
- J. Witzany, R. Zigler. The analysis of non-stress effects on historical stone bridge structures (monitoring, theoretical analysis, maintenance). *Journal of Civil engineering and Management*, Vol XIII, No 2, 2007: 157–167.
- J. Witzany, T. Cejka, R. zigler. Failure Resistance of Historic Stone Bridge Structure of Charles Bridge. II: Susceptibility to Floods. *Journal of Performance of Constructed Facilities*, Marc/April, Vol. 22, n.º 2, 2008: 83-91.
- J. Witzany, T. Cejka, R. zigler. Failure Resistance of the Historic Stone Bridge Structure of Charles Bridge. I: Susceptibility to Nonstress Effects. *Journal of Performance of Constructed Facilities*, Vol. 22, n.º 2, 2008: 71-82.
- J. Zak, D. Novak. Modelling of Charles Bridge in Prague: numerical analysis and statistical simulation. *Transactions on the Built Environment*, vol. 15, 1995: 303-310.
- J. Zeman, Jan Novák, M. Sejnoha, J. Sejnoha. Pragmatic multi-scale and multi-physics analysis of Charles Bridge in Prague. *Engineering Structures* 30, 2008: 3365-3376.

7 ANNEXES

7.1 Thermo-Elastic analysis

The elastic analysis was deeply studied in way to understand the structural behavior (before/after the last intervention) with a quick tool. The results, already shown in Par. 4.1 are here explained and commented in detail.

7.1.1 Comparison between Adina and SIFEL

Using the properties defined in Table 4.11 and Table 4.12 of Par. 4.1.7, a linear analysis is run with Adina (orange values) and with SIFEL (blue values), to compare the results. Considered outputs are:

- principal stresses due to only self-weight;
- principal stresses due to only temperature loading (“Temp.” lines in tables);
- principal stresses due to the combined effect of self-weight, temperature and live load (“Total” lines);
- vertical (Z) and transversal (X) displacements for all the upon mentioned cases.

The principal stresses are checked both in smoothed and un-smoothed form to evaluate the averaging process in the two software. Temperatures are considered with the four combinations defined in Par. 4.1.

From Table 7.1 and Table 7.2 it is possible to appreciate the accordance of displacements calculated by the two software while in Table 7.3 and Table 7.4 an error of 5-6% between the calculations emerges. The error is slightly higher if the smoothed stresses are considered.

Table 7.1 – Comparison of maximum displacements considering only selfweight (1975 model)

1975 Model		Self-weight Adina	
Displacement _{max} (mm)		Vertical (Z)	Transversal (X)
Adina		-0.75	-0.10
SIFEL		-0.75	-0.10
Inaccuracy		≈0.00%	≈0.00%

Table 7.2 – Comparison of maximum displacements for all the thermal combinations (1975 model)

1975 Model	Displ. _{max} in Comb. A (from average to summer)		Displ. _{max} in Comb. B (from average to winter)		Displ. _{max} in Comb. C (from winter to summer)		Displ. _{max} in Comb. D (from summer to winter)	
Case	Vert. (Z)	Transv. (X)	Vert. (Z)	Transv. (X)	Vert. (Z)	Transv. (X)	Vert. (Z)	Transv. (X)
Temp. Adina	3.42	1.25	-1.08	-0.60	4.40	1.76	-4.40	-1.76
Total Adina	2.65	1.31	-1.82	-0.61	3.64	1.74	-5.17	-1.77
Temp. SIFEL	3.42	1.25	-1.07	-0.60	4.44	1.73	-4.40	-1.73
Total SIFEL	2.65	1.31	-1.82	-0.60	3.63	1.72	-5.17	-1.75
Inaccuracy	≈0.00%	≈0.00%	-0.23%	≈0.00%	0.84%	-1.17%	≈0.00%	-1.17%
Average:-0.48%	≈0.00%	≈0.00%	≈0.00%	-0.81%	≈0.00%	-1.11%	≈0.00%	-1.16%

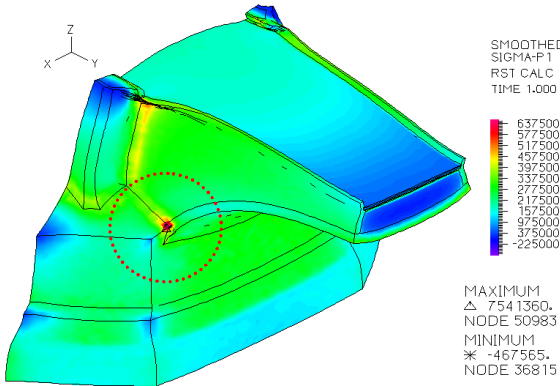
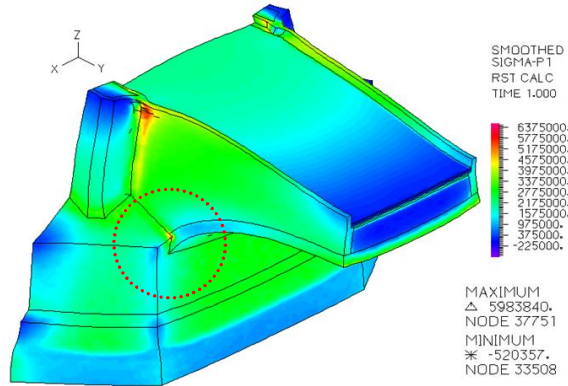
Table 7.3 – Comparison of max. principal stresses (unsmoothed) for combinations and temperature effects only

σ_P (MPa) unsmoothed	Self-weight	Comb. A only T	Comb. A	Comb. B only T	Comb. B	Comb. C only T	Comb. C	Comb. D only T	Comb. D
P1 _{max} Adina	0.83	2.62	2.57	11.34	7.93	4.04	3.99	16.61	15.10
P3 _{max} Adina	-3.37	-7.95	-8.73	-1.71	-2.02	-16.61	-20.06	-4.04	-4.10
P1 _{max} SIFEL	0.83	3.37	3.46	11.33	7.92	4.23	4.30	16.60	15.54
P3 _{max} SIFEL	-3.37	-7.95	-8.72	-1.71	-2.09	-16.60	-20.04	-4.23	-4.52
Inaccuracy	≈0.00%	28.83%	34.71%	-0.12%	-0.13%	4.70%	7.89%	-0.08%	2.91%
Average: 5.41%	≈0.00%	≈0.00%	-0.08%	≈0.00%	3.61%	-0.08%	-0.10%	4.70%	10.42%

Table 7.4 – Comparison of max. principal stresses (smoothed) for combinations and temperature effects only

σ_P (MPa) smoothed	Self-weight	Comb. A only T	Comb. A	Comb. B only T	Comb. B	Comb. C only T	Comb. C	Comb. D only T	Comb. D
P1 _{max} Adina	0.66	1.78	1.71	7.54	5.98	2.51	2.30	11.72	12.03
P3 _{max} Adina	-2.32	-7.95	-7.65	-1.33	-1.63	-11.72	-13.45	-2.51	-2.73
P1 _{max} SIFEL	0.66	2.16	2.03	7.60	6.62	2.62	2.41	13.22	13.65
P3 _{max} SIFEL	-2.40	-7.95	-7.65	-1.32	-1.63	-13.22	-13.67	-2.62	-2.84
Inaccuracy	≈0.00%	21.06%	18.21%	0.77%	10.75%	4.46%	4.70%	12.78%	13.43%
Average: 6.28%	3.72%	≈0.00%	≈0.00%	-0.64%	≈0.00%	12.78%	1.60%	4.46%	4.27%

From Table 7.3 and Table 7.4, it is possible to notice an “anomaly” about the maximum principal stress in combination B considering only temperatures (“Comb. B only T.”) happening in both software. The value (7.54 MPa for the smoothed case) has an higher gap from the stress considering also self-weight and live load (5.98 MPa) than in the other combinations. This effect is due only to temperature as can be confirmed by Figure 7.1 and it tends to disappear if also self-weight and live load are applied (red circle in Figure 7.2). The cause is likely in the sharp tetrahedral elements at the connection between pier and vault that provoked difficulties in the calculation of stresses or even before, in the original computation of temperatures.

Figure 7.1 – σ_1 (Comb. B, only temperature effects)Figure 7.2 – σ_1 (Comb. B)

The comparison between the two software shows really close displacements, and the averaged difference of results is adequate, but some cases reach inaccuracy of 30%. This is provoked by the different post-processing of values from really narrow elements generated by the automatic mesh in thin layers as the ones in the bridge deck (compare to Figure 7.3 and Figure 7.4, about an element in the fine grained concrete layer).

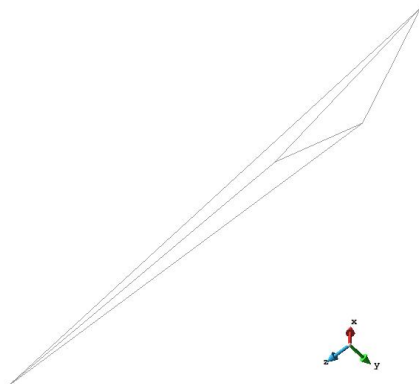


Figure 7.3 – Element No. 344566 (axonometric view)

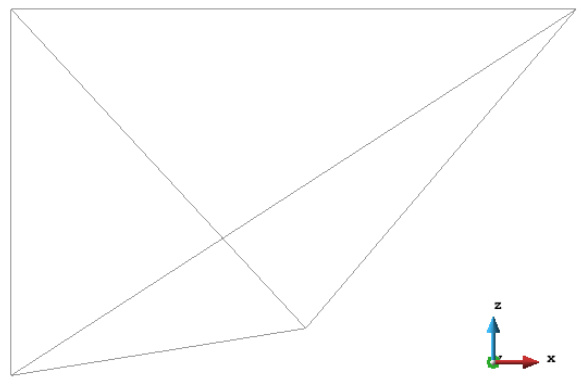


Figure 7.4 – Element No. 344566 (plane view)

Those elements are able to create high local concentrations of stress, especially if they are positioned at the boundary between two layers with different expansion coefficient. The case of Comb. A in the 1975 model was deeply analyzed, till understanding that element No. 344273 (Figure 7.5), location of the maximum value of principal tensile stress output of Adina (2.39 MPa) had the same value in SIFEL, but in this one it was overcome by the value in element No. 344565 (3.46 MPa), that is the already mentioned unreliable sharp mesh. It occurs also in other combinations and explains the anomalies. The post-processing algorithm used by Adina, likely averages peak values (so neglecting local stresses from narrow elements) while GiD, the post-processor used with SIFEL, considers them because it does not manipulate results.

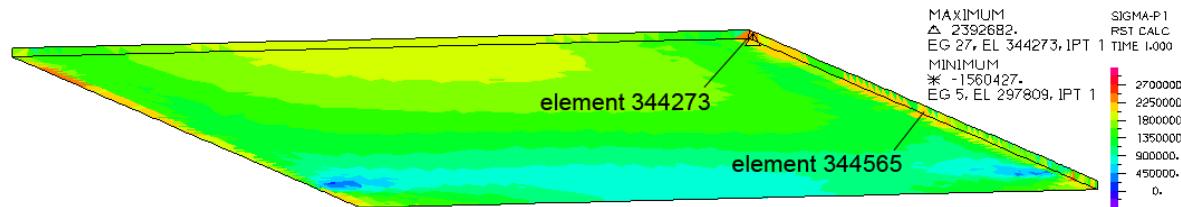


Figure 7.5 – Maximum principal stress in the fine grained concrete layer (Adina)

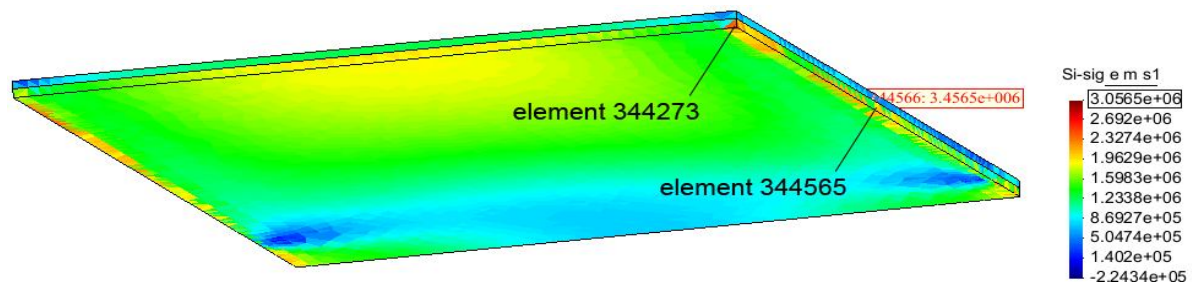


Figure 7.6 – Maximum principal stress in the fine grained concrete layer (SIFEL)

The comparison was carried out also for the 2010 model, obtaining the 0.5% of inaccuracy in displacements and less than 7% in smoothed principal stresses. The error was higher (27%) in the case of unsmoothed stresses since the formation of more groups with different thermal expansion coefficients and not plane contact surfaces aggravates the bad effects of the narrow elements, provoking high stress peaks. Since it is not possible to change the mesh (due to absence of geometry beyond it), the only way to lower this effect is to give closer values of thermal expansion coefficient in pavement layers (those where the narrow elements are more present).

7.1.2 Definitive properties and models comparison

The results of the model representing the last intervention can be compared with the 1975 configuration. It is possible to see that after the rehabilitation, the structure is less sensible to temperature changes, this allows to have 2% lower displacements and 5% lower principal stresses (smoothed). The lower displacement can be explained by the decrease of self-weight and by the absence of weak layers in the pavement (that would be represented by low Young Modulus, as explained at the end of the paragraph), while previous deck was degraded by water and salts. The most dangerous maximum principal stresses (Comb. B and Comb. D) do not vary significantly, what changes is the stress configuration. From the comparison between Figure 7.7 and Figure 7.8, it is evident that the “plastic mortar” joint decreases the stress at the connection between parapet and pier, especially in compression (red circles). The dilatation joint between concrete layers and railing let to avoid the tension at the whole side of the parapet (red rectangles), this is the positive effect of cutting the reinforcement connection that linked the two elements.

Similar outcome can be noticed also in Figure 7.9 and Figure 7.10 (comparison on Comb. D) but this time the avoided stress configuration along the parapet side is about compression state, since the previous connection obliged the stone masonry to follow the movement of the concrete slab (that has higher thermal expansion coefficient).

Comparing Figure 7.7 – Figure 7.10 with the stress plotting in Par. 4.1.6, it is evident an higher stress state in the parapet of the earlier mentioned images. This is the most evident effect of the chosen change in properties to approach the non-linear analysis. A pavement in granite blocks can be considered with really low elastic modulus (e.g., 1 GPa (Sejnoha, 2006)) since the blocks may move in their matrix but this would neglect the occurrence of cracks if the value were adopted in non-linearity.

Furthermore the pavement of the 1975 was fixed in a stiff cement mortar layer (and evaluated 14 GPa according to (Sejnoha, 2006)) while the intervention of 2007–2010 embedded the granite blocks in lime mortar with a sand substratum (requiring a lower elastic modulus, e.g. 7 GPa). Carefully looking to the colours of Figure 7.7 – Figure 7.10 it is possible to notice that the stresses on the pavement of 2010 model are lower than before, thanks to the mentioned elastic modulus and the dilatation layers at the contact with the parapet.

About the concrete layers in the deck, the 1975 configuration showed a fine grained concrete stratum (evaluated as 22 GPa of elastic modulus) and a lightweight (ceramsite) concrete layer comprising waterproofing and geotextile membrane (1 GPa, according to (Sejnoha, 2006)). The low value considers the interaction between the materials that were also in a bad conservation state (e.g., the waterproofing was failed and salts affected concrete). The stratigraphy after the last intervention includes a lightweight (levelling-draining) concrete layer whose elastic modulus is assumed 9 GPa, considering also the hydro-isolation that divides it from the lower layer. This is made of concrete with steel net, estimated in 16 GPa accounting the presence of the separation cloth on the slab side.

Since the contact with the producer did not bring to the exact properties of the materials added in the joints, acceptable values were chosen to model them (compare to Table 4.12 in Par. 4.1.7).

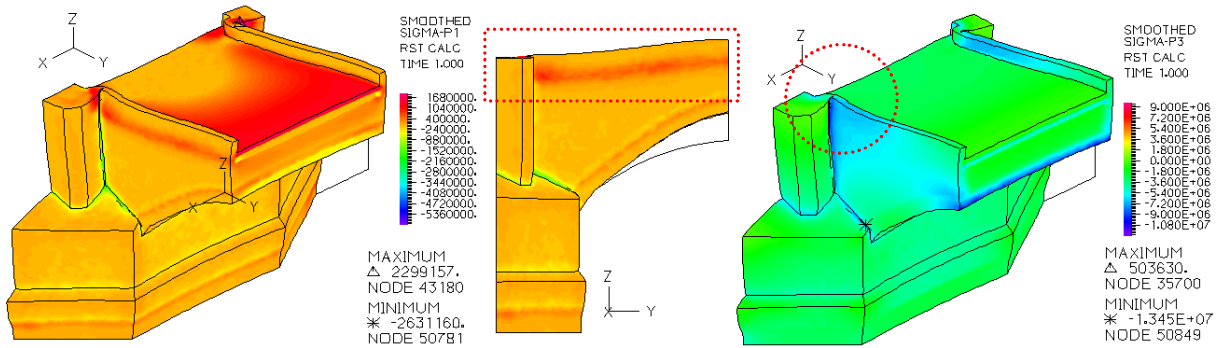


Figure 7.7 – 1975 model, Comb. C (from winter to summer), maximum and minimum principal stresses

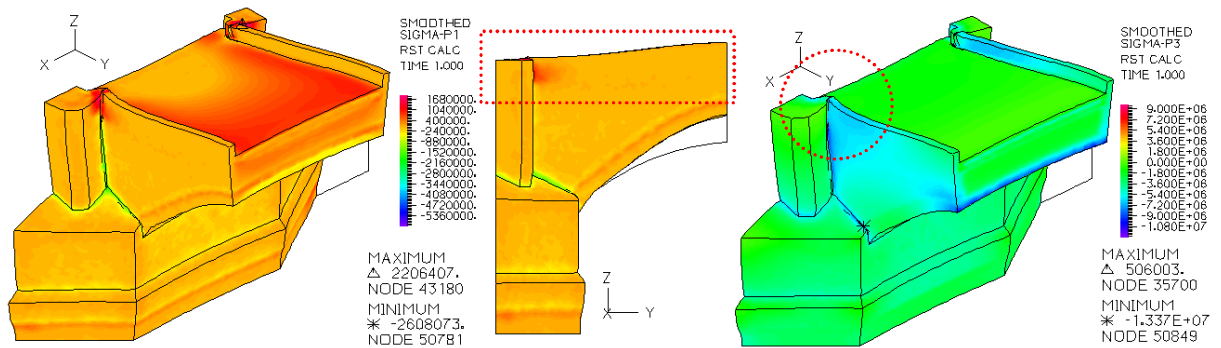


Figure 7.8 – 2010 model, Comb. C (from winter to summer), maximum and minimum principal stresses

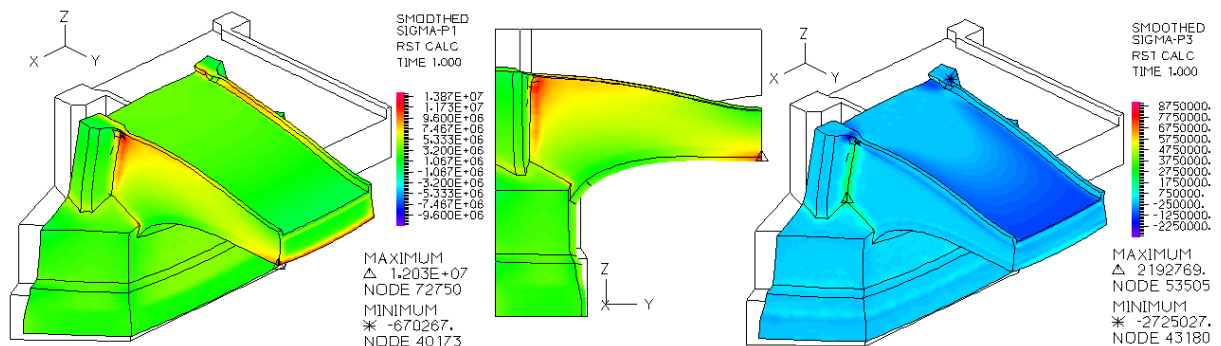


Figure 7.9 – 1975 model, Comb. D (from summer to winter), maximum and minimum principal stresses

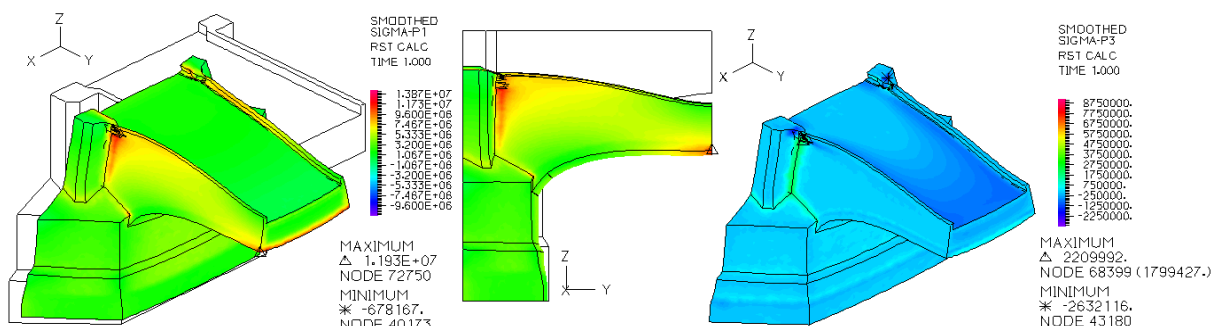


Figure 7.10 – 2010 model, Comb. D (from summer to winter), maximum and minimum principal stresses

7.1.3 Connection parapet – pier

The connection between the masonry of parapet and of pier is the position of highest stresses in the structure. As can be seen from Figure 7.11 and Figure 7.13, the increase of temperature "lifts" the arch crown compressing the parapet against the pier. This makes in them stresses according to the deformation in the images. The presence of the dilatation joint (Figure 7.12, Figure 7.14) is useful to relieve part of them with its deformation, therefore avoiding cracks in the masonry.

On the other hand, the decrease of temperature brings down the arch crown provoking tension at the keystone and at the connection parapet-pier. The movement deforms the railing toward the external side (Figure 7.15, Figure 7.17), creating tensile and compressive stresses that can be in part absorbed by the dilatation joint. The alternate deformation during seasons, creating tension on both sides of the parapet, is sure cause of cracks, as also it can provoke damage the stress band visible in Figure 7.11 at the connection between railing and concrete slab. The joints made in 2007–2010 in the parapet and between this and the pavement layers, are able to modify the behavior but with different levels of efficacy in different positions, as it will be explained during the non-linear analysis (Par. 4.2).

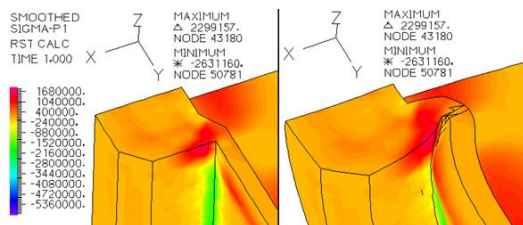


Figure 7.11 – σ_1 , Comb. C, 1975 model

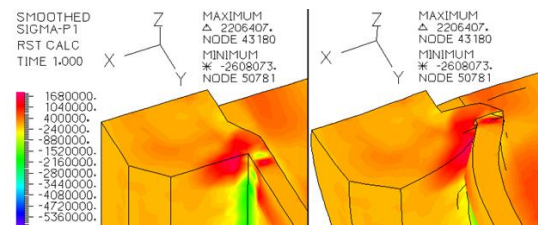


Figure 7.12 – σ_1 , Comb. C, 2010 model

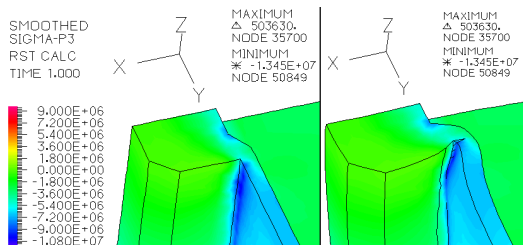


Figure 7.13 – σ_3 , Comb. C, 1975 model

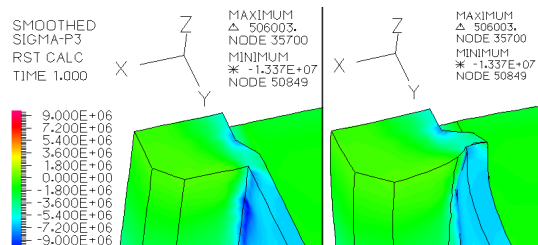


Figure 7.14 – σ_3 , Comb. C, 2010 model



Figure 7.15 – σ_1 , Comb. D, 1975 model

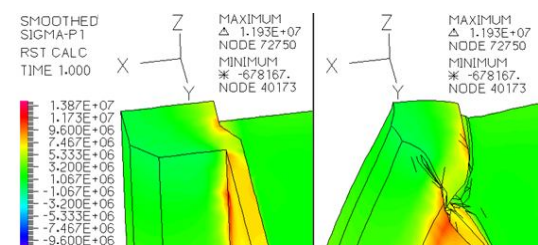


Figure 7.16 – σ_1 , Comb. D, 2010 model

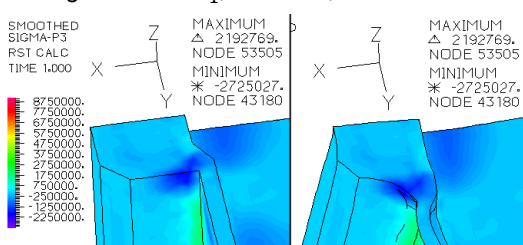


Figure 7.17 – σ_3 , Comb. D, 1975 model

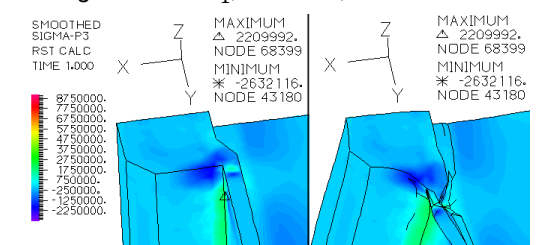


Figure 7.18 – σ_3 , Comb. D, 2010 model

7.2 Continuum damage mechanics

The damage is the reduction of strength and stiffness caused by propagation and interaction of defects (voids, cracks, delamination) that provoke loss of material integrity. Microstructural changes bring to a macroscale degradation of the material stiffness.

The focus is on quasi-brittle materials (as concrete and masonry), in them the evolution of strain brings to microcracks and microvoids; if the strain evolution continues, some microcracks localize in discrete cracks while the others stop to increase (localization of inelastic strains) (Koudelka, 2011). The phenomenon can be described by damage models that characterize density and orientation of microdefects toward (Jirásek, 1998):

- 1) an equation relating damage variables and apparent stiffness;
- 2) a loading function specifying the elastic domain (hence it says when the damage does not evolve);
- 3) a law governing the evolution of damage variables.

7.2.1 Isotropic scalar damage model

The isotropic scalar damage mode is the simplest damage model and it has only one (scalar) parameter. It starts from the assumption that the degradation is isotropic (stiffness modulus decreases proportionally in every direction, independently from the load direction) and that the Poisson's ratio is independent from the damage. Thanks to the second assumption it is not necessary to specify two damage variables (that would be necessary since the isotropic elastic material is characterized by two independent elastic constants) (Jirásek, 1998).

According to the model, the material can be in three states: virgin (no defects because it is still in elastic state), damaged or pseudo-undamaged (Koudelka, 2011). In the second one the nominal stress is considered to act on the original cross-section area while in the third one the effective stress acts on the undamaged area.

- 1) The damage stiffness tensor can be expressed as:

$$\mathbf{D}_s = (1 - \omega) \mathbf{D}_e \quad (7.1)$$

where \mathbf{D}_e is the elastic stiffness tensor (undamaged material), ω is the damage parameter ($\omega = A_d/A$, ratio between damaged area and total area) and \mathbf{D}_s is the secant stiffness relating total strain to total stress, according to:

$$\boldsymbol{\sigma} = \mathbf{D}_s : \boldsymbol{\varepsilon} = (1 - \omega) \mathbf{D}_e : \boldsymbol{\varepsilon} \quad (7.2)$$

- 2) A loading function is introduced to specify the elastic domain (and the states where damage evolves). The function f depends from the strain ε and a parameter k describing the evolution of the elastic domain. It is a scalar measure of the largest strain level ever reached in the material (if $\tilde{\varepsilon}_{n+1} > k_n$ then $k_{n+1} = \tilde{\varepsilon}_{n+1}$ else $k_{n+1} = k_n$). If $f(\varepsilon, k) < 0$, there is no damage, this appears when the state reaches the boundary of the elastic domain: $f(\varepsilon, k) \leq 0$, $k \geq 0$, $k f(\varepsilon, k) = 0$

- 3) Since they grow monotonically, k and ω can be explicitly related in their total values by the function g , that affects the shape of the strain-stress diagram, in form of:

$$\omega = g(k) \quad (7.3)$$

With this model the stress corresponding to a given evolution of strain can be easily evaluated.

It is possible to define the equivalent strain $\tilde{\varepsilon}$, that directly affects the shape domain (and relates real 3D cases with 1D models), in way to write the loading function as:

$$f(\boldsymbol{\varepsilon}, k) = \tilde{\varepsilon}(\boldsymbol{\varepsilon}) - k \quad (7.4)$$

Several loading surfaces (compare to (Jirásek, 1998)) can be obtained, according to different definitions of the equivalent strain:

- as the Euclidean norm of the strain tensor:

$$\tilde{\varepsilon} = \|\boldsymbol{\varepsilon}\| = \sqrt{\boldsymbol{\varepsilon} : \boldsymbol{\varepsilon}} = \sqrt{\varepsilon_{ij}\varepsilon_{ij}} \quad (7.5)$$

- as its energy norm:

$$\tilde{\varepsilon} = \sqrt{\frac{\boldsymbol{\varepsilon} : \mathbf{D}_e : \boldsymbol{\varepsilon}}{E}} = \sqrt{\frac{1}{E} D_{ijkl}^e \varepsilon_{ij} \varepsilon_{kl}} \quad (7.6)$$

Since microcracks grow mainly in tension, it is possible to take into account only positive normal strains, obtainin the equations:

$$\tilde{\varepsilon} = \|\boldsymbol{\varepsilon}\| = \sqrt{\langle \boldsymbol{\varepsilon} : \boldsymbol{\varepsilon} \rangle} \quad \text{or} \quad \tilde{\varepsilon} = \sqrt{\frac{\langle \boldsymbol{\varepsilon} : \mathbf{D}_e : \boldsymbol{\varepsilon} \rangle}{E}} \quad (7.7)$$

where $\langle \dots \rangle$ denotes the positive part of argument (Macaulay brackets):

for scalars $\langle x \rangle = \max(0, x)$ therefore $\langle x \rangle = x$ if $x > 0$; $\langle x \rangle = 0$ if $x < 0$

- as Rankine norm:

$$\tilde{\varepsilon} = \frac{1}{E} \max_{i=1,2,3} \langle \mathbf{D}_e : \boldsymbol{\varepsilon} \rangle_i \quad \text{or} \quad \tilde{\varepsilon} = \frac{1}{E} \|\langle \mathbf{D}_e : \boldsymbol{\varepsilon} \rangle\| = \frac{1}{E} \sqrt{\sum_{i=1}^3 \langle \mathbf{D}_e : \boldsymbol{\varepsilon} \rangle_{i=1}^2} \quad (7.8)$$

where $\langle \mathbf{D}_e : \boldsymbol{\varepsilon} \rangle_i$, $i = 1,2,3$ are positive parts of principal values of the effective stress tensor $\mathbf{D}_e : \boldsymbol{\varepsilon}$. The first equation is the Rankine criterion (continuous line in Figure 7.19) while the second rounds off the corners in the octants with more than one positive principal stress (dotted line in Figure 7.19) (Jirásek, 1998).

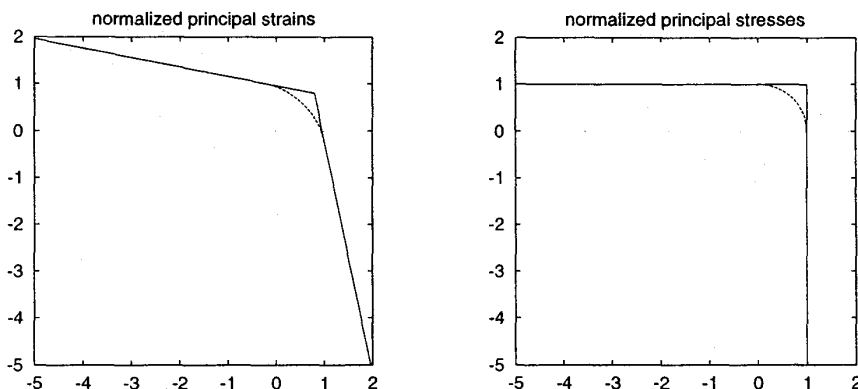


Figure 7.19 – Loading surface for Rankine definition of equivalent strain (Jirásek, 1998)

- as Mazars norm or Von Mises norm (SIFEL gr., 2008).

7.2.2 Isotropic scalar damage model: implementation in SIFEL

The isotropic damage model, used by SIFEL, holds only in tension and it is based on two relationships (SIFEL gr., 2008):

- relation between stress σ and crack opening u (one-dimensional case):

$$\sigma = f(u) = \sigma_t \exp\left(-\frac{u}{u_f}\right) \quad (7.9)$$

where σ_t is the tensile strength (in Pa) while u is the crack opening and u_f determines the initial slope of the softening branch.

- stress/strain relation:

$$\sigma = (1 - \omega)E\bar{\varepsilon} = (\bar{\varepsilon} - \varepsilon_e)E = \varepsilon_e E \quad (1D); \quad \sigma = (1 - \omega)\mathbf{D}_e : \bar{\boldsymbol{\varepsilon}} \quad (3D) \quad (7.10)$$

where ω is the damage parameter and $\bar{\varepsilon}$ is the strain without irreversible strains.

This damage model is “mesh sensitive” because, decreasing the element size, the dissipated energy decreases too. The implementation in SIFEL code of the method of the variable softening modulus is done to avoid it, in way to be able to assume the dissipated energy as material parameter, involving the characteristic element length into the damage evolution law (Koudelka, 2011).

The fracture energy is defined as:

$$G_f = \int_0^{\infty} \sigma_t e^{-\frac{u}{u_f}} du = \sigma_t u_f \quad (7.11)$$

and an additional condition is posed:

$$\varepsilon^e = \frac{\sigma_t}{E} < \frac{u_f}{h} \quad (7.12)$$

where ε^e is limit elastic strain and h expresses the generalized element size, defined as:

$h = l$ (length of the element, in 1D), $h = \sqrt{A}$ (area of the element, 2D) and $h = \sqrt[3]{V}$ in 3D.

Supposing $\tilde{\varepsilon} - \varepsilon_e \approx u/h$ (7.13) where $\varepsilon_e = \sigma/E$, it is possible to write (SIFEL gr., 2008):

$$\sigma = (1 - \omega)E\tilde{\varepsilon} = f\left(h\left(\tilde{\varepsilon} - \frac{\sigma}{E}\right)\right) \text{ from which:}$$

$$(1 - \omega)E\tilde{\varepsilon} = f(h(\tilde{\varepsilon} - (1 - \omega)E\tilde{\varepsilon})/E) \quad (7.14)$$

$$(1 - \omega)E\tilde{\varepsilon} = f(h\omega\tilde{\varepsilon})$$

$$0 = (1 - \omega)E\tilde{\varepsilon} - f(h\omega\tilde{\varepsilon}) \quad (7.15)$$

$$\text{and also: } (1 - \omega)E\tilde{\varepsilon} = f_t \exp\left(-\frac{h\omega\tilde{\varepsilon}}{u_f}\right) \quad (7.16)$$

Eq. (7.13) allows to smear the crack over the element, h is the characteristic element length and ω is the damage parameter. Combining Eq. (7.9), (7.10) and (7.13) it is possible to write Eq. (7.15) and Eq. (7.16), non linear equations for the damage parameter that can be solved by SIFEL using the Newton method.

According to (T. Koudelka 2011), in SIFEL the evolution damage law used for concrete (and quasi-brittle materials) is the formulation proposed by Papa and Talercio:

$$\omega = \frac{a(\varepsilon - \varepsilon_0)^b}{1 + a(\varepsilon - \varepsilon_0)^b} \quad (7.17)$$

where a and b are material parameters controlling peak value and softening branch, ε is the strain without irreversible strains and ε_0 is the strain threshold (after which the damage evolves).

Moreover, one of the most used equivalent strain $\tilde{\varepsilon}$ for quasi-brittle materials is the one defined by the Mazars' norm with principal strains ε_I :

$$\tilde{\varepsilon} = \sqrt{\langle \varepsilon_I : \varepsilon_I \rangle} = \sqrt{\sum_{I=1}^3 (\varepsilon_I)^2} \quad (7.18)$$

where the Macaulay brackets $\langle \dots \rangle$ indicate the selection of positive components (negative strains are neglected because crack in quasi-brittle materials are mainly provoked by tension). Eq. 7.18 can be written from $\tilde{\varepsilon} = \sqrt{\langle \varepsilon : \varepsilon \rangle}$ because the strain tensor is symmetric, therefore the positive part is a tensor having the same principal axes as the original one (with principal values replaced by their positive parts) (Jirásek, 1998).

7.2.3 Isotropic damage model for concrete

If a material has high ratio of compressive to tensile strength (as concrete), the simple isotropic damage model gives reliable results only for tensile failure. Experiments showed that concrete behavior in tension is almost linear up to the peak and that the subsequent non linear part of the $\sigma - \varepsilon$ diagram can be described by the exponential law:

$$\sigma = \sigma_t \exp\left(-\frac{\varepsilon - \varepsilon_0}{\varepsilon_f}\right) \quad (7.19)$$

where ε_0 is the strain at the elastic limit, $\sigma_t = E\varepsilon_0$ is the uniaxial tensile strength, and ε_f controls the post peak slope of the tensile $\sigma - \varepsilon$ curve and it can be related with the fracture energy or the material (Jirásek, 1998).

In compression, the concrete behavior is non-linear even before the peak and the total strain at peak stress is usually the double of the elastic strain.

A damage model specifically for concrete was designed by Mazars, using two damage parameters (instead of one as in the simplest damage model): ω_c (for compression) and ω_t (for tension), linearly combined in $\omega = \alpha_c \omega_c + \alpha_t \omega_t$ in way to have an independent control on the two curves. The coefficients α_c and α_t consider the character of the stress state.

7.2.4 Concrete damage model (Adina)

The material non-linearity is considered in the software through the “concrete material model”, valuable for 2D and 3D solid elements. Despite the name, its basic characteristics make the concrete model suitable for other materials. Due to the non-linearity, the stress-strain relation is linear only until the tensile failure (when critical stress happens). The general multiaxial stress-strain relations are derived from a uniaxial stress-strain relation $\tilde{\sigma}$ versus $\tilde{\varepsilon}$, where the curl symbol “~” identifies uniaxial qualities while the left superscript “ t ” refers to time t .

This is displayed in Figure 7.20 and it has 3 different strain phases: $\tilde{\varepsilon} \geq 0$; $0 > \tilde{\varepsilon} \geq \tilde{\varepsilon}_c$; $\tilde{\varepsilon}_c > \tilde{\varepsilon} \geq \tilde{\varepsilon}_u$. Specifically, $\tilde{\varepsilon}_c$ is the strain corresponding to the crushing stress $\tilde{\sigma}_c$ while $\tilde{\varepsilon}_u$ is the ultimate compressive strain.

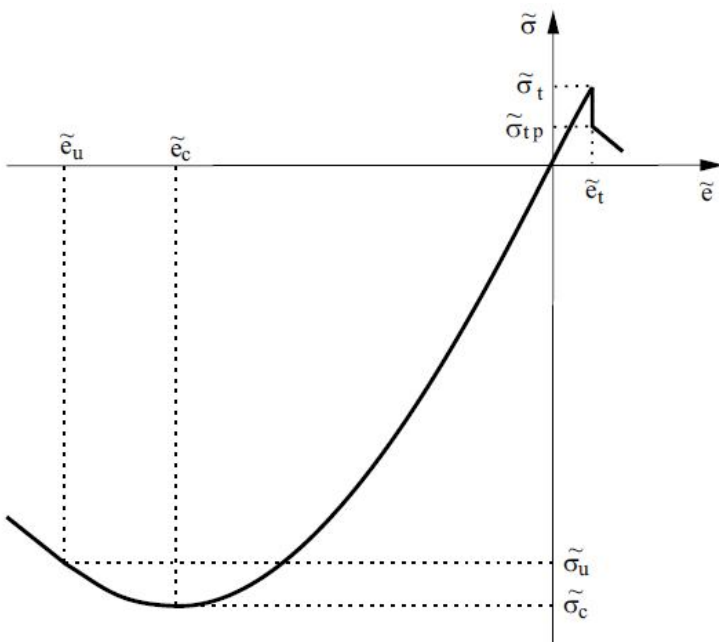


Figure 7.20 - Uniaxial stress-strain relation used in the concrete model (ADINA R & D, 2011)

Under multiaxial stress conditions, stress-strain relations are different whether the material is loading or unloading. Poisson's ratio is constant under tensile stress conditions but it can vary in the compressive region (ADINA R & D, 2011).

During unloading, the material is assumed to be isotropic while in loading it is considered orthotropic with the directions of orthotropy being defined by the principal stress directions. Once cracking occurs in any direction i , that direction is fixed from that point onward in calculating the principal stresses.

Tensile and compressive failure envelopes are used in Adina to establish the uniaxial stress-strain law accounting for multiaxial stress conditions, and to identify failure. For a complete description please compare to (ADINA R & D, 2011).

The post failure material behavior in the concrete model considers post tensile cracking (with open and closed cracks), post compression crushing, and strain softening behaviors.

7.2.5 Anisotropic damage model

Isotropic damage models have some deficiencies (Jirásek, 1998):

- using a proportional loading path in the stress space the ratio between individual strain components remain constant;
- if subjected to large extension in only one direction, the model loses stiffness in all the directions;
- the shape of the biaxial failure envelope is not realistic in the region of biaxial compression;
- no permanent strain is generated, hence unloading takes place to the origin.

To avoid these limitations, anisotropic damage models were developed.

The scalar isotropic damage model uses only one damage parameter, independently from principal direction and tension or compression. Therefore the parameter reduces the stiffness in every direction even if the limit strain is exceeded only in one principle direction. This is inaccurate because stiffness degradation is usually faster in the direction of largest stretching, making the macroscopic properties of the material turn in anisotropic. The disadvantage can be accepted if the stress state is mono-dimensional but not if it is three-dimensional. In this case it can be better described by an anisotropic damage model.

To take the anisotropy into account, the damage has to be tensorially represented. The general case uses an eight-order tensor Ω to transform the elastic stiffness D_e into the secant stiffness D_s of the damaged material:

$$D_{ijkl} = D_{ijkl}^e - \Omega_{ijklpqrs} D_{pqrs}^e \quad (7.20)$$

In particular, most of the successful anisotropic damage models deal with effective stress or strain, defined with one of the following principles (Jirásek, 1998):

- principle of strain equivalence (dealing only with effective stress);
- principle of stress equivalence (dealing only with effective strain);
- principle of energy equivalence (dealing with both stress and strain).

By simplification the effective quantities are used to reflect the conditions in the bulk material between microcracks and microvoids. Thanks to the effective quantities it is possible to specify the link between apparent and effective stresses or strains instead of that between elastic and damaged stiffnessess.

In general, starting from the already expressed formulation (Eq. 7.2):

$$\sigma = (1 - \omega) D_e : \epsilon$$

it is possible to introduce the damage tensor Ω and use it instead of the scalar damage parameter ω :

$$\sigma = (I - \Omega) : D_e : \epsilon \quad (7.21)$$

In this way the secant stiffness D_s would be generally not symmetric, which is thermodynamically inadmissible (Jirásek, 2008).

$$D_s = (I - \Omega) : D_e \quad (7.22)$$

To ensure symmetry of the resulting stiffness tensor, the principle of energy equivalence can be used and the density of complementary energy of the undamaged material subjected to stress σ is:

$$W^*(\sigma) = \frac{1}{2} \sigma : C_e : \sigma \quad (7.23)$$

The density of complementary energy of the damaged material is:

$$W^*(\boldsymbol{\sigma}) = W_e^*(\bar{\boldsymbol{\sigma}}) = \frac{1}{2} \bar{\boldsymbol{\sigma}} : \mathbf{C}_e : \bar{\boldsymbol{\sigma}} = \frac{1}{2} \boldsymbol{\sigma} : \mathbf{M}^T : \mathbf{C}_e : \mathbf{M} : \boldsymbol{\sigma} = \frac{1}{2} \boldsymbol{\sigma} : \mathbf{C}_s : \boldsymbol{\sigma} \quad (7.24)$$

where the damaged compliance tensor $\mathbf{C}_s = \mathbf{M}^T : \mathbf{C}_e : \mathbf{M}$ is always symmetric, independently of the properties of $\mathbf{M}(\Omega)$. The damage can be characterized by a symmetric second-order tensor Ω , described by 3 principal values Ω_1 , Ω_2 , and Ω_3 , and by the corresponding principal directions. The normal effective stresses can be expressed, in the principal damage coordinate system, as:

$$\bar{\sigma}_{11} = \frac{\sigma_{11}}{1-\Omega_1}; \quad \bar{\sigma}_{22} = \frac{\sigma_{22}}{1-\Omega_2}; \quad \bar{\sigma}_{33} = \frac{\sigma_{33}}{1-\Omega_3} \quad (7.25)$$

Thanks to calculation expressed in (Jirásek, 1998) it is possible to define the secant stiffness tensor \mathbf{D}_s (in way that the calculation of \mathbf{M} by inverting \mathbf{M}^{-1} is not necessary) as:

$$\mathbf{D}_s = \mathbf{M}^{-1} : \mathbf{D}_e : \mathbf{M}^{-T} \quad (7.26)$$

According to the introduction to Ch. 7.2, the definition of an equation relating damage variables and damage stiffness (or compliance tensors) is one of the three requirements of a damage model. The other two (loading function and damage evolution law) are to provide too (Jirásek, 1998).

7.2.6 Implementation in the software (SIFEL)

The anisotropic damage model requires many internal variables, and the laboratory measurements for them can be difficult. To avoid this a simplified (orthotropic) version was developed, based on 6 material parameters (half for tension and half for compression).

The model is based on the stress-strain relation:

$$\sigma_\alpha = (1 - H(\hat{\varepsilon}_\alpha)\omega_\alpha^t - H(-\hat{\varepsilon}_\alpha)\omega_\alpha^c) \left[\left(K - \frac{2}{3}G \right) \bar{\varepsilon}_{vol} + 2G\bar{\varepsilon}_\alpha \right] \quad (7.27)$$

where the index α is referred to the principal components of the given quantity, H is the Heaviside function, K is the bulk modulus, G is the shear modulus, $\bar{\varepsilon}$ is the strain vector written in tensorial form and ω_α^t , ω_α^c are the 2 sets of damage parameters, for tension and compression respectively. For them many evolution laws can be used, two are chosen in SIFEL. The first law is:

$$\omega_\alpha^\beta = \frac{A_\beta \left(|\bar{\varepsilon}_\alpha^\beta| - \bar{\varepsilon}_0^\beta \right)^{B\beta}}{1 + A_\beta \left(|\bar{\varepsilon}_\alpha^\beta| - \bar{\varepsilon}_0^\beta \right)^{B\beta}} \quad (7.28)$$

where A_β , B_β and $\bar{\varepsilon}_\alpha^\beta$ are material parameters in which β represents indexes t or c (tension or compression) and A controls the stress peak of the softening branch.

The law gives better results for compression but it has more difficult determination of material parameters than the second law, that counts the correction of the dissipated energy with respect to the size of the mesh elements and it works better for tension:

$$(1 - \omega_\alpha^\beta) E |\bar{\varepsilon}_\alpha^\beta| = f_\beta \exp \left(-\frac{D_\alpha^\beta h |\bar{\varepsilon}_\alpha^\beta|}{w_{cr0}^\beta} \right) \quad (7.29)$$

It is a non linear equation solved by Newton method, where f_β is the tensile or compressive strength, h the length of one element, while w_{cr0}^β counts the initial slope of the softening branches.

7.3 Non-linear analysis

7.3.1 Low-speed dynamics (feature of Adina)

Since the temperatures were computed in another software, they could be introduced in Adina as initial-final values (hence in one only step) or from an external mapping file (*.map) modified by hand to accomplish external values. The second way allowed to run a non-linear static analysis and 26 temperature steps were created (by hand) from the initial temperatures. This intricate procedure alone did not let to reach convergence, not even modifying the convergence criteria: the use of a low speed dynamics option was required. The technique allows to overcome convergence difficulties including dynamic effects in a static problem, adding inertia and stiffness proportional damping. Adina solves:

$$\alpha \mathbf{M}^{t+\Delta t} \ddot{\mathbf{U}}^{(i)} + \mathbf{C}^{t+\Delta t} \dot{\mathbf{U}}^{(i)} + {}^{t+\Delta t} \mathbf{K}^{(i-1)} \Delta \mathbf{U}^{(i)} = {}^{t+\Delta t} \mathbf{R} - {}^{t+\Delta t} \mathbf{F}^{(i-1)} \quad (7.30)$$

where \mathbf{M} is the mass matrix and α is a mass scaling factor (namely low-speed dynamics inertia factor, left 1.0 as default) to account for the dynamic inertia effect. \mathbf{U} is the vector of unknowns of displacement, \mathbf{R} is the vector of externally applied load and \mathbf{F} is the consistent nodal force vector (corresponding to element stresses due to displacement vector) (ADINA R & D, 2011). About indexes, t is temperature while i is related to the iteration number in the numerical iterative method (here Newton-Raphson method). The damping matrix $\mathbf{C} = \beta \mathbf{K}$ is formed by the initial total stiffness matrix (0 initial displacements) and the parameter β (namely low-speed dynamics damping factor) modified to reach convergence, therefore stiffness proportional damping was added to the problem. Since the required modification is substantial (it was impossible to follow the recommendation to use a time step size of at least $10^5 \beta$) an inaccuracy in the results is expected.

The incrementation by 5 times of the default damping factor (1×10^{-4}) was sufficient to reach the convergence but many trials were executed even with higher coefficients to study the feature. According to executed simulation on small 2D and 3D problems and comparisons in the results of the whole model run with different low speed dynamics options, the error is close to 5%.

The non-linear analysis is a sensitive tool and the change of low-speed dynamics damping factor affects the final result. An example of what can happen in the tensile stress plot, running the analysis modifying only the damping factor in 5×10^{-4} , 1×10^{-3} and 3×10^{-3} is exhibited in Figure 7.21: even if the final results have a discordance lower than 5%, the areas where the energy is released on the pavement (after reaching the maximum tensile strength) are different in number and configuration.

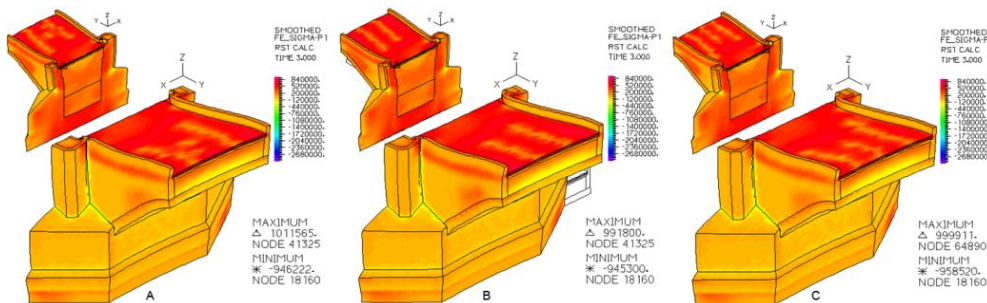


Figure 7.21 – Different configurations of max. princ. stress due to the use of low-speed dynamics damping factor

7.3.2 Comparison: one year cycle and computation from average values (SIFEL)

Results from the computation with 7 steps (representing a cycle of one year, in Par. 4.5) are compared with the previous analysis between average to summer/winter values of temperature (Par. 4.4), the same orthotropic damage model was used for both. Plottings are in the same scale and captions contain the comparative figure.

The analysis marks the lower crack width in direction P1 on 26/08/2011 (one year cycle, Figure 7.22) in respect to that from average to summer (1975 model), effect of the computation divided in steps.

While crack width in P1 and P2 directions (1975 model) about 12/02/2012 (one year cycle, Figure 7.28, Figure 7.30) shows higher results (structure is already weakened) as already said in Par. 4.5.

Moreover, the undeformed lateral elevations of 2010 model, related to summer step in both analysis (Figure 7.26, Figure 7.27), are shown in way to underline that the most damaged area is at the bottom of the dilatation joint, particular difficult to see in the deformed shape.

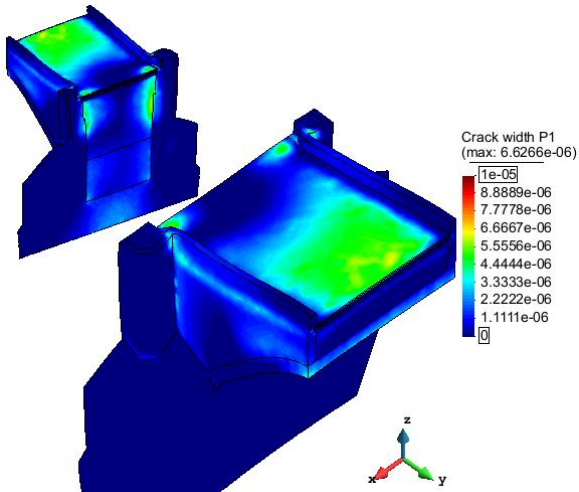


Figure 7.22 – Crack width P1 (1975 model), 26/08/2011
(compare to Figure 4.77)

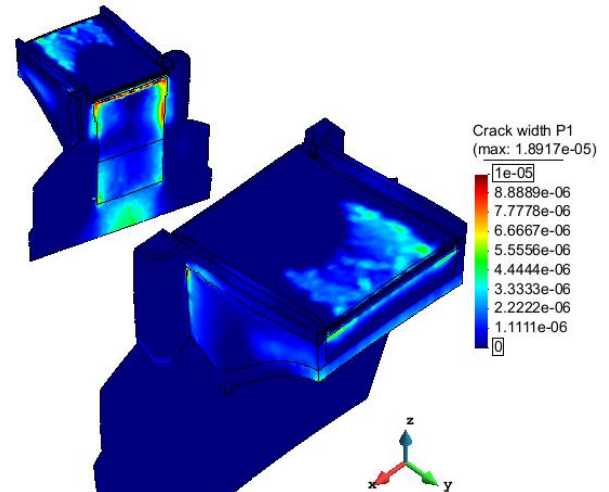


Figure 7.23 – Crack width P1 (2010 model), 26/08/2011
(compare to Figure 4.78)

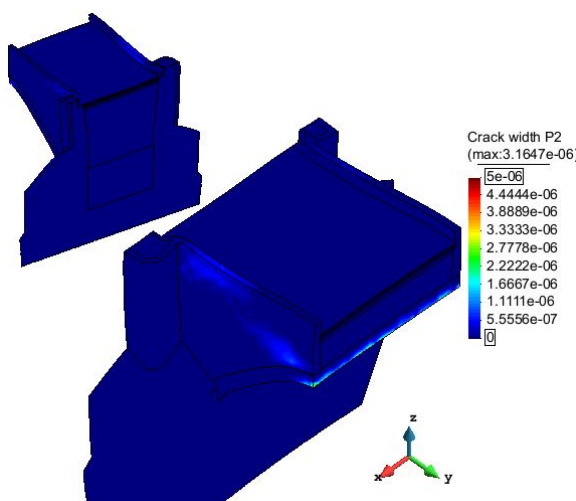


Figure 7.24 – Crack width P2 (1975 model), 26/08/2011
(compare to Figure 4.79)

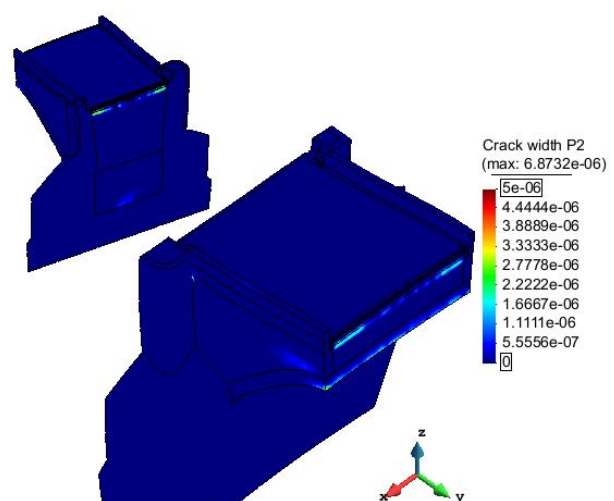


Figure 7.25 – Crack width P2 (2010 model), 26/08/2011
(compare to Figure 4.80)

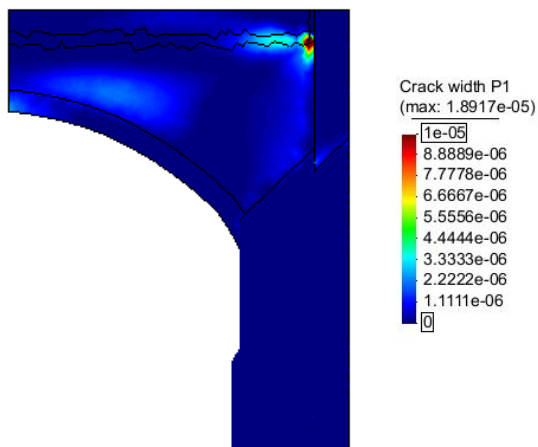


Figure 7.26 – Crack width P1 (2010 model), 26/08/2011
Underformed lateral elevation

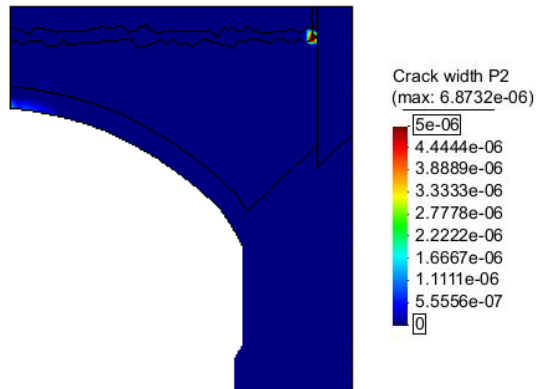


Figure 7.27 – Crack width P2 (2010 model), 26/08/2011
Underformed lateral elevation

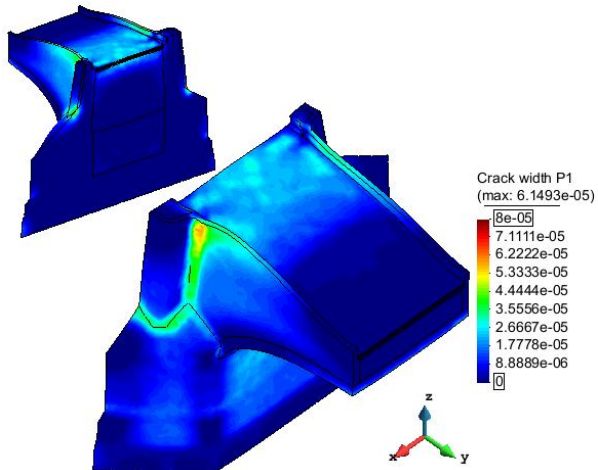


Figure 7.28 – Crack width P1 (1975 model), 12/02/2012
(compare to Figure 4.91)

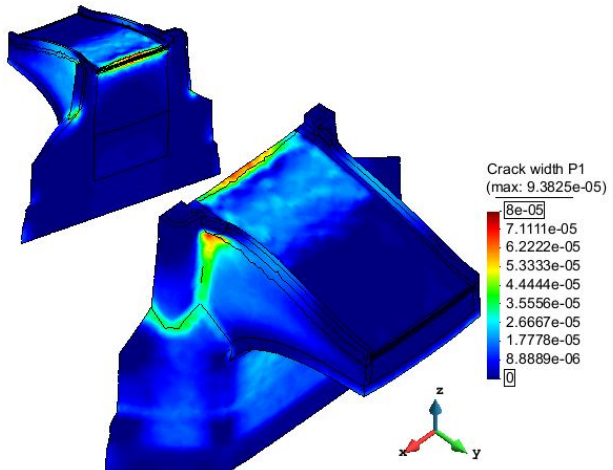


Figure 7.29 – Crack width P1 (2010 model), 12/02/2012
(compare to Figure 4.92)

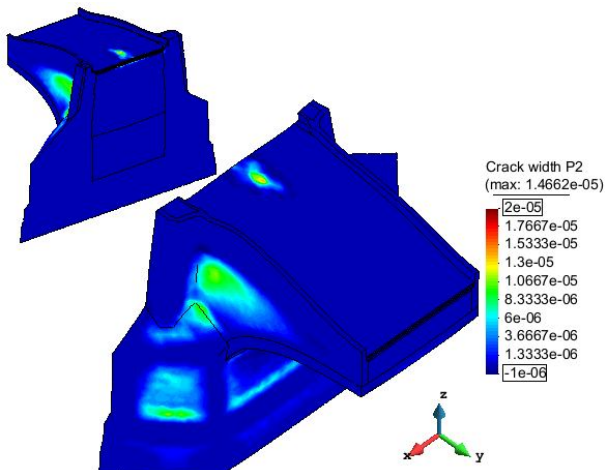


Figure 7.30 – Crack width P2 (1975 model), 12/02/2012
(compare to Figure 4.93)

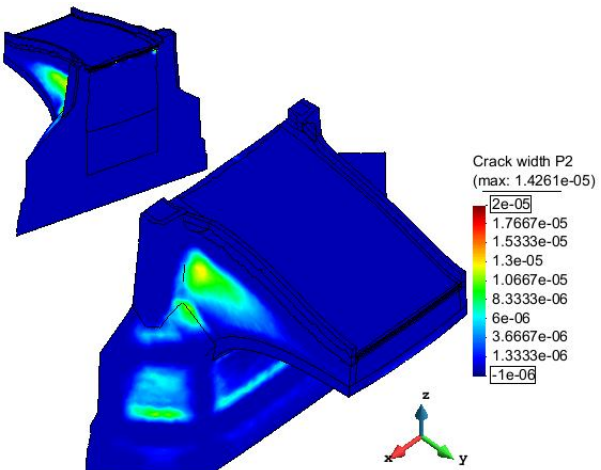


Figure 7.31 – Crack width P2 (2010 model), 12/02/2012
(compare to Figure 4.94)

7.3.3 Temperature steps

Temperature evolution on two years for noticeable nodes is provided in Figure 7.32. The nodes were already highlighted (and localized on the model) in Par. 4.1.1 and they are: number 890 (maximum summer temperature), 18978 (minimum summer temperature), 29195 (maximum winter temperature), 64852 (minimum winter temperature and maximum variation between average and winter), and 72535 (maximum variation between average and summer); for their values please compare to Table 4.1. Superficial nodes are sensitive to sun radiation, having fast daily oscillations, while inner points are not, receiving heat for conduction and therefore gradually changing value, with lower and smoothed peaks (reached in delay in respect to superficial points).

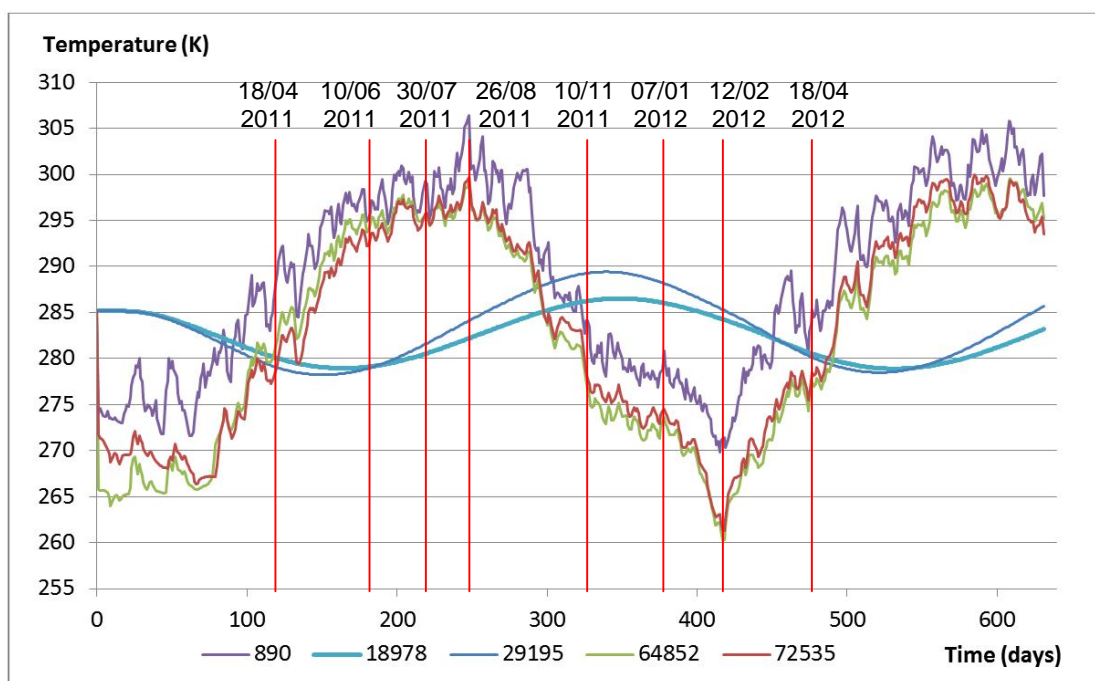


Figure 7.32 – Temperature evolution for representative nodes

Temperature evolution on the model for the one year cycle analysis is shown in following figures. To accelerate the thermal analysis, the model was divided in sub-domains, here visible in the irregular black lines.

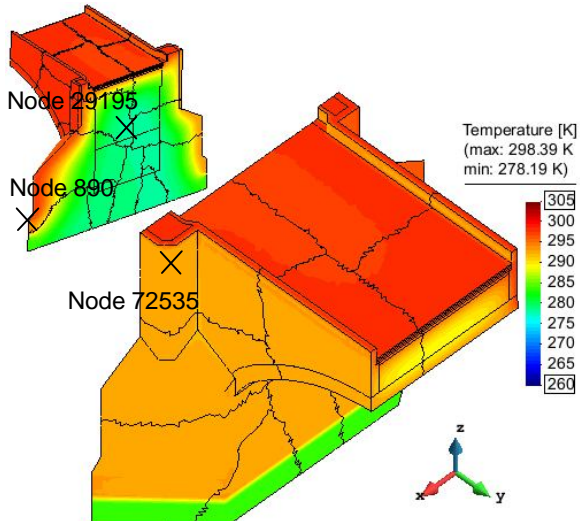


Figure 7.33 – Temperature values on 10/06/2011

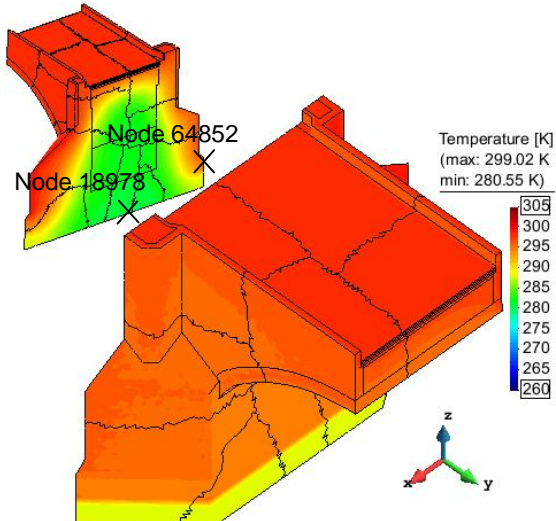


Figure 7.34 – Temperature values on 30/07/2011

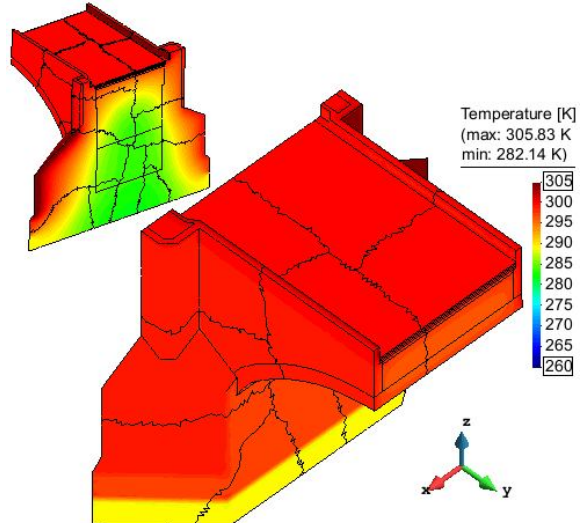


Figure 7.35 – Temperature values on 26/08/2011

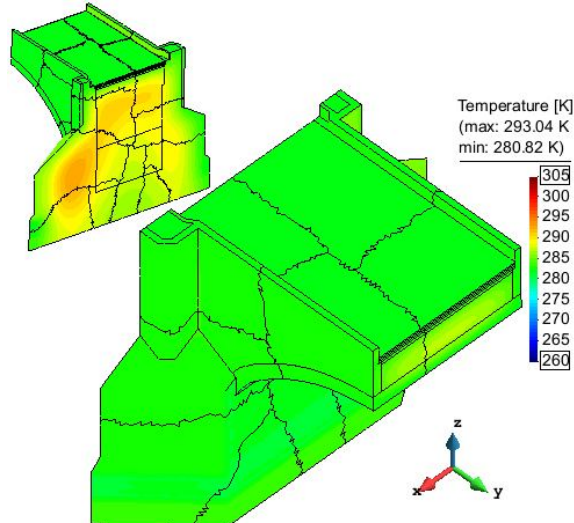


Figure 7.36 – Temperature values on 10/11/2011

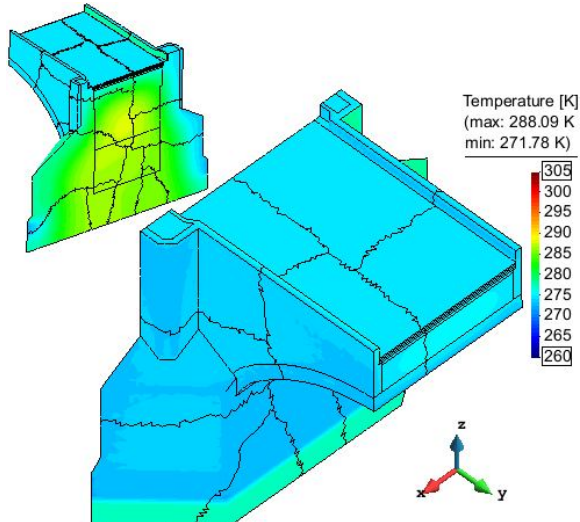


Figure 7.37 – Temperature values on 07/01/2012

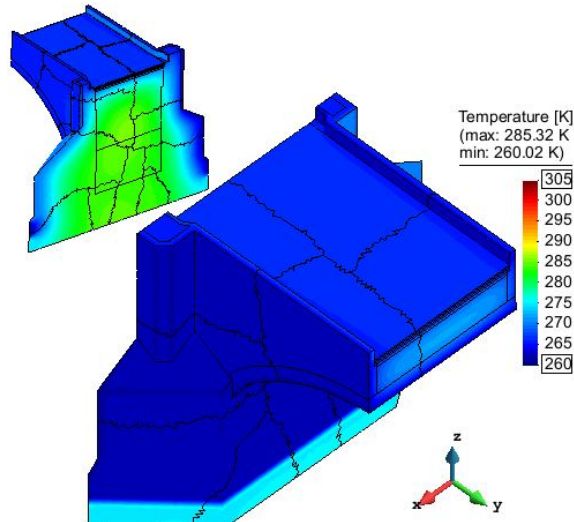


Figure 7.38 – Temperature values on 12/02/2012

7.4 Finite difference method (stretching of a plate)

The finite difference method (FDM), simple numerical approach, is used to investigate the stress state on a breast wall (including parapet), after the choice of adequate boundary conditions, to make then a rough comparison with FEM results.

The plane stress state ($\sigma_z = \tau_{xz} = \tau_{zy} = 0; \varepsilon_z \neq 0$) is considered. It is a problem of stretching of a plate (with uniform thickness) and it can be solved with deformation or force method: the second is chosen, having stresses as unknowns. In the 2D problem, equations of compatibility and of equilibrium are used, supported by Hooke's law (physical equations). Their combination brings to the Lévy's condition that, in this case ($\mu_{xy} = 0; \mu_x = \mu_y = E\alpha t$), can be written as (Prochazka, 1999):

$$\Delta(\sigma_x + \sigma_y + E\alpha t) + (1 + \nu) \left(\frac{\partial X}{\partial x} + \frac{\partial Y}{\partial y} \right) = 0 \quad (7.31)$$

where $\Delta = \frac{\partial^2}{\partial x^2} + \frac{\partial^2}{\partial y^2}$ is the Laplace harmonic operator and $E\alpha t$ introduces the thermal loading, with E as Young's modulus, α as thermal expansion coefficient, and t as variation of temperature.

To simplify the problem (7.31) in only one unknown, the Airy's stress function F is introduced, reaching:

$$\sigma_x = \frac{\partial^2 F}{\partial y^2}; \quad \sigma_y = \frac{\partial^2 F}{\partial x^2}; \quad \tau_{xy} = -\frac{\partial^2 F}{\partial x \partial y} \quad (7.32)$$

Substituting Eq. (7.32) into (7.31), a partial differential equation of the fourth order is obtained:

$$\Delta \left(\frac{\partial^2 F}{\partial y^2} + \frac{\partial^2 F}{\partial x^2} + E\alpha T \right) + (1 + \nu) \left(\frac{\partial X}{\partial x} + \frac{\partial Y}{\partial y} \right) = 0 \quad (7.33)$$

L'Hermite's analogy is used to obtain convenient boundary conditions with its two theorems (Prochazka, 1999):

- the derivative of the stress function F with respect to the direction of outward unit normal to the boundary is equal to the normal force on the fictitious frame. Its locus is identical with the boundary and the frame bears the same loading as the boundary of the plate; in formula:

$$\frac{\partial F}{\partial n} = N$$

- the stress function F at a boundary point is equal to bending moment at that point of the fictitious frame created from the shape of the boundary. Positive bending moment causes a tension in "internal fibres" of the frame; in formula:

$$F = M$$

Providing the assumption of volume loading has minor effect on the stress state, in comparison to temperature loading, the last component in equation (7.33) can be neglected: $(1 + \nu) \left(\frac{\partial X}{\partial x} + \frac{\partial Y}{\partial y} \right) = 0$ and the biharmonic equation with homogeneous biharmonic operator for the stress function F is obtained:

$$\Delta(\Delta F + E\alpha T) = 0 \quad (7.34)$$

As it is evident from the boundary conditions (constraints) in Figure 4.133 of Par. 4.7, the fictitious frame for L'Hermite's analogy is a statically undetermined structure. A principle of virtual displacements can be successfully applied for the resolution, and it can be written in general form as:

$$P \cdot \delta u = h \cdot \iint (\sigma_x \delta \varepsilon_x + \sigma_y \delta \varepsilon_y + \tau_{xy} \delta \gamma_{xy}) dx dy \quad (7.35)$$

where $\sigma_x, \sigma_y, \tau_{xy}$ are stresses, $\delta \varepsilon_x, \delta \varepsilon_y, \delta \gamma_{xy}$ are virtual strains, P is the unknown reaction and δu is the virtual displacement according to the unknown force. This equation must be completed by a kinematic condition of $\delta u = 0$.

Unfortunately, the calculation of all unknown reactions and virtual states is demanding and time consuming, therefore the simple estimation of boundary forces (stresses on the boundary) is adopted. The analogy with the fixed beam, where the axial stress is computed from the constant uniform temperature loading $\sigma_x = -E\alpha t$, is adopted, as already explained in Par. 4.7.

One possibility of solving the partial differential equation (7.33) is the finite difference method. The approximation of derivatives with their differences leads to a system of linear algebraic equations. Using the force method, the operator is biharmonic. The biharmonic equation is homogeneous when dealing with stretching, as in the analysed case. The consideration of constant thermal loading as externally applied action, allows to write Eq. (7.34) as:

$$\Delta(\Delta F + E\alpha t) = \frac{\partial^4 F}{\partial x^4} + 2 \frac{\partial^2 F}{\partial x^2 \partial y^2} + \frac{\partial^4 F}{\partial y^4} = 0 \quad (7.36)$$

The difference scheme (grid - mesh) is used for solving the biharmonic operator and it identifies nodal points with constant distance. The boundary should involve boundary nodal points (this makes it difficult to apply to general domains). Once the mesh is prepared, the template can be applied (Figure 7.40, Eq. (7.37)) (Prochazka, 1999), starting from the central point (i,j) and then placing it at each internal nodal point. $\delta = \delta_x = \delta_y$ is assumed for simplicity.

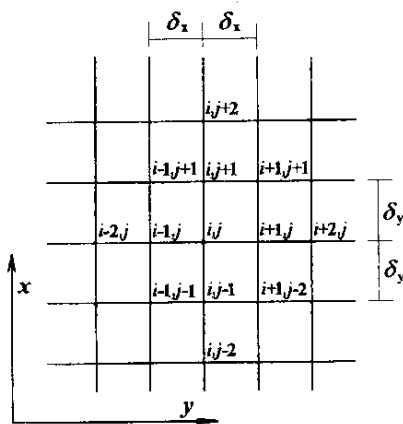


Figure 7.39 – Grid numeration
(Prochazka, 1999)

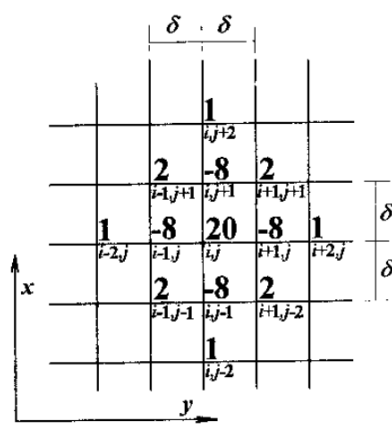


Figure 7.40 – Template of multipliers
(Prochazka, 1999)

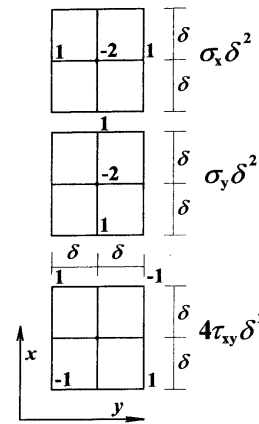


Figure 7.41 – Multipliers for stresses
(Prochazka, 1999)

Derivatives in Eq. (7.36) are expressed in final difference scheme obtaining Eq. (7.37), where multipliers in Figure 7.40 multiply the values of the stress function F at appropriate points.

$$20F_{i,j} - 8(F_{i+1,j} + F_{i,j+1} + F_{i-1,j} + F_{i,j-1}) + 2(F_{i+1,j+1} + F_{i+1,j-1} + F_{i-1,j+1} + F_{i-1,j-1}) + \\ + F_{i+2,j} + F_{i-2,j} + F_{i,j+2} + F_{i,j-2} = 0 \quad (7.37)$$

Fictitious nodal points are created since the template may overstep the nodal points in domain and boundary. Their values are considered additional unknowns and calculated from the boundary conditions. This numerical method possesses pivot dominance (members at the main pivot have higher values in comparison to other members in row or column) and the procedure leads to a system of algebraic linear equations.

Due to L'Hermite's analogy, $F = M$ at boundary points, while points outside the boundary are calculated according to the difference scheme of first derivative of external point in respect to internal point, e.g. $\frac{F_e - F_i}{2\delta} = \frac{\partial F}{\partial x}$ where $\frac{\partial F}{\partial x} = N$ if x is the direction of outward unit normal to the boundary.

According to Figure 7.41, it is possible to calculate stresses in Cartesian coordinates, as:

$$\sigma_x = \frac{\partial^2 F}{\partial y^2} = \frac{F_{j+1} - 2F_j + F_{j-1}}{h^2}; \quad \sigma_y = \frac{\partial^2 F}{\partial x^2} = \frac{F_{i+1} - 2F_i + F_{i-1}}{h^2} \quad (7.38)$$

$$\tau_{xy} = -\frac{\partial^2 F}{\partial x \partial y} = \frac{1}{4h^2} (-F_{i-1,j-1} + F_{i-1,j+1} - F_{i+1,j+1} + F_{i+1,j-1}) \quad (7.39)$$

Obtained the stresses in respect to Cartesian coordinates, principal stresses are calculated as:

$$\sigma_1 = \frac{\sigma_x + \sigma_y}{2} + \sqrt{\frac{(\sigma_x - \sigma_y)^2}{4} + \tau_{xy}^2}; \quad \sigma_2 = \frac{\sigma_x + \sigma_y}{2} - \sqrt{\frac{(\sigma_x - \sigma_y)^2}{4} + \tau_{xy}^2} \quad (7.40)$$

moreover: $\tan 2\alpha = \frac{2\tau_{xy}}{\sigma_x - \sigma_y}$ where α is the angle of incidence of the principal stress.

Finally, the comparison between σ_1 , σ_2 and following Eq. (7.41) and (7.42), coming from the rotation of original coordinate system from $Oxyz$ to $Ox'y'z'$ by α , allows to understand to which principal stress the angle α is referred.

$$\sigma'_x = \sigma_x \cos^2 \alpha + \sigma_y \sin^2 \alpha - \tau_{xy} \sin 2\alpha \quad (7.41)$$

$$\sigma'_y = \sigma_x \sin^2 \alpha + \sigma_y \cos^2 \alpha + \tau_{xy} \sin 2\alpha \quad (7.42)$$

7.4.1 Further development

The analysis performed with finite difference method was limited in considering the variation of temperature as constant on all the masonry body (breast wall plus parapet), but this is not realistic, as next pictures explain.

Figure 7.42 – Figure 7.44 show the temperature variance between seasons maintaining the same scale, while subsequent Figure 7.45 – Figure 7.47 mark the different distribution of values along the body, using each one a narrower plotting scale.

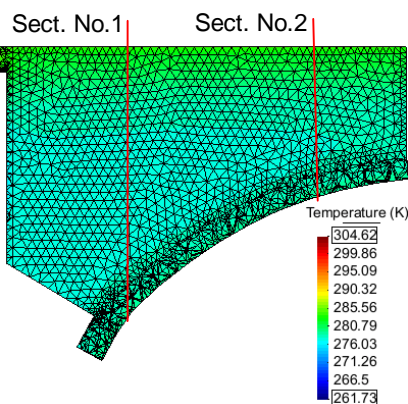


Figure 7.42 – Average temperatures

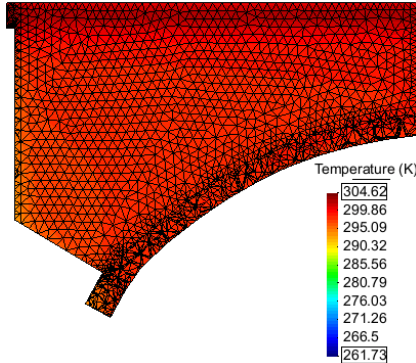


Figure 7.43 – Summer temperatures

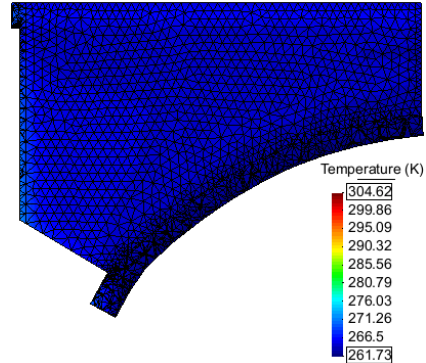


Figure 7.44 – Winter temperatures

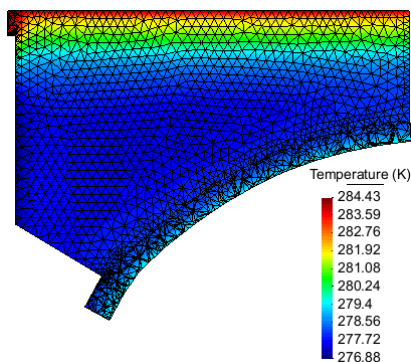


Figure 7.45 – Average temperatures

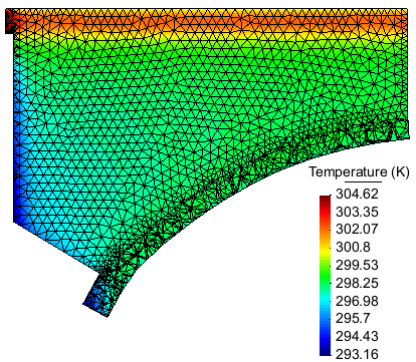


Figure 7.46 – Summer temperatures

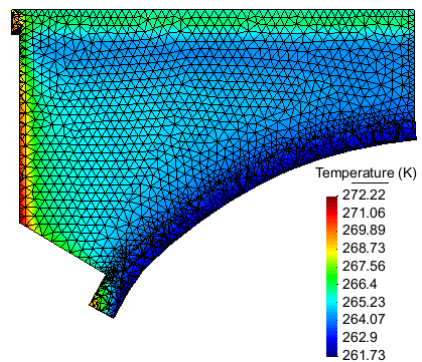


Figure 7.47 – Winter temperatures

The temperature values are almost constant along the length (at least in the upper part of the structure, where the attention is focused on, because highest damage was recorded) but vary along the depth. Figure 7.48 shows the trend, plotting results of two different sections (No.1 and No.2 as identified in Figure 7.42) and providing the maximum variation, lower in the average values of May, as expectable.

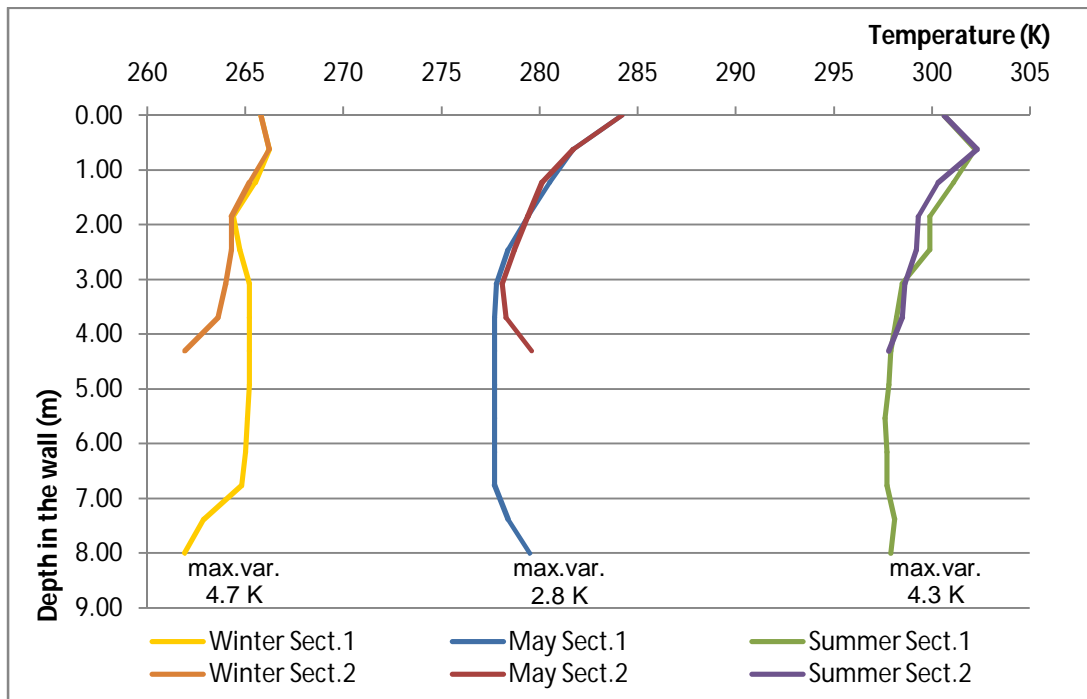


Figure 7.48 – Temperature distribution in April, August and February for 2 vertical sections

It is clear that these trends should be taken into account in the finite difference method analysis, as well as the variance of values from the average condition.

To do this, the non constant thermal loading in vertical direction can be approximated in way to provide a piecewise linearly increasing/decreasing loading function, that would be the new external load ($\sigma_x = -E\alpha t$), applied on the frame, as previously described in Par. 4.7. The effect would not be only of tension and compression, because the changing thermal loading would cause also shear stresses and bending, since some parts of the structure would expand/contract more than others.

Better accuracy in results would be obtained but the proficiency of this method cannot be compared with the outcome of computer-aided and “omni-comprehensive” FEM that, in fact, is the most used for this kind of simulations.

Furthermore, higher precision could be reached choosing a more refined mesh (hence reducing the grid step) but this would increase the number of equations, slowing their computation.

7.5 Rehabilitation

According to (Lourenco, 2002), the modern principles of intervention on historical buildings include aspects as:

- removability (total reversibility is often impossible);
- unobtrusiveness, minimum repair and respect of the original conception;
- safety of the construction;
- durability of materials;
- balance between cost and available financial resources;
- chemical, rheological, thermal and mechanical compatibility of materials (Gattesco, 2012).

Some of the required features of a correct intervention show a certain relationship and can be considered combined: for example, reversibility and non-obtrusiveness might be less considered if the materials are extremely durable and fully compatible with the existing ones. On the other side, if the materials are not "historically-durable" they should be fully reversible and not-obtrusive, this is for example the case of steel and FRP strengthening devices (Gattesco, 2012).

In general, masonry arches were not designed for actual traffic loads as well as breast walls were not designed to withstand out of plain actions (e.g. seismic action, filling thrust); as already explained, temperature may cause high stresses too. For these reasons cracks in the vault (Figure 7.49), separation between breast wall and arch, and vertical cracks in the breast wall (Figure 7.50) may appear.

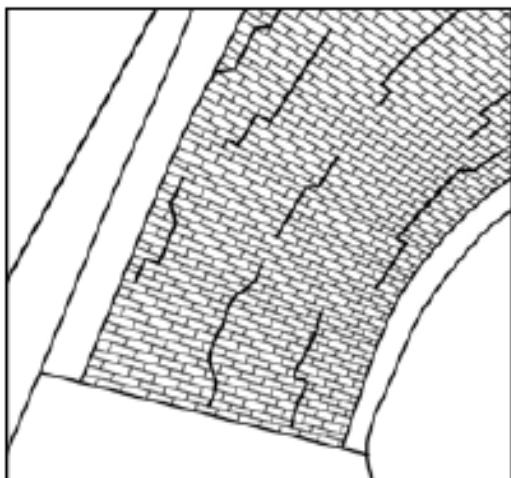


Figure 7.49 – Longitudinal cracks in the vault
(Gattesco, 2012)

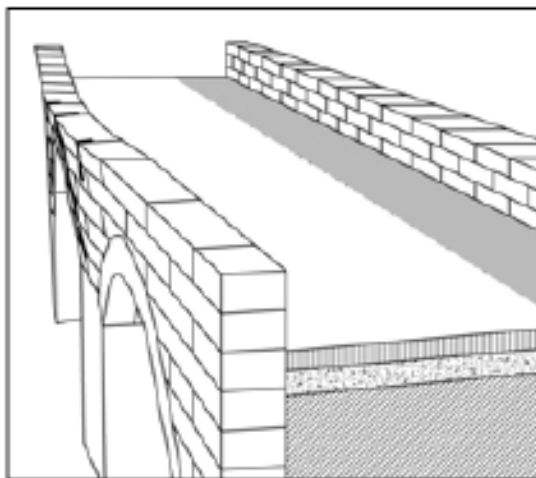


Figure 7.50 – Possible out-of-plane mechanism in the breast wall (Gattesco, 2012)

Furthermore, the structural performance is always affected by material deterioration, intensified by water contact that enhances freeze-thaw and chemical actions (Gattesco, 2012). Therefore a correct rehabilitation should deal with strengthening as well as chemical protection. (Gattesco, 2012) suggests different ways to solve problems related to in-plane shear on breast walls (due to filling thrust and temperature gradient) as well as out-of-plane flexure (caused by the lateral filling thrust or by earthquakes).

Grout injections in the different kinds of masonry can improve the interface contact between stone blocks (increasing the strength) and prevent the penetration of aggressive agents. If the infill has good mechanical properties, it is possible to use horizontal tie bars to connect the 2 opposite breast walls and to fasten them with the infill (Figure 7.51). Similar bars should be put prestressed also in holes drilled longitudinally in the vault, in way to contrast the tensile stresses due to temperature variations. Furthermore, the vertical application of tie bars to the breast walls would provide flexural resistance against horizontal seismic actions (Gattesco, 2012).

On the opposite side, if the inner material is coarse, the best solution is to remove it (reducing weight and lateral thrusts) and to replace it with internal spandrel walls (of properties similar to the external masonry), linked by transversal walls (Figure 7.52), to increase in-plane shear resistance and out-of-plane flexural resistance of breast walls (Gattesco, 2012). The effectiveness of the intervention would require also to strengthen vault and breast walls. The intervention on the vault can be made by adding a reinforced concrete coating at the extrados, adequately connected to the masonry; this action would increase tensile strength and bearing capacity.

Those actions should be carefully compared with the increased rigidity of the structure that, as already said, brings to sensibility toward non-stress effects. Testing and numerical simulations are useful tools for checking the effectiveness and backside-effects of the intervention.

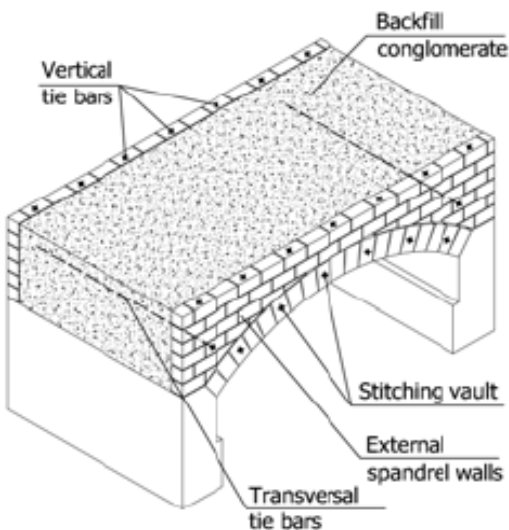


Figure 7.51 – Intervention without backfill removal

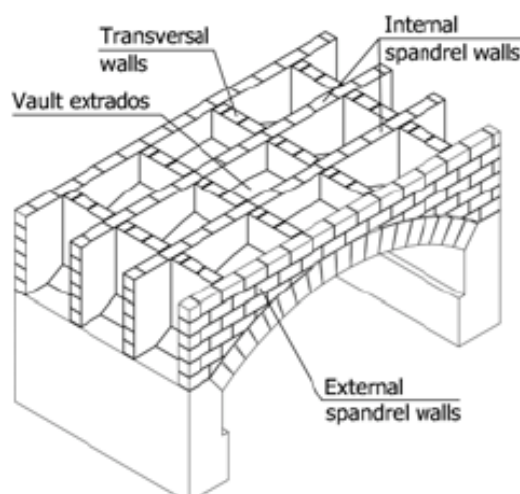


Figure 7.52 – Intervention with backfill removal

Proposed techniques (Gattesco, 2012) to strengthen the breast walls of a bridge (against actions mainly related to filling thrust and earthquake) deal with mortar coating, reinforced with a GFRP grid on both sides (Figure 7.53) or with the GFRP grid on one side and a net with small diameter stainless steel tendons on the other side (Figure 7.54). The second solution is used if the external wall cannot be plastered, embedding the steel tendons in the joints (of a brick masonry). The lime cement mortar coating with GFRP grid is 30-35 mm thick and 2 coatings are connected toward the wall by GFRP bars (or with stainless steel bars in the second solution) passing in holes drilled in the wall (6 per square meter). In the case with steel bars, the external 25 mm of mortar joint is removed, a first repointing

with high strength mortar is applied and after its curing the tendons are placed. Those are then fixed with the transversal steel connectors and then the repointing is completed. The strength advantage provided by coatings has to be carefully compared with the possible detrimental increase of rigidity.

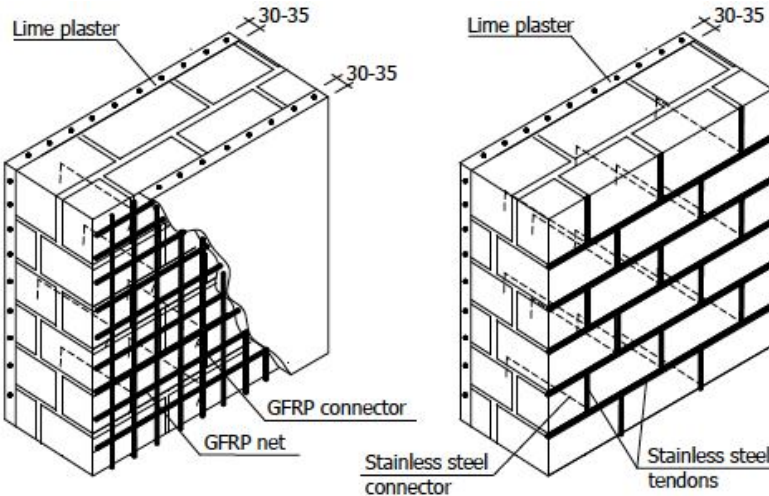


Figure 7.53 – Use of GFRP reinforced coating Figure 7.54 – Use of hybrid GFRP-stainless steel tendon net

About the already mentioned intervention on the vault adding a reinforced concrete coating at the extrados, a proposal to obtain it avoiding to stiffen and burden the structure, comes from (Jurina, 2012). The limit analysis "safe theorem" states that the arch is safe if it is possible to find a thrust line (in equilibrium with self-weight and external loads) that lies within the thickness of the arch. If the thrust line is inside the middle third of every section, the structure does not present tension stresses. If the thrust line reaches the boundary of the arch, a hinge is going to form there; 4 hinges (or 5, in a symmetric configuration) bring the structure to the collapse. Jurina's Reinforced Arch Method (RAM) consists in avoiding the formation of one of the plastic hinges (at the intrados or at the extrados) thanks to FRP or steel bars working in tension, in way to prevent the failure. It is possible to create an active system applying a predefined tension to the bars, in way to induce an axial compression between the blocks (re-centring the thrust line). The system does not add weight and does not interfere with the in situ material, respecting the original structural behavior. It allows to increase both limit load capacity and ductility of the vault, enhancing a better response to seismic action.

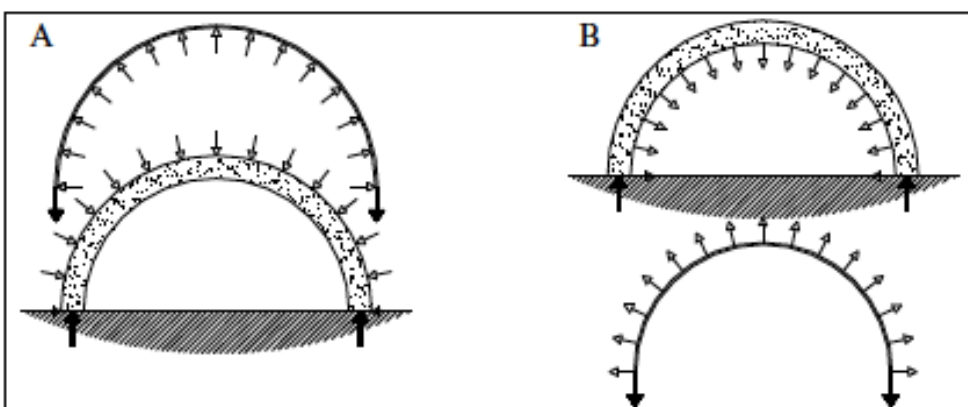


Figure 7.55 – Interaction forces between cable (in tension) and arch (in compression) when a post-tensioned cable is placed at extrados (A) or intrados (B) (Jurina, 2012)